UNIVERSITY OF SOUTHAMPTON
FACULTY OF PHYSICAL SCIENCES AND ENGINEERING
PHYSICS AND ASTRONOMY

X-ray Spectroscopy of Accreting Black Holes

by

Daniel Steven Plant

Thesis for the degree of Doctor of Philosophy
September 9, 2014

UNIVERSITY OF SOUTHAMPTON

ABSTRACT

FACULTY OF PHYSICAL SCIENCES AND ENGINEERING

PHYSICS AND ASTRONOMY

Doctor of Philosophy

X-RAY SPECTROSCOPY OF ACCRETING BLACK HOLES

by Daniel Steven Plant

Measuring black hole spin has become a key topic in astrophysics, and recent focus on the spin powering of jets in X-ray binaries has heightened the need for accurate measurements of spin. However, the effects of spin are subtle, and are only imprinted on emission from very close to the black hole. This is revealed since the black hole spin defines the radius of the last stable orbit of the accretion disc, which is smaller for larger spin. Recent advances in X-ray observatories and spectroscopic techniques have enabled spin estimates for a number of black holes in X-ray binaries, but the accuracy of these methods, and the link between spin and jet power, have become very controversial subjects. In this thesis I address the former of these problems through X-ray reflection, which is one of two leading X-ray spectroscopic methods to measure black hole spin (the other being the 'continuum' method).

Firstly, I investigate the systematic uncertainties associated with the X-ray reflection technique, and display how model degeneracies can severely affect the determination of spin. After establishing these potential flaws I then performed a systematic study of X-ray reflection during four hard state observations of the black hole GX 339−4, and show that the relativistic effects vary significantly over two orders of magnitude in luminosity. I show that this requires the accretion disc to be substantially truncated from the last stable orbit that is used to measure spin, thus rendering spin estimates impossible in the hard state. Following this I analyse over 500 archival observations of the same source with the *Rossi Timing X-ray Explorer*. Whilst these data cannot directly measure the inner disc radius, they allow a quantitative investigation of how X-ray reflection and the power-law co-evolve. Since the latter gives rise to the former, this allows changes in the accretion geometry to be revealed, which I show to be consistent with a truncated accretion disc in the hard state, and a gradual collapse of the corona in the soft state. Finally, I present three recent observations of GX 339−4 in the hard state with *XMM-Newton*, which allow an unprecedented simultaneous constraint on the inner accretion disc radius via the reflection *and* continuum methods. The two techniques agree, and present further compelling evidence for accretion disc truncation in the hard state.

CONTENTS

LIST OF TABLES

LIST OF FIGURES

ABBREVIATIONS

A&A	Astronomy and Astrophysics
ADAF	Advection Dominated Accretion Flow
AGN	Active Galactic Nuclei
ATCA	Australia Telescope Compact Array
BH	Black Hole
BHXRB	Black Hole X-ray Binary
CTI	Charge Transfer Inefficiency
EW	Equivalent Width
HEXTE	High Energy X-ray Timing Experiment
HID	Hardness-Intensity Diagram
HIMS	Hard-Intermediate State
HMXB	High-Mass X-ray Binary
HXD	Hard X-ray Detector
ISCO	Innermost Stable Circular Orbit
LFQPO	Low Frequency Quasi-Periodic Oscillation
LMXB	Low-Mass X-ray Binary
MAXI	Monitor of All Sky Image
MCMC	Markov Chain Monte Carlo
MNRAS	Monthly Notices of the Royal Astronomical Society
PCA	Proportional Counter Array
PDS	Power Density Spectra
PSF	Point Spread Function
QPO	Quasi-Periodic Oscillation
RID	RMS-Intensity Diagram
RF	Reflection Fraction
RXTE	Rossi X-ray Timing Explorer
SIMS	Soft-Intermediate State
XID	X-ray Imaging Spectrometer
XMM	X-ray Multi-Mirror Mission
XRB	X-ray Binary

DECLARATION

I, Daniel Steven Plant, declare that the thesis entitled *X-ray Spectroscopy of Accreting Black Holes* and the work presented in the thesis are both my own, and have been generated by me as a result of my own original research. I confirm that:

- this work was done wholly or mainly while in candidature for a research degree at this University;
- where any part of this thesis has previously been submitted for a degree or any other qualification at this University or any other institution, this has been clearly stated;
- where I have consulted the published work of others, this is always clearly attributed;
- where I have quoted from the work of others, the source is always given. With the exception of such quotations, this thesis is entirely my own work;
- I have acknowledged all main sources of help;
- where the thesis is based on work done by myself jointly with others, I have made clear exactly what was done by others and what I have contributed myself;
- parts of this work have been published as:
  - Revealing accretion on to black holes: X-ray reflection throughout three outbursts of GX 339−4, 2014, MNRAS, 442, pp. 1767–1785
  - The truncated and evolving inner accretion disc of the black hole GX 339−4, A&A, submitted
  - The low/hard state of GX 339−4 with the XMM-Newton small window mode, in prep.

Daniel Steven Plant, September 9, 2014

Acknowledgements

First and foremost, I would like to thank my supervisor, Rob Fender, who not only afforded this opportunity, but also guided me through the trials and tribulations of astronomy and academia, despite having to put up with my often 'florid' style of writing. Secondly, I must thank my MPhys supervisor at Lancaster, Anupam Mazumdar, who sparked my interest in black holes, and ultimately set me on this journey.

Much thanks must also go to everyone at Southampton, who made it such a brilliant place to live and work for three and a half years. Liz Bartlett, Dan Calvelo, Lee Townsend, Martin Bell – for all the banter, ranting, Jägerbombs (mainly Liz), IDL mastery (Liz again), flat-parties, and angry egg-throwing (Martin). I could not have asked for a better bunch of office-mates to begin my PhD with. Tana Joseph – for your unparalleled humour, and the football watching of course. You've even almost convinced me Stoke is a legitimate team to support. Almost. Sadie Jones – for not leaving when everyone else did! Gabriele Ponti – for knowing how to best annoy Teo. Mari Kolehmainen – for your dedication to Monday, Tuesday, Wednesday, Thursday and Friday pub. James Matthews/Teo Muñoz-Darias/Adam Stewart – for caring about football at least as much as I do. Also thanks to the staff at Southampton, especially Tom Maccarone, Phil Uttley and Christian Knigge for all your help. Shout-outs as well to Jess Broderick, Rene Breton, Gosia Pietka and Pieter van Oers.

I have also had the chance to collaborate for some brilliant people during my time at Southampton, to whom I owe so much. In particular, Mickäel Coriat – for spending countless hours introducing me to XSPEC; Gabriele – for, to this day, answering all my silly questions, and always finding the time to do so; and Teo – for the never-ending advice and support. Oh, and of course, no thesis acknowledgements would be complete without a mention of Simon Harris, a true computing hero.

I am immensely grateful for the relentless support of my parents, who throughout my studies have offered the utmost encouragement, enthusiasm, and also Mum's car whenever I needed it. Or when I didn't need it, and just wanted it. But in all seriousness, you have always backed me and I could not have made it this far without you. Thanks as well to Dave, Phil, Nick and Chris; I have known you most of my life, you have seen me dodge tax in various different ways as we have all taken different paths to different places, but you four are still by best friends, you guys make life DENCH. Also, Sid, Will, Tasha, Em, Mark and Andrew for all the fun times outside of work. And Simon, for enduring Arsenal with me (9 years! The wait is finally over!).

Finally, I am forever grateful to my girlfriend Rachael. Your unwavering support and belief have meant so much, particularly over the past year when I needed it most.

Daniel Steven Plant, September 9, 2014

For Mum and Dad

"*In my entire scientific life, extending over forty-five years, the most shattering experience has been the realization that an exact solution of Einstein's equations of general relativity, discovered by the New Zealand mathematician, Roy Kerr, provides the absolutely exact representation of untold numbers of massive black holes that populate the universe. This shuddering before the beautiful, this incredible fact that a discovery motivated by a search after the beautiful in mathematics should find its exact replica in Nature, persuades me to say that beauty is that to which the human mind responds at its deepest and most profound.*"

S. CHANDRASEKHAR (1975)

1 Introduction

1.1 An introduction to black holes

In lucid terms, black holes represent a body of such gravitational might that even light cannot escape. Despite the term ‘black hole’ being famously coined by John Wheeler in the 1960s, the notion of such an object has existed for more than 200 years. In 1783 John Michell, a Fellow of the Royal Society, noted that a body of radius 500 times that of the sun, and of the same density, would have an escape velocity equal to the speed of light, and thus all light emitted would not escape. With the advent of general relativity in 1915, Einstein’s theory of gravitation, the manner in which gravity was recognised changed forever. Whilst Newtonian mechanics describes gravity as a force through which two bodies attract, in general relativity gravity curves the surrounding space-time. The greater the mass, the greater space-time is distorted. It took only a matter of months for Karl Schwarzschild to demonstrate the solution for the space-time around a non-rotating spherically symmetric body. It was later realised that within the Schwarzschild metric, an observer at infinity (i.e. far from the black hole) sees time and distance tend to zero and infinity respectively near the central body. This location became known as the event horizon, which is characterised by the Schwarzschild radius.

The physical implication of this was not immediately recognised. In 1930 Subrahmanyan Chandrasekhar considered the structure of *white dwarfs*, and discovered that there exists a finite mass ($\sim 1.44\,M_\odot$) above which the degenerate electrons would become relativistic, and thus induce further gravitational collapse. This surprised the community, and for the first time brought to light the reality of a body collapsing to nothing more than a singularity. Once electron degeneracy pressure is overcome, it is expected that neutron degeneracy pressure will still resist gravity, and such an object is known as a *neutron star*. The limit by which this degeneracy is overwhelmed is uncertain, but around $3\,M_\odot$ appears to be a reasonable and popular limit. Beyond this gravitational collapse is unavoidable and a black hole can be formed.

Which compact object (white dwarf, neutron star or black hole) is initially born depends mainly on the mass of the original star. Most stars will form a white dwarf; the Sun for example, which is an average star, will form a white dwarf. Larger stars ($> 8\,M_\odot$) will undergo a supernova explosion driven by the gravitational collapse of the stellar core. The larger the star, the more compact the core will be, and thus it is expected that the core of a star of mass $> 20\,M_\odot$ will be able to directly form a black hole when it eventually collapses.

The most remarkable quality of black holes is that they are exceptionally simple; in general relativity they are described by just three parameters: mass M, charge Q and angular momentum (spin) J. Furthermore, on macroscopic scales the charge is expected to be neutralised. To this end, John Wheeler was again at hand to quip that *black holes have no hair*. All the information about the matter that has led to the formation of the black hole is lost, and is converted into just mass and spin. Since stellar mass black holes are relics of massive stars, which have short evolutionary timescales ($<10^6$ years), much less than the age of the Milky Way ($\sim 10^{10}$ years), there is expected to be a very large number of stellar mass black holes in our galaxy ($\sim 10^8$; van den Heuvel 1992). However, by definition one cannot observe a black hole directly; but instead, we can use their interaction with other objects.

1.1.1 Black hole binaries

An X-ray binary (XRB) is a binary system consisting of a star and a compact object companion. A sub-class of XRBs are black hole X-ray binaries (BHXRBs), in which the compact object is a black hole. Whilst such a system may sound exotic, around 70% of massive stars are expected to exist in binaries (Sana *et al.*, 2012). The companion star can feed matter on to the black hole via two modes: (1) Roche

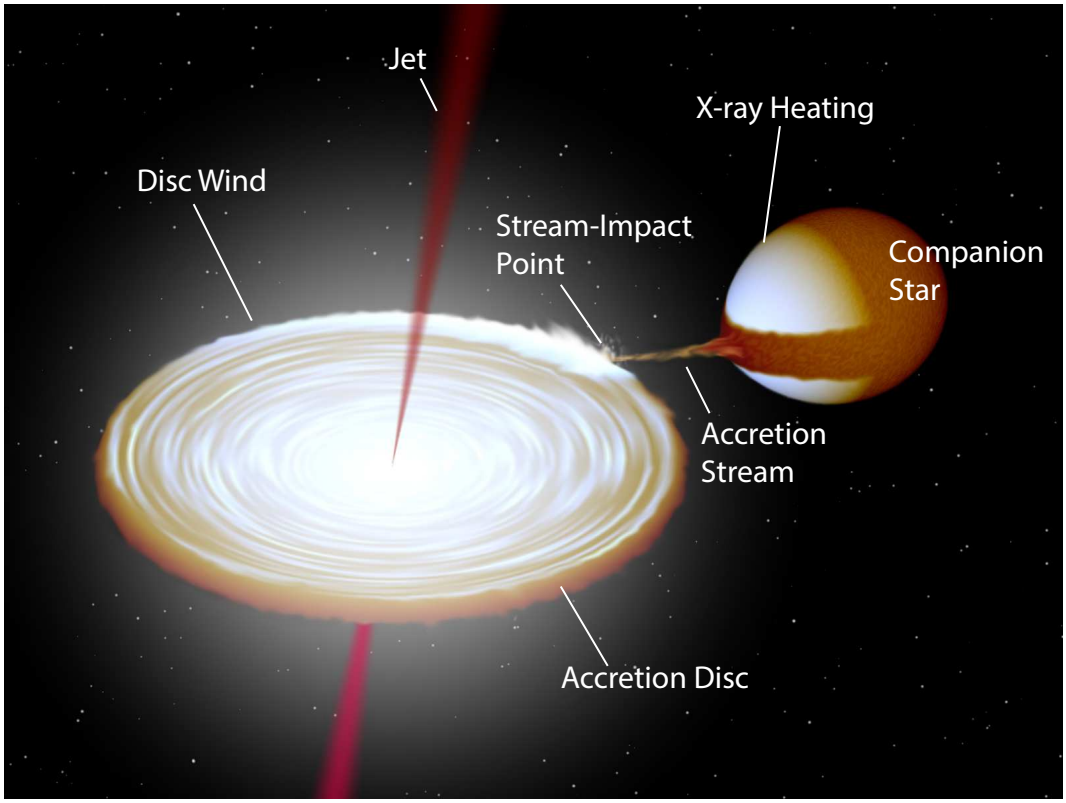

Figure 1.1: An artist's impression of a LMXB, with the key elements of the binary indicated. Adapted from Fender and Belloni (2012), created by Rob Hynes.

lobe overflow, where the binary separation becomes small enough that the outer material of the star can be removed by the gravitational field of the black hole; or (2) by stellar wind accretion, where the companion star ejects material which is then gravitationally captured by the black hole (for a review on the formation of XRBs, see Tauris and van den Heuvel 2006).

XRBs are separated into two distinct classes: Low-mass X-ray binaries (LMXBs; Fig. 1.1), which have an old ($> 10^9$ yrs) low mass ($M \sim 1\,M_\odot$) companion feeding via its Roche lobe; and High-mass X-ray binaries (HMXBs), which have a young ($< 10^7$ yrs) OB-type massive donor star ($M > 10\,M_\odot$) feeding via its stellar wind (Remillard and McClintock, 2006). There are 21 dynamically confirmed stellar mass black holes (i.e. $M_{\rm BH} > 3\,M_\odot$; Casares and Jonker 2013), plus an additional 30+ strong candidates (Özel *et al.*, 2010), and of those confirmed, only a few have high-mass companions.

The angular momentum of the in-falling matter must be conserved; thus, since the star and black hole are in orbit about each other, the matter spirals and forms a disc, known as an 'accretion disc' (Fig. 1.1).

1.2 Accretion on to black holes

For a given mass accretion rate, $\dot{M} = dm/dt$, the maximum luminosity of an accreting object of mass M and radius R is

$$L = G\dot{M}M/R. \tag{1.1}$$

Since a black hole has no solid surface, some portion of the accreted mass will pass beyond the event horizon without radiating. The efficiency of the accretion is represented by η, thus the luminosity of an accreting black hole is

$$L = \eta \dot{M} c^2 \tag{1.2}$$

where the R has been replaced by the Schwarzschild radius $R_{\rm S} = 2GM/c^2$, which represents the event horizon. However, the event horizon of a spinning black hole, as derived using the Kerr metric, is in fact smaller, and reduces to $\sim 1\, r_{\rm g}$[1] for a maximally spinning black hole. Furthermore, not every value of R has a stable orbit, and the innermost stable circular orbit (ISCO) is itself dependent upon the spin parameter a. The radius $R_{\rm isco}$ is $6\, r_{\rm g}$ and $1.235\, r_{\rm g}$ for a zero and maximal spin black hole respectively, which is discussed later in §1.5. Since the accreting matter can radiate closer to the black hole for larger values of spin, and therefore deeper within the potential well, the efficiency η also increases with spin. Thorne (1974) showed that $\eta \sim 0.06$ and $\eta \sim 0.3$ for Schwarzschild and maximal prograde Kerr ($a = 0.998$) black holes respectively, thus accretion is by far the most efficient form of energy conversion known in the Universe. To compare, the efficiency of nuclear burning of hydrogen to helium is $\eta_{\rm nuclear} \sim 0.007$, and for a neutron star, which has a solid surface, $\eta_{\rm NS} \sim 0.1$.

For the black hole to accrete, the gravitational force causing the matter to fall inward must exceed the radiation pressure moving outwards, which exerts a force as it scatters off the surrounding material. The inward gravitational force for a electron-proton pair at a distance R from a black hole of mass $M_{\rm BH}$ is

$$F_{\rm grav} = \frac{GM_{\rm BH}}{R^2}(m_{\rm p} + m_{\rm e}) \approx \frac{GM_{\rm BH}m_{\rm p}}{R^2} \tag{1.3}$$

where $m_{\rm p}$ and $m_{\rm e}$ are the mass of the proton and electron respectively. The outward radiation force is

[1] The unit $r_{\rm g}$ refers to the gravitational radius, where $1\, r_{\rm g} = GM/c^2$. The Schwarzschild radius $R_{\rm S}$ is therefore at $2\, r_{\rm g}$.

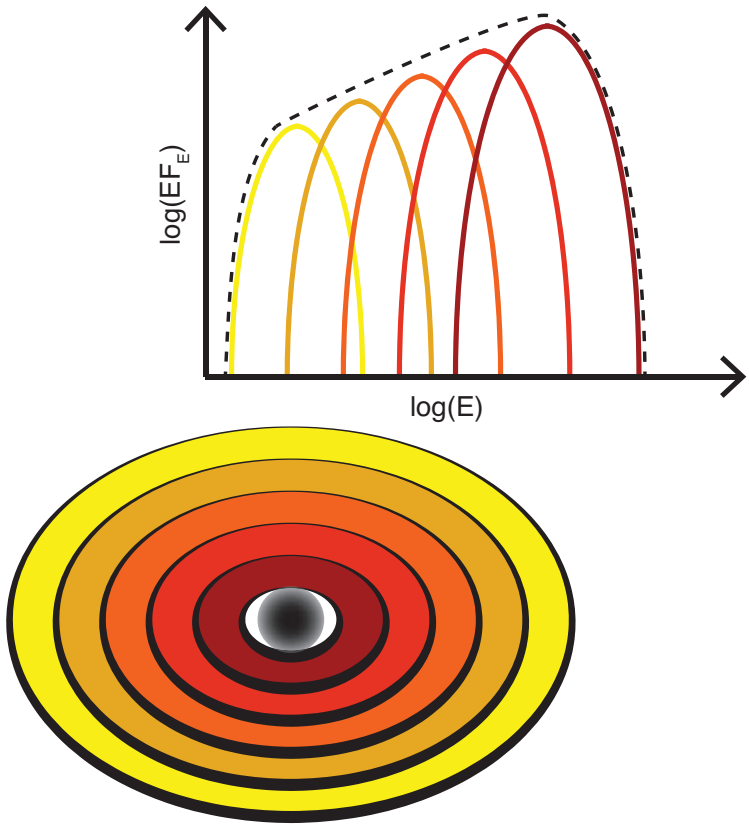

Figure 1.2: Each radius of the disc emits as a blackbody, thus the spectrum of the accretion disc forms a multi-colour blackbody shape. At smaller radii the peak temperature is larger (Eq. 1.6)

$$F_{\rm rad} = \frac{\sigma_{\rm T} L}{4\pi R^2 c} \tag{1.4}$$

where $\sigma_{\rm T}$ is the Thompson electron scattering cross-section, and L is the luminosity of the source accreting. In using the Thompson cross-section we are assuming that the gas is fully ionised. The point at which these two forces are equal corresponds to a limit on the amount of matter that can be accreted. This is known as the *Eddington luminosity*, and is given by

$$L_{\rm Edd} = \frac{4\pi G M_{\rm BH} m_{\rm p} c}{\sigma_{\rm T}} \approx 1.3 \times 10^{38} \left(\frac{M}{M_\odot}\right) \quad \text{erg s}^{-1}. \tag{1.5}$$

The corresponding Eddington mass accretion rate is $\dot{M}_{\rm Edd} = L_{\rm Edd}/\eta c^2$. It should be noted that this assumes spherically symmetric accretion of a pure hydrogen gas, which is likely to be unphysical.

The famous Shakura-Sunyaev α–disc model (Shakura and Sunyaev, 1973) describes a cool, optically thick, geometrically thin accretion disc. For a mass accretion rate of $\dot{M}$, moving inwards from $R \rightarrow R + \Delta R$, the rate of potential energy

released is $L = (G\dot{M}M_{\rm BH}/R^2) \times \Delta R$. The virial theorem ($2K + U = 0$) requires that half of the potential energy is converted into kinetic energy, thus only half of it can be radiated. The optically thick disc will quickly thermalise and therefore emit as a black-body $L = \Delta A \sigma T^4$, where $\Delta A = 2 \times 2\pi R \times \Delta R$, which is the area of the emitting ring (with the factor 2 for both sides), and $\sigma_{\rm SB}$ is the Stefan-Boltzman constant. Hence,

$$T = \left(\frac{G\dot{M}M_{\rm BH}}{8\pi R^3 \sigma_{\rm SB}} \right)^{1/4}. \tag{1.6}$$

The disc spectrum is therefore a sum of blackbody components from each radius, which each have a different characteristic temperature, essentially creating a multi-colour blackbody spectrum (see Fig. 1.2). From the above it can be seen that the temperature increases at smaller radii, thus the peak temperature of the spectrum comes from the inner edge of the accretion disc. For reasonable values[2], this shows that the disc spectrum of a BHXRB will peak in the soft X-rays.

Finally, by inserting $R = R_{\rm in} \approx R_{\rm S}$ we then find that

$$T_{\rm in} \propto M_{\rm BH}^{-1/4} \tag{1.7}$$

for a given Eddington ratio $\dot{M}/\dot{M}_{\rm Edd}$, since $\dot{M} \propto M_{\rm BH}$. Therefore, the peak temperature decreases considerably for larger masses. In the case of AGN, which typically have masses $10^6 - 10^9\,{\rm M}_\odot$, the disc spectrum peaks in the ultraviolet.

The model most commonly used to describe the accretion disc spectrum is DISKBB (Mitsuda *et al.*, 1984), which is parameterised by the apparent inner radius of the disc $R_{\rm in}$ and the peak temperature $T_{\rm in}$. However, there are a number of corrections required to determine the effective peak temperature, two being the boundary condition (Gierliński *et al.*, 1999) and relativistic corrections (Zhang *et al.*, 1997). The spectrum will also be modified by the opacity of this disc, which requires a colour-correction factor $f_{\rm col}$ of 1.6–2.0 (Shimura and Takahara, 1995; Merloni *et al.*, 2000; Davis *et al.*, 2005). Through Eq. 1.6 it can be seen that $L \propto T^4$; thus, by observing just L and $T_{\rm in}$, one can test whether the disc inner radius $R_{\rm in}$ remains constant over time. The DISKBB model is used a number of times in this thesis.

[2]For a black hole of mass $M_{\rm BH} = 10\,M_\odot$, accreting at $0.1\,\dot{M}_{\rm Edd}$ with an efficiency of $\eta = 0.1$, the peak temperature would be 1.7 keV.

1.3 Black hole spectral states

The two donor feeding mechanisms described at the start of §1.1.1 gives rise to two very different behaviours. Typically, HMXBs are persistently bright ($> 0.01\,L_{Edd}$), whereas LMXBs are transient, exhibiting bright outbursts lasting for months or even years, punctuated by long periods of quiescence ($< 10^{-6}\,L_{Edd}$; Fig. 1.3). These two classes of object are referred to as 'persistent' and 'transient' sources respectively. The transient nature is thought to be driven by accretion disc instabilities, and the leading candidate is the hydrogen instability model (see Meyer and Meyer-Hofmeister 1981; Coriat *et al.* 2012 and references therein). At low accretion rates the gas temperature is low, as is the opacity; however, the opacity increases steeply with temperature, which leads to a thermal runaway until the hydrogen is nearly completely ionised. This thermal instability leads to the viscous instability, whereby the mass accretion rate increases with temperature. The central mass accretion rate then exceeds the mass transfer rate from the donor star, which adds a duration limit for the outburst cycle. It is thought that persistent sources are able to keep the hydrogen sufficiently ionised by having a high donor mass accretion rate, which allows a consistently high accretion rate on to the black hole.

The typical X-ray spectrum of a BHXRB can be isolated into two main components: a soft (peak ~ 1 keV above $0.05\,L_{Edd}$) quasi-blackbody spectrum and a hard power-law tail. The quasi-blackbody spectrum arises from the geometrically thin, optically thick, accretion disc, as described before in §1.2 (see also Fig. 1.2). The power-law spectrum is believed to come from 'seed' photons from the disc being Compton up-scattered in a 'corona' of hot ($10^8 - 10^9$ K) electrons. The spectrum will also be absorbed by intervening material, which can be quite significant due to the distance of sources and that they are often located in, or close to, the galactic plane.

Three distinct spectral states have been observed depending on the relative contribution of these two components. I describe these below, but I also refer the interested reader to the excellent reviews by Remillard and McClintock (2006); McClintock *et al.* (2006); Done *et al.* (2007); Belloni *et al.* (2011); and Fender and Belloni (2012). Figure 1.4 displays the typical spectra of the canonical black hole Cygnus X-1 in these three states.

The low/hard state

The *low/hard state* (hereafter 'hard state') is dominated by a hard power-law component. The photon index is rather flat ($\Gamma \sim 1.4 - 1.7$, where $N(E) = N_0 E^{-\Gamma}$) and an exponential cut-off is often observed between 20–150 keV

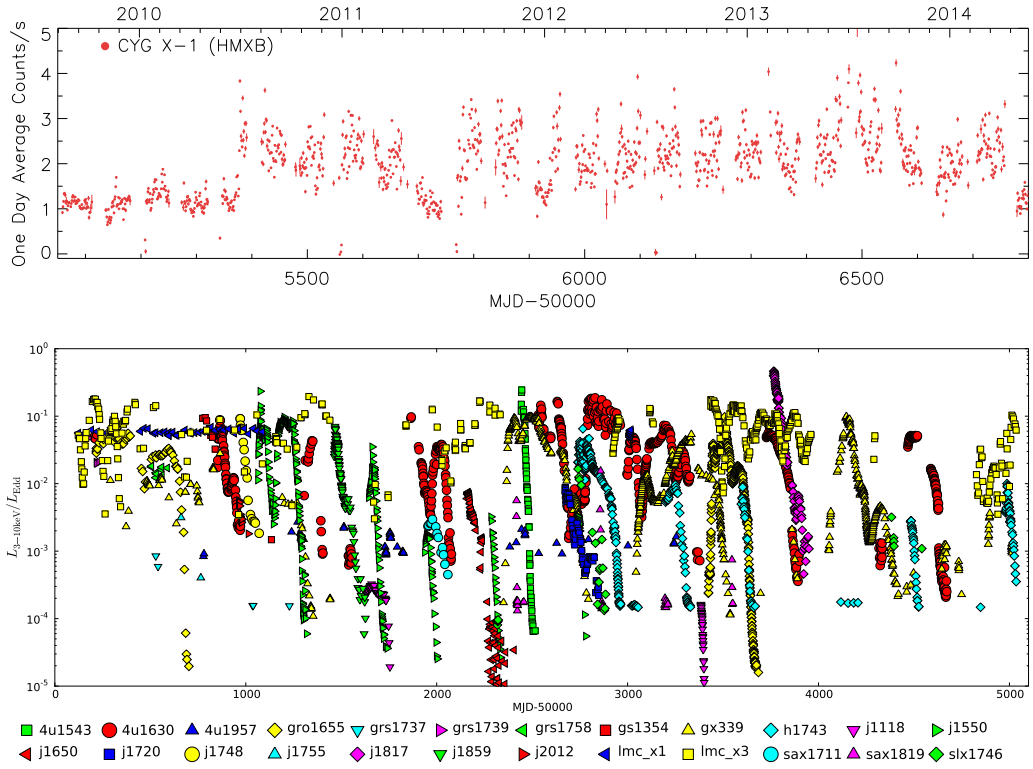

Figure 1.3: Top: A MAXI light-curve of the persistent HMXB Cygnus X-1, which maintains a high luminosity ($\sim 0.01\,L_{\rm Edd}$; Orosz *et al.* 2011). Bottom: An *Rossi X-ray Timing Explorer (RXTE)* light-curve of a sample of black hole systems taken from Dunn *et al.* (2010). Only LMC X-1 and LMC X-3 are HMXB and show a steady luminosity. In comparison many magnitudes are spanned by the LMXB sources.

(Motta *et al.*, 2009), which both suggest thermal Comptonisation to be the underlying physical process (Done *et al.* 2007; Chapter 4). As the source luminosity rises the photon index increases, whilst the high energy cut-off decreases, suggesting an increase in cool seed photons cooling the coronal electrons. Soft X-ray detectors often resolve a weak ($< 10\,\%$ of the total X-ray flux) and cool ($\sim 0.2\,$keV) quasi-blackbody component, which is expected to arise from the disc (Di Salvo *et al.*, 2001; Miller *et al.*, 2006a). The fractional contribution of the disc flux increases with source luminosity, but not significantly.

The hard state covers the largest range of luminosity, spanning from below $10^{-4}\,L_{\rm Edd}$ up to $\sim 0.2\,L_{\rm Edd}$, during which only slight softening of the X-ray colour is observed, which is likely to be due to a combination of increasing disc flux contribution and a steeper power-law slope. There is a high level of aperiodic variability (up to 50 %), which decreases gradually with source luminosity (van der Klis, 2006; Muñoz-Darias *et al.*, 2011). In bright stages

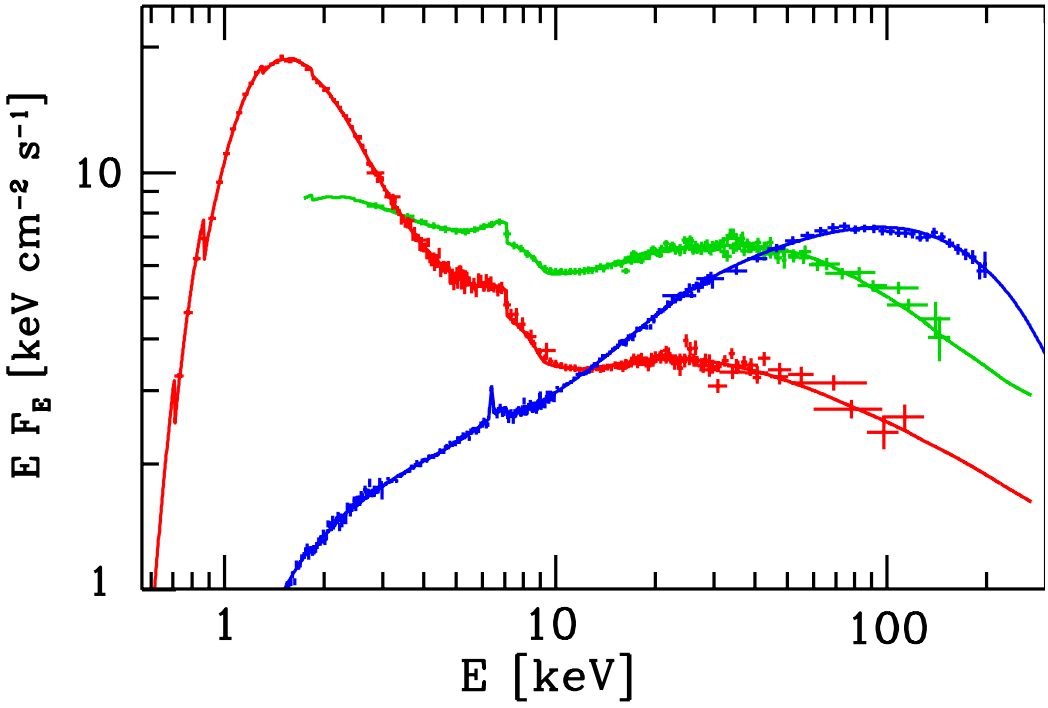

Figure 1.4: Characteristic X-ray spectra of Cygnus X-1 in the low/hard (blue), high/soft (red) and intermediate (green) states. The low/hard state is dominated by the power-law emission, peaking in power at around 100 keV. The turnover at this energy is thought to signify the temperature of the coronal electrons, leading to the interpretation of the spectrum as thermal Comptonisation. The high/soft state displays a dominant thermal blackbody spectrum peaking at around 1 keV, and a weak power-law tail which can extend up to MeV energies (Zdziarski *et al.*, 2002), thus likely to arise (at least mostly) from non-thermal Comptonsiation. The emission at 6 keV and curvature around $\sim$ 20 keV are strong signatures of X-ray reflection, which is described further in §1.4. The intermediate state is a mixture of the hard and soft states. This figure was adapted from Zdziarski *et al.* (2002).

($> 0.01\,L_{\rm Edd}$; Motta *et al.* 2011) a type-C low-frequency quasi-periodic oscillation (LFQPO)[3] is also observed, of which the centroid frequency increases with source flux (Motta *et al.*, 2011). Steady radio emission is also observed at GHz frequencies, associated with a steady compact jet (Fender *et al.*, 2004), and is well correlated with the X-ray emission (Corbel *et al.*, 2003; Gallo *et al.*, 2003, 2012; Corbel *et al.*, 2013a). The source spans many decades in X-ray luminosity as it rises up the hard state, but nevertheless shows little spectral evolution. There may be strong changes in the disc spectrum; how-

[3]LFQPOs are separated into three classes (Casella *et al.*, 2005): (A) Type-A are weak and broad. Very low amplitude red noise is observed and they peak around 8 Hz. (B) Type-B are narrow and occur at around 6 Hz, again during periods of weak red noise. They are also slightly stronger ($\sim$ 4 % RMS). (C) Type-C in contrast are much stronger (up to 16% RMS), narrow and the peak covers a broad range of frequencies (0.1–15 Hz). They are also associated with strong flat-top noise.

ever, this peaks in the optical-ultraviolet during this phase, which is subject to heavy extinction for most BHXRBs due to large columns of intervening material.

The high/soft state

In stark contrast, the *high/soft state* (hereafter 'soft state') is dominated by a soft quasi-blackbody spectrum, which arises from the accretion disc (Fig. 1.2). The peak disc temperature is now much hotter (1–2 keV) and contributes the majority of the X-ray flux ($> 80\,\%$). A hard power-law component still exists; however, it is weaker and considerably steeper ($\Gamma \sim 2$–3). Furthermore, the power-law appears unbroken and can extend up to MeV energies (Zdziarski *et al.*, 2002), which both suggest a significant contribution to the power-law spectrum comes from non-thermal Comptonisation. The soft state exists only above $0.01\,L_{Edd}$, and may extend all the way to the Eddington limit. The level of variability is significantly diminished (rms $< 5\,\%$) and the radio emission is now undetected, which is believed to signify quenching of the jet (Fender *et al.*, 2004; Russell *et al.*, 2011). In addition, accretion disc winds are observed in high-inclination sources ($i > 70^\circ$; where $i = 0^\circ$ and $i = 90^\circ$ are face-on and edge-on respectively), and are thus thought to be ubiquitous in this state (Ponti *et al.*, 2012).

The intermediate states

When sources switch between the canonical hard and soft states they enter the intermediate states. This phase lasts only a matter of days and naturally represents a mix of the hard and soft state characteristics. The disc and power-law components are now roughly equal in flux, whilst the respective temperature and slope are typically intermediate as well (i.e. $kT \sim 0.6\,keV$ and $\Gamma \sim 2 - 2.5$). The total flux rises by a factor of ~ 5 during this stage.

The intermediate state can be separated into two phases: the *hard-intermediate* (hereafter 'HIMS') and *soft-intermediate* (hereafter 'SIMS') states. Whilst their spectra are much alike, contrast is much more apparent via their temporal features. The HIMS occurs directly after (before) a transition from (to) the hard state, and temporally is an extension of the hard state: the power-spectrum is dominated by band-limited noise, which continues to decreases upon transition to the HIMS. The type-C QPO continues to increase in frequency as well. Instead, during the SIMS the band-limited noise disappears (fractional rms now $< 10\,\%$), and is replaced by power-law noise. A marked

type-B QPO is also apparent. For more information I refer the interested reader to the review by Belloni *et al.* (2011). During the intermediate states bright radio flares are also observed, which are often resolved as discrete relativistic plasma ejections (Fender *et al.*, 2004).

Persistent sources, of which there are few, are generally associated with one spectral state. LMC X-1 for example is only observed in the soft state. Some, like Cygnus X-1 and LMC X-3, sometimes make state transitions, but do not exhibit large changes in luminosity as a result (less than a factor of 10). However, transient systems undergo outbursts, whereby they showcase predictable cycles to and from quiescence. This is best portrayed in the hardness-intensity diagram (HID; Fig. 1.5 left; Homan *et al.* 2001; Fender *et al.* 2004).

A source will *always* rise out of quiescence into the hard state. At some luminosity (0.05–0.2 L_{Edd}) the system will transition to the soft state, via the intermediate states described previously. In the soft state the source gradually decays, although some brief excursions to the intermediate states sometimes occur. Upon reaching a luminosity of $\sim 0.02\,L_{Edd}$ the source transitions back to the hard state (Maccarone, 2003), where it will return to quiescence. All BHXRBs reach quiescence via the hard state. Furthermore, no black hole system has ever been observed to exhibit clockwise motion on the HID, although there are occasional clockwise excursions. This evolution has been observed for a number of transient black holes, of which many have undergone such outbursts on multiple occasions (Dunn *et al.*, 2010). The temporal evolution of the black hole is well portrayed by the rms-intensity diagram (RID; Muñoz-Darias *et al.* 2011; Fig. 1.5 right). These cycles typically last for a few hundred days (Fig. 1.5).

1.3.1 Accretion flows and the ISCO

It is now generally accepted that the accretion disc extends all the way to the ISCO in the soft state. Key evidence for this came via the $L \propto T^4$ relation (Eq. 1.6), which if followed represents a constant disc inner radius. Gierliński and Done (2004), and later Dunn *et al.* (2010), showed that many BHXRBs follow this trend in the soft state. Using constraints on the system parameters, they also found that the calculated inner radii are consistent with ISCO for a number of these sources. Steiner *et al.* (2010) later studied the persistent source LMC X-3, which is mostly observed in the soft state, using 26 years of observations with a number of X-ray observatories. They applied the relativistic accretion disc model KERRBB to these data,

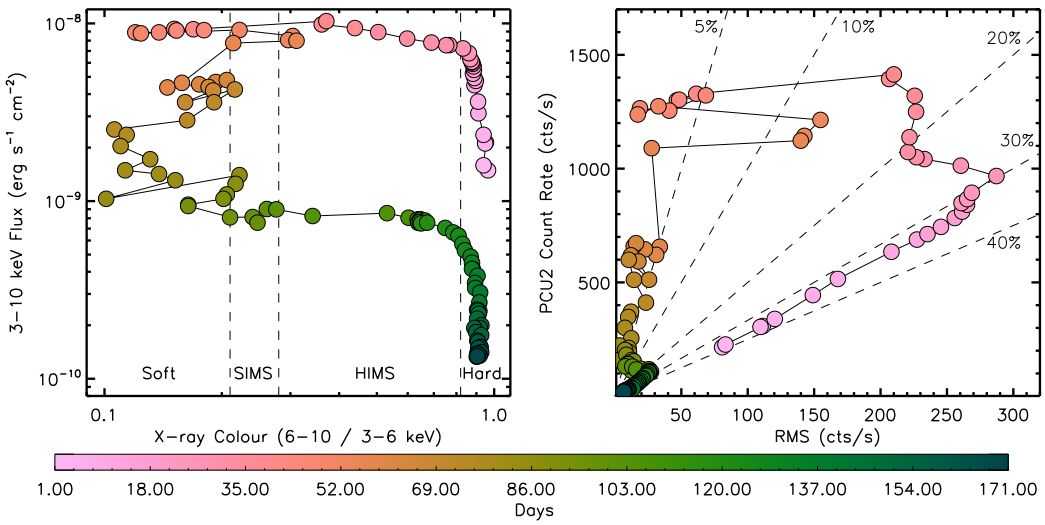

Figure 1.5: The spectral and temporal evolution of BHXRB outbursts, displaying using the 2007 outburst of GX 339−4 analysed in Chapter 4. Left: The hardness-intensity diagram (HID), which plots the X-ray colour (hard/soft bands) against the source flux. All sources evolve in a anti-clockwise manner, and the approximate spectral states have been separated using dashed lines. Right: The rms-intensity diagram (RID), which displays how the rms variability evolves with source intensity. Dotted lines indicates the respective fractional rms levels, indicating that the hard state is much more variable than the soft.

showing that the disc inner radius is consistent with being constant, and within $6\,r_{\rm g}$, over this long timeline.

The standard Shakura–Sunyaev thin disc model applies whenever the disc luminosity is somewhat below the Eddington luminosity $\mathrm{L_{Edd}}$, with the general consensus being that a limit of 30% applies (McClintock *et al.*, 2006). Above this the disc becomes too optically thick to radiate locally, and instead the radiation is trapped and advected inward. The 'slim disc' solution (Abramowicz *et al.*, 1988) describes a cool, optically thick, advection-dominated accretion flow (ADAF). A further ADAF solution exists at low values of $\dot{M}$ (Narayan and Yi, 1995; Esin *et al.*, 1997), whereby the flow is optically thin and the gas is unable to cool efficiently. This is the current favoured type of accretion flow for systems in quiescence (McClintock *et al.*, 1995; Narayan and Yi, 1995; Narayan *et al.*, 1996; Esin *et al.*, 1997; McClintock *et al.*, 2001; Esin *et al.*, 2001; McClintock *et al.*, 2003). However, the application of advection dominated accretion modes to explain the hard state and quiescence also coincides with a persistent outflow in the form of a jet, which can itself remove the need for the advection of energy beyond the event horizon (Fender *et al.*, 2003).

The spectral characteristics of the hard state have led many to believe that the

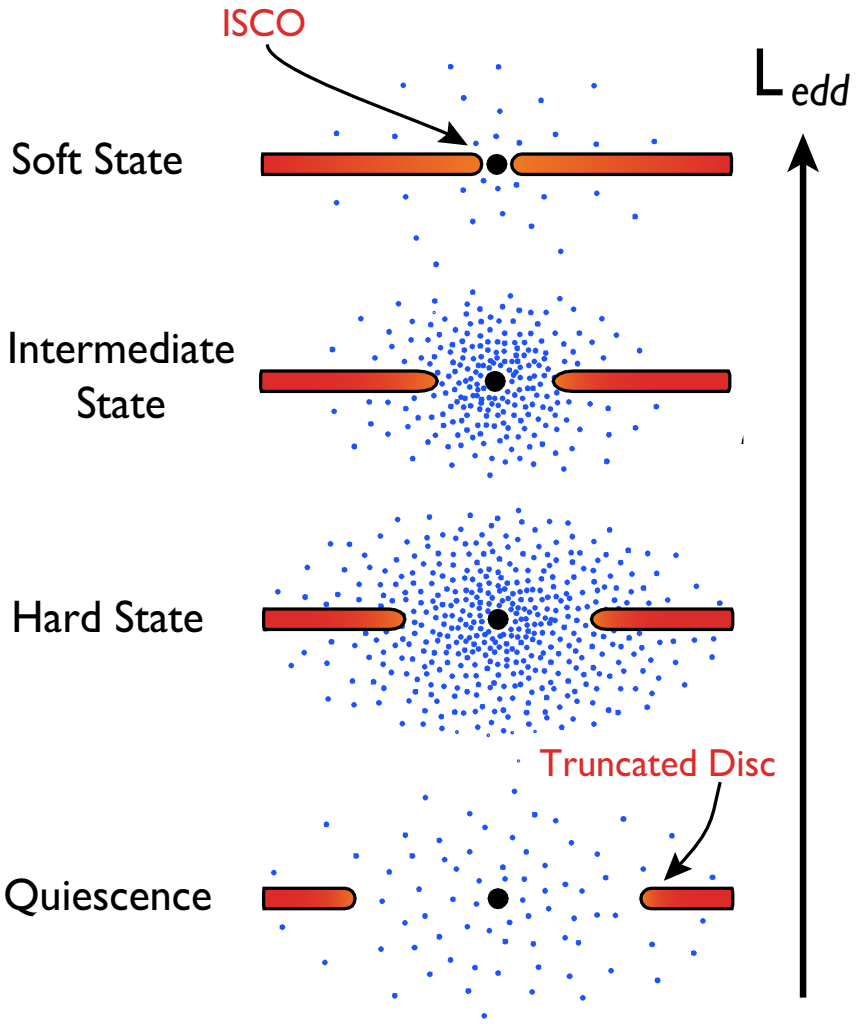

Figure 1.6: An illustration of the truncated disc model, adapted from a figure in Esin *et al.* (1997). As the mass accretion rate increases, the inner disc radius moves inwards, cooling the hot flow (blue). Eventually, in the soft state, the disc reaches the innermost stable circular orbit (ISCO).

standard optically thick and geometrically thin accretion disc is replaced in the inner regions by what is essentially its converse; a hot, optically thin, geometrically thick flow. This is commonly referred to as the 'truncated disc model', and is illustrated in Fig. 1.6. A typical hard state spectrum, which is fit by a thermal Comptonisation model of $\Gamma \sim 1.4$ with an exponential cut-off at $E_c \sim 100\,\mathrm{keV}$ (thought to represent the electron temperature), sees an increase and decrease in Γ and E_c respectively as the source luminosity rises. Both of these characteristics are consistent with an increasing amount of cool disc photons entering the hot flow and cooling it, hence softening the spectrum. Thus, as the accretion rate increases, the truncation radius of the inner disc is expected to decrease, and ultimately leads to the state transition, where is inner accretion disc is at, or close to, the ISCO.

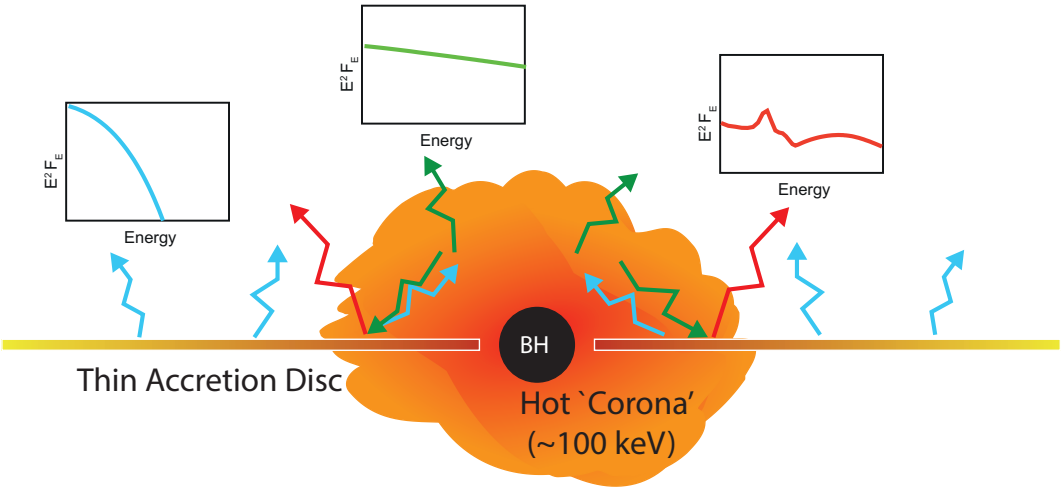

Figure 1.7: An illustration of the accretion geometry on to a black hole. The X-ray spectra can be well modelled by three components: thermal emission from the accretion disc (blue), power-law emission from disc photons Comptonised in a hot corona (green), and reprocessed ('reflected') emission arising from Comptonised photons irradiating the cool accretion disc (red).

However, there are two distinct claims in the literature strongly arguing against this even at relatively low luminosities in the hard state: (1) The detection of significantly broadened iron lines at low accretion rates (Miller *et al.*, 2002, 2006b; Reis *et al.*, 2008, 2010) offer evidence of relativistic effects at or near to the ISCO, although this is still strongly challenged both directly by the re-analysis of data (Done and Gierliński, 2006; Yamada *et al.*, 2009; Done and Diaz Trigo, 2010; Kolehmainen *et al.*, 2014) and indirectly through new observations (Tomsick *et al.*, 2009; Shidatsu *et al.*, 2011; Petrucci *et al.*, 2014). (2) A geometrically thin disc with a fixed inner radius will closely follow the $L \propto T^4$ relation (Gierliński and Done, 2004; Dunn *et al.*, 2011), and hence deviations from this can reveal truncation of the inner disc. The debate remains unresolved with arguments for (Gierliński *et al.*, 2008; Cabanac *et al.*, 2009) and against (Rykoff *et al.*, 2007; Miller *et al.*, 2006a; Tomsick *et al.*, 2008; Reis *et al.*, 2009, 2010) disc truncation.

1.4 X-ray reflection

Whilst photons up-scattered in the corona are observed directly as a hard power-law, many will also irradiate the cool optically-thick disc. This will lead to a number of reprocessing features, collectively known as the *reflection spectrum*. This environment is illustrated in Fig. 1.7.

A hard X-ray photon incident upon the relatively cool accretion disc is bound to

a number of possible interactions, and this subject is well reviewed in the literature (Fabian *et al.*, 2000; Reynolds and Nowak, 2003; Miller, 2007; Fabian and Ross, 2010). Ultimately the outcome is dependent upon the energy of the incident photon, and the ionisation state of the irradiated gas. I will first focus upon the former. Photons of low energy ($< 10\,\mathrm{keV}$) are likely to be photoelectrically absorbed by neutral atoms, which occurs when the photon energy exceeds the threshold energy of the respective photoelectric transition. In doing so a K-shell (n=1) electron is ejected, which is replaced by an L-shell (n=2) electron. The atom then de-excites through two possible mechanisms: the excess energy is emitted via a Kα fluorescent photon; or the energy is released through the ejection of a second L-shell electron (Auger de-excitation). Which process occurs is defined by the fluorescent yield, which represents the probability that de-excitation occurs via fluorescence rather than the Auger effect. The yield increases with atomic number, roughly as Z^4; thus, as a consequence of abundance and yield, iron is the strongest fluorescent emission line observed. The yield of neutral iron is 34%; however, this varies for higher ionisation stages (Frank *et al.*, 2002).

Due to photoelectric absorption, the reflection albedo is small below 10 keV. The photoelectric cross-section goes approximately as $\sigma \propto 1/E^3$; hence, for incident hard X-rays ($> 10\,\mathrm{keV}$) photoelectric absorption is no longer important. Instead, most of the hard X-rays are Compton scattered off free electrons. This results in an excess of photons around 20–50 keV, which is commonly referred to as the *Compton hump*. This was predicted by Lightman and White (1988) and was soon followed by George and Fabian (1991) and Matt *et al.* (1991), who performed Monte Carlo calculations of fluorescent emission resulting in estimates of equivalent widths, line strengths and angular dependence for the Fe K line. Figure 1.8 shows the result of a Monte-Carlo simulation modelling a power-law continuum of $\Gamma = 2$ incident on a slab of gas. The strength of the Fe Kα emission and Compton hump is immediately evident.

1.4.1 Ionised slab models

The surface layers of the accretion disc are likely to become ionised by the powerful irradiation arising from the corona, and has led to many works studying the effect of ionisation upon the reflection spectrum (Ross and Fabian, 1993; Matt *et al.*, 1993; Zycki *et al.*, 1994; Ross *et al.*, 1999; Nayakshin *et al.*, 2000; Nayakshin and Kallman, 2001; Ballantyne *et al.*, 2001; Ross and Fabian, 2005). In particular, Ross and Fabian (2005) presented the grid REFLIONX, which is today the most widely applied

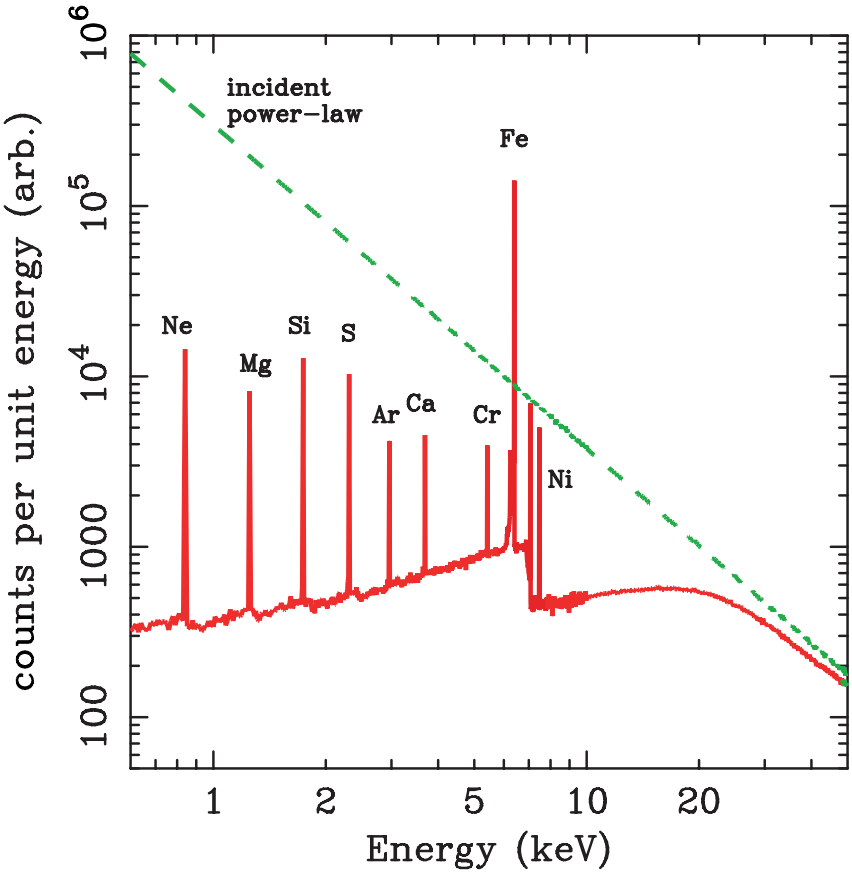

Figure 1.8: A Monte-Carlo simulation of the X-ray reflection from an illuminated slab of gas. The green dashed line indicates the power-law spectrum ($\Gamma = 2$) incident upon the disc, and solid red line shows the resultant reflected spectrum, including fluorescent emission and a down-scattering excess ('Compton hump') at ~ 20 keV). This figure was adapted from Fabian and Ross (2010), which was produced using the model described in Reynolds *et al.* (1994).

reflection model, taking into account the strongest emission lines and self-consistent treatment of the continuum. More recently, García and Kallman (2010) introduced XILLVER (see also García *et al.* 2011, 2013) which represents a further advance in the treatment of atomic processes, in particular making use of the photo-ionisation code XSTAR.

The extent of ionisation in the surface layers of the disc is defined by the ionisation parameter

$$\xi = \frac{4\pi F_{\rm x}}{n_{\rm e}} \quad \text{erg cm s}^{-1}, \tag{1.8}$$

where F_x is the illuminating X-ray flux over a given energy range (1–1000 Ry in the case of XILLVER[4]) and $n_e = 1.2\, n_H$, for which n_e and n_H are the electron and

[4] 1 Ry = 13.6 eV

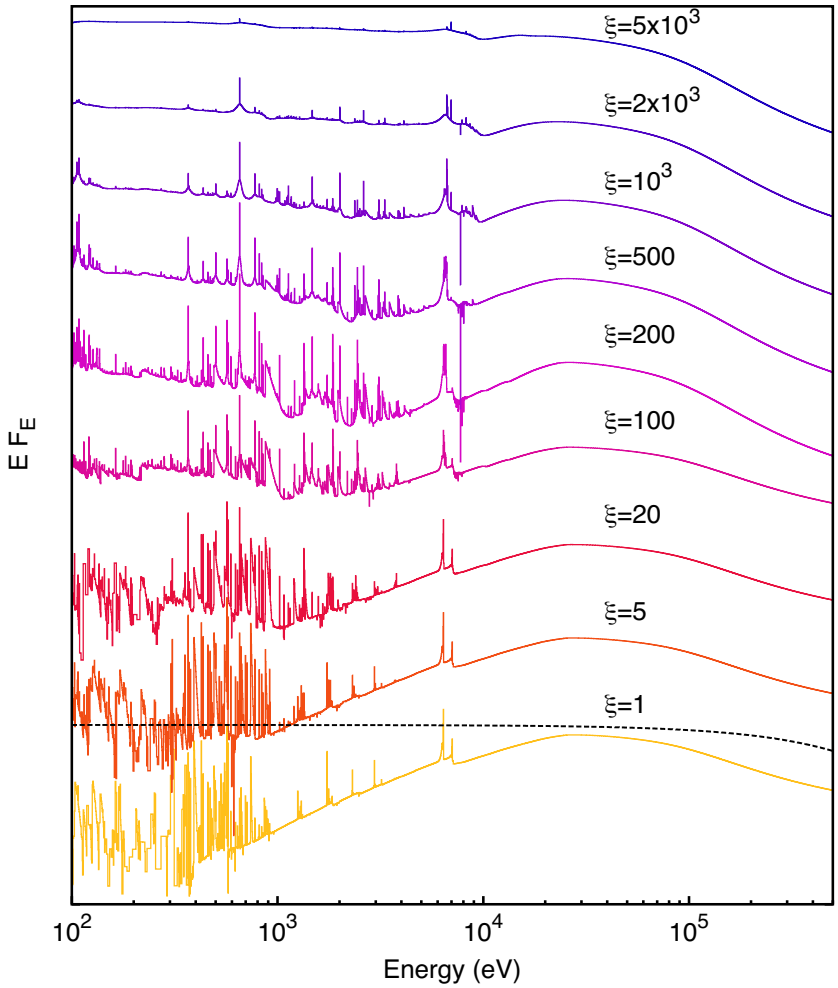

Figure 1.9: Reflection spectra for various ionisation parameter values from $\xi = 1$–5000 erg cm s^{-1}. As the disc surface layers become more ionised (for higher values of ξ), many elements become stripped of electrons. This depletes the forest of fluorescent lines seen at low ξ, and thus reduces the absorptive opacity, which increases the albedo at soft energies. The y-axis is arbitrary and spectra are shifted for clarity. The dashed line represents the incident power-law with slope $\Gamma = 2$ and the iron abundance is solar for each spectrum. This figure was adapted from one presented in García *et al.* (2013).

hydrogen number densities respectively (Tarter *et al.*, 1969; García *et al.*, 2013). The effect of ξ on the observed reflection is displayed in Figs. 1.9 and 1.10. Traditionally the ionisation parameter is split into four regimes, which I describe below.

$\xi < 100$ erg cm s^{-1}:

At such low levels of ξ the gas is only weakly ionised, and the resultant spectrum is similar to that from cold neutral material (Fig. 1.8). All of the Fe K emission arises at 6.4 keV and 7.1 keV through the α and β transitions. There is also a weak absorption edge evident above 7 keV. The absorbing

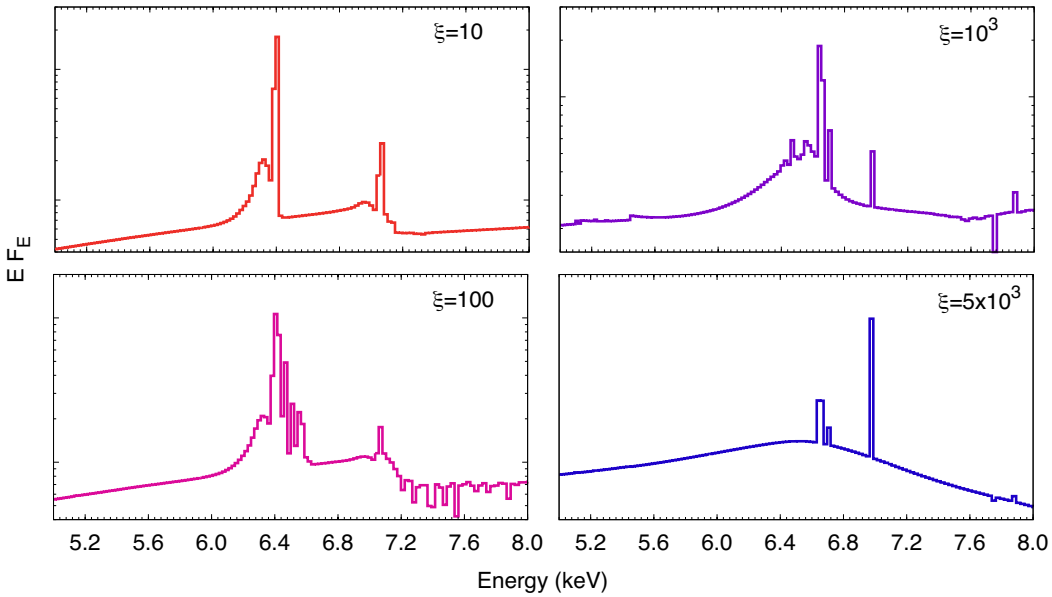

Figure 1.10: Reflected spectra in the Fe K region (5–8 keV) for various ionisation parameter values, under the same conditions as in Fig. 1.9. Higher levels of ξ results in Fe emission from more ionised states as surface layers of the disc become stripped. Adapted from a figure presented in García *et al.* (2013).

effect of the weakly ionised material is evident through the drop-off in the spectrum below 10 keV (Fig. 1.9).

$100 < \xi < 500$ erg cm s^{-1}:

In this *intermediate* regime Fe photons are produced from a range of ionisation states (Fig. 1.10), thus the resolved profile is broader. The Fe Kβ emission is weakened as a result of some Fe being highly ionised. The continuum and absorption are strengthened, whilst between 1–10 keV more fluorescent emission is observed from elements such as Mg, Al, Si, S, Ar and Ca being excited.

$500 < \xi < 5000$ erg cm s^{-1}:

Many low-Z elements are now fully ionised, which again raises the soft continuum and removes a lot of emission. In turn, elements such as O, Ne, Ar, Ca and Fe see an increase in emission with further illumination. Fe Kα emission arises almost entirely in its helium and hydrogen-like forms (at 6.67 and 6.97 keV), and a weak amount of Kβ emission is observed from recombination. Corresponding edges are observed at 8–9 keV. Strong back-scattered emission is also now evident at $\sim$ 6 keV, which is commonly referred to as the *Compton shoulder*.

$\xi > 5000$ erg cm s^{-1}:

The surface layers of the disc are now highly ionised leading to an obvious lack of atomic features, even from Fe. In this stage the albedo is approaching unity and ultimately the disc acts much like a mirror. As a result there is little contrast between the reflection continuum above and below 10 keV, which now appears very similar to the incident power-law.

Nearly all models of ionised gas slabs are aimed at modelling AGN X-ray spectra, thus assuming an illuminating power-law spectrum. In BHXRBs, lighter elements in the surface layers are expected to be fully stripped by the ionising power of the hotter disc (recall from Eq. 1.7 that $T_{\rm in}^4 \propto 1/M_{\rm BH}$ for a given Eddington ratio $\dot{M}/M_{\rm Edd}$), resulting in a high albedo and values of ξ (Ross and Fabian, 1993; Zycki *et al.*, 1994). This effect also leads to more effective Fe emission, since the fully ionised lighter elements are not able to absorb the emitted Fe photons (Matt *et al.*, 1993). It is therefore common for BHXRBs to be associated with larger values of ξ than AGN, and the field is lacking a self-consistent model that includes a true illuminating spectrum for a stellar mass black hole. Ross and Fabian (2007) investigated the inclusion of a black-body spectrum into their standard slab model (Ross and Fabian, 2005), which confirmed that the resultant BHXRB reflection spectrum appears considerably more ionised for a given value of ξ.

1.5 Measuring black hole spin

As described in §1.1, astrophysical black holes are characterised by just two parameters: mass and spin. The effect of mass is evident over large scales through gravity, and has been measured for decades through the interaction of the black hole with other objects. In the case of BHXRBs this can be done via the companion star (see Casares and Jonker 2013 for a recent review). However, the effect of spin is only evident very close to the black hole (but see § 1.5.3), and thus detailed studies of the accretion disc are required to expose the effects of spin.

Bardeen *et al.* (1972) revealed a distinct link between the innermost stable circular orbit (ISCO) and spin. In very simple terms, the effect of frame dragging allows stable particle orbits to exist closer to the black hole without plunging. Thus, by measuring the ISCO of the disc one can obtain an estimate of the black hole spin (Fig. 1.11). The dimensionless spin parameter can range from zero to 0.998, at which point the counter-acting torque produced by disc radiation being captured prevents further spin-up of the black hole (Thorne, 1974). A negative spin refers to

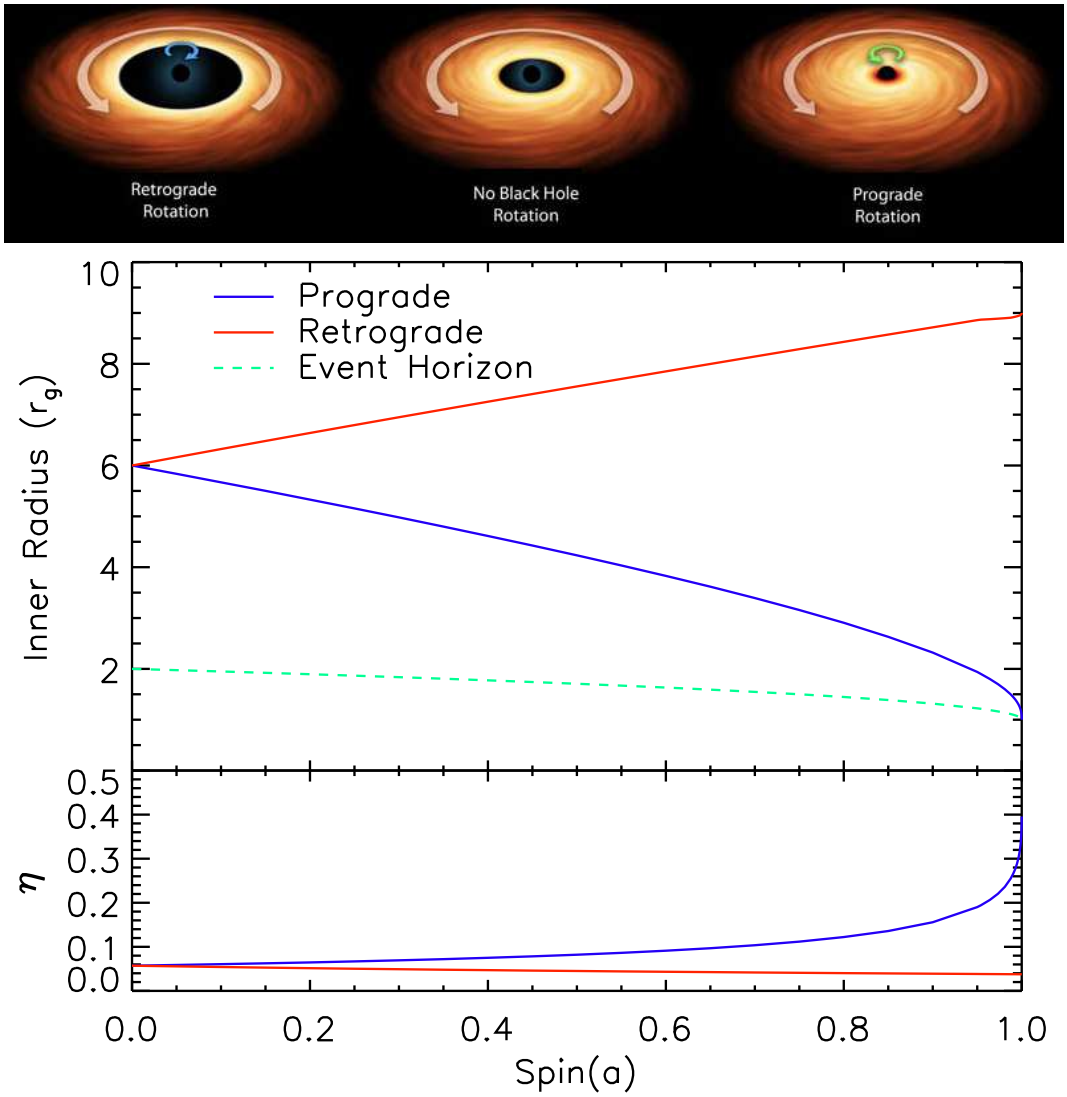

Figure 1.11: Top: An illustration of the accretion disc for different values of black hole spin. Image credit: NASA/JPL-CALTECH. Bottom: The variation of the ISCO and disc efficiency η for the full range of black hole spin. Retrograde and prograde discs are plotted with blue and red lines respectively. The black hole event horizon is also indicated by the dashed green line.

black holes with a non-zero spin rotating in the opposite direction to the accretion disc. Therefore, since the matter has retrograde orbits, such black holes are often referred to as being 'retrograde'. However, it is uncertain how retrograde black holes are formed. One suggestion is that fluctuations in wind-fed accretion could lead to a reversal in the rotational direction of the disc (Shapiro and Lightman, 1976; Zhang *et al.*, 1997). Reis *et al.* (2013a) also suggest that the tidal capture of a star in a globular cluster (Fabian *et al.*, 1975) could permit retrograde accretion. Recently, the observational evidence for retrograde spin has increased, with a number of works reporting results consistent with negative black hole spins (Gou *et al.*, 2010; Reis

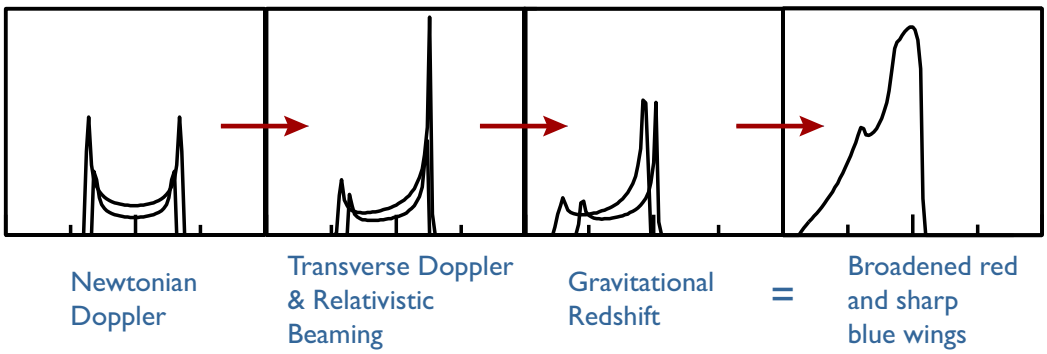

Figure 1.12: The various newtonian and relativistic effects leading to the broad relativistic Fe line. The severity of these effects is a function of how close to the black hole the emission occurs, thus it can be used to infer the spin of the black hole. The effect of spin is displayed in Fig. 1.13.

et al., 2013b; Middleton *et al.*, 2014; Morningstar *et al.*, 2014), although there is the significant caveat that a negative spin could just be a prograde black hole with a disc truncated from the ISCO. Finally, I note that a black hole is expected to retain its natal spin for a significant amount of its lifetime (King and Kolb, 1999; Maccarone, 2002).

There are two leading X-ray spectroscopic methods to estimate the spin of black holes: (1) The broad Fe line method and (2) the disc continuum method. I will describe both in the sections below.

1.5.1 The Fe line method

Material orbiting close to a black hole will undergo a number of Newtonian and relativistic effects, which will affect the emission observed at infinity. This was first displayed in Fabian *et al.* (1989), who concluded that the dynamics of a black hole can be inferred from observing these effects via the transformation of an emission line. An intrinsically narrow line will firstly be broadened by the Newtonian rotational effect of the disc. Two peaks will be formed through emission being blue and red-shifted as the material rotates towards and away from the observer respectively. The inner parts of the disc will also be travelling at mildly relativistic velocities; hence, relativistic aberration ("Doppler beaming") will occur, strengthening and weakening the blue and red peaks respectively. In addition, the transverse Doppler effect ("time-dilation") will redden such emission. Finally, the intense gravitational well of the black hole will gravitationally redshift the emitted photon. The resultant emission profile summed over all radii will be asymmetric, exhibiting broad red and sharp blue wings. This process is illustrated in Fig. 1.12, and a number of

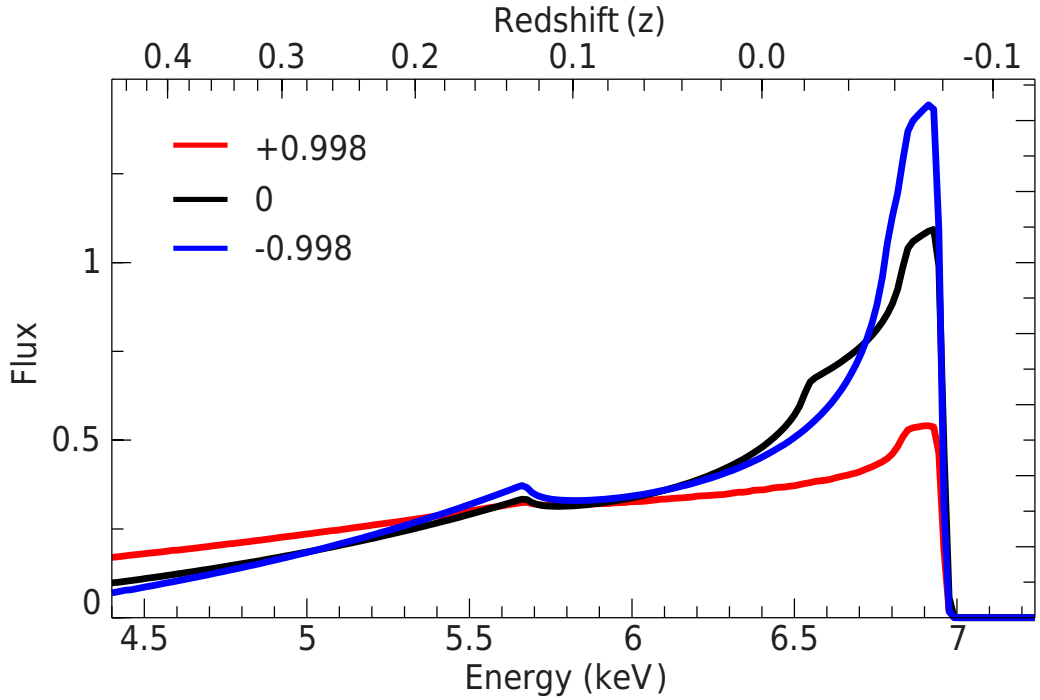

Figure 1.13: Relativistic Fe lines for different values of black hole spin, created using the model RELLINE. The inclination is set at 40° and an emissivity profile of R^{-3} is used. As higher prograde spin acts to bring the ISCO inwards, stronger red-shifting of the profile is observed, which smears the profile further. Note that the blue wing remains sharp and largely unchanged. This figure was adapted from one presented in Dauser *et al.* (2010).

codes exist modelling such profiles (Fabian *et al.*, 1989; Laor, 1991; Beckwith and Done, 2004; Dovčiak *et al.*, 2004; Brenneman and Reynolds, 2006; Dauser *et al.*, 2010). The Fe Kα is ideal for this technique, since it is abundant and carries a high fluorescent yield. It also occurs at 6.4 keV, where the continuum flux is relatively low in comparison to lighter elements. Relativistic broadened Fe Kα emission lines have been reported from AGN (Tanaka *et al.*, 1995), BHXRBs (Miller, 2007) and neutron stars (Cackett *et al.* 2008; but see also Ng *et al.* 2010).

These effects are naturally a function of the inner extent of the disc. Through the relation between the ISCO and spin (Fig. 1.11) the latter can be inferred assuming the disc is at the ISCO (Fig. 1.13). Should the disc be truncated from the ISCO this method can also be used to determine to what extent this occurs. This approach has now been used to estimate black hole spin in both AGN and stellar-mass black holes, for a number of sources. Rather than list all of them I refer the reader to the recent reviews of Miller (2007) and Reynolds (2013).

The biggest weakness of the Fe line method is the relatively small signal which the relativistic effects are imprinted upon. The profile is also dependent upon a num-

ber of additional factors. The emissivity profile of the disc must also be modelled, and currently all spin estimates have assumed a power-law function with radius. Only recently have models been produced to self-consistently calculate the emissivity profile via properties such as the height of the illuminating source. The emissivity, and fitted disc inclination, strongly affect the profile, which can lead to severe model degeneracies. I perform a detailed analysis of this in Chapter 2. When modelling a profile smeared over a larger energy range (usually 4–8 keV), the continuum model can considerably affect the inferred results (Kolehmainen *et al.*, 2011). To this end, the Fe line method is best applied to the hard state where the continuum at 6 keV is typically dominated by the power-law emission. However, as I show in Chapter 3, measuring spin in the hard state is impossible due to the inner accretion disc being truncated from the ISCO. Instrumental effects, particularly photon and pattern pile-up, can also severely alter the observed profile, and has been the subject of much debate in recent years (see e.g. Miller *et al.* 2010 versus Done and Diaz Trigo 2010 and Ng *et al.* 2010). As discussed in §1.4, the current reflection models lack the self-consistent treatment of a physical BHXRB illuminating spectrum. The application of the Fe line method to AGN is less susceptible to some of these flaws: the disc spectrum does not enter the continuum at 6 keV; count rates are much less, reducing pile-up; and the reflection models are aimed at AGN. However, AGN spectra can be considerably more complex, often complicated by substantial and variable levels of absorption (Miller *et al.*, 2008b). In some cases, apparent reflection features can be modelled entirely through a continuum modified by absorption. This is largely hampered by a lack of broadband coverage available for AGN, which are often too faint for hard X-ray detectors.

1.5.2 The continuum method

The ISCO can also be inferred from the accretion disc continuum flux through the Novikov–Thorne disc model (Novikov and Thorne, 1973), which is a relativistic generalisation of the Shakura–Sunyaev model described in §1.2 (see McClintock *et al.* 2011 for a recent review). The principle can be easily understood through the way a star's radius R_* is measured. The luminosity of a star is given by $L_* = 4\pi D^2 F_{\rm obs} = 4\pi R_*^2 \sigma T^4$; thus, if the flux $F_{\rm obs}$ and temperature T can be measured, one obtains $(R_*/D)^2$, which represents the solid angle subtended by the star. One can therefore obtain the star radius R_* if the distance D is known.

For an accretion disc we know that the flux emitted varies with radius, and thus so does the characteristic temperature (Eq. 1.6). But this function is embedded in

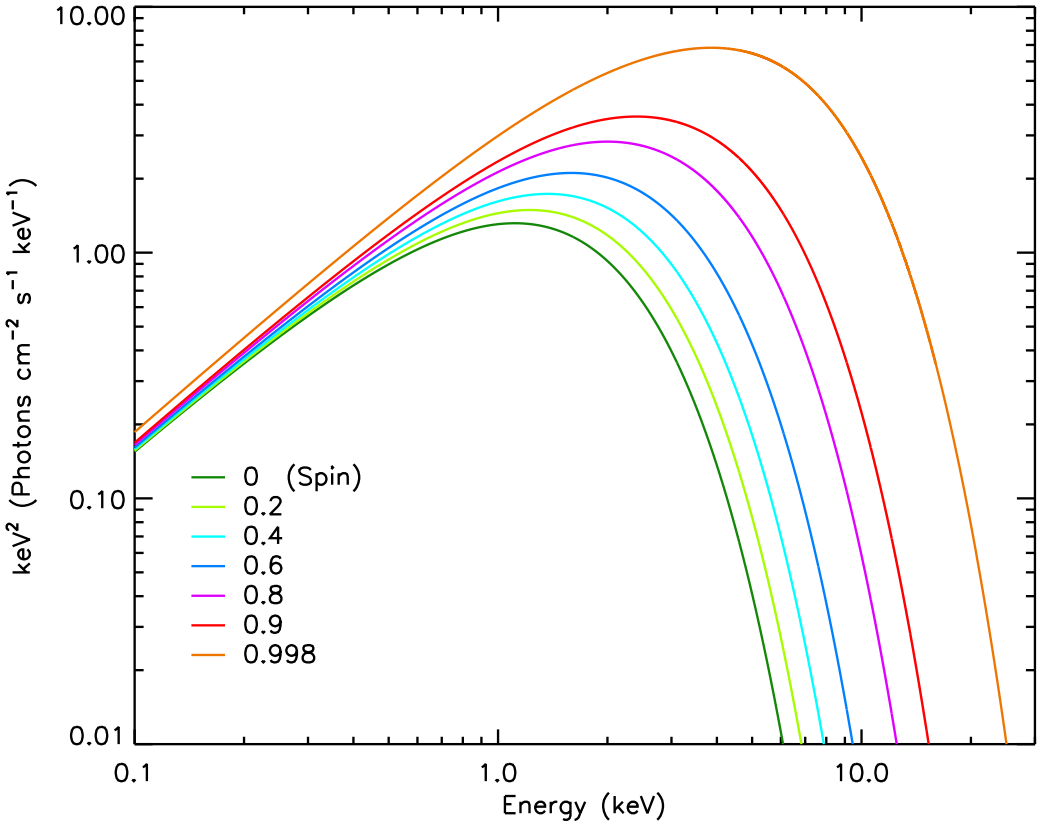

Figure 1.14: Relativistic accretion disc spectra created using the model KERRBB (Li *et al.*, 2005). Each model is produced for differing values of spin indicated by their respective colour. One can see that increasing spin acts to increase the peak temperature and flux of the spectrum. For all model spectra a black hole mass of $10\,M_{\odot}$, distance 10 kpc, inclination 60° and effective accretion rate 10^{18} g s^{-1} ($\sim 1.6 \times 10^{-8}\,M_{\odot}$/yr) were used.

the Novikov–Thorne model. A number of corrections apply, most importantly due to the disc inclination which will alter the solid angle of the disc, but the principle is there. This was first described in the pioneering work of Zhang *et al.* (1997). In the past decade a huge effort has been made to calculate the spin via the disc spectra of black holes, leading to two leading models KERRBB (Li *et al.*, 2005) and BHSPEC (Davis *et al.*, 2005). Figure 1.14 displays disc spectra modelled for different values of spin using KERRBB. This method has been successfully applied to a number of BHXRBs (McClintock *et al.*, 2011, 2013).

The biggest handicap of the continuum method is the requirement for the black hole mass, accretion disc inclination, and distance to the source to be known. Obtaining all three requires considerable effort, and despite a plethora of X-ray data much of it cannot be used due to a lack of these parameters. Non-blackbody effects must also be modelled as the radiation passes through the disc atmosphere

(the spectral-hardening factor). However, because of the extremely high signal of the disc spectrum ($> 80\,\%$ in soft-states), the continuum method can make use of low-resolution data, such as from *RXTE*, and thus a lot of its power comes from large systematic studies. It is, however, inherently flawed by the inverse relation between peak temperature and black hole mass (Eq. 1.7); hence, the disc spectrum from AGN will peak in the ultraviolet. This renders the disc spectrum heavily susceptible to extinction, and means the continuum method cannot be widely applied to AGN (but see also Done *et al.* 2013).

1.5.3 On the spin-powering of relativistic jets

Outflows in the form of jets are a ubiquitous component of accretion. From BHXRBs we observe two distinct types of jet; in the hard state the jet is deemed to be steady and compact, and is associated with a flat radio spectrum. In contrast, during the state transition bright radio flares are observed, which are often resolved to be discrete and powerful ejection events. During the soft state the core jet power appears to be reduced by orders of magnitude (Fender *et al.*, 2004; Russell *et al.*, 2011).

The idea of potentially tapping the black hole as a source of energy has been around for many decades (Penrose, 1969). Building on this, Blandford and Znajek (1977) displayed that a magnetic field supported by an accretion disc could lead to the electromagnetic extraction of angular momentum from the black hole, and thus power an astrophysical jet. Recently, with increasing measurements of jets and black hole spin, interest in this topic has been revived. The latest simulations suggest a very strong coupling between black hole spin and jet power (McKinney, 2005; Tchekhovskoy *et al.*, 2011).

Evidence for the observed range of jet power has proven to be elusive, and is particularly hampered by a lack of key characteristics (e.g. composition, field strength). Much focus therefore has now turned to comparing spin estimates with proxies of jet power. This was first attempted by Fender *et al.* (2010) who compared the full scope of spin estimates, and found no evidence for such a coupling. Considerable doubt exists in both of the spin estimation methods, and applying a fair proxy for jet power is particularly difficult; thus, they concluded that either could be in error, as well as that the coupling itself may not exist. This was followed by Narayan and McClintock (2012), who found that by using a select sample of spin estimates via the continuum method, and jet power derived from the peak radio flare, that a correlation existed. This, however, only included five sources, and a sixth was added in a later publication by Steiner *et al.* (2013). Russell *et al.* (2013) then showed using a

full sample that the peak radio flux differs considerably depending on the outburst, and found no statistically significant evidence for a correlation. Since this, at least one further source, a transient BHXRB in M31, appears to contradict the spin–jet relation (Middleton *et al.*, 2014).

1.6 GX 339−4

The source GX 339−4 features in Chapters 3, 4 and 5 of this thesis, and therefore deserves a short introduction. GX 339−4 was discovered in 1973 by the seventh *NASA Orbiting Solar Observatory* (Markert *et al.*, 1973), and has exhibited numerous outbursts since. Whilst GX 339−4 is transient, and covers many orders of magnitude in X-ray luminosity during outbursts, it never reaches a true quiescent state, and is always too bright to allow the companion to be detected (Shahbaz *et al.*, 2001). This means that the system parameters cannot be determined via the standard method: by measuring the radial velocity curve of the companion, typically via photospheric absorption lines (Casares and Jonker, 2013). Instead, Hynes *et al.* (2003) were able to dynamically confirm GX 339−4 as a black hole using emission lines as the companion is strongly irradiated during a bright phase of an outburst. Following this, Muñoz-Darias *et al.* (2008) provided an improved constraint on the mass ratio, setting a lower limit to the companion mass of $M_{\rm C} \geq 0.17\,M_{\odot}$.

The mass function is used to describe binary systems, which is defined as

$$f(M) = \frac{M_{\rm BH} \sin^3 i}{(1+q)^2} \tag{1.9}$$

where $M_{\rm BH}$ is the black hole mass, i is the orbital inclination of the system, and $q = M_{\rm BH}/M_{\rm C}$ is the mass ratio. Using the mass function constrained by Hynes *et al.* (2003; $f(M) = 5.8\,M_{\odot}$), for $M_{\rm C} = 0$ and $M_{\rm BH} = 20\,M_{\odot}$ respectively, the inclination of the system must be $i > 41.4^{\circ}$. A larger $M_{\rm C}$, or smaller $M_{\rm BH}$, would increase the lower limit on the binary inclination. In addition, the limit of $M_{\rm BH} = 20\,M_{\odot}$ is very extreme, and $\sim 5\,M_{\odot}$ larger than any known stellar-mass BHXRB (Casares and Jonker, 2013). Therefore, $i > 41.4^{\circ}$ represents a strict lower limit on the binary inclination. It has recently been shown that accretion disc winds are ubiquitously observed via narrow absorption features in the soft states of high-inclination BHXRBs ($i > 70^{\circ}$; Ponti *et al.* 2012). The soft state of GX 339−4 has never been observed to have such features, nor has it ever been seen to show dips, or eclipses, in its light-curve, which are the hallmark of a high-inclination source. We can therefore also set a tentative upper limit to the binary inclination of $i < 70^{\circ}$ (assuming the binary

and disc inclination are aligned).

GX 339−4 is one of the most active transient systems, and has exhibited four complete outburst cycles (with state-changes) in the past twelve years. As a result, GX 339−4 is one of the most studied transient systems, and an extensive archive of X-ray data has been amassed, allowing unique systematic studies of a transient BHXRB (Chapters 3 and 4). To this end, it has formed the basis of many important works key to our understanding of BHXRBs (see e.g. Belloni *et al.* 2005; Dunn *et al.* 2010; Corbel *et al.* 2013a and references therein).

1.7 Thesis Overview

In this introduction I have presented our current understanding of the X-ray properties of BHXRBs. I have paid particular attention to black hole spin estimates, which is a controversial and important area, and in a large part motivated this thesis. In Chapter 2 I investigate the accuracy of spin estimates using the broad Fe line method, which may be falsely masking the lack of evidence for a correlation between spin and jet power. Chapter 3 looks at the Fe line in the hard state of the black hole GX 339−4, where I find the strongest direct evidence to date for inner disc truncation. This work also rules out the potential for black hole spin estimates through reflection in the hard state, which is the ideal period to apply this technique. In Chapter 4 I present the largest ever systematic study of X-ray reflection using a self-consistent treatment. This allows the geometrical evolution of the disc and corona to be mapped, and attempts to establish the dynamics behind BHXRB outbursts. Chapter 5 presents analysis of three recent *XMM-Newton* observations of GX 339−4 using the small window science mode, which allow an excellent constraint and comparison of the disc inner radius through the disc and reflection methods. Finally, in Chapter 6 I discuss the scientific impact of these studies and look towards future prospects.

2

Testing black hole spin measurements: on the systematic errors in X-ray reflection fitting

In this chapter I examine the systematic errors associated with measuring black hole spin through X-ray reflection spectroscopy. I test a variety of models against three *XMM-Newton* observations which display clear relativistically broadened Fe Kα emission lines, and show that model degeneracies can significantly affect the resolved parameters. I display how this is particularly prevalent in relativistic line models, which I conclude should *never* be used as a means to measure black hole spin. Self-consistent reflection modelling is less susceptible to degeneracies, but can nevertheless be significantly affected as well. In particular, the inclination parameter is a source of a lot of uncertainty, and this work emphasises how necessary it is to have constraints on the disc inclination via other established means, such as the jet or binary inclination, if a stringent measurement of spin is to be achieved.

2.1 Introduction

Much debate surrounds the measurement of black hole spin through X-ray spectroscopy. The two methods applied, continuum and reflection fitting, are quite contrasting in their approach. Continuum fitting fits the quasi-blackbody component of the accretion disc, which can often account for $>90\,\%$ of the X-ray flux in soft states (see e.g. Figure 4.13), hence offering excellent constraints. However, to fit the accretion disc spectrum one requires an accurate determination of the binary parameters – mass, distance and inclination – which are often difficult to obtain. Reflection fitting is, however, independent of mass and distance, but the Fe Kα line, on which the relativistic effects are imprinted, offers only a small % of the overall signal. Furthermore, it requires the fitting of many other parameters which also directly impact the inferred spin, and are not otherwise constrainable (e.g. the ionisation stage and emissivity profile; see §1.5 for more details on the two spectroscopic methods used to measure black hole spin).

Another contrast between the two methods is often in the spin estimate they produce (see e.g. GRO J1655-50 Shafee *et al.* 2006; Reis *et al.* 2008, 2010). At a minimum, if one is to have any confidence in the two methods, then they must yield the same result, and thus at least one of the techniques must be in error if they differ. Relativistic jets may be able to extract energy via black hole spin (Blandford and Znajek 1977; Tchekhovskoy *et al.* 2011), and hence correlations should exist between the spin and jet power. Fender *et al.* (2010) compared the two and found that there was no evidence for such a correlation, and concluded that at least one of the following statements is true: (1) The jet power estimates are in error; (2) the spin estimates are in error; (3) black hole spin does not power relativistic jets. Narayan and McClintock (2012) found evidence for a correlation between jet power and spin, but relied on a small and select sample of spin estimates, and the statistical significance of their work was also later challenged by Russell *et al.* (2013).

To some extent, the confidence limits reported for spin estimates may be serving to conflict the two methods. For example, (Reis *et al.*, 2009) published a spin estimate of 0.935 ± 0.01(statistical)± 0.01(systematic), whereby the systematic error comes from the comparison of results from two observations. Motivated by this, and conclusion (2) of Fender *et al.* (2010), in this Chapter I analyse three *XMM-Newton* observations to investigate how accurate spin estimates using X-ray reflection are.

2.2 Observations and data reduction

To obtain the best possible analysis of the reflection features, this investigation was restricted to only high-resolution observations with a large effective area at 6 keV. This action was taken in order to best resolve the Fe K emission, and ultimately constrained the investigation to *XMM-Newton* and *Suzaku*. In particular this study aims to investigate how accurately black hole spin can be measured with the currently available instruments. In Chapter 3 of this thesis I show that in the hard state of BHXRBs the inner accretion disc is probably truncated from the ISCO, and therefore the Fe line profile is independent of the spin of the black hole. Later in Chapter 4 I display how the Fe line profile is at its most prominent in the hard-intermediate state (HIMS), and recent works have shown this stage to display profiles clearly broadened by relativistic effects (Hiemstra *et al.*, 2011; Reis *et al.*, 2011; Walton *et al.*, 2012), making the HIMS the ideal state for this study. A recent investigation by Kolehmainen *et al.* (2011), showed that in the case of the disc and power-law components having equal fluxes around the Fe K range, fitting a broader disc component can significantly alter the line profile, leading to very contrasting spin estimates. This. therefore, makes observations in the soft-intermediate (SIMS) and soft states inadequate for this study.

2.2.1 Photon and pattern pile-up

Pile-up occurs when several photons hit two neighbouring pixels (pattern pile-up), or the same pixel (photon pile-up), during one read-out cycle. If this happens the events are counted as one single event carrying an energy of the sum of the two or more incident photons, leading to a loss of flux or spectral hardening depending on whether the energy-rejection threshold is exceeded. It is, therefore, a very important issue when observing bright sources, such as BHXRBs. The effects of pile-up are still not fully understood, and how it transforms the Fe line profile is particularly uncertain: simulations suggest that pile-up narrows line profiles (Miller *et al.*, 2010), whilst observations instead seem to display increased broadening (Done and Diaz Trigo, 2010; Ng *et al.*, 2010). Since this investigation focuses on determining the accuracy of the current Fe line models, the uncertainty in how pile-up affects the Fe line profile means that it is only sensible to use datasets which are free from pile-up.

Dealing with pile-up requires the removal of central regions of the point-spread function (PSF); however, this drastically reduces the quality of the spectrum and

the effective area of the instrument, which is already largely in decline at and beyond 6 keV. Thus, the significant reduction in the quality of the data when mitigating pile-up presents another very good reason to avoid piled-up observations. The *XMM-Newton* 'fast modes' available for the EPIC-pn camera can significantly reduce the effect of pile-up. For example, in the 'timing' mode 'macropixels' are formed of 10 pixels in the read-out direction, and one pixel orthogonal to this. This allows a much faster read-out time than standard imaging modes, and therefore allows much higher incident count-rate to be observed (up to $\sim$ 800 cts/s). However, BHXRBs are highly variable, and some read-out cycles may be piled-up at count rates approaching this limit. I note as well that Miller *et al.* (2010) suggest that EPIC-pn timing mode can still be susceptible to pile-up below this limit. Therefore, to maintain a best-case scenario for this investigation, I only use data that requires no mitigation of pile-up.

Nevertheless, the benefit of *XMM-Newton* is that the EPIC-pn camera includes well calibrated 'fast' readout options which can deal with the high-count rates common for galactic BHXRBs. *Suzaku* on the other hand lacks a well calibrated mode of this sort, and unsurprisingly no suitable datasets free from pile-up were found in the archives. Therefore the work presented here employs only HIMS observations made with *XMM-Newton* in an EPIC-pn 'fast' mode. In addition, and where available, I used simultaneous *RXTE* data to increase the broadband coverage. The following introduces the three sources used in this chapter and the data reduction procedure.

2.2.2 The standard data reduction procedure

2.2.2.1 XMM-Newton

For the reduction of *XMM-Newton* observations I employed the Science Analysis Software (SAS) version 11.0. I only used the EPIC-pn camera (Strüder *et al.*, 2001) data sets taken in one of the 'fast' (timing and burst) modes to avoid photon pile-up (see e.g. Done and Diaz Trigo 2010). The respective nominal pile-up limits for timing and burst modes are 800 c/s and 60000 c/s respectively, which all of the observations used here are well below. For all sources I applied the SAS task EPATPLOT to assess the extent of any pile-up within the spectrum, and in each case found it to be insignificant.

The standard tools were applied to create response and ancillary files (RMFGEN and ARFGEN), and only single and double events were used (PATTERN$\leq$4), whilst

ignoring bad pixels with FLAG==0. Additionally all spectra were re-binned using the FTOOL GRPPHA to have at least 20 counts per channel. Finally, I found all background regions were contaminated, indicated by background spectra clearly following that of the source. This is a common occurrence with the 'fast' modes of the EPIC-pn, since the telescope PSF exceeds the CCD boundaries (see e.g. Ng *et al.* 2010). The source flux was high enough in all the observations that the background should be < 1 % of the total observed counts (Ng *et al.* 2010; see also Chapter 5 which was at a similar flux level), thus I deemed it acceptable to proceed without implementing any background subtraction.

Before extracting the spectra I applied the SAS task EPFAST to the timing mode observations to allow for any effect due to charge-transfer inefficiency (CTI)[1]. CTI results in a gain shift and can hence affect the energy spectrum. In all the observations the residuals around the instrumental Si and Au features were apparent, and the 1.75–2.35 keV region was ignored for all fits. Many mysterious "soft excesses" have been reported in binaries, the origin of which remains uncertain and appears to not be limited to the timing mode (see the XMM-Newton Calibration Technical Note (0083)[1] and references therein). The hallmark of this is a significant residual below 1 keV, which can severely affect the fit, and has already been reported for two sources in this study (Hiemstra *et al.*, 2011; Reis *et al.*, 2011). After confirming the residual, which was also present in GX 339−4 in Chapter 3, I followed the same procedure as Hiemstra *et al.* (2011) and Reis *et al.* (2011) in setting a 1.3 keV lower limit to the bandpass. No such residual was found for XTE J1650−500, thus the full available bandpass down to 0.7 keV was used.

2.2.2.2 RXTE

The *RXTE* spectra were prepared by Dr. Mickäel Coriat, which I summarise here. The data reduction used HEASOFT software package v6.11 following the standard steps described in the (RXTE) data reduction cookbook[2]. The PCA spectra were extracted from the top layer of the Proportional Counter Unit (PCU) 2 which is the best calibrated detector out of the five PCUs. The response matrix was then created and the background was modelled. A systematic uncertainty of 0.5 % was also added to all spectral channels in order to account for calibration uncertainties in the PCA response matrix. Recently, it has been noted (see Hiemstra *et al.* 2011;

[1] I did not apply EPFAST to the burst mode observations of XTE J1650−500 since it strongly affects the Fe line profile (Walton *et al.*, 2012). This is likely to be because of the extremely high count rate of this observation being inappropriate for the tool.

[2] http://heasarc.gsfc.nasa.gov/docs/xte/data_analysis.html

Kolehmainen *et al.* 2014) that there is a conflict in the cross-calibration of the PCA and EPIC-pn, whereby there is an energy-dependent discrepancy, at least below ~ 7 keV, and I therefore employed this as the lower limit of the bandpass. In all cases the PCA was fit up to 20 keV.

For HEXTE, the response matrix was produced and the necessary dead-time correction was applied. The HEXTE background is measured throughout the observation by alternating between the source and background fields every 32s. The data from the background regions were then merged. When possible data from both detector A and B was used to extract source and background spectra. However, from 2005 December, due to problems in the rocking motion of Cluster A, spectra from Cluster B could only be extracted. On 2009 December 14, Cluster B stopped rocking as well. From this date, only PCA data were used in the analysis, which only affects the analysis of XTE J1752−453. HEXTE channels were grouped by four and fit in the 20–120 keV band.

2.2.3 Selected sources

2.2.3.1 XTE J1652−453

XTE J1652−453 (hereafter J1652) was discovered by RXTE in 2009 (Markwardt *et al.*, 2009c), and subsequent follow-up observed a spectrum consistent with a black hole, including a strong residual around 6.4 keV corresponding to Fe Kα emission (Markwardt *et al.*, 2009a; Markwardt and Swank, 2009). Simultaneous observations with *XMM-Newton* (ID: 0610000701) and *RXTE* (ID: 94432-01-04-00) were taken during the same outburst on August 22, and previous analysis identifies the source as residing in the hard-intermediate state, with a broad Fe emission line and corresponding edge a prominent feature in the spectrum (Hiemstra *et al.*, 2011; Han *et al.*, 2011).

This EPIC-pn observation was operated in timing mode and the source spectrum was extracted from a region of RAWX [30:46], covering the entire RAWY strip as is standard. The EPIC-pn spectrum was fit in the 1.3–10 keV band as a result of a "soft excess" being present, as already indicated in Hiemstra *et al.* (2011).

Currently there is no constraint on any of the binary parameters of J1652 and therefore the inclination was fit freely other than where stated for the purpose of analysis.

2.2.3.2 XTE J1752−223

XTE J1752−223 (hereafter J1752) is also a recent discovery (Markwardt *et al.*, 2009b). Initial spectral fits suggested the source to be a black hole candidate and at that stage residing in the low-hard state, with a prominent Fe K line also reported (Shaposhnikov *et al.*, 2009; Muñoz-Darias *et al.*, 2010). J1752 was later observed with *XMM-Newton* (ID: 0653110101) and simultaneously with *RXTE* (ID: 95360-01-11-04) on April 6-7 2010 during the decay of it's 2009 outburst. J1752 was reported to be in the decay phase of the low-hard state during the observation (Reis *et al.*, 2011); however, we find that the spectrum is consistent with the source still residing in the hard-intermediate state (see also Shaposhnikov *et al.* 2010; Curran *et al.* 2011).

The EPIC-pn dataset was again taken in timing mode and I extracted the spectrum from a region in RAWX [30:46]. The resultant good exposure time was 18 ks. Once again the EPIC-pn spectrum was constrained to the 1.3–10 keV region due to a strong residual at lower energies (Reis *et al.*, 2011).

J1752 already has some useful constraints on its binary parameters (e.g. Shaposhnikov *et al.* 2010). Of specific interest to this study Miller-Jones *et al.* (2011) find the inclination angle of the jets to be $\theta < 49^{\circ}$ using optical and radio observations. Although the inclination angle of relativistic jets may not necessarily correspond to the inclination of the accretion disc (Maccarone, 2003), I apply this as a tentative, yet useful, constraint in the investigation of this source.

2.2.3.3 XTE J1650−500

Conversely XTE J1650−500 (hereafter J1650) is not only a well studied source, but it also has one of the most analysed Fe Kα emission lines in the literature, utilising observations by *XMM-Newton* (Miller *et al.*, 2002; Reis *et al.*, 2010; Walton *et al.*, 2012) and *BeppoSAX* (Miniutti *et al.*, 2004; Done and Gierliński, 2006).

I report on the same *XMM-Newton* observation first discussed in Miller *et al.* (2002) and later in Reis *et al.* (2010) and Walton *et al.* (2012), where the source was noted to be consistent with residing in the HIMS state and exhibiting a strong Fe K line in the spectrum. J1650 was observed in burst mode with the EPIC-pn camera onboard *XMM-Newton* on September 13 2001. The spectrum was extracted from a region in RAWX [27:46] and RAWY [<160]. I applied the RAWY constraint following the recommendation of Kirsch *et al.* (2006) where an analysis of the Crab nebula showed that pile-up can become an issue at large RAWY when observing

intense sources[3]. I used the full 0.7–10 keV energy range; however, there was no simultaneous *RXTE* observation to extend the bandpass.

The only constraint on the binary inclination of J1650 is a lower limit of $50^\circ \pm 3$ (Orosz *et al.*, 2004). Later on in the analysis I show that applying this limit is not necessary. However, introducing an upper constraint of 70°, as applied in an investigation by Reis *et al.* (2010), masks a significant degeneracy in the line models. It is not clear what is the physical motivation for the 70° upper limit, but presumably this comes from the lack of absorption features and eclipses, which are the hallmark of an accretion disc with $i > 70^\circ$ (Ponti *et al.*, 2012). I also note that spectral and temporal X-ray properties of XTE J1650−500 suggest that the accretion disc inclination is low ($< 60^\circ$; Ponti *et al.* 2012; Muñoz-Darias *et al.* 2013; Motta *et al.* 2014).

2.3 Analysis and results

2.3.1 Models used

2.3.1.1 The continuum

The X-ray spectrum of black hole binaries can generally be described by a combination of a thermal blackbody component originating from the disc and a power-law of Compton up-scattered seed photons, with the entire intrinsic spectrum subsequently modified by interstellar absorption. The continuum model used in this study consists of a disc blackbody DISKBB (Mitsuda *et al.*, 1984) and a POWERLAW, in addition to an interstellar photoelectric absorption component PHABS. I assume the standard abundances of ANGR (Anders and Grevesse, 1989) and BCMC (Balucinska-Church and McCammon, 1992) in XSPEC and all parameters were fitted freely, unless otherwise stated. XSPEC version 12.8.0 was used for all the analysis presented in this chapter.

I initially fit the PHABS∗(DISKBB+POWERLAW) model with the Fe K band (4–7 keV) ignored to ensure any reflection residuals there do not effect the continuum parameters calculated. Figure 2.1 displays the subsequent fits for all of the sources, plus the data/model ratio with the ignored Fe K region restored to indicate its prominence with respect to the continuum. For J1650, it appears that the excluded

[3]Whilst this violates my strict criteria to not analyse sources with pile-up, this action was taken only as a matter of caution. Even if the full RAWY strip is used EPATPLOT recorded no pile-up in the spectrum. I note as well that the analysis of Kirsch *et al.* (2006) was based on observations of the Crab, which is a much brighter source than XTE J1650−500 was in this observation.

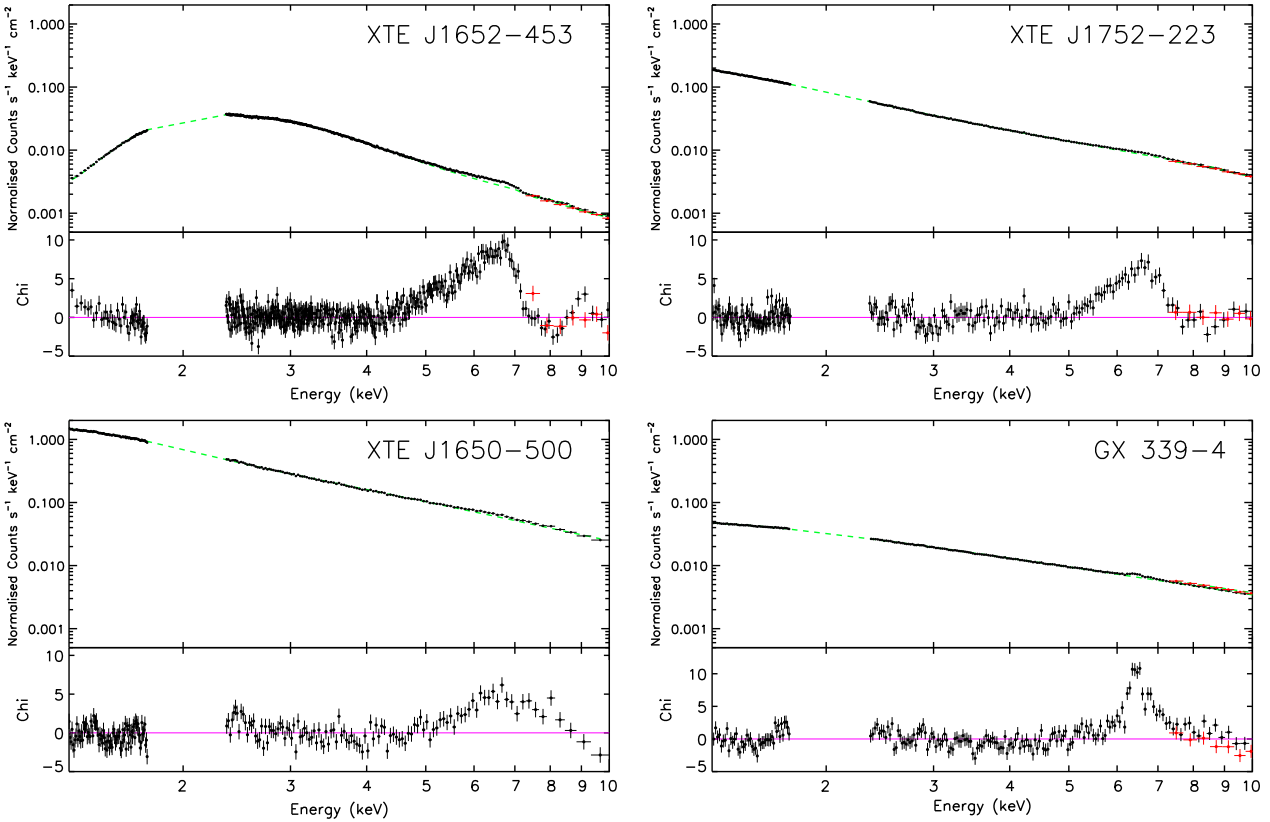

Figure 2.1: The *XMM-Newton* and *RXTE* spectra when fit to the continuum model (see §2.3.1.1). The 4–7 keV region was not included in the fit ('ignored' in XSPEC) to ensure only the continuum was being modelled, then it was added back in ('noticed') to display its relative strength to the fitted continuum. The top section displays the XMM (black) and PCA (red) data divided by the response effective area at each channel, with the green dotted line indicating the folded model. The lower section shows the data-model residuals in terms of sigma, with each point having an error bar of one sigma. All spectra are re-binned for the purpose of plotting only, and each x and upper–y axis scale is equivalent. In addition, a hard state observation of GX 339−4 is included for comparison (Observation 2 in Chapter 3), which clearly displays a significantly narrower Fe line than the other three observed in the HIMS.

4–7 keV region is too narrow for the Fe line profile; however, I still applied the 4–7 keV exclusion to maintain a consistent analysis of the three sources. I note that the use of different extraction regions (e.g. 5–8 keV) had no effect on the fit parameters listed in Tables 2.1-2.3. All of the continuum spectra were modelled successfully with these three components (see §2.3.2) and I hence employed this as the only continuum model for the entire investigation. Since a power-law is not a physical model, I also performed fits using the thermal Comptonisation model NTHCOMP; however, for all three sources the fit was not improved, hence I continued using the power-law model to allow a direct comparison to the previous analyses of these data sets, which all used a power-law.

2.3.1.2 The Fe Kα Line

Specifically my aim was to investigate the effect of any degeneracies within the line fitting method upon the determination and confidence level of black hole spin estimates. Therefore for this analysis I applied the two most widely used models LAOR (Laor, 1991) and KYRLINE (Dovčiak *et al.* 2004; recently up-dated version, private communication with M. Dovčiak), plus the most recent addition RELLINE (Dauser *et al.*, 2010).

LAOR is the dominant line model applied in the literature; however, the model table has much poorer resolution relative to more recent models. Despite its flaws, the LAOR model generally agrees with alternative models and offers an excellent comparison to previous work. It profiles the broadened line from an accretion disc orbiting a maximal Kerr black hole. Although the spin parameter is fixed one can still estimate the disc properties through the resolved inner radius parameter. However, KYRLINE and RELLINE are part of a new generation of line modelling, where the spin parameter is able to be fitted freely in addition to much higher resolution tables.

To maintain consistency I applied the following constraints in fits with all three models. I assume a single power-law dependence for the emissivity which scales as R^{-q}. Therefore when a model includes a broken power-law emissivity (e.g. RELINE), *i.e.* where there are two rings of contrasting radial emissivity separated by a specific transition radius, I linked the two power-laws to be equal and fixed the radius. Except where stated, I constrained the rest line energy to be between 6.4–6.97 keV, corresponding to the range of neutral to H-like Fe Kα emission. Additionally, the outer radius R_{out} is fixed to be $400\,r_g$ in all cases, which corresponds to the highest value of R tabulated for the LAOR model. KYRLINE and RELLINE

are tabulated to $1000\,r_{\rm g}$, but I use the same value to maintain consistency between the three models. I also note that emission beyond $400\,r_{\rm g}$ makes a negligible contribution to the profile for the range of emissivity profiles fitted in this study. The remaining parameters are fitted freely except where stated in section 2.3.2. Finally, I applied the standard LAOR limb-darkening law ($F(\mu_e) \propto 1 + 2.06\mu_e$)[4] in all the line models. This describes the effect of the angle of emission μ_e upon the line flux and in the other models alternative laws can be used, such as for limb-brightening. I used the limb-darkening law for two reasons: firstly to allow the most direct comparison with previous work, and secondly to ensure each model used the same law. However, it should be noted that the angular emissivity law can impact the derived profile of the line (Beckwith and Done, 2004), and in the case of limb-darkening lead to a possible enhancement of the red wing, and hence an increase in the inferred spin/radial emissivity (Svoboda *et al.*, 2009).

2.3.1.3 Self-consistent reflection spectrum fitting

Instead of modelling just the Fe Kα line, one can also use a self-consistently calculated reflection model to describe the full reprocessed spectrum (see §1.4.1 for a detailed discussion of these models). To do this I applied REFLIONX (Ross and Fabian, 2005), which describes reflection from a constant density ionised disc illuminated by a power-law spectrum. This allows a large range of ionisation states and transitions, as well as the Compton hump, to be modelled self-consistently.

REFLIONX, however, only models the reflected emission, hence it is necessary to apply a convolution component to allow for the relativistic effects observed at infinity. In this investigation I focus upon three such models: KDBLUR (for a LAOR profile), KERRCONV (Brenneman and Reynolds, 2006) and RELCONV (for a RELLINE profile). The former represents the most widely used model, but like LAOR only resolves the inner radius assuming a maximal Kerr black hole. KERRCONV includes the spin of the black hole as a free parameter and is the most widely used model to measure the spin of black holes. RELCONV represents a recent improvement of the KERRCONV model, and is the only model to include the option of retrograde spin. I use this method as a means to investigate whether self-consistent reflection fitting can offer more confident spin estimates than the line fitting routine. To maintain this comparison I used the same constraints as in the line fitting method where applicable.

Since REFLIONX only models the reflection spectrum I still used the underlying

[4] μ_e is the angle of emission of a photon emitted from the accretion disc

continuum of PHABS(DISKBB+POWERLAW), and coupled the photon index parameter from the POWERLAW component to the input illuminating spectrum used by REFLIONX. The additional ionisation parameter ξ (see Eq. 1.8) is fitted freely in all cases. The Fe abundance is fixed to be solar for all spectral fits. I took this approach since studies of chemical abundances in LMXBs have found metallicity values consistent with solar (see e.g. González Hernández *et al.* 2011).

2.3.1.4 Markov Chain Monte Carlo analysis

As I will display later in this section, X-ray reflection fitting is highly susceptible to degeneracies, which is further complicated by the high number of free parameters in fitting. To further assess this possibility a Markov Chain Monte Carlo (MCMC) statistical analysis was performed on the best fit results employing RELCONV∗REFLIONX. This technique is also later applied in Chapters 3 and 5.

For this I used the Metropolis–Hastings algorithm included in XSPEC. For each dataset two 55,000 element chains were run, of which the first 5000 elements were discarded ('burnt'). Each chain began at a random perturbation away from the best fit parameters (Tables 2.1–2.3). The proposal distribution was taken from the diagonal of the covariance matrix calculated from the best fit, which was assumed to be a Gaussian distribution, and a rescaling factor of 10^{-3} was applied. Using the resultant 100,000 element chain I then investigated the probability distributions of individual and correlated parameters, which is analysed in the following section.

2.3.2 Results from spectral fitting

2.3.2.1 XTE J1652−453

The pn-PCA-HEXTE bandpass over 1.3–4 and 7–120 keV is well fitted by the continuum model ($\chi^2/\nu = 1452/1077$). The major residuals are a slight excess around 20 keV, which is likely to be a 'Compton hump', and a sharp dip between 8–11 keV in both the *XMM-Newton* and *PCA* spectra, which is likely to be an absorption edge. The addition of an edge (EDGE in XSPEC), with the threshold energy constrained to 7–10 keV, considerably improves the fit ($\chi^2/\nu = 1247/1075$). Although such a component is a characteristic element of the reflection spectrum, this was still required at the same energy when the self-consistent reflection mode REFLIONX was applied.

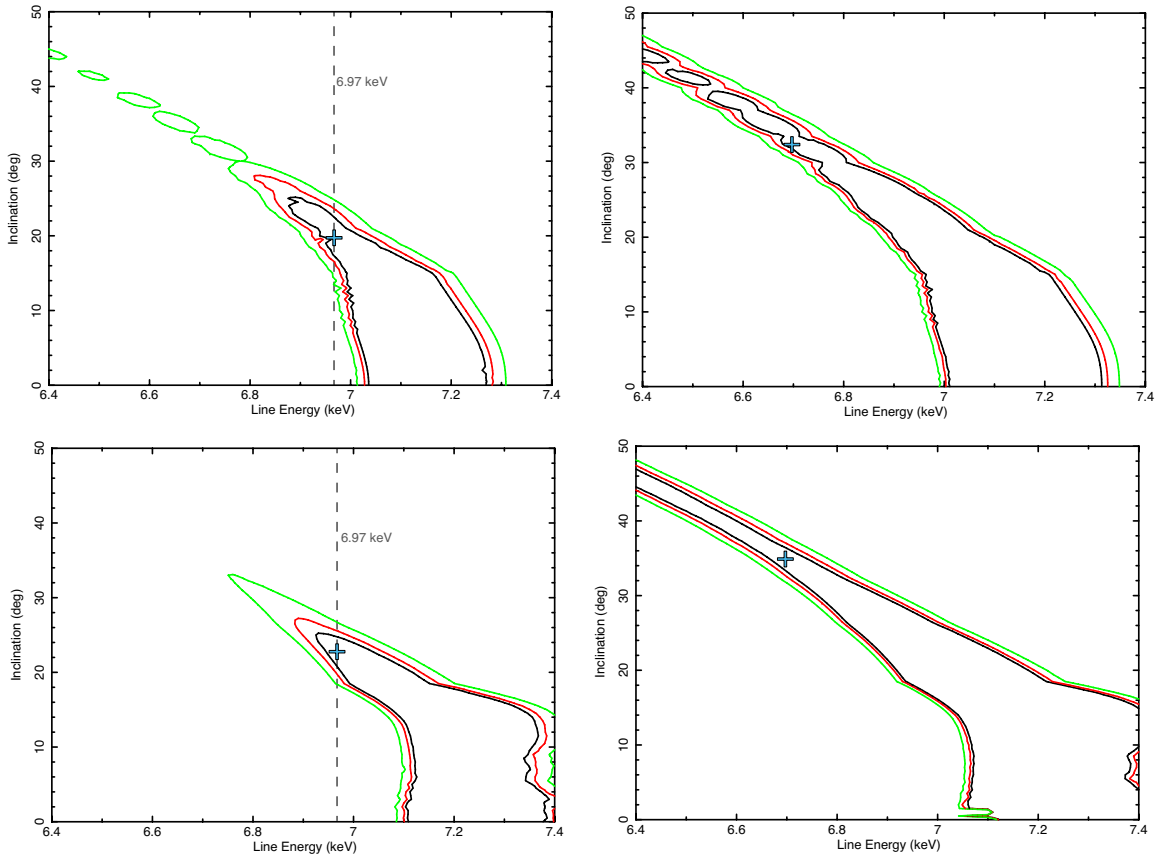

Figure 2.2: XTE J1652−453: Line energy versus inclination contour plots using the LAOR (top) and RELLINE (bottom) line models, indicating a clear degeneracy between the two parameters. The left plots indicate the confidence regions for the best-fit when the line rest energy has been fitted between 6.4–6.97 keV, and the right plots display the same but for the best-fit for when the line energy was fixed at 6.7 keV (but then 'thawed' to create this plot). Fits are at the 68% (black), 90% (red) and 99% (green) confidence levels respectively, and the blue cross shows the point of best-fit (Table 2.1).

This was interpreted by Hiemstra *et al.* (2011) as a possible deficiency in the model, whereas Chiang *et al.* (2012) later suggested that it may signify a rapidly outflowing accretion disc wind.

With the continuum model deemed to be acceptable I then restored the 4–7 keV region, which exposed a significant residual due to the Fe Kα emission (Figure 2.1). I first performed fits using the three chosen line models, the results of which are collated in Table 2.1. Initially I fit all of the line parameters freely except for the line energy, which was constrained to between 6.4–6.97 keV (see section 2.3.1.2), covering the full range of neutral to H-like Fe Kα emission. I note that this is the standard procedure used in the literature (see e.g. Reis *et al.* 2010). I found that all three models reproduce the profile very well, with KYRLINE and RELLINE showing excellent consistency with each other. Whilst LAOR found slightly different results (e.g. 19.6° (LAOR) vs 22.7° (KYRLINE/RELLINE)), they were not significantly different and mostly consistent within errors, which would suggest only slight differences in the models. This may be due to LAOR having a fixed spin value of 0.998. However, for all three models the line energy parameter E_{rest} pegs at the upper limit of 6.97 keV. There are two conclusions to be drawn from this: (1) The emission is coming from exclusively H-like Fe or (2) there is a degeneracy or error in the model forcing it to this value. The former is quite unlikely since disc illumination studies often show a mixture of states, which arise as deeper surface layers are expected to be less ionised because less irradiation reaches them (see e.g. García and Kallman 2010; García *et al.* 2011). The results are consistent within errors with those presented in Hiemstra *et al.* (2011).

To test hypothesis (2) I ran the same fit again for all three models, but allowed the line energy to be fit without constraint. As can be seen in Table 2.1, the line energy prefers a fit to a much higher value of 7.12 keV (LAOR), 7.21 keV (KYRLINE) and 7.20 keV (RELLINE) respectively. Additionally, I observed a significant lowering of the predicted inclination, and a moderate increase (decrease) in the inner radius (spin). The remaining parameters were fairly consistent.

Explaining this degeneracy is quite simple (see Figure 2.2). The inclination is calculated from the blue wing of the emission line, *i.e.* a more blue-shifted profile indicates a higher inclination. The line energy can be thought of in a similar manner too, a higher value essentially being a blue-shift of the rest energy of the emission. Therefore, a similar profile can be obtained by fitting a higher line energy and lower inclination, or vice versa, thus shifting the line energy to unphysical values. However, the effect of the trend is not completely uniform upon the profile, hence the variation in other parameters, specifically the spin/inner radius.

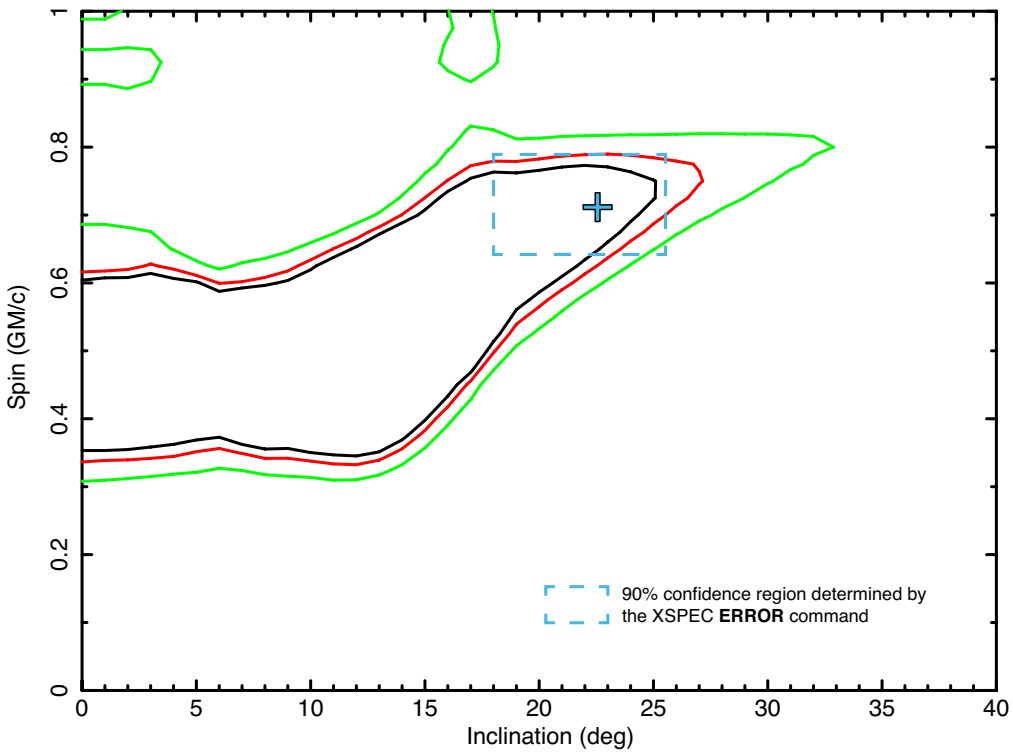

Figure 2.3: XTE J1652−453: Black hole spin versus inclination contour plot using the line mode RELLINE after fitting the line energy between 6.4–6.97 keV, indicating a clear degeneracy between the two parameters. Fits are at the 68% (black), 90% (red) and 99% (green) confidence levels respectively, and the blue cross shows the point of best-fit (Table 2.1). The blue dashed box indicates the 90% confidence region determined by the ERROR command (Table 2.1), which clearly does not represent the true parameter space.

Since the line energy is significantly affected by the degeneracy, it brings into question whether the dominant emission stage is even H-like Fe. He-like Fe Kα emission occurs at 6.7 keV, and is the direct ionisation state before that of H-like emission at 6.97 keV. I thus continued the analysis by fixing the line energy parameter to be at 6.7 keV, which produced the same trend again. The inclination value increased to nearly 35°, following the same relation between itself and the line energy outlined before. Additionally the inner radius (spin) followed the same trend, now reaching lower (higher) values. Through the change of just one ionisation state the spin varied by nearly 10% of its theoretical range (−0.988 to 0.988), hence revealing that when a degeneracy occurs between other parameters the effect on the spin can still be quite profound. This is a systematic error which is never reported in confidence limits. Figure 2.3 reveals the relationship between inclination and spin, and displays how the true error on the spin parameter is considerably larger. There is also an increase in the emissivity parameter; however, this is not very significant,

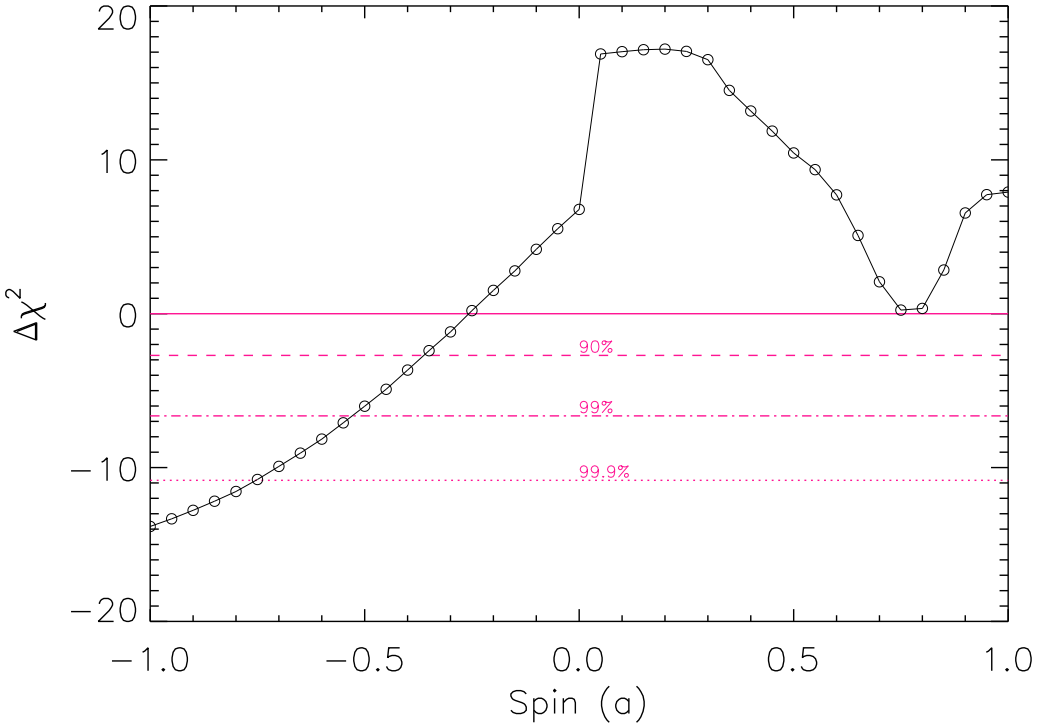

Figure 2.4: XTE J1652−453: The χ^2 confidence contours of the RELCONV∗REFLIONX spin parameter, which was fitted between 0–0.998 (the solid line indicates the best-fit: Table 2.1) and then allowed to explore the full parameter space (−0.998 to 0.998). The solid line dashed, dash-dot and dotted lines display the 90%, 99% and 99.9% confidence levels, clearly indicating that a retrograde spin is much preferred. If the spin is constrained to be prograde, then there is a clear minimum at $a \sim 0.8$.

and is again likely due to the slight change in the overall profile caused by the other parameters.

The EDGE component is fit at 8.74 ± 0.06keV ($\tau_{max} = 0.14 \pm 0.02$) when using all three line models, which lies between the respective edges of Li-like ($\sim$ 8.69 keV) and He-like ($\sim$ 8.83 keV) emission. Assuming this is the corresponding edge of the emission line, this suggests that the results extracted for a line fixed at 6.7 keV are more likely to be correct than those fitted freely in the Fe Kα ionisation range, which peg at 6.97 keV. I finally applied the self-consistent reflection model REFLIONX, which can more accurately gauge the ionisation stage of the emission. The edge is still required (see also Hiemstra *et al.* 2011; Chiang *et al.* 2012), although the depth is half of that recorded when fitting the line models. All three relativistic blurring models converge on an inclination and spin of $i \sim 32^\circ$ and $a \sim 0.8$ respectively, which is again consistent with the line results for a rest energy of 6.7 keV.

As one final test I extended the spin parameter range of RELCONV to −0.998 to 0.998, since the model allows for retrograde spin. For the fit when the spin was well

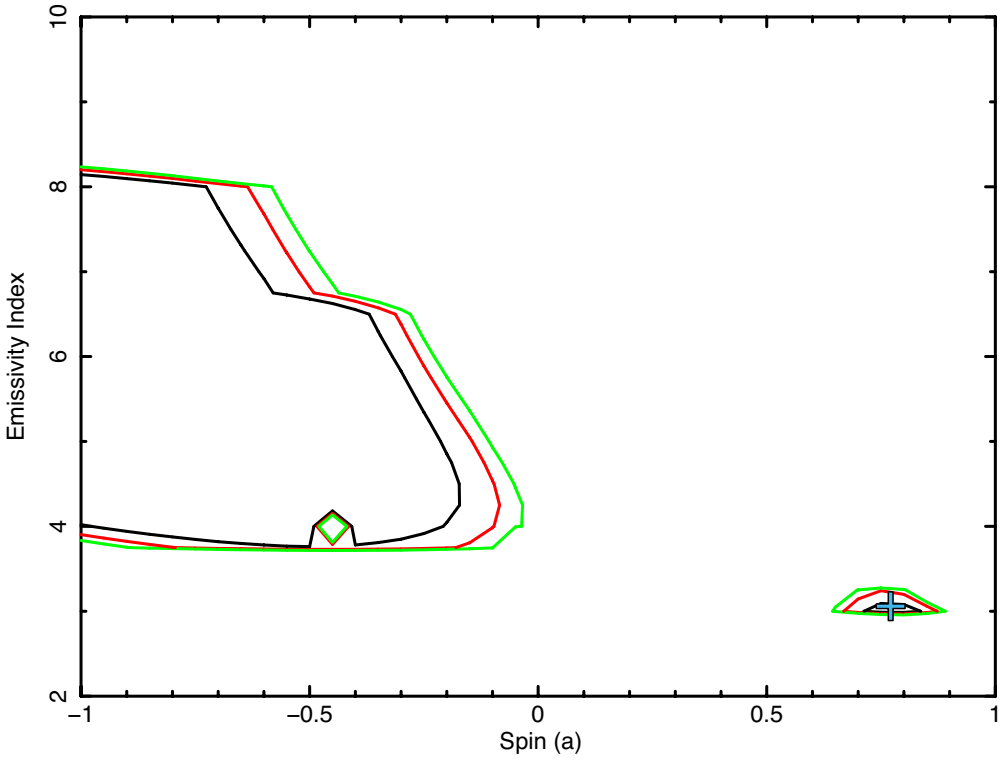

Figure 2.5: XTE J1652−453: A plot of the confidence regions between the spin parameter and emissivity index, calculated for the best-fit using RELCONV∗REFLIONX when the spin parameter was constrained to be prograde (0–0.998). Evidently, an equally good fit exists for a high index–low spin. Fits are at the 68% (black), 90% (red) and 95% (green) confidence levels respectively, and the blue cross shows the point of best-fit found when assuming prograde spin (Table 2.1).

constrained between 0–0.998, Figure 2.4 shows the variation in χ^2 for both prograde and retrograde spin, and reveals that in fact retrograde spin is much preferred by the data. This was confirmed by the subsequent extended fit (Table 2.1). Most of the parameters remained fairly constant within errors, and in particular the inclination was unaffected; however, the emissivity parameter rose considerably (although the errors were much larger too; Table 2.1). Figure 2.5 shows the confidence region between the spin and emissivity parameters, which hints at a degeneracy; however, as Fig. 2.4 also shows, the degeneracy is not forcing the fit, since it is poorest intermediate to the two fits ($a = 0 - 0.5$). This suggests that the effect a rapidly spinning black hole has on the space-time, and hence the emission profile, is crucial to the fit. It should be noted, however, that for a retrograde spin the emissivity index is not expected to be > 4 (Dauser *et al.*, 2013). Since the spin parameter hits the hard limit of -0.998 I also tested whether the disc may be truncated beyond $9\,r_g$ (the ISCO for a black hole spin of -0.998); however, the inner radius parameter

converged around $9\,r_g$ so no certain conclusion can be drawn on this.

The probability distributions derived from the MCMC analysis (§ 2.3.1.4) confirm that the spin, inclination and emissivity parameters are well determined (Fig. 2.6). The emissivity index varies between 5–10, and smaller values are generally associated with higher spin, although this does not appear to be a strict correlation. Nevertheless, this is not unusual, since, as described before, a larger emissivity index yields a larger contribution to the profile from the inner disc, thus affecting the red wing much like increasing the spin does. There is also a hint at a correlation between the inclination and spin parameters (Fig. 2.7). The MCMC probability distribution more accurately accounts for such degeneracies, and thus (assuming the inner disc is at the ISCO) yields an upper limit on the spin of <-0.65, which is larger than that determined by the XSPEC ERROR command. How a retrograde system is formed is quite uncertain (see the discussion in §1.5); however, this result would add to a number of recent works have reporting negative spins from LMXBs (Gou *et al.*, 2010; Reis *et al.*, 2013b; Middleton *et al.*, 2014; Morningstar *et al.*, 2014).

2.3.2.2 XTE J1752−223

The continuum model provided a good description of the J1752 spectrum ($\chi^2/\nu = 1170/1043$ fitted between 1.3–4 and 7–20 keV). The main residual appeared to again be an absorption feature present at 8–10 keV, and as for J1652 this was accounted for with an edge component, which improved the fit further to $\chi^2/\nu = 1096/1041$. There was no obvious indication of a 'Compton hump', but this may not be apparent due to the upper energy limit of 20 keV without available HEXTE data. When the ignored 4–7 keV region was substituted back into the data a very prominent broadened Fe Kα emission line was evident (see Figure 2.1).

Again I began the analysis by fitting the three line models with the rest energy constrained between 6.4–6.97 keV, all of which resulted in an excellent fit to the line profile (e.g. $\chi^2/\nu = 1632/1637$ with LAOR). Furthermore, all three reported similar results: an inclination and spin parameter of $\sim 36^\circ$ and ~ 0.55 respectively (refer to Table 2.2 throughout this section), which are consistent with those reported in Reis *et al.* (2011). However, once again, the rest energy pegged at the upper constraint of 6.97 keV, suggesting another degeneracy could be driving the results. Indeed, when rest energy constraints were removed, the parameter shifted to much higher values

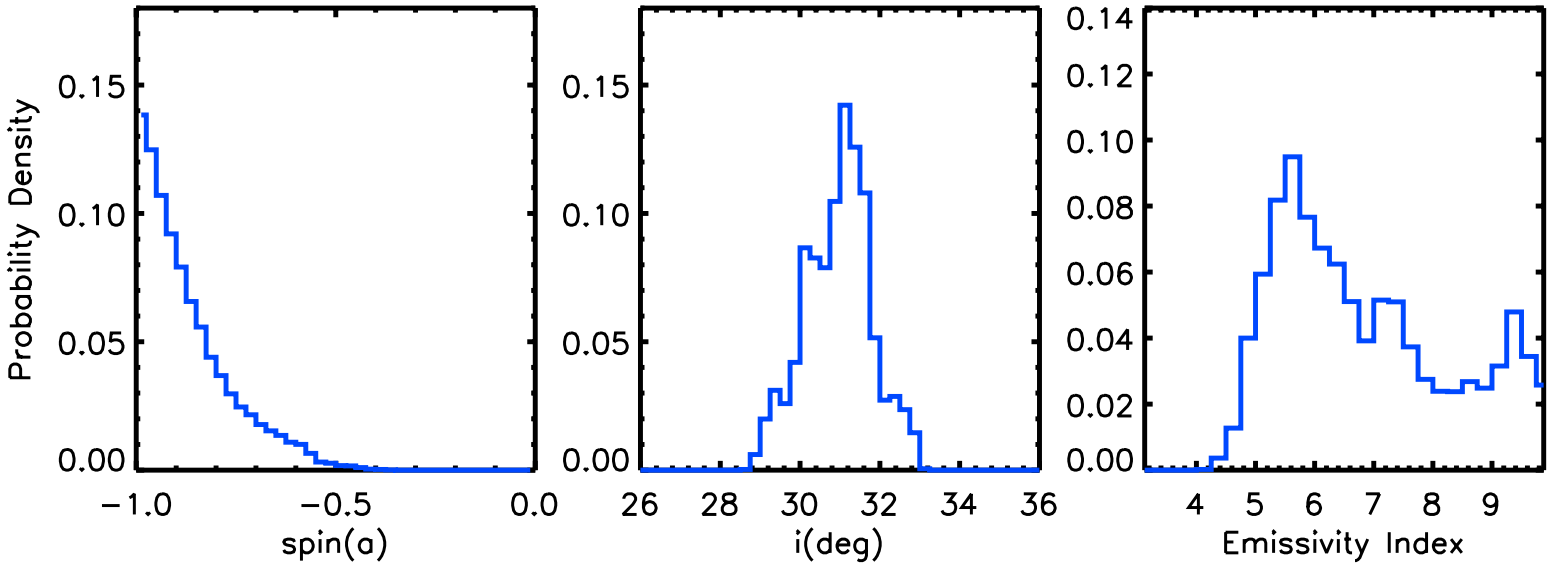

Figure 2.6: XTE J1652−453: Probability distributions of the spin, inclination and emissivity index parameters for the MCMC derived 100,000 element chain, based on the best-fit of RELCONV∗REFLIONX. Each bin corresponds to a width of $a = 0.025$, $i = 0.25^{\circ}$ and $q = 0.25$ respectively.

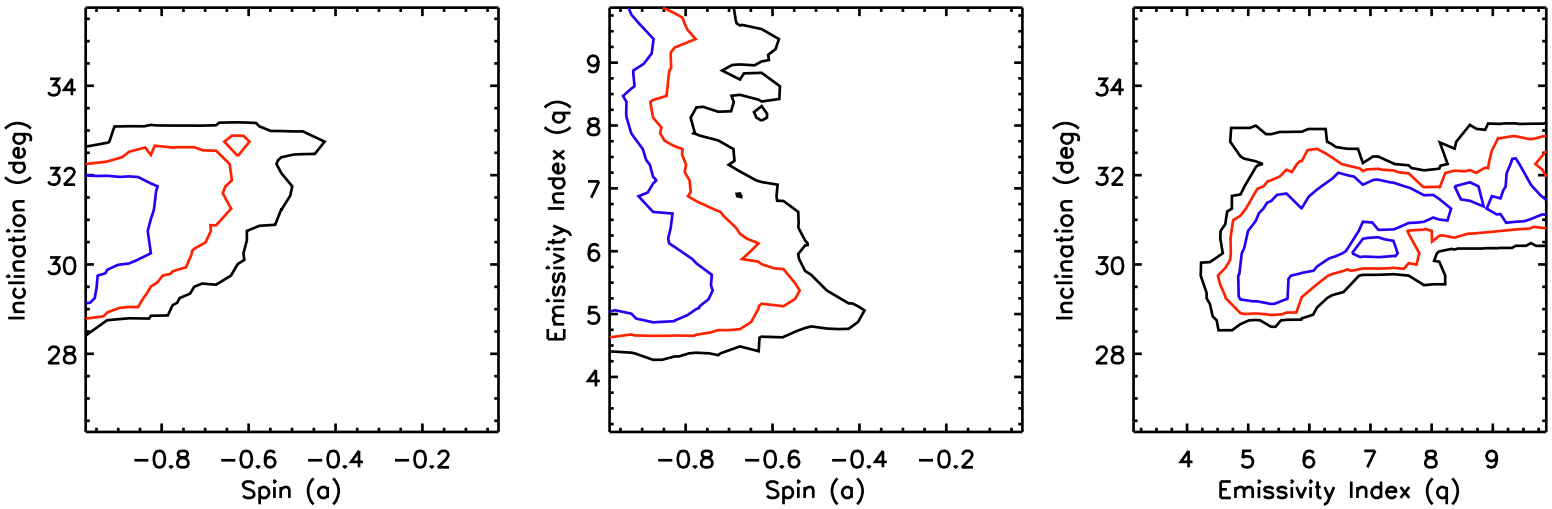

Figure 2.7: XTE J1652−453: Two-dimensional probability distributions of the same three parameters. For each panel I plot contour levels at the 68% (blue), 90% (red) and 99% (black) confidence levels. Each plot contains the full distribution for the whole parameter range with the axis reduced for clarity.

(~ 7.56 keV LAOR/RELLINE; 8.45 keV KYRLINE) which yielded a marginally better fit ($\Delta\chi^2 \sim -5$). Many parameters varied in addition to the rest energy: the inclination lowered; the spin (inner radius) decreased (increased); and the emissivity slightly increased. The contrasting results recorded by KYRLINE occur because the spin parameter pegged at the zero lower limit, whereas RELLINE and LAOR are able to go below zero and beyond $6\,r_g$ (the ISCO for a Schwarzschild black hole) respectively. Fits where the rest energy was fixed at 6.7 keV confirmed the same trends (i.e. this time to higher inclination and spin etc).

Figure 2.8 displays the confidence region of the inclination parameter against the rest energy (top) and spin (bottom). It is quite evident that the same degeneracy observed for J1652 between the inclination and rest energy is present. Particularly at 90% and 95% confidence it is clear that increasing rest energy gives equivalent results to lower inclination values. Applying the upper constraint of 6.97 keV actually forces what is quite a large parameter space into a much smaller region, yielding a misleadingly good constraint on both parameters. Two regions are exposed which correspond to the parameter space for the 'constrained' and 'free' fits respectively, and this is also apparent when inclination is plotted against the spin, which itself varies significantly.

At a 90% confidence the line energy could very well be closer to neutral (6.4 keV) for a high inclination. Importantly, there exists an upper limit of the inclination angle of the relativistic jets observed (Miller-Jones *et al.*, 2011), which should correspond to the inclination angle of the inner disc (but see Maccarone 2003). Without this constraint a very large range of spin parameter is possible above 50° (Figure 2.8) and would thus essentially render a spin estimate at a reasonable confidence (e.g. 90%) impossible through this method.

Fitting the self-consistent reflection spectrum of REFLIONX I found that contrasting results exist between the convolution models. KDBLUR finds a very large upper limit on the emissivity; however, given the slightly truncated disc predicted ($15.4^{+9.6}_{-1.06}$) the emissivity parameter is ultimately more difficult to constrain. In contrast, KERRCONV and RELCONV converged on moderate spins (~ 0.37), but the emissivity parameter pegged at the hard limit of 10. Figure 2.9 exposes two distinct confidence regions in the inclination-emissivity plane: the emissivity index can be around 3 for $i \sim 30°$ or 6–10 for $i \sim 42°$. Without any strong constraint on the disc inclination (e.g. via the binary inclination) both regimes are possible; however, given that the emissivity index has pegged at the extremely high value of 10, it is likely that a degeneracy is forcing the fit. I reproduced the fit fixing the emissivity parameter at 3 which confirmed a similar fit existed ($\Delta\chi^2 = +3.36$ for 1 extra degree

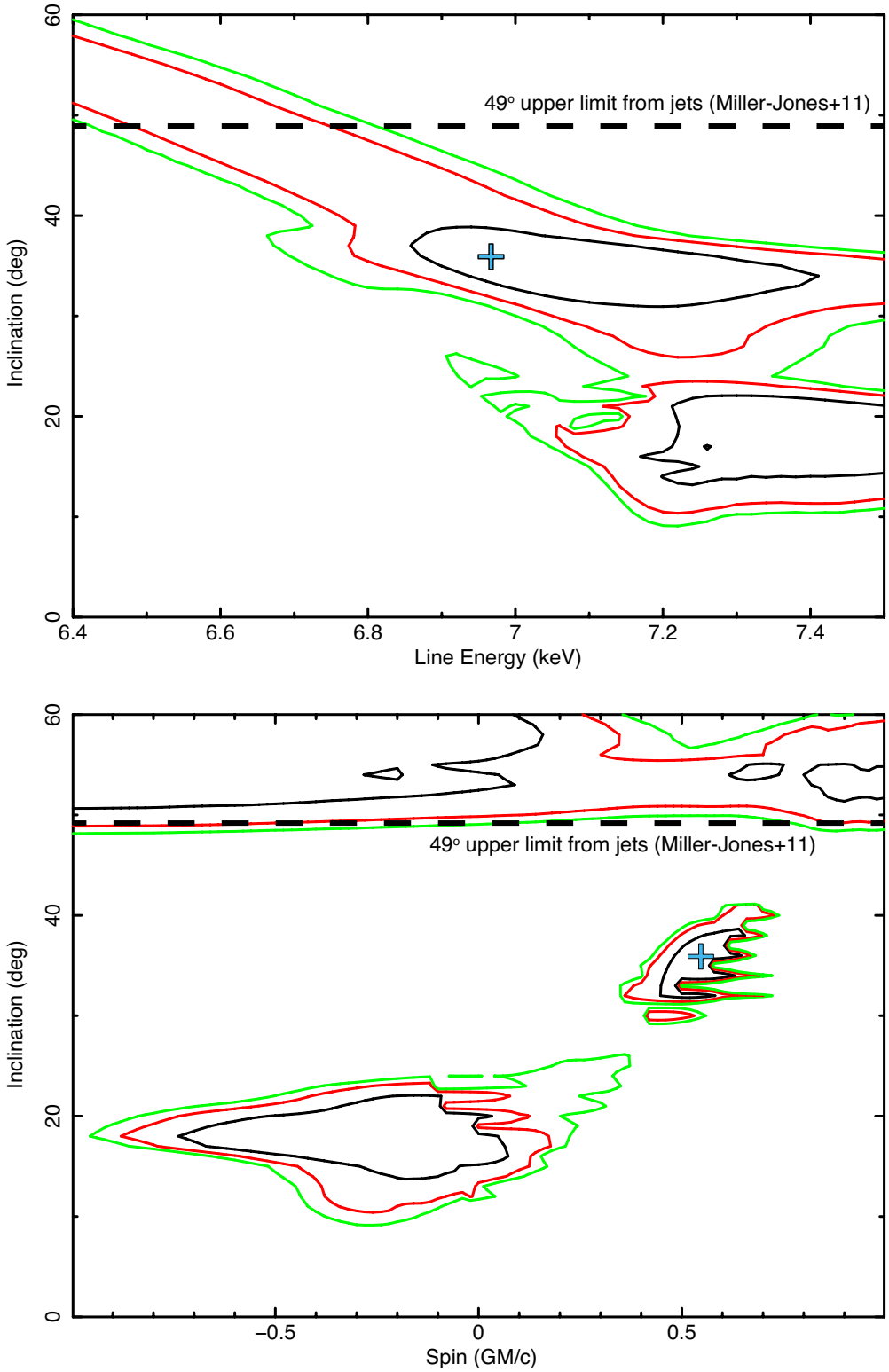

Figure 2.8: XTE J1752−223: Plots of the confidence region for the inclination parameter against the rest energy (top) and spin (bottom). These were calculated for the best-fit using RELLINE when the rest energy was constrained to between 6.4–6.97 keV. Contours are at the 68% (black), 90% (red) and 95% (green) confidence levels respectively, and the blue cross shows the point of best-fit (Table 2.2). Distinct degeneracies are observed between the parameters which clearly impact the confidence in measuring spin.

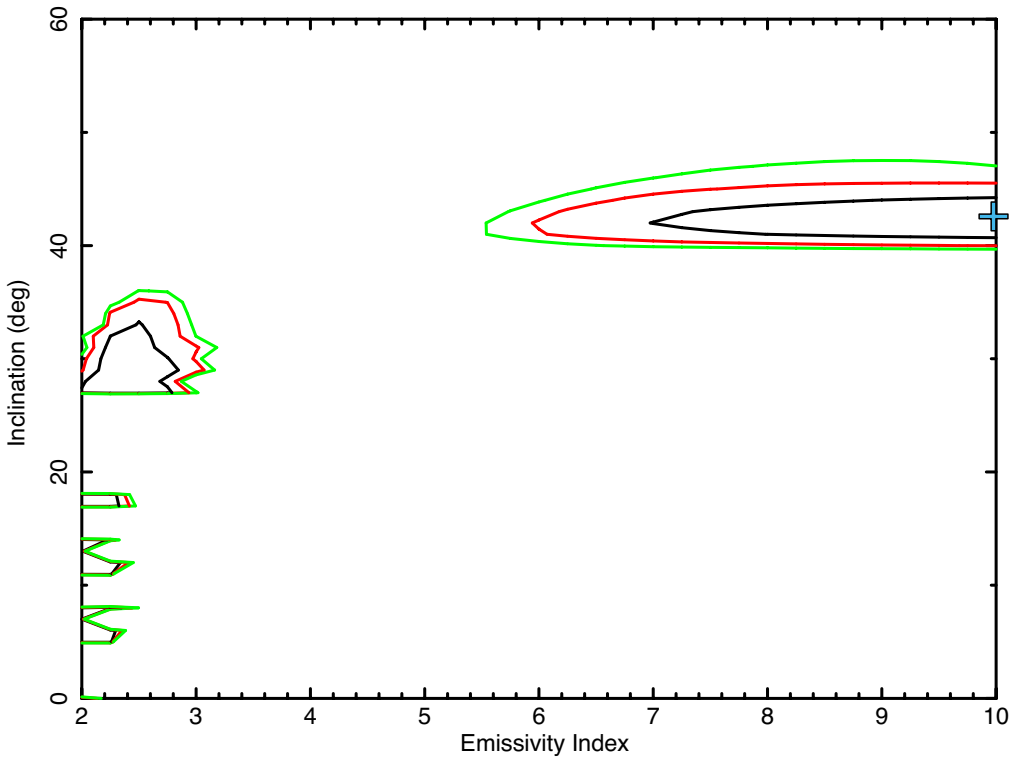

Figure 2.9: XTE J1752−223: A plot of the confidence region of the inclination parameter against the emissivity index. This was calculated for the best-fit using RELCONV∗REFLIONX, which indicates that two distinct areas of confidence exist, and the two parameters may be degenerate (a similar trend was found in Reis *et al.* 2011). Contours are plotted at the 68% (black), 90% (red) and 95% (green) confidence levels respectively, and the blue cross shows the point of best-fit (Table 2.2).

of freedom). Interestingly, this also reduced the spin parameter to the hard limit of -0.998. By allowing the inner radius to be a free parameter[5] an improved fit was found for $r_{in} \sim 15\, r_g$, in agreement with the results of KDBLUR, and thus suggests that in fact the accretion disc of J1752 during this observation was truncated, and therefore a spin estimate is not possible. This emphasises the danger of implicitly assuming the accretion disc is at the ISCO.

I explored the truncated disc fit further using MCMC analysis (see § 2.3.1.4 for further details). In Figure 2.10 I display the probability distribution of the inner radius, inclination and emissivity parameters, which also converges on a truncated inner disc of radius $\sim 16\, r_g$. Furthermore, $6\, r_g$ (the ISCO for a Schwarzschild black hole) and $9\, r_g$ (the ISCO of a maximal retrograde black hole) are ruled out at the

[5]For this fit the spin parameter was fixed at 0.998, since it could be degenerate with the inner radius and allows the largest range of r values to be spanned. This also then allows a direct comparison to the results with KDBLUR, which has a fixed spin value of 0.998.

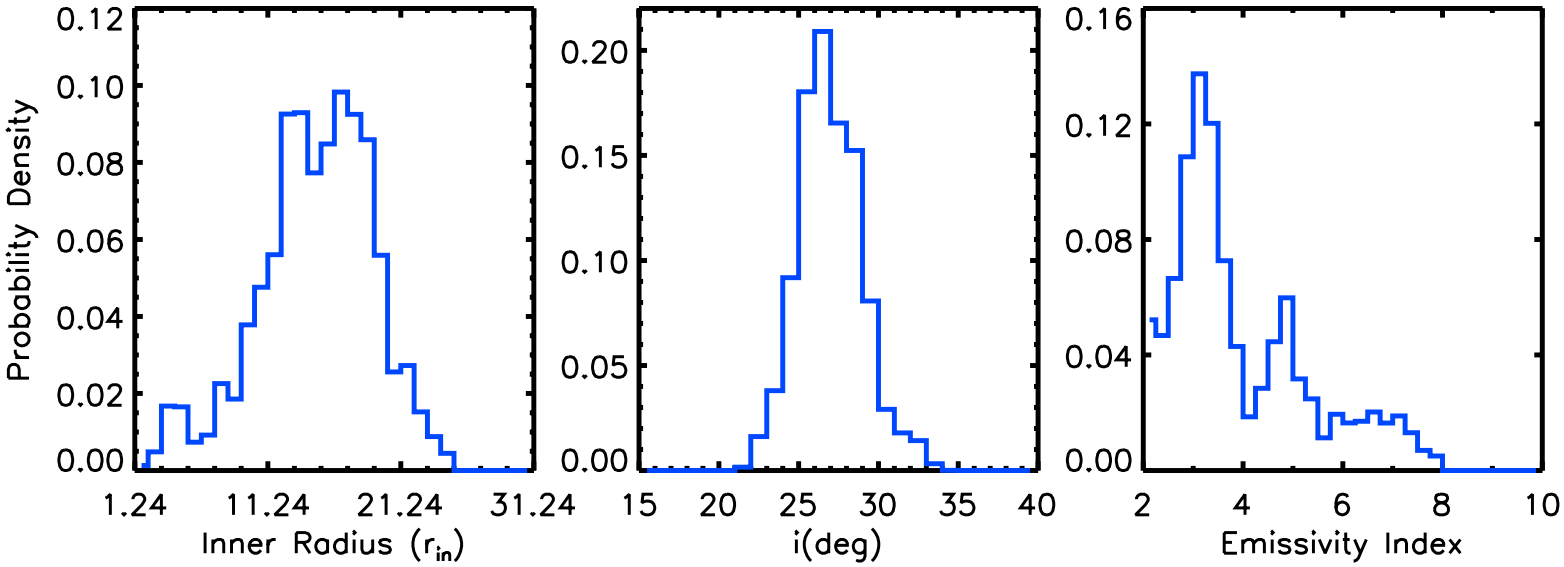

Figure 2.10: XTE J1752−223: Probability distributions of the inner radius, inclination and emissivity index parameters for the MCMC derived 100,000 element chain, based on the best-fit of RELCONV∗REFLIONX. Each bin corresponds to a width of $r_{\rm in} = 1\,r_{\rm g}$, $i = 1^{\circ}$ and $q = 0.25$ respectively.

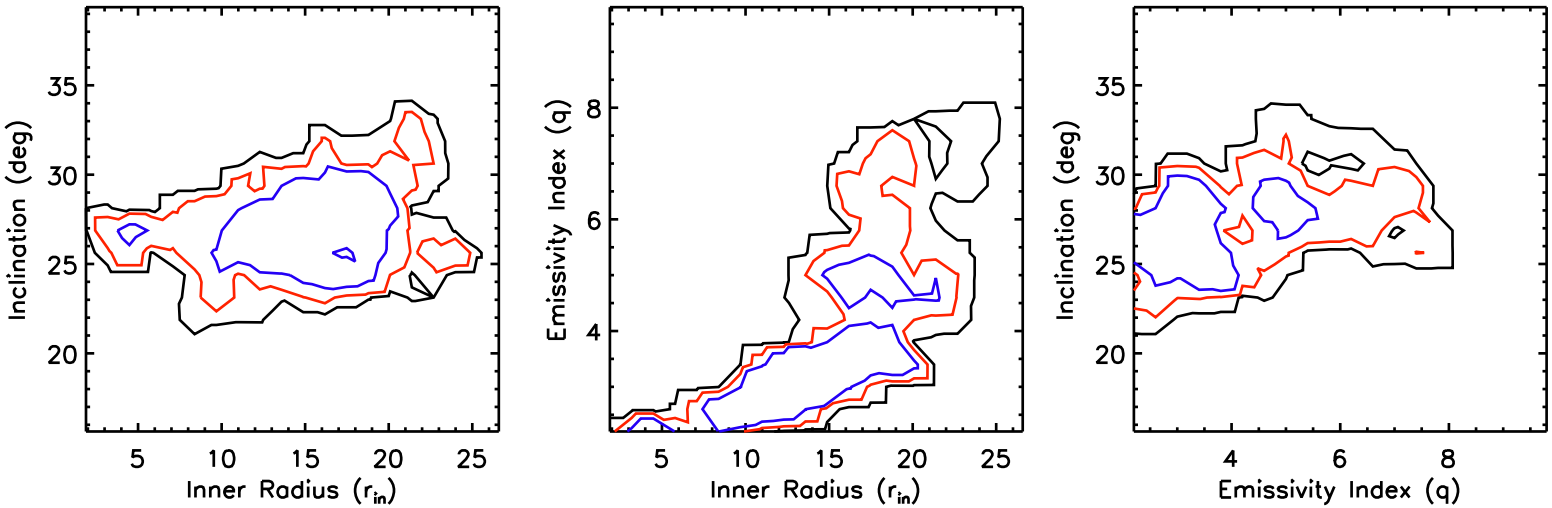

Figure 2.11: XTE J1752−223: Two-dimensional probability distributions of the same three parameters. For each panel I plot contour levels at the 68% (blue), 90% (red) and 99% (black) confidence levels. Each plot contains the full distribution for the whole parameter range with the axis reduced for clarity.

95% and 90% level respectively. An emissivity index of 3 is preferred, as expected for a truncated disc; however, the confidence regions between the emissivity and inner radius parameter suggest that a degeneracy may be present in Fig. 2.11, thus no definitive measurement of the radius can be drawn. Note that this is the same degeneracy uncovered during the MCMC analysis of J1652, since the spin parameter is in essence a measurement of the inner radius.

2.3.2.3 XTE J1650−500

The continuum model fits well to the XMM EPIC-pn spectrum of J1650 in the 0.7–4 7–10 keV band ($\chi^2/\nu = 1424/1120$). There is a slight soft residual remaining below 1 keV; however, the main disparity is above 7 keV and adding the 4–7 keV region back reveals that this is largely due to the blue wing of the Fe emission (Figure 2.1). This is indicative of a high inclination source, since the projected velocity of the rotating material increases as the disc becomes more edge on. The results referred to in this section are presented in Table 2.3.

As in the previous sections, I began the analysis by fitting the relativistic line models. In a previous investigation of this dataset, Reis *et al.* (2010) constrained the inclination parameter to be in the range 47–70°, hence I also initially applied this limit to allow a direct comparison to this work. Later I relax this constraint, but see §2.2.3.3 for the physical motivation of including these limits. I found an excellent agreement between KYRLINE and RELLINE, whilst LAOR is consistent within errors. All three models find an inclination of 70°, hence pegging at the hard limit imposed, as do the line energy (6.97 keV) and spin (0.998) parameters. The emissivity index is also extremely high (~ 9.5), and in all represents an extremely broad profile. Unsurprisingly when the inclination parameter is allowed to extend up to 89° it pegs at this value. In turn the line energy now pegs at its lower limit of 6.4 keV, whilst the spin and emissivity reduce to 0.66 and 2.3 respectively. The model LAOR records slightly different results, but follows the same trends. The significant variation in all the parameters makes disentangling the underlying degeneracies very difficult. The fit may be compromised further by the lack of *RXTE* data above 10 keV, especially since the blue wing of the profiles extends up to 9 keV (Figure 2.1).

The self-consistent reflection treatments agreed well, and were able to freely converge upon an inclination of $\sim 72°$. The emissivity index is very high (~ 7) and the spin parameter pegs at the upper limit of 0.998, thus the Fe profile is extremely broadened by relativistic effects. To this end, since the spin and emissivity are

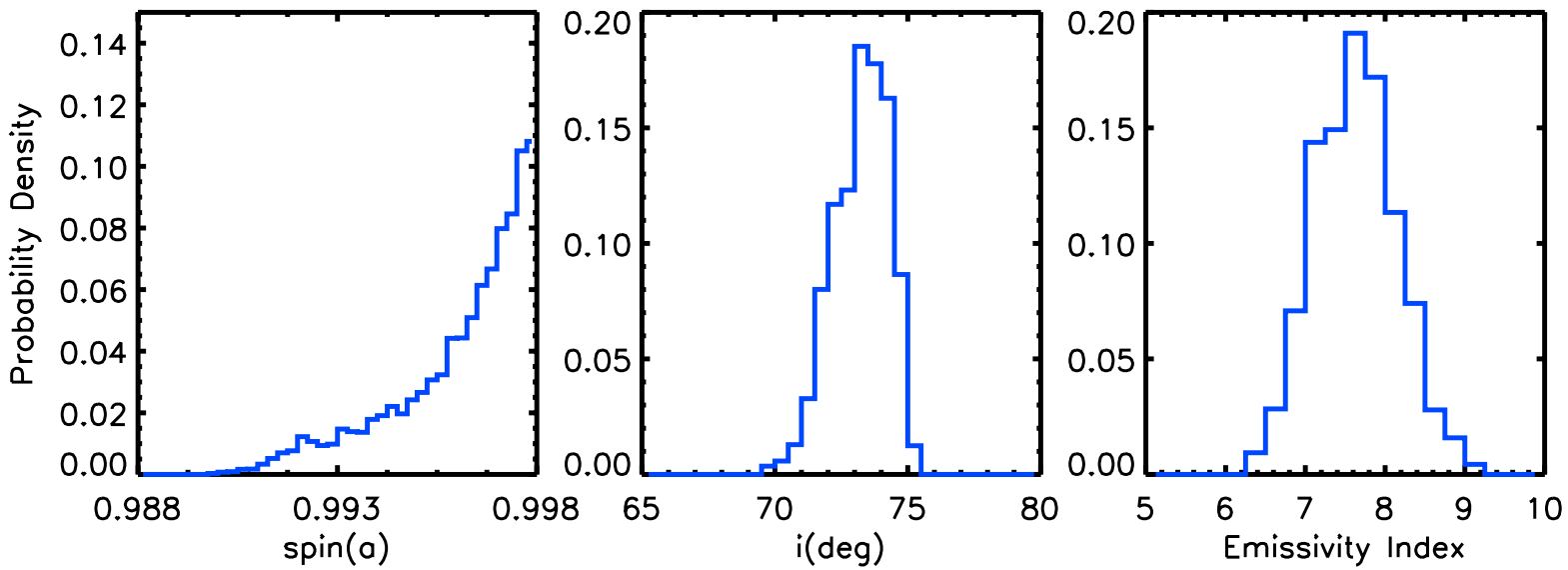

Figure 2.12: XTE J1650−500: Probability distributions of the spin, inclination and emissivity index parameters for the MCMC derived 100,000 element chain, based on the best-fit of RELCONV∗REFLIONX. Each bin corresponds to a width of $a = 2.5\text{E}{-}04$, $i = 0.5^\circ$ and $q = 0.25$ respectively.

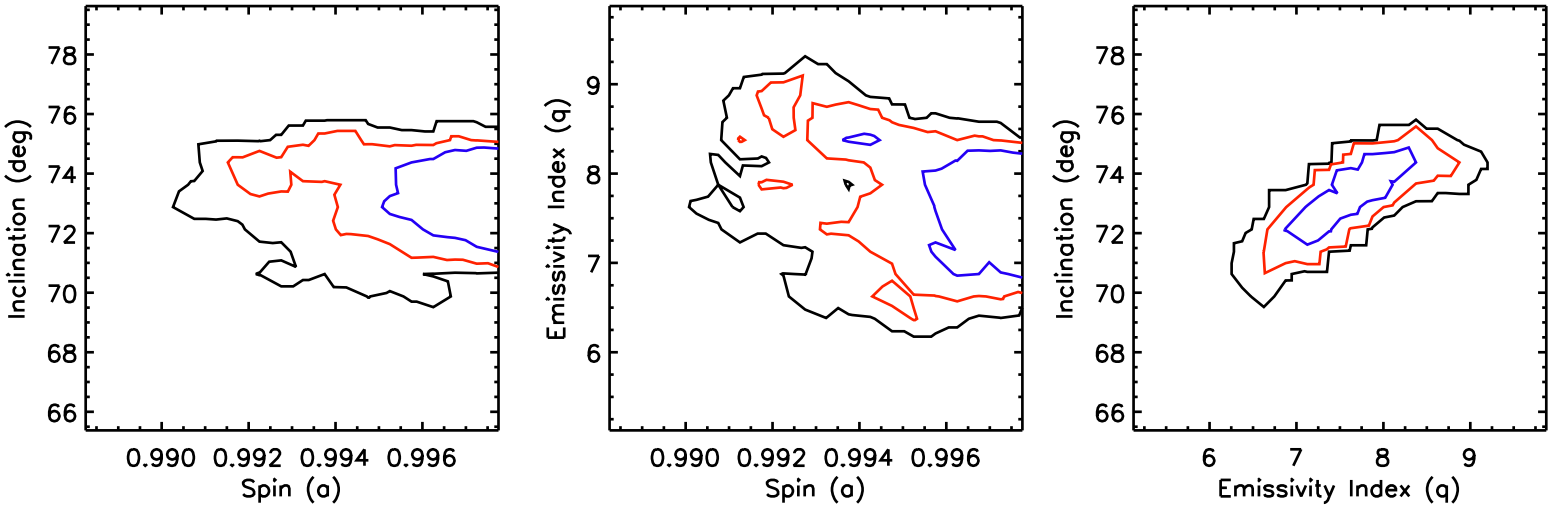

Figure 2.13: XTE J1650−500: Two-dimensional probability distributions of the same three parameters. For each panel I plot contour levels at the 68% (blue), 90% (red) and 99% (black) confidence levels. Each plot contains the full distribution for the whole parameter range with the axis reduced for clarity.

at the edge of their respective parameter spaces, it may be that the inclination is constrained by this rather than being truly fit. It should be noted that the inclination upper limit of J1650 is not well determined. Because of the lack of X-ray dips and eclipses, in conjunction with the relatively small mass function (Orosz *et al.*, 2004), the inclination is almost certainly below 70°. Furthermore, no absorption features indicative of an accretion disc wind have been reported, which only occur in high inclination (>70°) sources. It is compelling as well though that the spectral and temporal properties of J1650 suggest that it is, in fact, a low inclination source (<60°; Muñoz-Darias *et al.* 2013; Motta *et al.* 2014).

I performed another fit using RELCONV∗REFLIONX with a fixed inclination of 60° to test how this may affect the spin estimate, and also potentially uncover any parameter degeneracies. The emissivity index decreased to a more moderate value (4.7) and the spin lessened slightly to 0.95, which hints at a degeneracy between the parameters. However, the fit with $i = 60°$ was considerably worse ($\Delta\chi^2 = +37$ for one extra degree of freedom). I performed a MCMC analysis on the best fit, which confirmed that all the parameters were well and correctly determined (Figures 2.12 and 2.13) by the standard methods in XSPEC. In addition, a degeneracy is also apparent between the inclination and emissivity parameters; however, the parameter space this affects is quite small, and does not appear to affect the spin value determined. All evidence points towards a near-maximal Kerr black hole, as previously found by Reis *et al.* (2010) and Walton *et al.* (2012).

2.4 Discussion and conclusions

In this chapter I have investigated the accuracy of spin determination through modelling the relativistic effects imprinted in X-ray reflection. In doing so I invoked a number of strict criteria to ensure the best case scenario was analysed. I used only *XMM-Newton* observations, which offers the greatest effective area at 6 keV of any CCD instrument. Only data where pile-up was certainly *not* present were used. I also employed only hard-intermediate state observations, which offer a clear and simple power-law continuum beneath the broad Fe line at 6 keV. I note as well that each of the three spectra used in this study display clear relativistic broadened Fe profiles (Figure 2.1), which were previously used for measuring the spin of their respective black hole (Reis *et al.*, 2010; Hiemstra *et al.*, 2011; Reis *et al.*, 2011; Walton *et al.*, 2012). In all, the three observations employed offer the best case scenario for measuring black hole spin through X-ray reflection at present.

I analysed the use of both relativistic line models (e.g. LAOR) and self-consistent reflection treatments (e.g. RELCONV∗REFLIONX) to measure spin, employing the current range of models applied in the literature. Here I summarise the main findings, and how this could affect current and future spin estimates through X-ray reflection.

The line rest energy and inclination parameters are extremely degenerate

The rest energy and inclination parameters are very difficult to concurrently determine, since increasing their respective values acts to shift the profile blue-wards. The rest-energy does this by definition, whilst at higher inclinations the projected velocity of disc particles is higher[6]. Clear degeneracies between the rest energy and inclination parameters are displayed in Figures 2.2 and 2.8. I note that using self-consistent reflection treatments, such as REFLIONX, removes this issue since the rest energy is hard-wired into the model.

Inclination affects the measurement of spin

The increased projected velocity of the material with inclination serves to broaden the profile, of which the strength of the two peaks is affected by aberration, and the influence of both of these effects is dependent upon how far the disc extends to the black hole, which is of course determined by the spin. At small gravitational radii (i.e. at the ISCO) the relationship between spin and inclination is quite complex. For example, there is a trade-off between emission from smaller radii, which has an increased radial velocity and thus stronger beaming, and the increased gravitational redshift closer to the black hole. Nevertheless, it is easy to see how inclination can mimic some of the effects that spin has upon the profile. For J1652 and J1752 it is very evident that for smaller inclination fits the spin decreases, and vice versa (Table 2.1 and 2.2). Conversely, for J1650 the opposite actions occur, but still result in a large variation in spin. Exploring the confidence regions between spin and inclination indicates how degenerate the two can be (Figure 2.2 and 2.8), and thus in the absence of any reasonable constraint on the disc inclination value a large range of spin is possible. To truly test this a comparison of inclination fitted via reflection against other well established means is required, such as through the binary system or relativistic jets.

[6]Further spectral evidence for this comes from higher peak disc temperatures observed from accretion discs at higher inclination (Muñoz-Darias *et al.*, 2013)

The emissivity profile affects the measurement of spin

The emissivity profile and spin ultimately go hand-in-hand. A larger emissivity index q yields a stronger contribution from the inner regions of the disc to the line profile, where the emission is more strongly transformed by relativistic effects. Thus, increasing q broadens the profile in a similar manner to how increasing the spin does. MCMC analysis of the best-fit models for all three sources reveals slight trends between the two parameters (Figures 2.7, 2.11 and 2.13; see also Figure 2.5). Future models self-consistently treating the nature and spectrum of the illuminating source (i.e. height, size, shape) along with the associated reflection will go some way to breaking this degeneracy.

Line models should not be used to measure black hole spin

As displayed throughout the analysis, and discussed previously, using line models is highly susceptible to degeneracy. Imposing hard limits on parameters, such as 6.4–6.97 keV for the rest energy, only forces the spin into a confined parameter space, and does not yield any useful constraint.

The disc of XTE J1752−453 is truncated in this observation

An improved fit was found when allowing the inner radius to be a free parameter, which converged on a value of $15\,r_g$. Further MCMC analysis confirms that the disc is larger than $9\,r_g$ and $6\,r_g$ at the 90% and 95% confidence levels respectively. Since the disc is not at the ISCO a spin measurement can not be obtained for this observation.

The spin of XTE J1650−500 is near-extreme

I confirmed the results of Reis *et al.* (2010) and Walton *et al.* (2012) that the spin of the black hole in XTE J1650−500 is near extreme. The best-fit converged on a slightly higher than expected inclination; however, for a more reasonable value of 60°, the spin was only mildly affected (still >0.94).

None of the models appear to be exclusively flawed

The LAOR model is over two decades old and is hence limited, particularly in resolution (see Beckwith and Done 2004; Dovčiak *et al.* 2004 and Dauser *et al.* 2010). Despite this, where comparable, the results determined by LAOR and KDBLUR are not significantly different to those obtained by the latest models. The rather subtle disparities observed are likely to be due to the hard-wired spin of 0.998, and the relatively small table does not appear to make it more susceptible to degeneracy with the data currently available. Nevertheless, it goes without saying that RELLINE is the package of choice to measure

black hole spin, since it is the only one covering the full range (-0.998 to 0.998).

Narrow Fe lines are also highly susceptible to degeneracy

Finally, I note that degeneracies also affect the narrow Fe profiles of highly truncated accretion discs, such as those observed in the hard state (Chapter 3). Figure 3.12 displays how the inferred inner radius is strongly dependent upon the assumed inclination, which acts to broaden the profile as the relative doppler shift increases as the disc becomes more edge on. At large radii the relation between the inclination and inner radius is much simpler since the effects of aberration and gravitational redshift are greatly reduced.

Table 2.1: Various line model fits for XTE J1652−453. For all of the analysis I used the continuum model PHABS(DISKBB+POWERLAW). All errors presented are at the 90% confidence level. Where limits are displayed as a bracketed number this indicates that the respective hard limit has been reached within that confidence range. When no limit is presented this denotes that the local minimum is pegged at the respective hard limit. Finally if there is no upper or lower limit given this indicates that the parameter is fixed at this value.

		6.4–6.97 keV Line			Free Line			Line Fixed At 6.7keV			Self-Consistent Reflection			
Component	Parameter	LAOR	KYRLINE	RELLINE	LAOR	KYRLINE	RELLINE	LAOR	KYRLINE	RELLINE	KDBLUR	KERRCONV	RELCONV	RELCONV
PHABS	N_H (10^{22} cm^{-2})	$4.60^{+0.02}_{-0.02}$	$4.60^{+0.01}_{-0.02}$	$4.60^{+0.01}_{-0.01}$	$4.58^{+0.02}_{-0.02}$	$4.58^{+0.02}_{-0.02}$	$4.58^{+0.01}_{-0.01}$	$4.60^{+0.02}_{-0.02}$	$4.60^{+0.02}_{-0.02}$	$4.60^{+0.02}_{-0.02}$	$4.60^{+0.02}_{-0.02}$	$4.60^{+0.01}_{-0.01}$	$4.60^{+0.02}_{-0.02}$	$4.57^{+0.02}_{-0.02}$
DISKBB	T_{in} (keV)	$0.57^{+0.01}_{-0.01}$	$0.57^{+0.01}_{-0.01}$	$0.57^{+0.01}_{-0.01}$	$0.57^{+0.01}_{-0.01}$	$0.57^{+0.01}_{-0.01}$	$0.57^{+0.01}_{-0.01}$	$0.57^{+0.01}_{-0.01}$	$0.57^{+0.01}_{-0.01}$	$0.57^{+0.01}_{-0.01}$	$0.57^{+0.01}_{-0.01}$	$0.57^{+0.01}_{-0.01}$	$0.57^{+0.01}_{-0.01}$	$0.58^{+0.00}_{-0.00}$
	N_{BB}	1253^{+44}_{-52}	1249^{+36}_{-35}	1249^{+37}_{-35}	1204^{+47}_{-53}	1192^{+45}_{-25}	1200^{+39}_{-36}	1273^{+50}_{-49}	1265^{+53}_{-49}	1276^{+53}_{-49}	1259^{+57}_{-47}	1266^{+6}_{-15}	1266^{+46}_{-57}	1228^{+58}_{-53}
POWERLAW	Γ	$2.31^{+0.04}_{-0.04}$	$2.32^{+0.03}_{-0.03}$	$2.32^{+0.03}_{-0.02}$	$2.31^{+0.04}_{-0.04}$	$2.32^{+0.04}_{-0.04}$	$2.31^{+0.03}_{-0.03}$	$2.32^{+0.03}_{-0.04}$	$2.30^{+0.04}_{-0.04}$	$2.31^{+0.04}_{-0.04}$	$2.32^{+0.05}_{-0.04}$	$2.30^{+0.01}_{-0.02}$	$2.31^{+0.05}_{-0.05}$	$2.25^{+0.05}_{-0.05}$
	N_{PL}	$0.22^{+0.02}_{-0.02}$	$0.22^{+0.01}_{-0.01}$	$0.22^{+0.01}_{-0.01}$	$0.22^{+0.02}_{-0.02}$	$0.22^{+0.02}_{-0.01}$	$0.22^{+0.02}_{-0.01}$	$0.22^{+0.02}_{-0.02}$	$0.21^{+0.02}_{-0.02}$	$0.21^{+0.02}_{-0.02}$	$0.17^{+0.02}_{-0.02}$	$0.16^{+0.01}_{-0.01}$	$0.17^{+0.02}_{-0.02}$	$0.13^{+0.02}_{-0.02}$
RELATIVISTIC	a	—	$0.71^{+0.04}_{-0.08}$	$0.71^{+0.08}_{-0.07}$	—	$0.51^{+0.03}_{-0.07}$	$0.50^{+0.02}_{-0.04}$	—	$0.83^{+0.03}_{-0.04}$	$0.81^{+0.04}_{-0.04}$	—	$0.79^{+0.01}_{-0.01}$	$0.78^{+0.07}_{-0.09}$	$-0.998^{+0.23}$
LINE/	E_{rest} (keV)	$6.97_{-0.10}$	$6.97_{-0.06}$	$6.97_{-0.05}$	$7.12^{+0.06}_{-0.05}$	$7.26^{+0.06}_{-0.05}$	$7.22^{+0.03}_{-0.05}$	6.7	6.7	6.7	—	—	—	—
BLURRING	α	$3.41^{+0.13}_{-0.06}$	$3.60^{+0.11}_{-0.05}$	$3.59^{+0.11}_{-0.08}$	$3.43^{+0.08}_{-0.07}$	$3.55^{+0.10}_{-0.21}$	$3.53^{+0.05}_{-0.07}$	$3.55^{+0.23}_{-0.09}$	$3.92^{+0.19}_{-0.18}$	$3.81^{+0.19}_{-0.17}$	$2.97^{+0.13}_{-0.09}$	$3.05^{+0.06}_{-0.06}$	$3.04^{+0.15}_{-0.13}$	$6.87^{+2.95}_{-1.56}$
	r_{in} (r_g)	$3.04^{+0.48}_{-0.27}$	—	—	$3.65^{+0.33}_{-0.07}$	—	—	$2.58^{+0.16}_{-0.13}$	—	—	$2.78^{+0.27}_{-0.30}$	—	—	—
	i (deg)	$19.6^{+5.8}_{-2.1}$	$22.7^{+3.2}_{-2.1}$	$22.7^{+2.9}_{-4.7}$	$5.1^{+2.7}_{-5.1}$	$2.9^{+8.0}_{-2.8}$	$1.0^{+2.3}_{-1.0}$	$32.3^{+2.8}_{-1.0}$	$35.3^{+1.6}_{-1.7}$	$34.8^{+1.7}_{-1.7}$	$31.0^{+2.6}_{-1.6}$	$32.7^{+0.1}_{-0.3}$	$31.8^{+1.9}_{-1.9}$	$30.7^{+1.0}_{-1.1}$
	N_L (10^{-2})	$0.15^{+0.02}_{-0.02}$	$0.15^{+0.01}_{-0.02}$	$0.15^{+0.01}_{-0.01}$	$0.14^{+0.01}_{-0.01}$	$0.14^{+0.01}_{-0.01}$	$0.14^{+0.01}_{-0.01}$	$0.16^{+0.02}_{-0.01}$	$0.17^{+0.02}_{-0.02}$	$0.17^{+0.02}_{-0.02}$	—	—	—	—
REFLIONX	ξ	—	—	—	—	—	—	—	—	—	1478^{+941}_{-343}	1861^{+31}_{-68}	1662^{+673}_{-653}	2663^{+466}_{-324}
	N_R (10^{-6})	—	—	—	—	—	—	—	—	—	$1.29^{+0.94}_{-0.56}$	$0.97^{+0.09}_{-0.03}$	$1.11^{+1.08}_{-0.34}$	$0.53^{+0.08}_{-0.07}$
	χ^2	1770.86	1775.24	1775.58	1759.19	1759.96	1764.57	1778.64	1784.67	1790.79	1760.52	1756.98	1760.8	1746.97
	ν		1671			1671			1672			1671		

Table 2.2: Various line model fits for XTE J1752−223. For all of the analysis I used the continuum model PHABS(DISKBB+POWERLAW). All errors presented are at the 90% confidence level. Where limits are displayed as a bracketed number this indicates that the respective hard limit has been reached within that confidence range. When no limit is presented this denotes that the local minimum is pegged at the respective hard limit. Finally if there is no upper or lower limit given this indicates that the parameter is fixed at this value.

		6.4–6.97 keV Line			Free Line			Line Fixed At 6.7keV			Self-Consistent Reflection				
Component	Parameter	LAOR	KYRLINE	RELLINE	LAOR	KYRLINE	RELLINE	LAOR	KYRLINE	RELLINE	KDBLUR	KERRCONV	RELCONV	RELCONV	RELCONV
PHABS	N_H (10^{22} cm^{-2})	$0.13^{+0.01}_{-0.01}$	$0.12^{+0.02}_{-0.01}$	$0.12^{+0.01}_{-0.02}$	$0.15^{+0.01}_{-0.02}$	$0.15^{+0.02}_{-0.02}$	$0.15^{+0.02}_{-0.02}$	$0.13^{+0.01}_{-0.01}$	$0.13^{+0.02}_{-0.02}$	$0.13^{+0.02}_{-0.02}$	$0.19^{+0.02}_{-0.02}$	$0.16^{+0.01}_{-0.01}$	$0.16^{+0.02}_{-0.02}$	$0.18^{+0.02}_{-0.02}$	$0.19^{+0.02}_{-0.02}$
DISKBB	T_{in} (keV)	$0.45^{+0.01}_{-0.01}$	$0.46^{+0.01}_{-0.01}$	$0.45^{+0.01}_{-0.01}$	$0.43^{+0.01}_{-0.01}$	$0.43^{+0.01}_{-0.01}$	$0.43^{+0.01}_{-0.01}$	$0.44^{+0.01}_{-0.01}$	$0.45^{+0.01}_{-0.01}$	$0.45^{+0.01}_{-0.01}$	$0.41^{+0.01}_{-0.01}$	$0.44^{+0.01}_{-0.01}$	$0.44^{+0.01}_{-0.01}$	$0.42^{+0.01}_{-0.01}$	$0.41^{+0.01}_{-0.01}$
	N_{BB}	541^{+52}_{-33}	528^{+72}_{-60}	530^{+65}_{-58}	688^{+97}_{-101}	704^{+112}_{-93}	692^{+111}_{-96}	588^{+66}_{-46}	561^{+99}_{-72}	559^{+94}_{-76}	911^{+151}_{-139}	620^{+53}_{-82}	627^{+92}_{-109}	830^{+149}_{-122}	919^{+172}_{-145}
POWERLAW	Γ	$1.74^{+0.00}_{-0.01}$	$1.74^{+0.01}_{-0.01}$	$1.74^{+0.01}_{-0.01}$	$1.76^{+0.01}_{-0.01}$	$1.76^{+0.01}_{-0.01}$	$1.76^{+0.02}_{-0.01}$	$1.75^{+0.01}_{-0.01}$	$1.74^{+0.02}_{-0.01}$	$1.74^{+0.01}_{-0.01}$	$1.77^{+0.02}_{-0.02}$	$1.74^{+0.00}_{-0.01}$	$1.74^{+0.02}_{-0.03}$	$1.77^{+0.01}_{-0.01}$	$1.78^{+0.01}_{-0.02}$
	N_{PL}	$0.22^{+0.00}_{-0.00}$	$0.22^{+0.00}_{-0.00}$	$0.22^{+0.00}_{-0.00}$	$0.23^{+0.01}_{-0.00}$	$0.24^{+0.01}_{-0.00}$	$0.23^{+0.01}_{-0.00}$	$0.23^{+0.00}_{-0.00}$	$0.22^{+0.01}_{-0.00}$	$0.22^{+0.01}_{-0.01}$	$0.24^{+0.01}_{-0.02}$	$0.21^{+0.01}_{-0.01}$	$0.21^{+0.01}_{-0.02}$	$0.23^{+0.01}_{-0.01}$	$0.24^{+0.01}_{-0.02}$
RELATIVISTIC	a	—	$0.56^{+0.12}_{-0.10}$	$0.55^{+0.15}_{-0.09}$	—	$0.15^{+0.27}_{-0.00}$	$-0.36^{+0.31}_{-0.34}$	—	$0.75^{+0.10}_{-0.11}$	$0.77^{+0.08}_{-0.12}$	—	$0.36^{+0.14}_{-0.13}$	$0.38^{+0.21}_{-0.15}$	$-0.998^{+0.73}$	0.998
LINE/	E_{rest} (keV)	$6.97_{-0.12}$	$6.97_{-0.27}$	$6.97_{-0.27}$	$7.57^{(9)}_{-0.35}$	$8.45^{(9)}_{-0.52}$	$7.56^{(9)}_{-0.28}$	6.7	6.7	6.7	—	—	—	—	—
BLURRING	α	$4.78^{+0.34}_{-0.39}$	$4.92^{+0.55}_{-0.54}$	$4.93^{+0.69}_{-0.56}$	$5.75^{+2.09}_{-1.77}$	$8.29^{(10)}_{-2.85}$	$5.30^{+2.20}_{-1.09}$	$10_{-3.95}$	$5.34^{+1.73}_{-0.75}$	$5.48^{+1.73}_{-0.82}$	$3.65^{(10)}_{-1.14}$	$10_{-1.70}$	$10_{-3.23}$	3	$3.71^{(10)}_{-0.86}$
	r_{in} (r_g)	$3.63^{+0.38}_{-0.25}$	—	—	$6.25^{+0.86}_{-1.31}$	—	—	$2.04^{+0.16}_{-0.08}$	—	—	$15.93^{+8.83}_{-9.58}$	—	—	—	$15.91^{+11.46}_{-7.39}$
	θ (deg)	$35.5^{+2.6}_{-1.5}$	$35.8^{+3.9}_{-3.9}$	$35.8^{+3.7}_{-3.7}$	$17.1^{+2.6}_{-5.1}$	$13.8^{+2.1}_{-2.1}$	$17.4^{+2.0}_{-1.7}$	$58.5^{+3.1}_{-3.9}$	$45.2^{+6.6}_{-3.4}$	$46.1^{+5.4}_{-4.5}$	$26.5^{+3.3}_{-2.8}$	$41.6^{+2.4}_{-3.9}$	$42.5^{+2.0}_{-1.9}$	$29.6^{+1.3}_{-2.9}$	$27.2^{+3.3}_{-8.2}$
	N_L (10^{-3})	$1.48^{+0.13}_{-0.12}$	$1.45^{+0.15}_{-0.14}$	$1.45^{+0.15}_{-0.14}$	$0.98^{+0.17}_{-0.11}$	$1.00^{+0.14}_{-0.13}$	$0.97^{+0.14}_{-0.11}$	$1.54^{+0.16}_{-0.08}$	$1.49^{+0.20}_{-0.16}$	$1.61^{+0.18}_{-0.18}$	—	—	—	—	—
REFLIONX	ξ	—	—	—	—	—	—	—	—	—	1115^{+677}_{-537}	1079^{+51}_{-180}	1005^{+247}_{-187}	1030^{+218}_{-238}	1075^{+955}_{-327}
	N_R (10^{-6})	—	—	—	—	—	—	—	—	—	$0.94^{+0.41}_{-0.27}$	$1.50^{+0.08}_{-0.08}$	$1.60^{+0.38}_{-0.32}$	$1.09^{+0.12}_{-0.15}$	$0.97^{+0.28}_{-0.35}$
	χ^2	1631.82	1636.35	1636.48	1630.67	1635	1633.28	1633.74	1639.33	1639.94	1630.00	1632.53	1632.98	1636.34	1630.05
	ν		1637			1637			1638		1639	1639	1639	1640	1639

Table 2.3: Various line model fits for XTE J1650−500. For all of the analysis I used the continuum model PHABS(DISKBB+POWERLAW). All errors presented are at the 90% confidence level. Where limits are displayed as a bracketed number this indicates that the respective hard limit has been reached within that confidence range. When no limit is presented this denotes that the local minimum is pegged at the respective hard limit. Finally if there is no upper or lower limit given this indicates that the parameter is fixed at this value.

		6.4–6.97 keV Line			$47 \leq i \leq 70$			Self-Consistent Reflection			
Component	Parameter	LAOR	KYRLINE	RELLINE	LAOR	KYRLINE	RELLINE	KDBLUR	KERRCONV	RELCONV	RELCONV
PHABS	N_H (10^{22} cm^{-2})	$0.54^{+0.01}_{-0.01}$	$0.54^{+0.01}_{-0.01}$	$0.54^{+0.01}_{-0.01}$	$0.54^{+0.01}_{-0.01}$	$0.54^{+0.01}_{-0.01}$	$0.54^{+0.01}_{-0.01}$	$0.56^{+0.01}_{-0.01}$	$0.56^{+0.01}_{-0.01}$	$0.57^{+0.01}_{-0.01}$	$0.54^{+0.01}_{-0.01}$
DISKBB	T_{in} (keV)	$0.30^{+0.01}_{-0.01}$	$0.30^{+0.01}_{-0.01}$	$0.30^{+0.01}_{-0.01}$	$0.30^{+0.01}_{-0.01}$	$0.30^{+0.01}_{-0.01}$	$0.30^{+0.01}_{-0.01}$	$0.34^{+0.01}_{-0.02}$	$0.33^{+0.01}_{-0.01}$	$0.34^{+0.01}_{-0.01}$	$0.32^{+0.01}_{-0.01}$
	N_{BB}	61820^{+7668}_{-6209}	60124^{+5682}_{-5614}	60597^{+3391}_{-6060}	58397^{+6003}_{-5647}	59121^{+4521}_{-5606}	57963^{+5679}_{-2390}	24449^{+5196}_{-3800}	30068^{+253}_{-3269}	23009^{+402}_{-496}	43318^{+5386}_{-4476}
POWERLAW	Γ	$2.16^{+0.01}_{-0.03}$	$2.15^{+0.02}_{-0.02}$	$2.16^{+0.03}_{-0.01}$	$2.14^{+0.02}_{-0.02}$	$2.15^{+0.01}_{-0.02}$	$2.15^{+0.01}_{-0.02}$	$2.14^{+0.02}_{-0.02}$	$2.13^{+0.01}_{-0.01}$	$2.14^{+0.01}_{-0.01}$	$2.10^{+0.01}_{-0.01}$
	N_{PL}	$3.28^{+0.13}_{-0.11}$	$3.24^{+0.09}_{-0.10}$	$3.26^{+0.12}_{-0.11}$	$3.20^{+0.08}_{-0.09}$	$3.21^{+0.06}_{-0.09}$	$3.21^{+0.04}_{-0.09}$	$2.13^{+0.20}_{-0.10}$	$2.29^{+0.05}_{-0.05}$	$2.10^{+0.07}_{-0.11}$	$2.40^{+0.10}_{-0.12}$
RELATIVISTIC	a	—	$0.66^{+0.14}_{-0.66}$	$0.65^{+0.15}_{-0.11}$	—	$0.99^{+0.01}_{-0.01}$	$0.99^{+0.01}_{-0.01}$	—	$0.99^{+0.01}_{-0.01}$	$0.99^{+0.01}_{-0.01}$	$0.95^{+0.03}_{-0.01}$
LINE/	E_{rest} (keV)	$6.4^{+0.06}$	$6.4^{+0.04}$	$6.40^{+0.04}$	$6.97_{-0.11}$	$6.97_{-0.21}$	$6.97_{-0.21}$	—	—	—	—
BLURRING	α	$3.02^{+0.34}_{-0.34}$	$2.31^{+0.22}_{-0.17}$	$2.32^{+0.28}_{-0.11}$	$8.60^{(10)}_{-0.93}$	$9.82^{(10)}_{-1.03}$	$9.54^{(10)}_{-0.72}$	$6.72^{+1.28}_{-0.67}$	$6.58^{+0.19}_{-0.28}$	$7.23^{+0.31}_{-0.83}$	$4.69^{+0.67}_{-0.56}$
	r_{in} (r_g)	$2.39^{+1.20}_{-0.97}$	—	—	$1.49^{+0.10}_{-0.05}$	—	—	$1.24^{+0.15}_{-1.24}$	—	—	—
	i (deg)	$87.0^{(89)}_{-0.6}$	$89.0_{-1.5}$	$89.0_{-1.9}$	$68.1^{(70)}_{-3.3}$	$70.0^{(70)}_{-3.7}$	$70.0^{(70)}_{-3.8}$	$71.1^{+3.0}_{-1.7}$	$71.4^{+0.7}_{-1.2}$	$72.4^{+1.1}_{-2.1}$	60
	N_L (10^{-2})	$2.46^{+0.45}_{-0.48}$	$2.40^{+0.39}_{-0.54}$	$2.53^{+0.51}_{-0.47}$	$2.53^{+0.57}_{-0.35}$	$2.53^{+0.33}_{-0.35}$	$2.61^{+0.29}_{-0.46}$		—	—	—
REFLIONX	ξ	—	—	—	—	—	—	569^{+76}_{-39}	601^{+39}_{-12}	561^{+18}_{-8}	1061^{+219}_{-203}
	N_R (10^{-5})	—	—	—	—	—	—	$9.00^{+1.99}_{-2.89}$	$6.42^{+0.14}_{-0.29}$	$9.68^{+0.73}_{-1.21}$	$1.84^{+0.59}_{-0.44}$
	χ^2	1893.64	1896.43	1896.38	1896.96	1897.70	1897.96	1807.67	1798.20	1806.55	1844.03
	ν		1716			1716		1716	1716	1716	1717

3

The truncated and evolving inner accretion disc of GX 339−4

In this Chapter I present results from an analysis of four archival *XMM-Newton* and *Suzaku* observations of the black hole GX 339−4 in the canonical low/hard state. These high-resolution datasets are able to resolve the relativistically broadened Fe emission line, which I use to track any variation of the disc inner radius and establish the first systematic study of the inner accretion disc in the low/hard state. The study reveals that the accretion disc extends closer to the black hole at higher luminosities, and is consistent with being truncated throughout the entire low/hard state. I demonstrate that each emission profile cannot be replicated exclusively by relativistic effects and to this end expose the significant broadening mechanism of ionisation. Taking this into account reveals that the inner accretion disc truncates at hundreds of gravitational radii, which I additionally confirm through further analysis of a hard-intermediate state observation. I also show that the evolution of the spectral inner disc radius corresponds very closely to the trend of the break frequency in Fourier power spectra, further supporting the interpretation of a truncated and evolving disc in the low/hard state.

3.1 Introduction

A truncated inner accretion disc provides a geometric interpretation to explain the spectral changes observed in BHXRBs (Done *et al.* 2007; Chapter 4). Here, the standard optically thick and geometrically thin accretion disc is replaced in the inner regions by what is essentially its converse; a hot, optically thin, geometrically thick flow (Esin *et al.*, 1997). As the accretion rate increases the truncation radius of the disc is expected to decrease, eventually extending fully to the innermost stable circular orbit (ISCO). However, there are two distinct claims in the literature strongly arguing against this even at relatively low luminosities in the hard state. (1) The detection of significantly broadened Fe lines at low accretion rates (Miller *et al.*, 2002, 2006b; Reis *et al.*, 2008, 2010) offer evidence of relativistic effects at or near to the ISCO, although this is still strongly challenged both directly (Done and Gierliński, 2006; Yamada *et al.*, 2009; Done and Diaz Trigo, 2010) and indirectly (Tomsick *et al.*, 2009; Shidatsu *et al.*, 2011). (2) A geometrically thin disc with a fixed inner radius will follow the $L \propto T^4$ relation (Gierliński and Done 2004; Dunn *et al.* 2011; Eq. 1.6), and hence deviations from this can reveal truncation of the inner disc. The debate again remains unresolved with arguments for (Gierliński *et al.*, 2008; Cabanac *et al.*, 2009) and against (Rykoff *et al.*, 2007; Miller *et al.*, 2006a; Tomsick *et al.*, 2008; Reis *et al.*, 2009, 2010) disc truncation. Furthermore, there is evidence that the disc may also be truncated in the hard intermediate state (Kubota and Done, 2004; Done and Kubota, 2006; Tamura *et al.*, 2012), or at the ISCO (Hiemstra *et al.*, 2011).

GX 339−4 is a key source in the inner disc truncation debate. Investigations by Miller *et al.* (2006b) and Reis *et al.* (2008) of strongly broadened Fe lines have suggested that the disc is at the ISCO at $\sim 0.05\,\mathrm{L_{Edd}}$ in the hard state. However, Done and Diaz Trigo (2010) demonstrated that these data can be largely affected by photon pile-up, and presented evidence that the emission line could be significantly narrower. Studies by Tomsick *et al.* (2009), Shidatsu *et al.* (2011) and Petrucci *et al.* (2014) have examined the Fe line region further at lower luminosities providing evidence for a truncated disc, and hints at a correlation between the inner radius estimates and luminosity. Currently, therefore, our understanding of the state of the inner accretion disc in the hard state of GX 339−4 is uncertain. It is essential that we are confident of how the inner disc evolves in the hard state in order for us to measure the BH spin through the X-ray reflection method. This requires that the inner disc is at the ISCO and relies heavily on studies of the hard state, where irradiation of the disc is high and the underlying continuum around 6 keV is relatively

simple (see e.g. Kolehmainen *et al.* 2011 for issues with softer spectral states).

Besides the investigations of Shidatsu *et al.* (2011) and Petrucci *et al.* (2014), who re-analyse the data used in Tomsick *et al.* (2009), and the recent study by Kolehmainen *et al.* (2014), each observation has been examined independently which gives rise to complications when comparing the respective results. Firstly, the parameters derived from reflection modelling can be highly degenerate (see Chapter 2) and can significantly affect conclusions if not accounted for. This can be observed through the range of inclination angles fitted in the mentioned previous studies. The inclination angle of GX 339−4 has not been accurately measured (see §1.6) and freely fitting this parameter can crucially affect the inner radius estimate (Tomsick *et al.*, 2009). Additionally, assorted interpretations of the spectra have led to a variety of models being applied which can again skew results. Table 3.1 is a compilation of all of the inner radius estimates of GX 339−4 in the hard state using *XMM-Newton* and *Suzaku*. Directly comparing each result is difficult due to the contrasting approaches. Note as well, that whilst the range of inclination values can significantly skew the inner radius measured, a number of the values in Table 3.1 are also inconsistent with the strict lower limit on the binary inclination of GX 339−4 ($i > 41.4^{\circ}$; see §1.6).

In this Chapter I present the first systematic study of the evolution of the Fe line region in the hard state of a transient BHXRB. I analyse the four selected observations simultaneously, which enables potentially degenerate parameters to be tied, and for the first time establish a consistent analysis absent of the issues described before.

3.2 Observations and data reduction

In this Chapter I utilise the Fe line region as a probe of disc evolution with luminosity. To undertake such a task, which requires high precision, the work presented here considers just high resolution observations with a large effective area in the Fe K band: *XMM-Newton* and *Suzaku*. I focused on the hard and hard-intermediate phases of the outburst, since the state of the inner disc is unclear during this phase, and has subsequently led to much debate in recent years. This is also ideal since a study by Kolehmainen *et al.* (2011) demonstrated that in the case of the disc and power-law components having equal fluxes around the Fe K range, i.e. the soft and soft-intermediate states, the ability to determine the width of the Fe profile is severely hampered. Whilst the data I ignored restricts the ability of the sample to

% L_{Edd}	Telescope (CCD)	r_{in} (r_g)	$\theta(^\circ)$	q	Model	Ref.
0.14	Suzaku (XIS)	>65	18 (fixed)	2–3	(A)	(1)
0.14[a]	Suzaku (XIS)	>100	50 (fixed)	2.3 (fixed)	(B)	(2)
0.14[a]	Suzaku (XIS)	>180	20 (fixed)	3 (fixed)	(C)	(3)
$\sim$ 0.3	Suzaku (XIS)	>30	20 (fixed)	3 (fixed)	(C)	(3)
$\sim$ 0.4	Suzaku (XIS)	>10	20 (fixed)	3 (fixed)	(C)	(3)
$\sim$ 0.5	Suzaku (XIS)	>70	20 (fixed)	3 (fixed)	(C)	(3)
$\sim$ 1.1	Suzaku (XIS)	40^{+240}_{-25}	20 (fixed)	3 (fixed)	(C)	(3)
2.0	Suzaku (XIS)	13±6	46±8	2.3±0.1	(D)	(2)
2.0[b]	XMM (EPIC-pn)	>100	60 (fixed)	3 (fixed)	(E)	(4)
3.5	XMM (MOS)	5±0.5	20^{+5}_{-10}	3 (fixed)	(F)	(5)
3.5[c]	XMM (MOS)	2.1±0.1	$20^{(20)}_{-1.7}$	3.1±0.1	(G)	(6)
3.5[c]	XMM (EPIC-pn)	170±70	60 (fixed)	3 (fixed)	(C)	(7)
3.5[c]	XMM (EPIC-pn)	140^{+60}_{-50}	60 (fixed)	3 (fixed)	(E)	(4)
15	XMM (EPIC-pn)	47^{+10}_{-7}	60 (fixed)	3 (fixed)	(E)	(4)

Table 3.1: A compilation of previous reflection analyses of GX 339−4 with *XMM-Newton* and *Suzaku*. The contrasting models and inclination makes comparing the different works difficult.

References: (1) Tomsick *et al.* (2009); (2) Shidatsu *et al.* (2011); (3) Petrucci *et al.* (2014); (4) Kolehmainen *et al.* (2014); (5) Miller *et al.* (2006a); (6) Reis *et al.* (2008); (7) Done and Diaz Trigo (2010).

[a] A re-analysis of the observation used in (1).
[b] The Suzaku observation forms part of three over $\sim$ 12d, during which the XMM observation took place.
[c] A re-analysis of the observation used in (5).

(A) POWERLAW+LAOR
(B) POWERLAW+DISKLINE+DISKLINE – the extra DISKLINE is for Fe Kβ emission.
(C) DISKBB+POWERLAW+KDBLUR*REFLIONX
(D) DISKBB+COMPPS+COMPPS+DISKLINE+DISKLINE – the extra DISKLINE is for Fe Kβ emission.
(E) DISKBB+COMPTT+NTHCOMP+KDBLUR*RFXCONV*NTHCOMP
(F) DISKBB+PO+KDBLUR*CDID – CDID refers to the constant density ionised disc reflection model of Ballantyne *et al.* (2001).
(G) POWERLAW+KDBLUR*REFLIONX

	ObsID	State	Net Count Rate (cts/s)	Exposure
1	403067010	Hard (Decay)	2 ± 0.01	105 ks
2	0605610201	Hard (Rise)	132 ± 0.1	32 ks
2b	405063010	HIMS (Decay)	20 ± 0.02 (29)	22 ks
3	0204730201 0204730301	Hard (Rise)	259 ± 0.1	155 ks
4	0654130401	Hard (Rise)	352 ± 0.2 (988)	25 ks

Table 3.2: Selected observations of GX 339−4 in hard and hard-intermediate states. Observations 2, 3, 4 were taken with *XMM-Newton*, whilst 1 and 2b are *Suzaku* datasets. Exposures correspond to that remaining after the reduction process, and hence used in the analysis. Count rates in brackets refer to before any pile-up removal was applied.

probe the inner disc evolution, the inner disc is already widely accepted to have extended to the ISCO in the soft states (see §1.3.1).

The remainder of this section introduces the data reduction procedure, and the five observations found in the archives which met the above criteria are described in Table 3.2.

3.2.1 XMM-Newton

In this study I do not consider data from the EPIC-MOS camera (Turner *et al.*, 2001), and instead utilise only the EPIC-pn (Strüder *et al.*, 2001), for which the three observations were all taken in 'timing' mode. In §3.2.1.1 I outline the reasons for this and how the effects of pile-up were mitigated. All spectra were extracted from a region in RAWX [31:45], following the procedure described in §2.2.2.1. In §3.3.3.1–3.3.3.4 I fit the EPIC-pn spectra in the 4–10 keV band. This enables simultaneous fitting of the spectra with tied parameters and a well calibrated bandpass in a reasonable timescale ($\sim$ weeks to fit and calculate errors). I then check the consistency of these results in §3.3.4 by fitting each observation individually in the full bandpass of 1.3–1.75 and 2.35–10 keV following Chapter 2, as is the standard method for X-ray studies of BHXRBs. I note that applying EPFAST did not produce any noticeable changes in the spectra, which is probably due to the low count rate of the observations. This has also been found at similar count rates in timing mode (see *e.g.* Chiang *et al.* 2012).

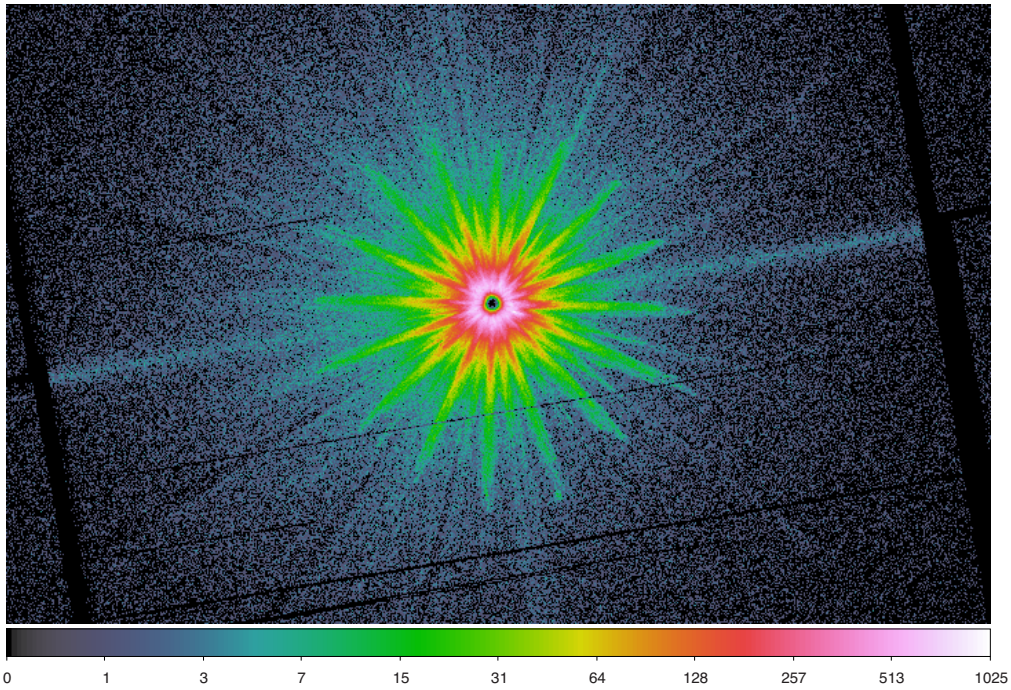

Figure 3.1: An example of pile-up in the *XMM-Newton* EPIC-MOS camera 1 data (Observations 3 in Table 3.2). A clear cavity is observed at the centre of the image, which is the hallmark of extreme pile-up.

3.2.1.1 Evaluating pile-up in the EPIC-pn data

Pile-up occurs when several photons hit two neighbouring pixels (pattern pile-up), or the same pixel (photon pile-up), during one read-out cycle (see §2.2.1). The EPIC-pn timing mode collapses the data into a one-dimensional row, hence the extraction region becomes a box. In the case of pile-up treatment, brighter columns around and including that centred on the source are removed, leaving in essence two source boxes separated by the excluded region. How many central columns are removed depends on how severe the pile-up treatment is required to be.

In this study I only utilise the EPIC-pn camera, and in the main this was to ensure pile-up is mitigated. For Observation 4 the EPIC-MOS data cannot be studied since only the EPIC-pn camera was operated. In Observation 3 the MOS was active and suffers significantly from pile-up (Fig. 3.1). This dataset was taken in the full-frame imaging mode, for which WebPIMMS (using values from Table 3.4) predicts a count rate of over 100 times the nominal pile-up limit of 0.7 cts/s recommended in the XMM Users Handbook. Since such a large annulus region was required to solve for this, the resultant spectra had less than 2 % of the counts registered in the EPIC-pn dataset between 4–10 keV, which I later determine to be pile-up free. The MOS dataset for Observation 2 was taken in timing mode, which should be free

of pile-up. However, given that the EPIC-pn was certainly free of pile-up for this observation, and is a much superior instrument at 6 keV, I decided the EPIC-pn was the best option for this study. A further motivation for this is that using only the EPIC-pn reduces the calibration dependence of this analysis.

The default check for pile-up is to examine the registered count rate and compare it to the nominal limit for pile-up recommended by the XMM team. For the EPIC-pn timing mode this is 800 cts/s, of which Observations 2 and 3 were well below (see Table 3.2), however, Observation 4 exceeded even this threshold. A more detailed test comes from the SAS task EPATPLOT, which displays how the distribution of single and double-pixel (and higher) events compare to their expected values. If the two diverge this acts as strong evidence for pile-up and I hence applied this to all three *XMM-Newton* observations. Again Observations 2 and 3 show no evidence for pile-up, although Observation 4 does. I found that the removal of the inner 3 RAWX columns in Observation 4 resolved the event distribution in EPATPLOT, and also reduced the net count rate to a very acceptable 352 cts/s. However, it should be noted that BHXRBs are very variable X-ray sources, and flares could lead to unique pile-up events, despite the reduced mean count rate.

As I described before in Chapter 2, the effect of pile-up in the energy-spectrum is highly debated. However, with more certainty I can say that pile-up will lead to an overall spectral hardening, as low energy photons are in essence shifted to higher energies. One can therefore use this to verify that a chosen level of pile-up correction is sufficient. As a final check, I compared the spectra extracted using regions with increasing central sections removed, as listed in Table 3.3. A simple absorbed power-law was fit between 1.3–10 keV to Observations 2 and 3 with full extraction regions, and Observation 4 with the three central columns removed. These were the optimal extraction regions determined before through the count rate and EPATPLOT. The 1.75–2.35 keV region was removed, which contains instrumental edges, and a lower bound of 1.3 keV was chosen due to calibration uncertainties at energies below this, referred to as the 'soft excess' (see the XMM-Newton Calibration Technical Note (0083)[1]; Chapter 2). The 5–8 keV band was also removed to avoid fitting the Fe line, as is standard when fitting the continuum. I then added spectra with alternative extraction regions (Table 3.3) with the column density and photon index fixed as determined with the optimal datasets. By normalising each spectrum to be equal between 1.3–1.75 keV this then allowed any spectral hardening to be exposed.

[1] http://xmm.vilspa.esa.es/external/xmm_sw_cal/calib/documentation.shtml

	Net Count Rate (cts/s)			
	Full Column	Inner 3	Inner 5	Inner 7
2	132 ± 0.1	47 ± 0.1	26 ± 0.1	
3	259 ± 0.1	93 ± 0.1	53 ± 0.1	
4	988 ± 0.1	352 ± 0.1	194 ± 0.1	114 ± 0.1

Table 3.3: A comparison of net count rates for the EPIC-pn datasets after correcting for pile-up. A full column corresponds to the region 31–45 in RAWX. Removal of the inner 3, 5 and 7 columns refers to the regions of 37–39, 36–40 and 35–41 being excluded. The latter region was only included for Observation 4 as a means to compare two larger regions to the optimum extraction region used in this study.

The data/model ratios for these three observations are plotted in Fig. 3.2. Piled-up data will be harder, hence having a roughly constant increasing excess at higher energies as compared to spectra with less or no pile-up present. The fit itself was not expected to be precise as X-ray reflection and the thermal disc component (if present in the bandpass) were not being modelled. However, the deviation from a single power-law allows the effects of pile-up to be easily detected.

Observation 2 showed little deviation between the three spectra. Above 8 keV there was some softening; however, this is not expected to be due to pile-up, which should show a gradual hardening of affected data throughout the bandpass. When each spectrum was fitted individually the photon index variation was very small (<0.05). Instead, this is likely to be due to calibration uncertainties. The line profile itself appeared unaffected, and hence I concluded that the full extraction region can be used for this observation.

Observation 3 is very similar to Observation 2, again showing some softening above 8 keV when columns were removed. No significant hardening was seen in the spectra using a full extraction region and the line profile remains consistent, hence confirming that the full extraction region is free of pile-up, as was indicated by the count rate and EPATPLOT. For Observation 4 the spectra with 3 columns removed was fitted since a full region was found be modified by pile-up by EPATPLOT, whilst also having a count rate above the recommended threshold. In Fig. 3.2 it can be seen that the spectra with a full extraction region is significantly harder and shows a disparate line profile. The fitted spectra with three columns removed exhibits a drop above 8 keV; however, this is due to a strong Fe edge emphasised by the large reflection fraction (Table 3.5; see also §3.3.2). Spectra with 5 and 7 columns removed look very similar to the fitted data, albeit showing some further softening above 8 keV consistent with the other observations. The Fe profile ap-

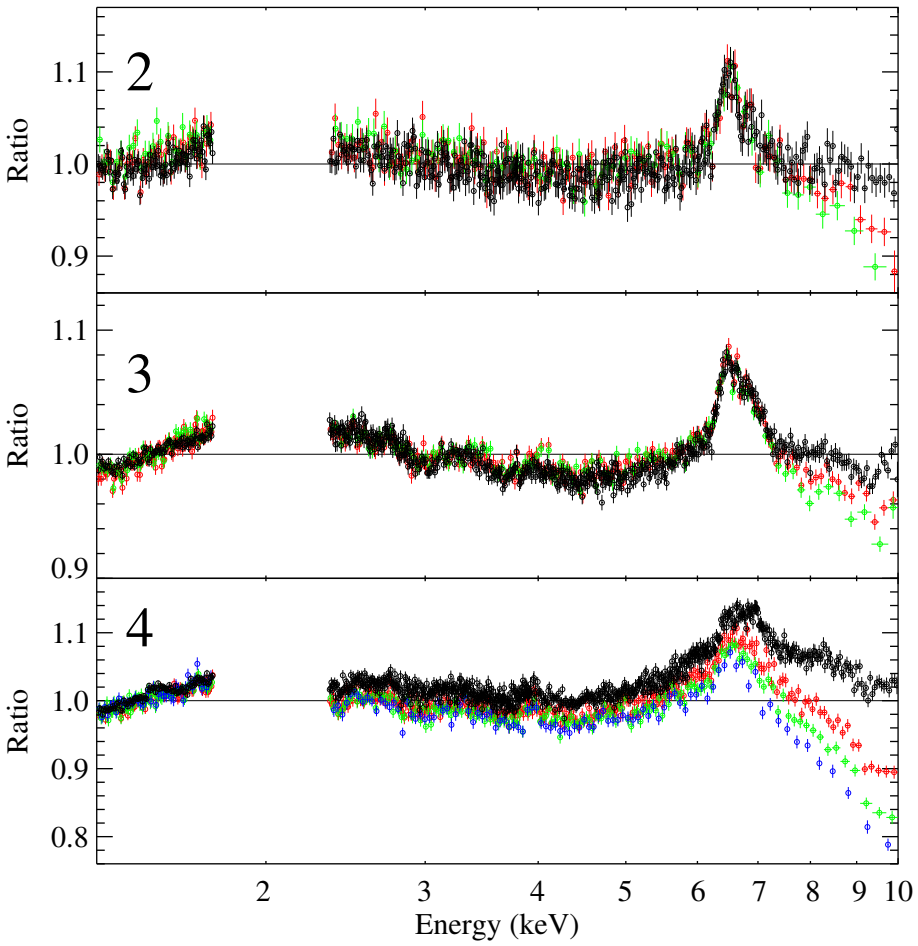

Figure 3.2: A comparison of pile-up effects in the EPIC-pn datasets using various extraction regions. The top, middle and lower panels refer to Observations 2, 3 and 4 respectively (Table 3.2). All spectra were extracted from a region of 31–45 in RAWX. Red, green and blue indicate that the inner 3, 5 and 7 columns have been removed. The black spectra utilises the full strip. In this study I used the full strip for Observations 2 and 3, and Observation 4 has the inner three columns removed, hence I analysed these datasets and compared how the other spectra match-up after normalising the 1.3–1.75 regions to be equal. If pile-up is present the spectra are expected to be systematically harder, i.e. increasing data/model ratio towards higher energies, and display a modified Fe profile.

pears unchanged, and in all this suggests that the removal of three columns leaves the data free from pile-up as determined before.

The small softening effects seen above 8 keV are probably due to calibration uncertainties in the determination of the effective area for a PSF with central holes. This was confirmed by the XMM-Newton EPIC calibration team, who noted that the variation is less than 10 %, and the most recent EPIC calibration status quotes the uncertainty in the effective area to be ± 5 %[2]. Regardless of observation (*i.e.* source count rate), or the number of columns removed, the softening occurs, and would suggest that the effect is not due to pile-up. For example, in Table 3.3 one can see that Observation 2 with a full strip is at 6 times below the recommended limit of 800 cts/s. Removing 3 and 5 columns reduces the count rate further to 17 and 30 times below the limit, respectively, yet the softening still occurs. It would be very unlikely that the softening effect is pile-up at such low count rates; however, I cannot definitively rule out this is the case, and, as discussed in §2.2.1, it is uncertain how this would effect the Fe line profile.

To test how this softening might affect the results in this Chapter, I compared results from fitting Observation 4 when 3 or 5 columns were removed. The model PHABS(DISKBB+POWERLAW+RELCONV∗XILLVER) was applied between 1.3–10 keV. The inclination was fixed at 42° to be in line with the value fitted later in the analysis using all four spectra (§3.3.3.2), but otherwise all remaining parameters were fit freely. The result is extremely consistent, with the inner radius being exactly the same ($67\,r_{\rm isco}$). The only parameter not consistent at 90 % confidence was the photon index, although only the slightest difference was recorded: 1.63 ± 0.01 (5 columns) vs 1.60 ± 0.01 (3 columns). This may be due to the energy dependence of the point spread function. Such a small variation does not ultimately make much difference, and pile-up is expected to create a much more severe discrepancy (see Ng *et al.* 2010 for examples of strong pile-up in spectra). The modelled reflection was unaffected which is of most importance to this study. Therefore, any uncertainty due to removing columns in Observation 4 has no bearing on the conclusions in this Chapter.

3.2.2 Suzaku

Suzaku carries four X-ray Imaging Spectrometer detectors (XIS; Koyama *et al.*, 2007), one of which is 'back-illuminated' (BI), in addition to the three 'front-illuminated' (FI) ones. Each covers the 0.2–12 keV band. On 2006 November 9,

[2]http://xmm.vilspa.esa.es/docs/documents/CAL-TN-0018.pdf

XIS2, one of the FI detectors, failed and hence was not considered in this work. Furthermore the Hard X-ray Telescope (HXD; Takahashi *et al.*, 2007; Kokubun *et al.*, 2007) extends coverage to the 10–70 keV (PIN) and 50–600 keV (GSO) regions respectively.

The unfiltered event files were processed following the *Suzaku Data Reduction Guide* using the HEADAS v6.11.1 software package. Clean event files were then produced using the FTOOL AEPIPELINE, applying the calibration products (HXD20110913, XIS20120209 and XRT20110630). Suzaku undergoes wobbling due to thermal flexing leading to a blurring of the image. Therefore the script AEATTCOR.SL[3] was used to create a new attitude file, which was then applied to each clean event file using the FTOOL XISCOORD. For the XIS, XSELECT was then used to extract the spectral and background products. A source region with a radius of 200 pixels centred on the image peak was used for all observations. Observation 2b, however, employed the $1/4$ window mode, therefore the extraction region was larger than the window itself, and hence the effective region extracted was an intersection of the 200 pixel radius circle with a rectangle of 1024×256 pixels. Background events were extracted using a circle of 100 pixels located away from the source.

To check for the effects of photon pile-up the tool PILE_ESTIMATE.SL[4] was used which creates a two-dimensional map of the pile-up fraction. Observation 2b required treatment, hence the source circle was exchanged for an annulus with an inner region with a radius of 30 pixels, which limited the effect of pile-up to $<5\%$. Observation 1 was found to be free from any pile-up. The tools XISRMFGEN and XISSIMARFGEN were used to create the response and ancillary files respectively. For the analysis the two FI cameras (XIS0 and XIS3) were combined using the FTOOL ADDASCASPEC, whilst the BI instrument (XIS1) was not used since it has a smaller effective area at 6 keV, and is generally less well calibrated. Each of the spectra were required to have a minimum of 20 counts per bin using the FTOOL GRPPHA. As with the *XMM-Newton* observations, I fit the XIS spectra between 4–10 keV in §3.3.3.1–3.3.3.4 to allow simultaneous fitting with tied parameters and a well calibrated bandpass in a reasonable timescale. For §3.3.4 the bandpass was extended to 0.7–10 keV and the 1.7–2.4 keV region was ignored, which like the EPIC-pn showed strong residuals.

In §3.3.2 I also make use of the PIN instrument to extend the bandpass examining the continuum emission. Appropriate response (depending on whether the pointing

[3]http://space.mit.edu/CXC/software/suzaku/aeatt.html

[4]http://space.mit.edu/CXC/software/suzaku/pest.html

was XIS or HXD) and tuned non-X-ray background (NXB) files were downloaded. I then applied the FTOOL HXDPINXBPI which produces a dead time corrected PIN source spectrum plus the combined PIN background (non X-ray and cosmic). Again a minimum of 20 counts per bin was required and the PIN was fit in the 15–50 keV bandpass, as recommended by the HXD instrument team. The GSO instrument was not used in this analysis.

3.2.3 RXTE

The reduction of the *RXTE* observations was performed by Dr. Mickäel Coriat, following the procedure described in §2.2.2.2. The PCA data were fit in the energy range 7–30 keV for Observations 2 and 3. For Observation 4 the HEXTE was then not operational, hence I only included the PCA data, but extended its range up to 50 keV given that it is a significantly longer and brighter exposure. For the variability analysis in §3.3.3.5 only the PCA data were used, and for this the data were reduced by Dr. Teodoro Munõz-Darias. The data modes GoodXenon1_2s and E_125us_64M_0_1s were utilised depending on the case. Power density spectra (PDS) were computed following the procedure reported in Belloni *et al.* (2006), using stretches 1024s long and PCA channels 0–95 (2–40 keV).

3.3 Analysis and results

The Fe line region in some of these observations, or contemporaneous ones, has previously been analysed (see *e.g.* Tomsick *et al.* 2009; Done and Diaz Trigo 2010; Shidatsu *et al.* 2011; Cassatella *et al.* 2012). At the time of analysis this was, however, the first work to make use of Observations 2b and 4. These have since been reported in Petrucci *et al.* (2014) and Kolehmainen *et al.* (2014). Quite simply, one can compare the results from each previous analysis to probe any correlation between the Fe line region and luminosity. However, such a process introduces many issues which could bias results and hence conclusions. For example, the use of different models; the effects of degeneracies in the models; and the range of values of constant parameters like inclination, are just a few of these potential complications.

To gain a real insight into evolution throughout outburst one must keep analysis between each observation as consistent as possible. This is the key approach of this work. The observations were fit simultaneously, hence applying the same model to each dataset. Furthermore, degenerate parameters, such as inclination (see Fig. 3 of

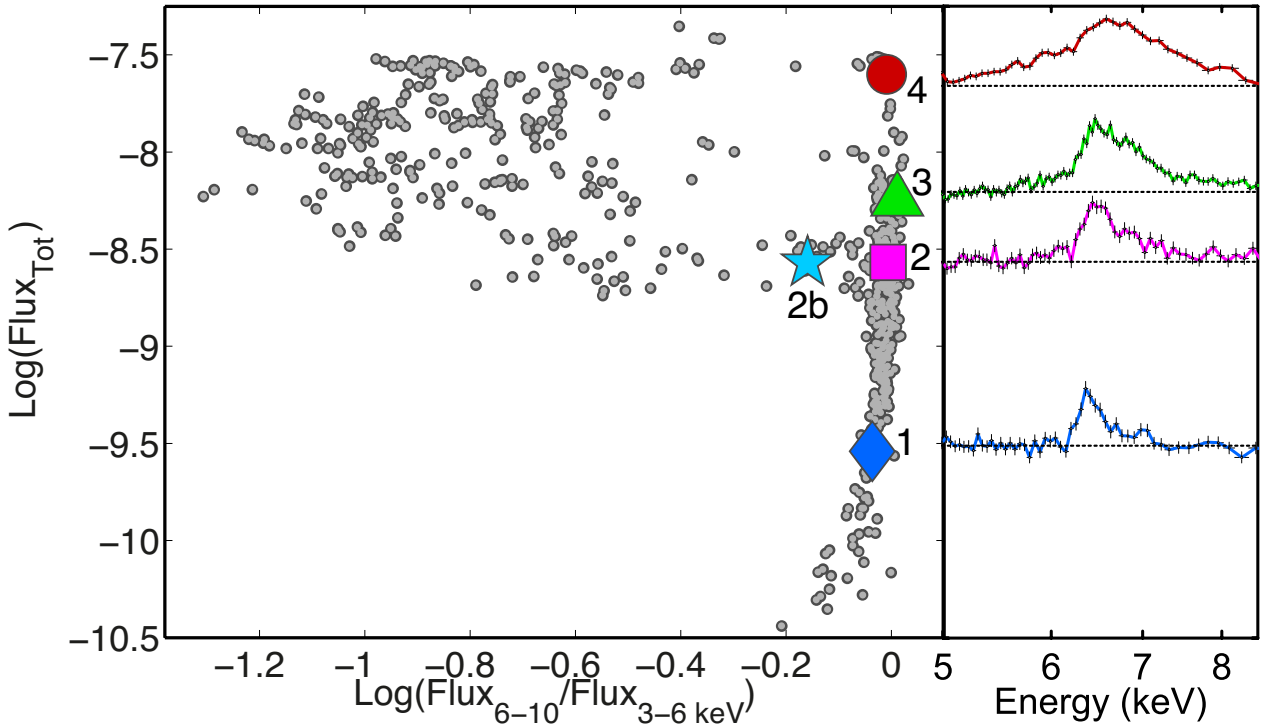

Figure 3.3: Left: A Hardness intensity diagram (HID) of all GX 339−4 outbursts monitored by RXTE (1995-2011; grey points). The large coloured symbols indicate the positions of the chosen observations described in Table 3.2: blue/diamond (1), magenta/square (2), green/triangle (3), red/circle (4), and cyan/star (2b). The flux has units of erg cm^{-2} s^{-1}. Right: The data/model ratio of continuum fits to the four hard state spectra when the 'ignored' energy range (5–8 keV) in Table 3.2 are added ('noticed' in XSPEC) back in, indicating the shape and strength of the Fe line region between observations. Note the y-scale is the same as for the left figure and data have been re-binned for plotting purposes. The cyan HIMS observation (2b) is not shown. This is since it would overlap the Observation 3 ratio and was in a different spectral state to the others. The line profile is, however, displayed in Fig. 3.8.

Tomsick *et al.* 2009), were then able to be tied, allowing not only a better constraint in their measurement, but also mitigation of the effects of degeneracy. To this end it was not the aim to present what the exact inner radius value is for each observation. Instead, the relative change of parameters was investigated between each observation. This is a crucial step towards an accurate investigation of the Fe line region, and thus the simultaneous analysis of each spectrum with tied parameters forms the basis of this investigation (§3.3.3.1–3.3.3.4).

3.3.1 Selected models

The X-ray spectrum of BHXRBs can generally be described by three components. Two of these are a thermal blackbody component originating from the accretion disc and a power-law likely due to Compton up-scattered seed photons. The third, known as the 'reflection spectrum' (Fabian and Ross, 2010), occurs due to the irradiation of the disc by the up-scattered photons, resulting in, but not exclusively, X-ray fluorescence. The most prominent signature of this is Fe Kα emission due to its high abundance and fluorescent yield.

The hard state itself is dominated by the power-law component, whilst the disc is weak ($kT < 0.5$ keV) above 1 keV (Miller *et al.*, 2006a; Reis *et al.*, 2010). Because of this the region below 4 keV was ignored, above which the disc contribution is negligible, thereby simplifying the spectrum to just 2 components. Whilst this removes a large amount of the spectra, I show later that the results are fully consistent with those using a full bandpass §3.3.4. The interstellar absorption was modelled using the model PHABS fixed at 0.5×10^{22} cm^{-2}. There were two reason for this. Firstly, by only fitting above 4 keV the ability to constrain the column freely is significantly reduced. Secondly, the neutral hydrogen value towards GX 339−4 is well resolved to be within the range $(0.4\text{–}0.6)\times10^{22}$ cm^{-2} (Kong *et al.*, 2000). Hence, the fixed value was chosen to be at the centre of these limits, noting that the effect of such a range above 4 keV is negligible. Whilst variability in the absorption has been suggested (Cabanac *et al.*, 2009), this was, however, found not to be the case when fitting individual photoelectric absorption edges in high-resolution X-ray spectra (Miller *et al.*, 2009).

To model the reflection I applied the two methods used in Chapter 2: (1) the Fe Kα line technique (§2.3.1.2), and (2) self-consistent reflection modelling (§2.3.1.3). To model the Fe Kα line (method 1), and apply relativistic blurring in method 2, the RELLINE and RELCONV models of Dauser *et al.* (2010) were applied respectively. For the reflection spectrum the code XILLVER (García and Kallman, 2010; García

Observation	Γ	N_{PL}	Flux	χ^2/ν
1	1.565±0.012	0.011±0.001	0.82	777/791
2	1.437±0.008	0.098±0.001	8.30	714/668
2b	1.807±0.009	0.144±0.003	8.46	882/789
3	1.476±0.003	0.186±0.001	15.05	812/666
4	1.647±0.004	0.919±0.006	59.61	765/658

Table 3.4: Results of continuum fits to the five selected observations of GX 339−4 using the model PHABS*POWERLAW, ordered by increasing flux. An additional SMEDGE was added to Observation 4 to account for the significant residual beyond 8 keV. The unabsorbed flux is in units of $\times 10^{-10}$ erg cm^{-2} s^{-1} and calculated in the 0.5–10 keV energy range using the model CFLUX.

et al., 2011) was used, which goes beyond the resolution of the most widely used publicly available model REFLIONX (Ross and Fabian, 2005). However, some analysis with REFLIONX was included to allow comparison with previous investigations, and ensure the results with XILLVER were consistent. For this work XSPEC version 12.8.0 was used, and all quoted errors are at the 90 % confidence level unless otherwise stated.

3.3.2 The Continuum

To begin, I analysed each observation individually, removing the Fe line region from the fit (5–8 keV) in order to accurately estimate the continuum emission upon which the reflection is superimposed[5]. At this point I wanted to test two properties of the continuum: (1) Whether an absorbed power-law is an acceptable description of the continuum, and (2) that the description of the continuum is consistent with the later analysis when the reflection was modelled. It is imperative that the continuum is correctly modelled since the shape of the reflection spectrum is strongly dependent upon it, hence I used this initial analysis as a sanity-check for the later sections. To this end, the motivation for fitting each observation individually in this section was that it allows me to extend the broadband coverage. The main focus, the EPIC-pn and XIS cameras, will only be covering the 4–10 keV region to constrain

[5]The choice of 5–8 keV, which is different to the 4–7 keV region used in Chapter 2, was chosen to best suit the broad profile shown later in Observation 4. If 4–7 keV was used, then a strong residual remained above 7 keV. In addition, since much of this study uses a short 4–10 keV bandpass, the 4–5 keV portion is necessary to well constrain the soft part of the continuum. I note that this could impact the results, since the Fe line profile may well extend to 4 keV; however, later I investigate a larger bandpass down to $\sim$ 1 keV (§3.3.4), and show that the Fe line profile is too narrow to affect the continuum below 5 keV, meaning that the choice of 5–8 keV does not affect these initial continuum fits, or the profiles displayed in Fig. 3.3.

the continuum for the majority of this investigation. I added simultaneous PCA-HEXTE observations to the EPIC-pn, and made use of the PIN on-board Suzaku to extend the coverage up to 100 keV and 50 keV respectively. A constant normalisation factor must be allowed between each detector; however, the only one well calibrated enough to be fixed is between the XIS and PIN (both of the Observations were taken in the XIS nominal position, hence I fixed the constant to be 1.16). The cross-normalisation between the PCA, HEXTE and EPIC-pn are all uncertain, so the PCA constant was fixed to be 1 and the EPIC-pn and HEXTE datasets were allowed a free constant. These were $\sim$0.85 and $\sim$0.8 for the EPIC-pn and HEXTE respectively. I note again that I fit each epoch individually in this section, since, given that there were 5 detectors from three separate missions, simultaneous fitting would potentially render the results degenerate if any parameters were tied between the datasets.

I fitted a single absorbed power-law to the whole broadband spectrum, tying the photon index and normalisation parameters between detectors, whilst allowing a constant to float between them as described before. The continuum model was found to be a good fit to all of the observations (Table 3.4), and no cut-off was required at high energies, although this may exist beyond the upper energy limit. A significant smeared edge was required for Observation 4 suggesting a large amount of reflection was present. The majority of residuals lie beyond 10 keV, the likely source of which is a Compton 'hump' from the reflection of hard X-rays by the cool accretion disc. Interestingly, this was not present in Observations 1 and 2, suggesting that the level of reflection increased in the higher luminosity observations. Later, in Chapter 4, I show that the level of reflection does in fact increase at higher luminosity in the hard state. Given the good description of the continuum by this model I used it as the base continuum in the later sections unless stated otherwise.

For now I only consider the hard state spectra. I display the continuum data to model ratio with the Fe line region added back into the plot (i.e. 'noticed' in XSPEC) for the hard state observations in Fig. 3.3. Immediately one can see a distinct evolution of the Fe line region. At higher luminosities the profile extends further in both the red and blue wings, and the peak appears to shift to higher energies. A higher spin and inclination will broaden the red wing and blueshift the peak respectively. However, these two parameters will be constant between observations so I can rule out their influence.

Two remaining variables can increase the profile's extension to lower energies. Were the inner disc radius to change, specifically to extend closer to the BH, the relativistic effects would increase and an increase in the broadening of the red wing

would be observed. Additionally, the emissivity can generate this effect. More centrally concentrated emission would mean a larger contribution to the profile by the regions experiencing stronger relativistic effects, so therefore increased red wing broadening. However, the emissivity is not expected to vary so intensively between hard state observations, given that previous investigations have yielded $q \sim 3$ (the emissivity is defined to scale as r^{-q}; Table 3.1). Thus, inner radius variation should dominate the red wing variation observed. The shift in the peak of the profile is almost certainly due to an increase in the disc ionisation. A more ionised disc means emission from higher rest energies, hence a shift in the peak. Also, larger ionisation results in increased Compton scattering and emission from multiple ionisation stages, which can both contribute an overall broadening of the profile (García and Kallman 2009; see also García and Kallman 2010 and García *et al.* 2011), thus extending the blue wing.

Therefore, inspection of Fig. 3.3, just by eye, implies that at higher luminosities in the hard state the accretion disc is extending closer to the BH, and becoming more ionised.

3.3.3 The Fe line region

3.3.3.1 Fe line modelling

To gain a more accurate description of how the disc is evolving, the Fe line region must be modelled, and to begin I fitted the Fe Kα by applying the model RELLINE (Dauser *et al.*, 2010). Again, this analysis only focuses upon the hard state for now. The observations were fit simultaneously, tying the inclination between each observation, and the emissivity and spin parameters were fixed to be r^{-3} and 0.9. The impact of these choices are discussed in §3.3.4.2 and §3.4.1 respectively. The outer radius of the disc was also fixed at $1000\,r_{\rm g}$, since it is very difficult to constrain. In order to fit the four epochs simultaneously, I now only used the EPIC-pn and combined XIS datasets, and fit these between 4–10 keV. The absorbed power-law continuum described in §3.3.2 was used, applying those results as the initial parameter values. The results are presented in Table 3.5 which report a reasonable best fit of χ^2/ν = 6608/5100, with the majority of residuals remaining in the Fe K band, as displayed in Fig. 3.4. The feature around 7 keV in Observation 1 is likely to be Fe Kβ emission, consistent with the near-neutral Fe Kα fit of 6.46±0.02 keV. A similar residual was also seen in Observation 2, but below 7 keV, which possibly arises from emission from a higher ionisation stage (e.g. H-like at 6.97 keV) or Compton

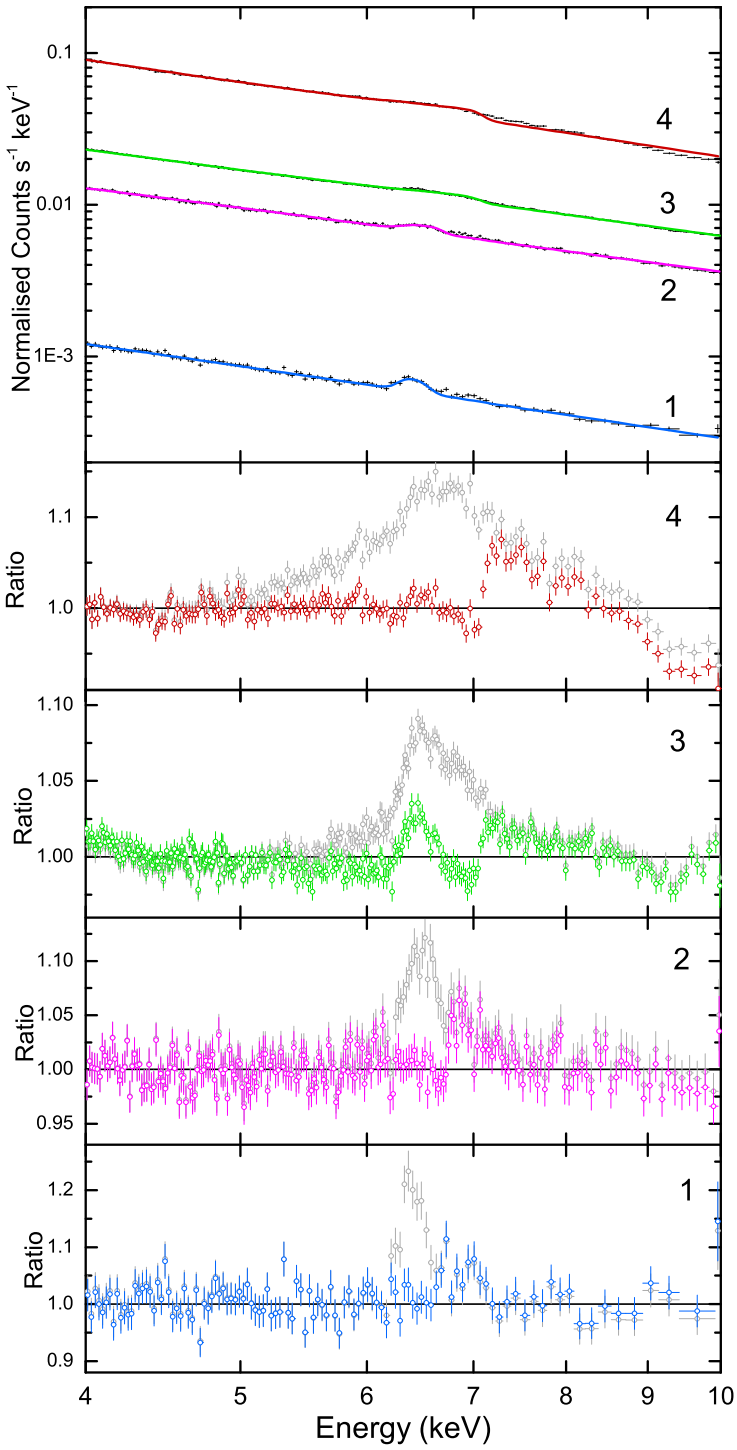

Figure 3.4: The four hard state datasets simultaneously modelled using RELLINE for the Fe Kα emission line. The top panel shows the resultant best fit with the remaining panels displaying the model residuals for each observation using the same colour scheme as in Fig. 3.3. Additionally the model residuals from Fig. 3.3 are overlaid in grey. These correspond to the absorbed power-law continuum (PHABS*POWERLAW) before the Fe line was fitted, as described in §3.3.2. This therefore indicates how the RELLINE model is fitting the overall shape of the Fe band. All of the spectra have been re-binned for the purposes of plotting.

Model	Parameter	1	2	3	4
POWERLAW	Γ	1.59±0.02	1.42±0.01	1.47±0.01	1.64±0.01
	N_{PL}	0.011±0.001	0.096±0.001	0.18±0.01	0.91±0.01
RELLINE	E (keV)	6.46±0.02	$6.55^{+0.02}_{-0.03}$	$6.94^{+0.02}_{-0.03}$	$6.97_{-0.01}$
	θ (°)		18±0.1		
	r_{in} (r_{isco})	79^{+68}_{-26}	36^{+11}_{-8}	$3.7^{+0.2}_{-0.1}$	3.0±0.2
	N_L (10^{-4})	0.37±0.05	2.61±0.22	$7.85^{+0.30}_{-0.25}$	59.3±3.0
	E.W. (eV)	61^{+10}_{-7}	40^{+4}_{-5}	75^{+3}_{-5}	154^{+13}_{-6}
χ^2/ν			6608/5100		
POWERLAW	Γ	$1.72^{+0.15}_{-0.03}$	1.44±0.01	1.47±0.01	1.60±0.01
	N_{PL}	0.013±0.002	0.087±0.004	0.16±0.01	$0.37^{+0.06}_{-0.04}$
RELCONV	θ (°)		42^{+11}_{-6}		
	r_{in} (r_{isco})	>344	295^{+131}_{-163}	137^{+71}_{-32}	67^{+60}_{-23}
XILLVER	$\log(\xi)$	$1.52^{+0.32}_{-0.40}$	$2.58^{+0.03}_{-0.04}$	$2.61^{+0.02}_{-0.01}$	$2.88^{+0.03}_{-0.02}$
	N_R (10^{-6})	$6.50^{+25.6}_{-3.91}$	$3.31^{+0.27}_{-0.24}$	$4.82^{+0.15}_{-0.14}$	$20.6^{+0.09}_{-0.07}$
	RF	0.13±0.05	0.13±0.03	0.14±0.01	1.29±0.25
χ^2/ν			5467/5100		
POWERLAW	Γ	1.66±0.03	1.45±0.01	1.49±0.01	$1.53^{+0.03}_{-0.07}$
	N_{PL}	0.012±0.001	0.097±0.001	0.18±0.01	$0.44^{+0.12}_{-0.13}$
RELCONV	θ (°)		36^{+3}_{-6}		
	r_{in} (r_{isco})	>321	419^{+7}_{-277}	54^{+9}_{-22}	31^{+18}_{-9}
REFLIONX	$\log(\xi)$	$2.06^{+0.08}_{-0.34}$	$2.38^{+0.02}_{-0.01}$	2.47±0.03	3.36±0.01
	N_R (10^{-6})	2.47±0.31	$8.38^{+1.00}_{-0.51}$	$8.44^{+0.84}_{-0.93}$	$6.57^{+0.38}_{-0.35}$
	RF	0.10±0.03	0.06±0.03	0.06±0.01	0.73±0.21
χ^2/ν			5482/5100		

Table 3.5: Results from fitting the four hard state observations simultaneously with the RELLINE line profile (top section) and a blurred reflection model RELCONV*XILLVER (middle section), RELCONV*REFLIONX (bottom section). The photon index in the reflection models was tied to that of the continuum power-law and the Fe abundance was assumed to be solar. The emissivity index and spin parameters were fixed to be 3 and 0.9 respectively, whilst the outer radius of the disc was fixed to be $1000\,r_g$. The reflection fraction (*RF*) was calculated as the ratio of the flux from the reflected emission and the power-law continuum flux. Both were calculated using CFLUX in the 4–10 keV band. If an upper or lower limit is not shown this indicates that the parameter has reached a hard limit. In some cases the inner radius parameter has reached the largest tabulated value in the model ($1000\,r_g$), therefore only the lower limit is presented in this case.

scattering broadening the profile, which is not accounted for by RELLINE. However, Fe Kβ emission cannot be ruled out as a possibility. The effect of multiple ionisation stages is also seen in Observation 3 where a feature at 6.4 keV remains, most likely due to neutral emission from the less irradiated outer disc, and a broad residual is seen beyond 7 keV, probably again since scattering is not modelled. In Observation 4 the disc is likely to be more ionised from increased irradiation, removing the former issue; however, the latter becomes even more significant as a result, leading to even larger residuals. A large smeared edge is also clearly present.

These results indicate consistently that the inner accretion disc is more recessed at lower luminosities. Evolution from $79\,r_{\rm isco}$ to $3\,r_{\rm isco}$ is observed over less than two magnitudes of $L_{\rm Edd}$. However, it should be stressed that the recorded values may not be a true representation of the inner disc radius, as it is possible that degeneracies in the model could skew its accuracy. Furthermore, it can be seen from Fig. 3.4 that the reflection was not well fitted by a single relativistic line. The key result here is the strong relative trend of a disc extending closer to the BH at higher luminosities. This confirms the initial prediction from the line profiles in Fig. 3.3. Additionally, the rest energy of emission also increases with luminosity, approaching the upper limit of the allowed range (6.97 keV; H-like Fe Kα emission) for Observations 3 and 4. Hence, this predicts that the disc surface layers are more ionised at higher luminosities, confirming the second and third predictions made by eye. The tied inclination parameter was found to be 18°, which is consistent with previous analysis using a single Fe line (Miller *et al.*, 2006b; Reis *et al.*, 2010; Done and Diaz Trigo, 2010). However, an inclination lower than $\sim 40°$ is very unlikely since it will result in a black hole mass of $>20\,M_{\odot}$ (see §1.6), although the inner disc may not be necessarily aligned with the binary inclination (Maccarone, 2002). If this is the true accretion disc inclination then it would signify a significant misalignment with the binary orbit, which would probably produce a substantial warp in the disc. If the inclination were larger the trend should be largely unaffected, which I show later for the self-consistent reflection model over a full range of $\cos i$ (§3.3.4.1).

The equivalent width of the lines in the rise data increases with luminosity, indicating a larger area of reflection (*i.e.* a smaller inner radius). However, Observation 1, which was in decay, does not fit this trend. It is likely though that this is the only profile well described by one ionisation stage, and hence would yield a larger value compared to other observations, which instead leave significant residuals in their fit. Therefore, the reflection fraction (*RF*) calculated in §3.3.3.2 is expected to be a more accurate method to draw any conclusions from the relative flux between components (see also Chapter 4).

3.3.3.2 Self-consistent reflection fitting

As noted in the previous section, and displayed in Fig. 3.4, although the fit was reasonable when line modelling was applied, there were significant residuals remaining in the Fe band. This suggests that the reflection is more complex than just Fe Kα emission from one ionisation stage. Such a shortcoming is likely to arise due to Comptonisation and emission from regions of the disc with different physical conditions. Both would generate further broadening and structure in the resolved emission line, and these mechanisms are *not* taken into account by any Fe line model. Therefore such a model, if these processes were present, would either artificially broaden in order to fit, for example by over-predicting the relativistic effects present, or leave the additional broadening not modelled, and consequently residuals in the spectra.

Therefore, the next step is to compare the results from line modelling to that of relativistically blurred self-consistent reflection from an ionised disc. The model employed, on top of the standard continuum, was RELCONV*XILLVER (Dauser *et al.*, 2010; García and Kallman, 2010; García *et al.*, 2011). Again, a single absorbed power-law was used as the underlying continuum, with the results in §3.3.2 utilised as the initial parameter values, which were otherwise fitted freely. As for the RELLINE analysis, the inclination was tied between each observation, and the emissivity and spin were fixed to be r^{-3} and 0.9 respectively, whilst the outer radius of the disc was fixed at $1000\,r_{\rm g}$. The input photon index in the reflection model was tied to that of the power-law and solar abundances were assumed. The fit was much improved (χ^2/ν = 5467/5100; Table 3.5), and all four observations were found to harbour a significantly more truncated disc relative to the values obtained from modelling the Fe Kα line only. The evolution of the inner radius was found to be less significant statistically than for method 1; however, strong evidence still exists for evolution between Observations 4 with 1 and 2, and Observation 3 with 1.

The much larger values recorded for the inner radii can be driven by two effects. A much larger inclination was found (42° vs. 18°) and the smaller doppler shifts at low inclinations would require a smaller inner radius to recover the same profile width (Done and Diaz Trigo, 2010). However, as discussed in the previous section, the much lower value found by the single Fe line method is highly unlikely given the constraints on the binary parameters of GX 339−4 (see §1.6). Thus, the inner radii values found for the self-consistent reflection method are more likely to be correct. This is tested further in §3.3.4.1 and 3.4.2. Additionally, the ionisation parameter, ξ (see §1.4.1) will lead to a broader profile through increased Comptonisation and

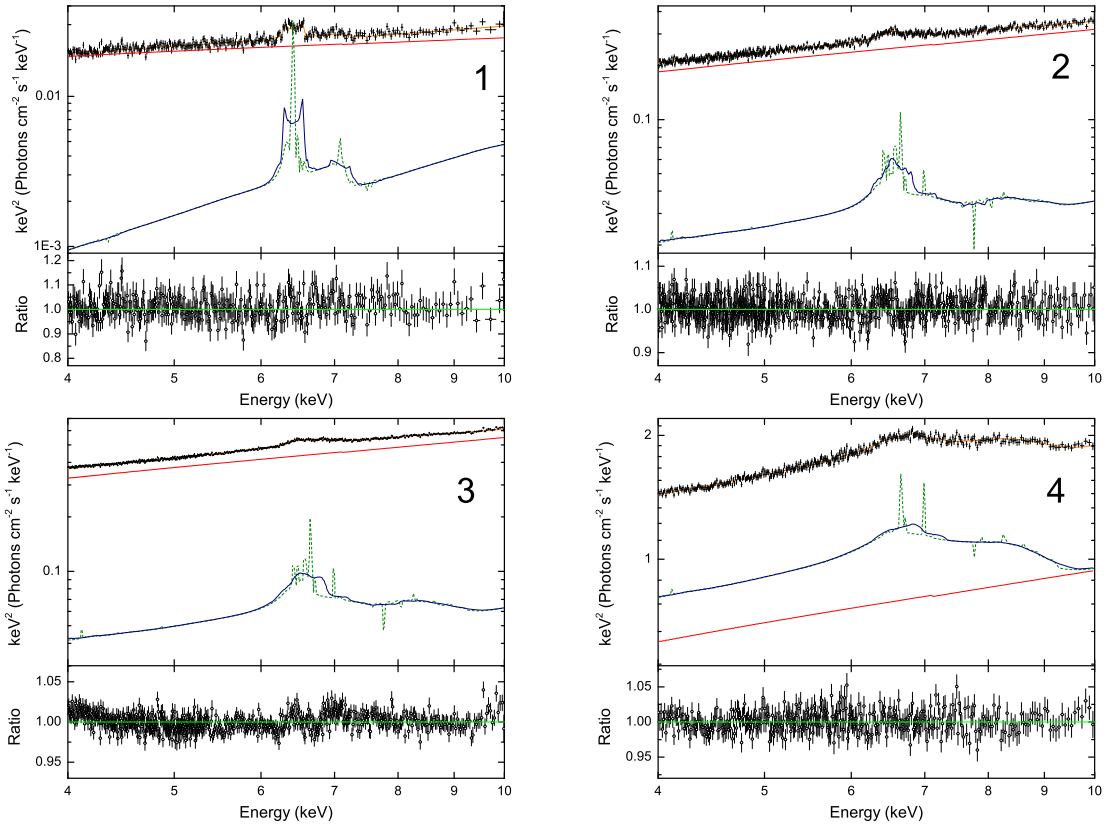

Figure 3.5: The unfolded spectral fit and data/model ratios of the simultaneous fitting of the four hard state observations in Table 3.2, using the blurred reflection model RELCONV*XILLVER. The up-scattered disc emission is indicated by the red lines and the composite model is overlaid in orange. The reflection component is displayed in two ways: the blue solid lines show the blurred reflection as fitted, whilst the green dashed lines display the reflection spectrum when the relativistic blurring (RELCONV) is removed. Please note that the green dashed lines are not part of the fit, they are purely to allow the evolution of the profile due to ionisation and relativistic effects to be viewed separately. All of the spectra have been re-binned for the purposes of plotting. I note here that unfolded spectra can be very misleading, since the data points are determined in a model-dependent way. Throughout this thesis I use unfolded spectra only as a means to effectively display the contribution of the model components.

multiple ionisation stages. I find that the ionisation parameter spans over a magnitude in range, yielding reasonable values in comparison to previous work. Also present is a trend to higher ionisation with luminosity, consistent with what one would expect: as the accretion rate increases the disc will become warmer, and hence more ionised. Additionally, the more luminous hard component, driving the vertical track on the HID, will irradiate the disc more and more, again increasing the ionisation of the surface layers responsible for the reflection spectrum. Figure 3.5 displays how the ionisation stage evolves through the green lines, which are the reflection spectrum when the relativistic blurring has been removed. Mainly neutral emission and the significance of Fe Kβ is seen for Observation 1, whilst Observation 4 requires only H and He-like Fe Kα emission from an almost fully ionised disc, with a hint of Fe Kβ arising from recombination. Intermediate to this in luminosity, Observations 2 and 3 indicate a moderately ionised disc with emission from a range of stages.

The flux of each component was calculated using the convolution model CFLUX, keeping all parameters free and tied as before. The reflection fraction (*RF*), defined at the ratio of the flux from the reflection emission and power-law continuum flux, also shows some increase with luminosity, although strong conclusions are limited by the small bandpass. Nevertheless, if the accretion disc is moving inwards it presents a larger solid angle as seen by the illuminating source, therefore increasing the portion of flux due to reflection. An increasing *RF* hence agrees with the evolution of the inner disc, and displays consistency with other investigations of the hard state (see e.g. Gilfanov *et al.* 1999; Chapter 4). The values of the power-law photon index show good consistency with those found over a larger bandpass (Table 3.4; §3.3.2), although some variation is expected as the reflection spectrum, which may add curvature to the spectrum, is then accounted for with XILLVER and REFLIONX. Nevertheless, this indicates that the reflection spectrum was being fitted in a correct and self-consistent manner.

This result stresses the importance in taking into account non-relativistic broadening mechanisms when fitting a line profile. In fact, for Observations 1 and 2, only a lower limit was found for the inner radius, making them consistent with requiring no relativistic broadening at all at the 90% confidence level. Upon reaching the limits of the model in terms of radii, the line profile shape becomes dominated by ionisation rather than relativity, making the inner radius parameter difficult to constrain. The consistency of the evolution found between observations brings strong evidence that the inner accretion disc can be substantially truncated in the hard state, even at relatively high luminosities (up to $\sim$0.15 L_{Edd}, assuming a BH mass of 8 $M_{\odot}$

at a distance of 8 kpc).

Finally, the analysis was repeated replacing XILLVER with the reflection model REFLIONX (Ross and Fabian, 2005), and similar evolution was found. For this analysis, I applied the same parameter conditions to REFLIONX as I did to XILLVER. The inner radius parameter follows the same trend, although having smaller values for each observation. The inclination was found to be less ($\sim 36^{\circ}$), and this decrease is likely to drive the trend to lower values of $r_{\rm in}$ in the same way proposed for the line only method (see also §3.3.4.1). Observations 1 and 2 are still consistent with requiring no relativistic broadening at the 90 % confidence level. The ionisation parameter finds different values; however, this is likely due to differences between the two models, and the trend of higher ionisation with increasing luminosity is still very clear.

3.3.3.3 Markov Chain Monte Carlo analysis

The three different models applied have unanimously demonstrated the same trends; however, applying χ^2 fitting to such a large number of free parameters (21; Table 3.5) across four datasets brings with it the considerable possibility that a local minimum is mistaken for the global best fit. Furthermore, as discussed previously, the precise resolution required in reflection fitting, and the subtle effect that parameters have, is highly susceptible to degeneracies, which can force the parameter space a fit occupies. In order to assess this possibility a Markov Chain Monte Carlo (MCMC) statistical analysis was performed on results with XILLVER. This technique has recently been successfully used by Reynolds *et al.* (2012) to constrain the black hole spin of NGC 3783, which also required a large number of free parameters.

Starting a random perturbation away from the best fit (Table 3.5), four 55,000 element chains were run, of which the first 5000 elements of each chain were discarded ('burnt'). The chain proposal is taken from the diagonal of the covariance matrix calculated from the initial best fit. For this it was assumed that the probability distributions were Gaussian, and a rescaling factor of 10^{-3} was applied. The resultant 200,000 element chain can thus be used to determine the probability distribution for each parameter, and allow comparison with the results found through the standard XSPEC ERROR command. For observations 1 to 4 the best fit inner radii and MCMC-determined 90 % confidence intervals were >302, 295^{+125}_{-120}, 137^{+84}_{-24} and 67^{+52}_{-15} respectively, hence being very consistent with those quoted in Table 3.5.

Figure 3.6 (top panels) displays the values of the inner radius for the four observations from every 200th step of the 200,000 elements. Each distribution shows no

sign of significant deviation or trend, thus suggesting that the global minimum has in fact been found, offering even more certainty to the inner radius evolution uncovered previously. The lower panels of Fig. 3.6 show the probability distribution for the inner radius, in-keeping with Table 3.5. For each observation the inner disc being at the ISCO is definitively ruled out.

Another benefit of MCMC analysis is that it allows one to reveal any correlations between parameters. In Fig. 3.7 I present two-dimensional probability distributions of the inner radius with inclination and ionisation. Each axis is chosen for clarity rather than to span the entire parameter space of the model, but still encompasses the full probability distribution for both parameters. Each distribution shows little sign of a correlation, indicating that no significant parameter degeneracies are at play and that the global best fit has indeed been found.

3.3.3.4 Does disc evolution monotonically track luminosity? - Comparing rise and decay

So far only the four hard state observations have been analysed, hence ignoring the 2011 hard-intermediate dataset (Observation 2b). This observation took place in decay at a very comparable luminosity to Observation 2, which was taken whilst GX 339−4 was in its rise through the hard state. Therefore, if disc evolution is solely a trend with luminosity, then one should expect to obtain similar results between the two observations. The middle panel of Fig. 3.8 shows the data/model ratio of the continuum fit to Observation 2b. A strongly broadened Fe line was found, much more asymmetric than the hard state profiles, indicating that the relativistic broadening is more significant. To probe this conclusion the inclination was fixed to that resolved by the hard state observations (Table 3.5), and the results are presented in Table 3.6. The same fixed values were used for the spin (0.9), emissivity index (3) and disc outer radius ($1000\,r_{\rm g}$).

For both the line and reflection fitting techniques the inner accretion disc radius is estimated to be significantly smaller for the intermediate state observation. This strong contrast in the inner radius of the disc suggests a possible hysteresis in how the inner disc evolves throughout the outburst. Furthermore, the disc inner radius found through both methods is smaller than for all of the hard state observations at 90% confidence. Therefore, this strongly suggests that the disc is truncated from the ISCO throughout the hard state, even in Observation 4 which was at $\sim 0.15\,L_{\rm Edd}$[6].

[6]assuming a BH mass and distance of $8\,M_{\odot}$ and 8 kpc respectively

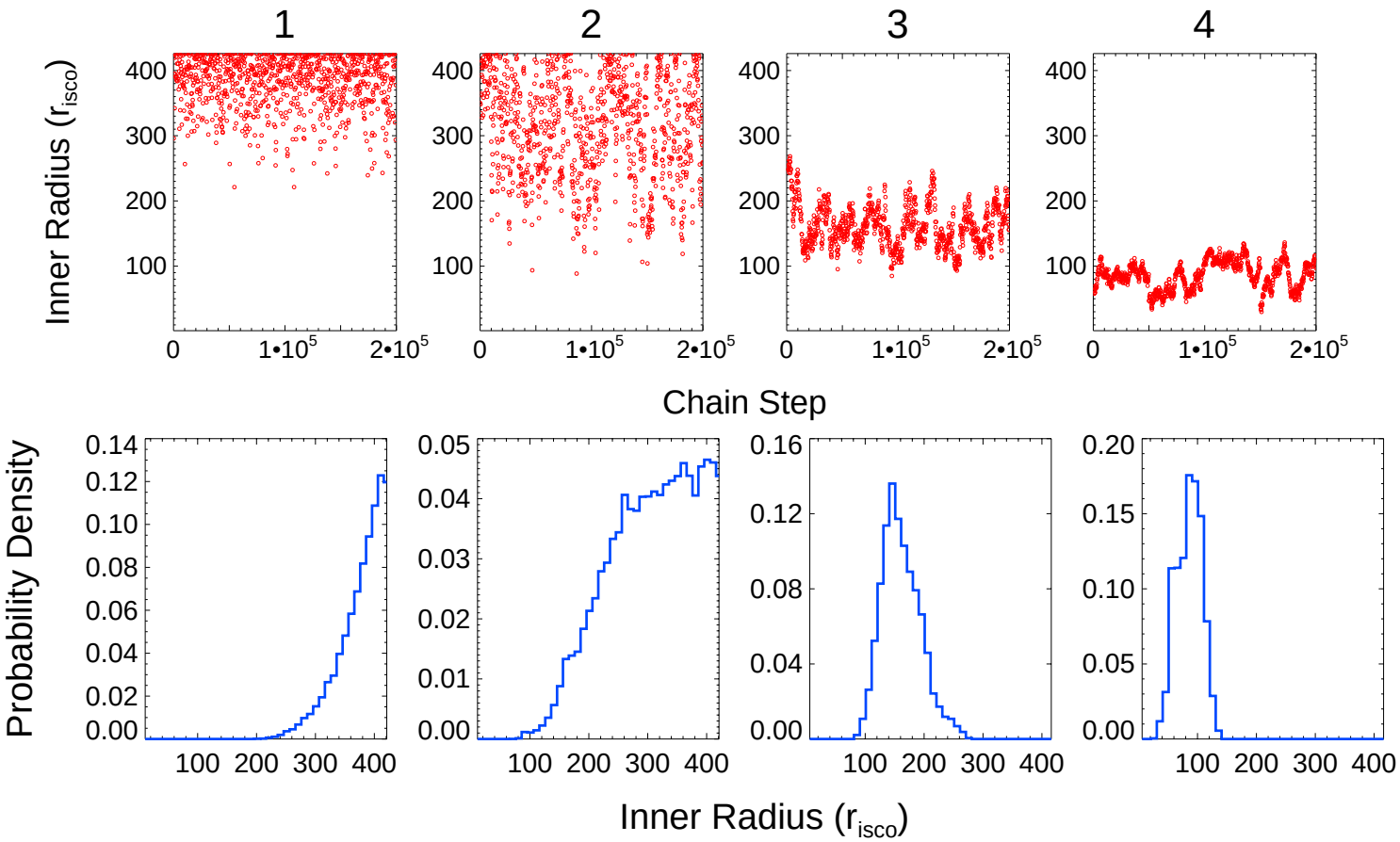

Figure 3.6: Inner radius results from the MCMC based analysis displayed from left to right for Observations 1 to 4 respectively. Top panels: The distribution of inner radius values along the 200,000 element chain with every 200th element displayed for clarity. Lower panels: Probability distributions for the inner radius, each bin has a width of $10\,r_{\rm isco}$.

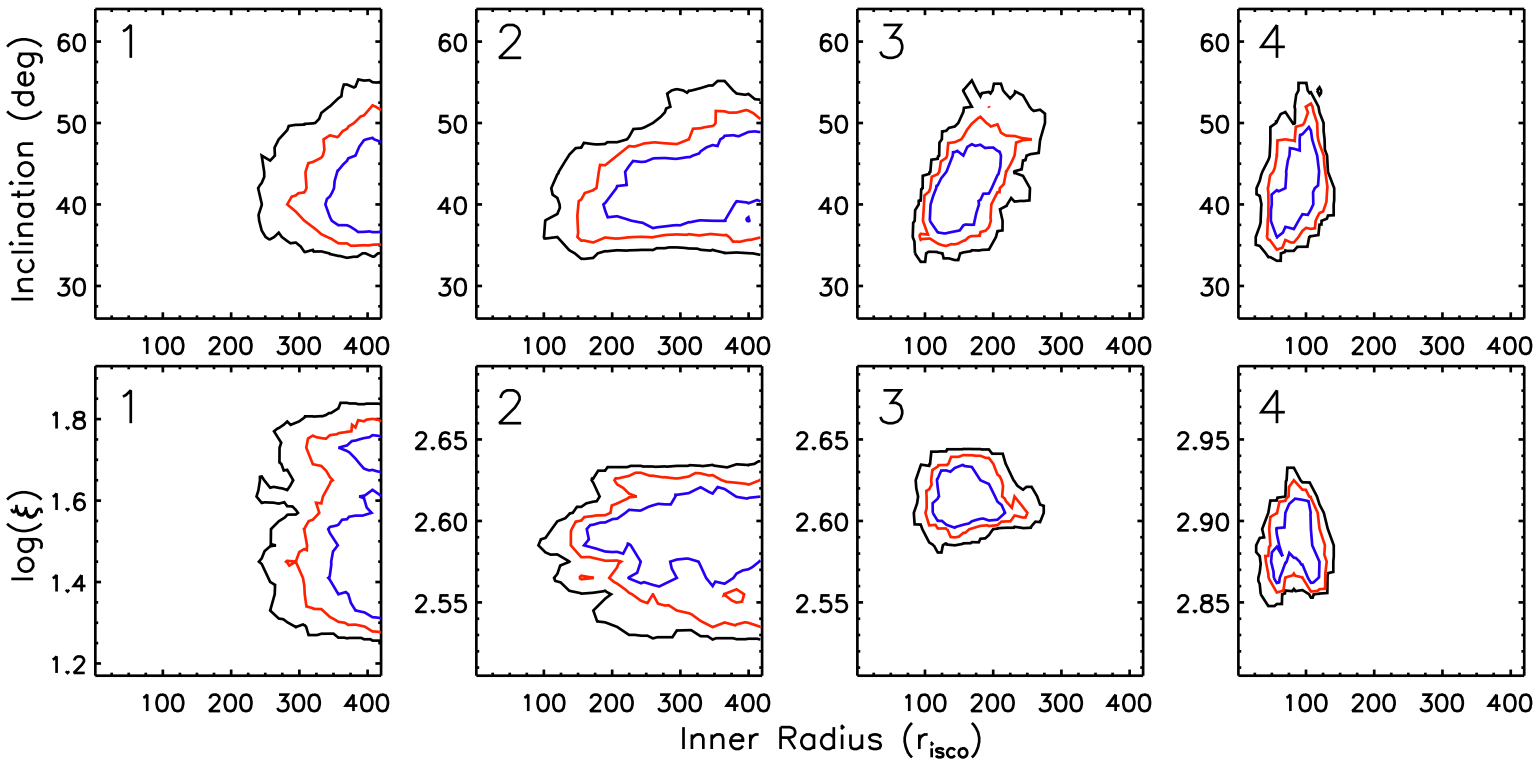

Figure 3.7: Two-dimensional probability distributions of the inclination (top) and ionisation (bottom) parameters with the inner radius. For each upper panel I plot contour levels at the 68% (blue), 90% (red) and 99% (black) confidence levels. Each plot contains the full distribution for the whole parameter range with the axis reduced for clarity. In all eight distributions there is no indication of a significant correlation between the parameters.

Parameter	Line Only	Reflection
Γ	1.84 ± 0.02	$1.85^{+0.04}_{-0.03}$
N_{PL}	0.15 ± 0.01	0.13 ± 0.03
E (keV)	$6.97_{-0.06}$	...
r_{in} (r_{isco})	$2.3^{+0.3}_{-0.4}$	$12.5^{+7.2}_{-5.8}$
N_L (10^{-4})	$6.69^{+1.05}_{-1.00}$	...
$\log(\xi)$	...	$2.65^{+0.22}_{-0.52}$
N_R (10^{-6})	...	$1.50^{+5.01}_{-0.50}$
E.W. (eV)	152^{+29}_{-30}	...
RF	...	0.23 ± 0.12
χ^2/ν	1563/1518	1556/1518

Table 3.6: Results from fitting Observation 2b with the RELLINE (left section) and RELCONV∗XILLVER (right section) models respectively. The inclination and outer radius parameters were frozen to those found in the hard state for the respective model used (see Table 3.5).

This conclusion is further supported by the small difference in fit between the two methods (only $\Delta\chi^2 = +7$ for no additional degrees of freedom using RELLINE; Table 3.6), meaning that the profile in the hard-intermediate state is dominated by relativistic effects from emission close to the BH.

The ionisation parameter is similar ($\log\xi \simeq 2.6$), although slightly larger in decay. The decay spectrum is softer (as defined by the hard-intermediate state) since there is more thermal emission from the disc (compare *e.g.* Hiemstra *et al.* 2011 with Reis *et al.* 2010). This will lead to increased heating of the surface layers of the disc where the reflection spectrum originates from, and therefore display broader line profiles (Ross and Fabian, 2007), similar to that of a larger ionisation parameter. The current publicly available models do not take this into account (see §3.4 for further discussion of this), and it is likely that the hard-intermediate state observation would then require a larger ionisation parameter to solve for this.

3.3.3.5 Power density spectra

The power spectra of BHs in the hard state display similar characteristics (van der Klis, 1995, 2006). Typically they are described by a flat region of power $P(\nu) \propto \nu^0$ below a frequency ν_b, known as the 'break frequency'. Above ν_b the power spec-

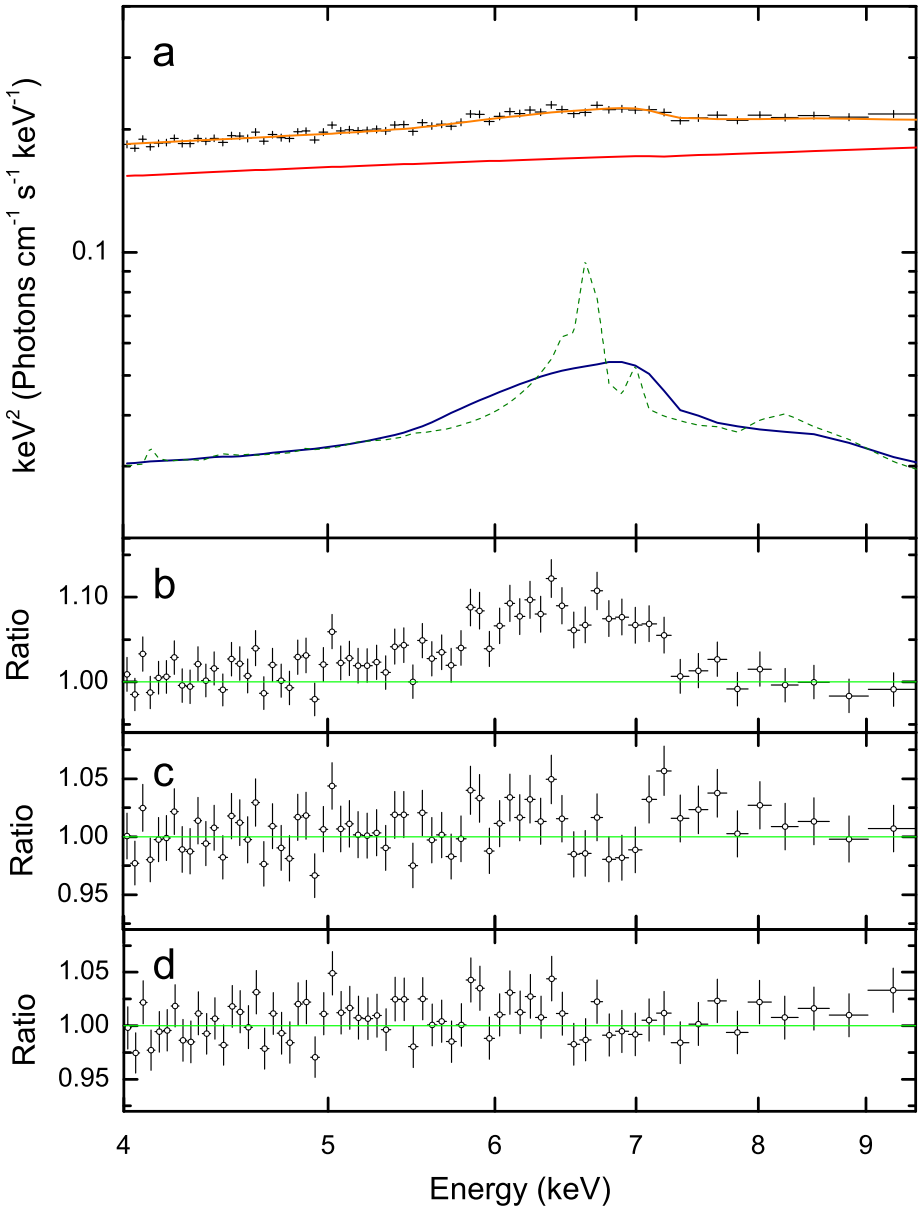

Figure 3.8: (a) The unfolded spectral fit for the 2011 HIMS observation (Observation 2b) using RELCONV*XILLVER to model the reflection component. The colour scheme follows that of Fig. 3.5. (b) The data/model ratio for the continuum fit in Table 3.4 displaying strongly broadened Fe Kα emission. (c) The model residuals when using RELLINE to model the Fe line. (d) The data/model ratio when the reflection was modelled using RELCONV*XILLVER. The spectra have been re-binned for the purposes of plotting.

	ObsID	Date	ν_b (Hz)
1	93702-04-01-00	2008-09-24 00:29:53	$0.00255^{+0.00065}_{-0.00048}$
	93702-04-01-01	2008-09-25 06:23:06	
	93702-04-01-02	2008-09-25 11:06:06	
	93702-04-01-03	2008-09-25 19:00:14	
2	94405-01-03-00	2009-03-26 11:04:44	$0.00808^{+0.0026}_{-0.0017}$
3	90118-01-07-00	2004-03-18 18:01:16	$0.0474^{+0.0028}_{-0.0026}$
4	95409-01-12-01	2010-03-28 03:13:35	$0.195^{+0.007}_{-0.006}$

Table 3.7: Fitted break frequencies (ν_b) for RXTE observations simultaneous to that of the high-resolution spectra listed in Table 3.2. In order to analyse the lowest flux epoch four contemporaneous observations were combined. Quoted errors are at the 1σ level.

tra steepen to roughly $P(\nu) \propto \nu^{-1}$. This break frequency is coupled with the BH mass and accretion rate (McHardy *et al.*, 2006; Körding *et al.*, 2007) and gradually increases as the source progresses through the hard state (see *e.g.* Migliari *et al.* 2005). Furthermore, a number of correlations have been found, notably with a steepening of the Comptonised spectrum and an increasing amount of reflection (Gilfanov *et al.*, 1999). Both of these trends can be interpreted as an increasing penetration of the cool accretion disc into the inner hot flow which gives more seed photons to cool the flow. Therefore, it has been suggested that ν_b is associated with the truncation radius of the inner disc (Gilfanov *et al.*, 1999; Churazov *et al.*, 2001).

For each of the hard state observations listed in Table 3.2 the power density spectra (PDS) of simultaneous RXTE observations were analysed. Where more than one observation was available the one with the best signal-to-noise was chosen. Unfortunately, the nearest observation to Observation 2b was not of sufficient quality to be used, and hence this epoch was ignored. Figure 3.9 displays all four PDS and a clear evolution to higher frequencies can be seen for ν_b as the luminosity increases. PDS fitting was carried out by Dr. Teodoro Munõz-Darias with XSPEC by using a one-to-one energy-frequency conversion and a unit response. The noise components were fitted with one zero-centred Lorentzian, plus two Lorentzians centred at $\sim$ few Hz (see Belloni *et al.* 2002 for details on the standard procedure). For Observation 4 another narrow Lorentzian was added due to the presence of a weak quasi periodic oscillation. The break fitted for each PDS follows the expected trend to higher frequencies with luminosity (Table 3.7).

Earlier in this work the reflection spectrum was utilised to uncover how the inner

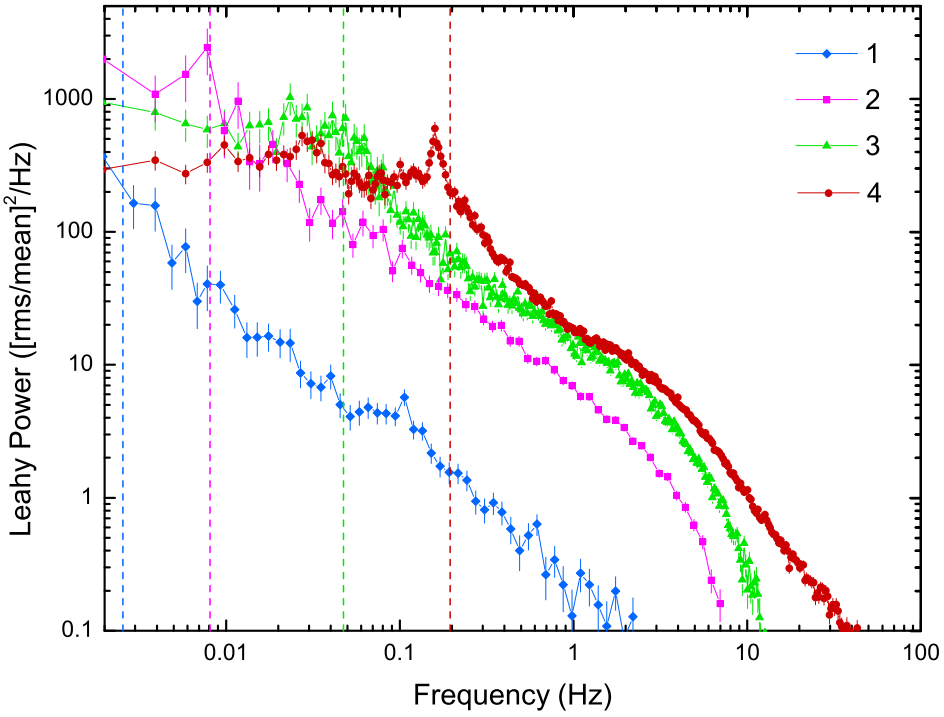

Figure 3.9: The Leahy normalised PDS (Leahy *et al.*, 1983) of the four RXTE observations of GX 339−4 in Table 3.7, clearly showing that the break frequency shifts to higher frequencies in the higher luminosity observations. The dashed lines indicate the fitted break frequency for each observation (Table 3.7). The same colour/shape scheme as Fig. 3.3 is used.

radius of the disc evolves through the hard state. If ν_b corresponds to the inner radius of the disc it allows an independent measure of this, and hence Fig. 3.10 compares the trend from both methods. The dynamical and viscous timescales (both of which could be tracking the inner radius) for accretion on to a BH are proportional to $R^{3/2}$. Therefore, one should expect to find that the ν_b increases with luminosity, which is the exact trend I find. However, as I described before, other correlations have been found, and it is not certain which is driving the break. Again, as an example, both the softening power-law photon index and increasing reflection fraction trends are consistent with a decreasing inner radius of the disc (Done *et al.* 2007; Chapter 4). Mass accretion rate may also influence the break frequency, or be intrinsically linked to the inner radius (Migliari *et al.*, 2005; McHardy *et al.*, 2006).

Nevertheless, the evolution is remarkably similar. For both the line and reflection methods the evolution from Observations 1 to 2 and 3 to 4 is quite steep, whereas from 2 to 3 the change is more moderate. The break frequency follows this same pattern, suggesting it too tracks the inner radius of the disc, extending closer to the

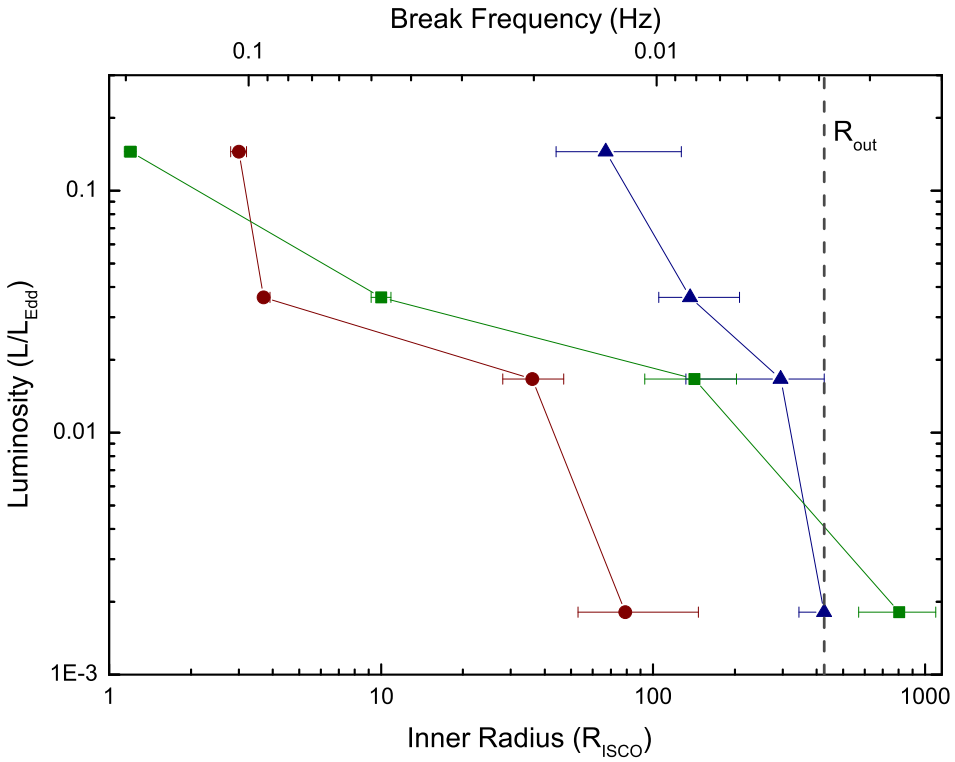

Figure 3.10: Evolution of estimated inner radii (bottom x-axis; Table 3.5) using RELLINE (red/circle) and RELCONV*XILLVER (blue/triangle), and the fitted break frequency (green/square) from simultaneous RXTE observations (top x-axis; Table 3.7), as a function of luminosity (assuming a BH mass and distance of $8\,M_{\odot}$ and 8 kpc respectively). In order to allow a fair comparison I applied the scaling $\nu \propto R^{-3/2}$ to the x-axis (*i.e.* that the log space of the bottom x-axis is a factor of $3/2$ larger than the top). This corresponds to the dynamical and viscous timescales for accretion on to a BH. The black dashed line indicates the disc outer radius which was fixed to be $1000\,r_{\rm g}$ ($\sim 426\,r_{\rm isco}$). The contrasting results between RELLINE and RELCONV*XILLVER are discussed in §3.3.3.2, but I note that the latter represents a much better fit to the data (Table 3.5).

BH as it progresses through the hard state. To see how the trend continues, the final hard state RXTE observation of the 2010 outburst (ObsID: 95409-01-13-06) was analysed, which is the same outburst as Observation 4. The break frequency was now found to be at 0.53 ± 0.03 Hz, more than a factor of two larger than Observation 4, clearly indicating that the evolution continues through the hard state. Therefore, if the inner radius of the accretion disc and the break frequency are physically linked, the inner disc radius must continue to evolve throughout the hard state. Furthermore, as the source transitions into the intermediate states, the break frequency is seen to continue above 1 Hz (see also Belloni *et al.* 2005; van der Klis 2006).

3.3.4 Testing the full bandpass

So far I have restricted the analysis to above 4 keV, since this allows a simpler continuum model to be fit in the computationally intensive task of fitting four datasets with tied parameters. Including the data below 4 keV firstly adds a considerable amount of extra degrees of freedom that need to be fit. But of further importance is that it presents a much more complex continuum. Above 4 keV the continuum is a simple power-law, but below this the thermal emission from the disc quickly becomes significant, and adds considerably more curvature to the continuum. Furthermore, the requirement of a DISKBB model to fit this, and the much stronger effect of interstellar absorption requires three additional free parameters to be fit per spectrum. All of these factors combined make jointly fitting the four hard state spectra simultaneously, with tied parameters and a self-consistent treatment for reflection (as applied in §3.3.3.2), impossible in a reasonable timescale if the full bandpass is used.

Another potential issue is that the weak thermal component can be mistaken for the soft excess in the reflection model. Also, the lower part of the bandpass contains strong edges in the effective area, and is hence generally less well calibrated. Since the statistics are better at lower energies these features could drive the reflection fit, rather than the more revealing Fe K emission. Whilst ignoring the data below 4 keV restricted the bandwidth, it significantly decreased the calibration dependence as well. This procedure is standard practice in the AGN community where the majority of X-ray reflection studies have taken place, be it in systematic investigations (see *e.g.* Nandra *et al.* 2007; de La Calle Pérez *et al.* 2010) or single observations (see *e.g.* Fabian *et al.* 2002; Ponti *et al.* 2009).

The focus of this Chapter is to systematically uncover how the inner disc is evolving in one source, hence tying parameters and minimising calibration and model dependence is of utmost importance. As I have outlined, by necessity this requires fitting above 4 keV, but this then also throws away a large amount of the soft X-ray spectrum. Whilst the reflection spectrum is weaker than the thermal and Comptonised emission below 4 keV, it is still significant, and in particular this part of the reflection spectrum holds important information about the ionisation stage. Furthermore, the most broadened Fe profiles, i.e. that of a maximally rotating black hole, may be mistaken for the continuum when only fitted above 4 keV. It is therefore essential that I examine the full bandpass of each spectrum to ensure that the results from fits above 4 keV are not in error.

To examine this consistency I thus fitted each spectrum individually using a full

bandpass, as is the standard approach in snapshot X-ray studies of BHXRBs. For the *XMM-Newton* observations the full bandpass covers the 1.3–1.75 and 2.35–10 keV ranges. The *Suzaku* observations were fitted in the 0.7–1.7 and 2.4–10 keV bands (see §3.2 for more details on the bandpass used). Since the inclination cannot be jointly determined I fixed it to the value determined with XILLVER (Table 3.5; 42°) to allow a fair systematic comparison of each dataset. Because the inclination is measured from the sharper blue wing of the Fe Kα profile this should be well determined even if the analysis above 4 keV was in error. I nevertheless test the effect of different inclination angles over the full bandpass in §3.3.4.1. With the added disc component, the full model was now
PHABS(DISKBB+POWERLAW+RELCONV∗XILLVER) which I fitted with the additional parameters for the inner disc temperature and normalisation allowed to be free. The column density was now also fitted freely due to the strong impact of interstellar absorption below 4 keV, and the results can be found in Table 3.8. Unfortunately, due to the lower cut-off of 1.3 keV used for the EPIC-pn data, the weak disc component could not be constrained in Observations 2 and 3. The remaining observations were all well fitted by the added disc model, all reporting a reduced-χ^2 of ≤ 1.10 (Table 3.8), except for Observation 3. The main cause of the poor fit to Observation 3 is in the soft region of the bandpass (< 4 keV), and is probably due to some un-modelled thermal emission being present there (Figure 3.11). Kolehmainen *et al.* (2014) also found poor fits for this dataset, despite using different continuum and reflection models, but the Fe line was nevertheless still well fit.

For all of the observations each parameter remained consistent at the 90 % confidence level with those in §3.3.3.2, and clearly indicates that the results in that section were not driven by fitting only above 4 keV. In particular, the inner radius parameter shows little change and the trend of the disc extending closer to the BH with increasing luminosity still remains. I note that even with the extended bandpass down to $\sim$ 1 keV, it may be that the continuum is not being correctly modelled, which is well known to be an issue in studies of ultraluminous x-ray sources (Roberts, 2007). However, the analysis of data > 10 keV in §3.3.2 confirms that this is not the case in this study. Additionally, the power-law photon index shows very little variation indicating that the continuum was still very well constrained when the fit was restricted to above 4 keV. If a broad red wing from a disc at the ISCO was present then it is possible this could have been masked by a harder photon index when fitting only above 4 keV. However, little variation found when fitting the full bandpass confirms that the profiles in the hard state show little relativistic broadening, consistent with

Model	Parameter	1	2	3	4	2b
PHABS	N_H ($\times 10^{22}$)	0.62±0.04	0.30±0.01	0.24±0.01	0.32±0.03	$0.38^{+0.02}_{-0.01}$
DISKBB	T_{in} (keV)	0.16±0.01	...	...	$0.22^{+0.02}_{-0.04}$	0.27±0.01
	N_{BB} ($\times 10^3$)	$3.72^{+2.12}_{-1.52}$	...	...	$14.0^{+27.0}_{-7.5}$	$3.94^{+1.50}_{-0.96}$
POWERLAW	Γ	1.68±0.02	1.45±0.01	1.49±0.01	1.60±0.01	1.90±0.01
	N_{PL}	0.013±0.001	0.086±0.003	0.16±0.01	0.41±0.07	0.13±0.01
RELCONV	θ (°)			42		
	r_{in} (r_{isco})	>320	213^{+218}_{-99}	110^{+30}_{-15}	69^{+37}_{-29}	17^{+9}_{-5}
XILLVER	$\log(\xi)$	$1.83^{+0.04}_{-0.10}$	$2.61^{+0.03}_{-0.01}$	2.63±0.01	2.86±0.03	$2.78^{+0.04}_{-0.10}$
	N_R (10^{-6})	$1.60^{+0.57}_{-0.29}$	$3.29^{+0.22}_{-0.24}$	5.11±0.08	$20.3^{+0.9}_{-0.8}$	$1.33^{+0.33}_{-0.19}$
χ^2/ν		2275/2227	1774/1614	2920/1614	1671/1612	2378/2226

Table 3.8: Results from fitting the four hard state observations individually with PHABS(DISKBB+POWERLAW+RELCONV*XILLVER). The photon index in the reflection models was tied to that of the continuum power-law and the Fe abundance was assumed to be solar. The same fixed values were used as for Table 3.5. In some cases the inner radius parameter has reached the largest tabulated value in the model (1000 r_g), therefore only the lower limit is presented in this case.

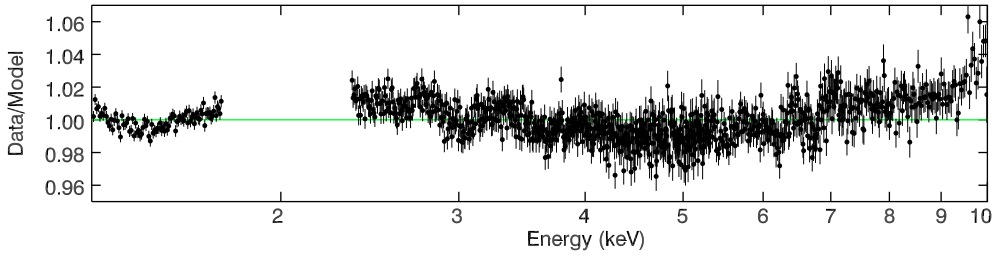

Figure 3.11: The data/model ratio of the full bandpass fit to Observation 3 (Table 3.8), which shows some residual curvature. This is probably due to the disc emission not being modelled, which was not possible due to the 1.3 keV cut-off. The Fe line region still appears to be well modelled. The data has been re-binned for plotting purposes.

a truncated disc throughout the hard state.

3.3.4.1 The unknown inclination of GX 339−4

The orbital inclination of GX 339−4 is unknown, but, as discussed in §1.6, we are able to constrain the inclination to be $40^\circ < i < 70^\circ$. The respective strengths of the different relativistic effects is determined by the inclination of the accretion disc, one obvious example being aberration. Each effect ultimately transforms, and most importantly broadens, the line profile in different ways, thus the inclination parameter is very degenerate with the inner radius. A key aspect of this work is that I jointly determined the inclination across all four hard state spectra (see §3.3.3.2). However, this was only possible between 4–10 keV since the additional disc model parameters and degrees of freedom render this infeasible using a full bandpass in XSPEC. I thus instead tested the effect of the inclination by fitting each full bandpass dataset individually for a range of fixed inclination values, investigating the full range of $\cos i$ in steps of 0.05.

Figure 3.12 displays how the absolute value of the inner radius varies throughout the range of $\cos i$. The influence of the inclination parameter is immediately clear, fitting smaller inner radii as the inclination decreases. As previously described in §3.3.3.2, this is a consequence of the reduced doppler shift when a disc is face-on, thus as the inclination increases (becoming more edge-on) a larger inner radius is required to replicate the observed profile width. This degeneracy underlines the importance of the simultaneous approach taken in §3.3.3.2, and highlights the limitation of snap-shot analysis often employed in X-ray spectroscopy. Table 3.9 details the complete results of the analysis. I note that although Observation 1 appears to remain at a constant inner radius regardless of inclination, this is because the parameter is pegged at the hard limit. The consistent relationship between the inner

$\cos(i)$	Observation Number			
	1	2	3	4
0.05	>373	>328	209^{+49}_{-35}	148^{+136}_{-81}
0.1	>377	>327	208^{+52}_{-32}	148^{+131}_{-73}
0.15	>382	>341	206^{+53}_{-30}	145^{+126}_{-66}
0.2	>380	418^{+8}_{-94}	241^{+28}_{-70}	139^{+126}_{-60}
0.25	>376	408^{+18}_{-105}	235^{+28}_{-56}	136^{+121}_{-59}
0.3	>373	385^{+41}_{-108}	228^{+27}_{-54}	132^{+116}_{-57}
0.35	>371	357^{+69}_{-102}	219^{+27}_{-52}	107^{+130}_{-37}
0.4	>374	337^{+89}_{-102}	206^{+28}_{-49}	119^{+102}_{-50}
0.45	>368	319^{+107}_{-102}	189^{+30}_{-43}	114^{+96}_{-49}
0.5	>364	297^{+129}_{-98}	152^{+44}_{-18}	106^{+88}_{-45}
0.55	>362	272^{+154}_{-91}	155^{+35}_{-27}	96^{+82}_{-39}
0.6	>354	291^{+135}_{-127}	145^{+30}_{-25}	86^{+73}_{-34}
0.65	>345	266^{+160}_{-146}	132^{+27}_{-20}	75^{+61}_{-28}
0.7	>337	239^{+187}_{-108}	121^{+25}_{-17}	63^{+57}_{-20}
0.75	>318	207^{+219}_{-94}	107^{+30}_{-14}	64^{+38}_{-25}
0.8	>291	171^{+240}_{-76}	108^{+13}_{-18}	49^{+38}_{-15}
0.85	>241	132^{+189}_{-56}	104^{+18}_{-22}	43^{+33}_{-10}
0.9	>165	106^{+146}_{-45}	102^{+14}_{-15}	49^{+20}_{-15}
0.95	258^{+168}_{-149}	218^{+93}_{-142}	113^{+18}_{-29}	54^{+34}_{-16}

Table 3.9: The fitted inner radius of each observation (Table 3.2) for different fixed values of inclination. Errors are quoted at the 90 % confidence level. In some cases the inner radius parameter has reached the largest tabulated value in the model ($1000\,r_{\rm g}$), therefore only the lower limit is presented in this case.

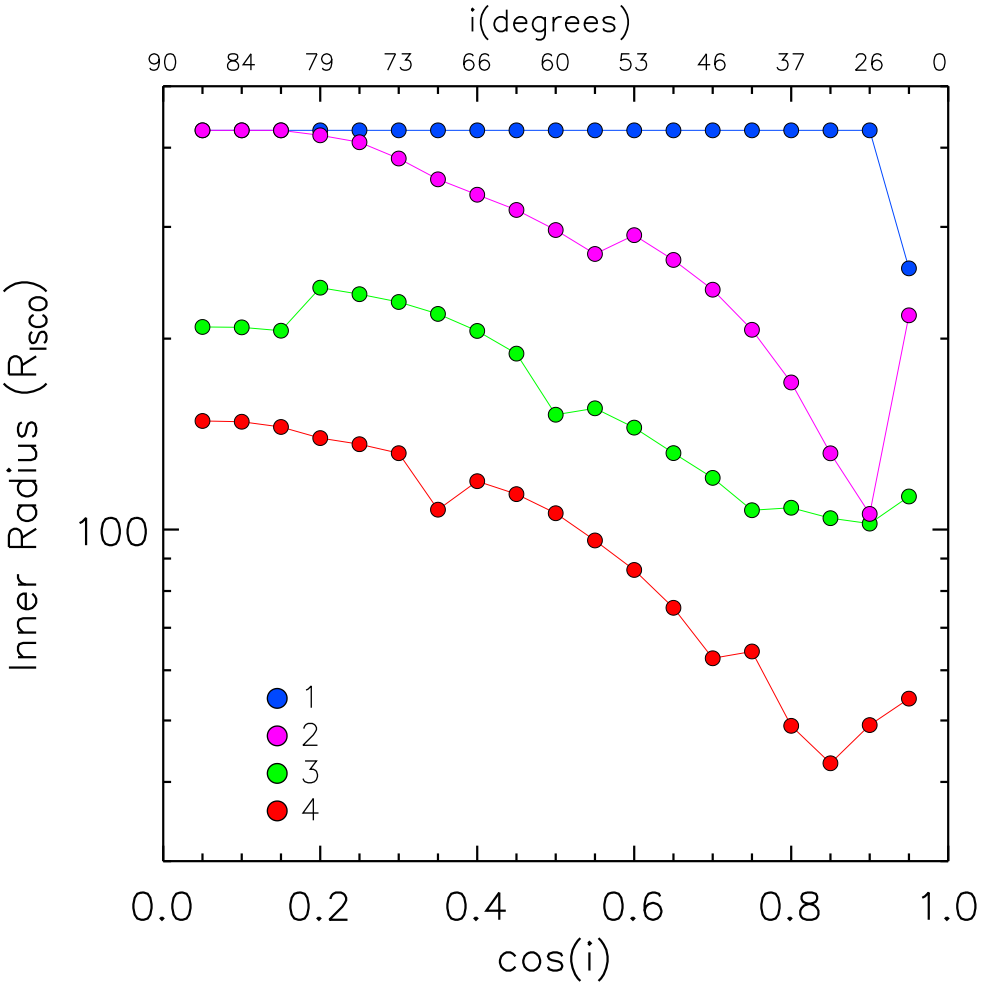

Figure 3.12: The fitted inner radius parameter for different fixed values of inclination, fitted individually using a full bandpass. The coloured symbols indicate the four observations in Table 3.2: blue (1), magenta (2), green (3) and red (4). For clarity errors are not plotted but are instead listed in Table 3.9.

radius and inclination means that the inner radius ubiquitously decreases with increasing source luminosity for any assumed disc inclination. The hard state itself is also ubiquitously associated with a truncated disc for any assumed inclination. Furthermore, this again confirms that the trend presented in §3.3.3.2 is not an artefact of the reduced bandpass.

Additionally, I investigated how the chi-square value of each observation varies throughout the analysis in an attempt to resolve the preferred inclination. Figure 3.13 displays this, and at first glance the distribution appears to be inconclusive: Observations 1 and 3 show a strong preference for low and high inclinations respectively, and Observations 2 and 4 lean towards a high inclination, but with insufficient significance. However, Observation 1 is pegged at a hard limit throughout

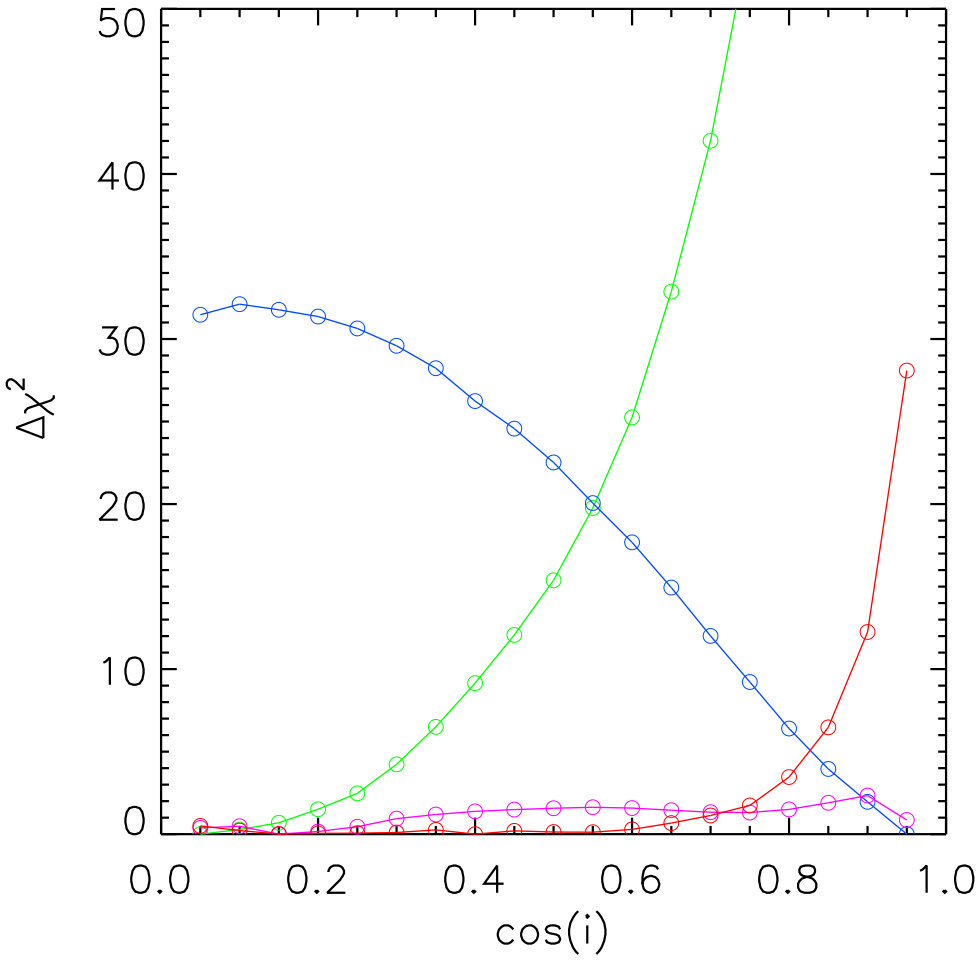

Figure 3.13: The chi-square distribution for different fixed values of inclination, fitted individually using a full bandpass. The colour-scheme follows Fig. 3.12. The y-axis reflects the increase in χ^2 from the best fit value.

almost the entire range of $\cos i$ (Figure 3.12), meaning that the parameters are not being globally constrained. If Observation 1 is ignored, then the other three observations all point towards a preference for a high inclination for GX 339−4. This is not surprising, since it is known that for the binary inclination $\cos i \lesssim 0.7$ (see §1.6), and thus I conclude that the accretion disc is substantially truncated in all four observations (Table 3.9).

3.3.4.2 The emissivity parameter

Throughout this study I have fixed the emissivity parameter of each observation due to the high level of degeneracy it has with the inner radius parameter. Additionally, previous works fitting the Fe line in the hard state have regularly found emissivity parameter values consistent to the r^{-3} law that I adopted (Table 3.1). A larger

emissivity index than this yields increased emission from the inner regions of the disc, hence increasing the significance of the relativistic effects upon the overall profile. This is somewhat analogous to having an inner disc radius closer to the BH where the influence of relativity becomes stronger. I do acknowledge, however, that the profile I assumed may be incorrect and could evolve throughout the outburst depending on the geometry of the hard X-ray source.

The value of 3 that I used for the emissivity parameter is the value for a Newtonian disc. In General Relativity, however, one would expect the hard X-ray source to be more focused on the inner regions because of light-bending, resulting in a steeper fall off with radius (i.e. a larger emissivity index; Miniutti and Fabian 2004). Furthermore, decreasing the scale height of the corona would further this effect. To account for this a broken power-law profile may instead be required to describe the contrasting emission from the inner region. A recent study by Wilkins and Fabian (2012) investigates further emissivity profiles for different coronal geometries, the general trend being towards a value of roughly 3 outwards of $\sim$10–30 $r_{\rm g}$, hence radii much smaller than I found for the disc inner radius in this Chapter. Additionally, as discussed in Fabian *et al.* (2012), it is only in the innermost region ($<2r_{\rm g}$) where a steeper inner profile is strictly necessary. Nevertheless, it is possible that a varying emissivity profile may be contributing to the inner radius trend I have revealed.

To test this precedent I fit a broken emissivity to each observation individually using a full bandpass. The emissivity indices, both represented by the parameter q in the form r^{-q}, were fit in the ranges 3–10 and 2–3.5 for the inner and outer region respectively. The larger range selected for the inner index reflects the influence of light-bending, and in any case the index should be greater than 2 for the outer region of the disc, but not significantly larger than the Euclidean value of 3 (Wilkins and Fabian, 2012). The break radius $r_{\rm br}$ was allowed to span the range 2.32–10 $r_{\rm g}$, whereby the lower bound is the ISCO for a spin of 0.9. For all four observations the inner region index and break radius were unable to be resolved, both being insensitive to the fit as a significantly truncated inner radius, much larger than $r_{\rm br}$, was still preferred. To stabilise the fit I fixed the inner index to the smallest expected value of 3 and break radius to 6 $r_{\rm g}$ respectively, fitting the outer index as previously. I note that the choice of the inner index and break radius values do not affect the results since $r_{\rm in}>r_{\rm br}$.

The inner radius of Observation 1 remained pegged at the hard limit (as in the previous analysis; Tables 3.5 and 3.8), thus consistent with requiring no relativistic broadening. Hence, this means that the emissivity index has no influence on the fit

Parameter	1	2	3	4
$h(r_g)$	>92	>94	>98	>86
$\Delta\chi^2$	+65	+39	+116	0

Table 3.10: The source height h of the corona fitted for an inner accretion disc at the ISCO using the model RELCONV-LP.The parameter $\Delta\chi^2$ refers to the additional χ^2 in comparison to fitting a truncated disc model for the same degrees of freedom (Table 3.8). In all cases the source height h pegged at the hard limit of $100\,r_g$, therefore only lower limits were calculated.

and is unresolved. The lower limit on the inner radius was virtually unchanged by the free emissivity parameter (>319 versus $>320r_{isco}$; Table 3.8). Observation 2 prefers an index of 3.5, but was unable to constrain the emissivity within the 2–3.5 range. Again this is not surprising given the small relativistic broadening required to fit the narrow profile. Despite the emissivity index being free, the constraint on the inner radius was again barely affected ($214^{+212}_{-108}\,r_{isco}$). In Observation 3 the broader profile now allows an index of >2.7 to be constrained, whilst the inner radius shifted slightly ($129^{+16}_{-24}\,r_{isco}$), but is still consistent with the value determined using a fixed index of 3.

The emissivity index of Observation 4 was found to be <2.5, thus being the only observation to require an index less than the Euclidean value of 3. This may represent some change in the corona, possibly linked to the imminent state transition. Due to the decreased centralisation of the emission, where the relativistic effects are stronger, the moderately broad profile is recovered by a decrease in the inner radius to $12^{+14}_{-3}\,r_{isco}$, confirming the degeneracy described before. Nevertheless, this still represents a significant level of truncation in this observation and only serves to isolate it further from the more truncated hard state observations at lower luminosities. Therefore, the decision to fix the emissivity index at 3 in the analysis has little influence on the trend presented in Fig. 3.10.

Recently Fabian *et al.* (2014) performed simulations to investigate how the nature of the corona affects the determination of the inner radius, concluding that the profile width is strongly dependent upon the coronal height (see also Dauser *et al.* 2013). Ultimately, increasing the coronal height leads to a reduction in the fraction of photons illuminating the inner regions of the disc, hence a narrow profile could be a signature of coronal elevation rather than disc truncation. I applied the same lamp-post illumination model RELCONV-LP (replacing RELCONV) employed in the simulations of Fabian *et al.* (2014) to investigate whether the height of the corona can alone describe the narrow profiles found in all four hard state observations. I

fixed the inner radius of the disc to be at the ISCO and allowed the height of the corona h to be fit freely between 2–100 r_g. The photon index was tied to that of the POWERLAW model. All observations preferred a source height larger than 85 r_g, whilst no fit was improved, and was significantly poorer for Observations 1-3 (Table 3.10). To summarise, the source height alone could not replicate the narrow line profiles observed as well as a truncated disc. Fixing the black hole spin to be zero (*i.e.* a larger ISCO) yielded the same result. As discussed in Fabian *et al.* (2014), such a large source height is unlikely, and in conjunction with the poorer fit emphasises the presence of inner disc truncation in the hard state of GX 339-4.

3.4 Discussion

In this work I have analysed the Fe line region of GX 339−4 and applied it as a probe of how the inner accretion disc evolves, presenting evidence that the Fe line profile changes with luminosity. These results indicate that even at relatively high luminosities the inner disc radius is still somewhat truncated, although following a trend of decreasing radius with increasing luminosity. This brings into question at which point, if any, the inner disc has reached the ISCO in the canonical hard state. Such a finding has a direct impact upon the use of reflection features to measure BH spin. The entire range of prograde BH spin is spanned within the inner 5 gravitational radii of the disc, and hence even a slight truncation, much smaller than the extent presented here, will have a profound impact upon the confidence of spin determination.

I investigated the use of both the line and self-consistent reflection fitting methods, and found at all stages that the disc is predicted to be significantly more recessed using the latter technique. Self-consistent reflection modelling takes into account Comptonisation and multiple ionisation stages, which themselves broaden the line profile. These effects are a consequence of disc ionisation, and hence a degeneracy could occur between relativistic broadening, for example the inner disc radius, and the ionisation parameter. An increasing trend of the ionisation parameter with luminosity was recorded. On the HID (Fig. 3.3) the hard state track is near-vertical, keeping a roughly constant hardness, meaning most of the power is consistently going mainly into the hard, illuminating, component, rather than the soft disc. By definition the ionisation parameter is proportional to the flux of the illuminating component, and therefore it should be expected to increase with luminosity. An extensive MCMC analysis confirmed that there was no degeneracy

between the inner radius and ionisation parameters (Fig. 3.7).

One major issue currently with the publicly available reflection models is that they describe the illumination of an otherwise cold slab of gas. This assumption is acceptable for use in fitting the spectra of AGN, where the disc is relatively cold. However, in the case of BHXRBs, the hotter surface layers of the disc will have a significant effect upon the reflection spectrum (Ross and Fabian, 1993, 2007). Additionally, there is the presence of the thermal disc component in the soft X-ray bandpass, which may be mistaken as reflection by the model. This problem is further compounded by better statistics at lower energies, which hence can drive the fit in this range rather than the more revealing Fe line region. I removed the latter issues by fitting only above the energy range where the disc is significant, and hence the continuum description is a much simpler absorbed power-law. The effects of the hotter disc are not so straightforward to determine. The increased ionisation has clear broadening effect on the line profile as discussed in (Ross and Fabian, 2007); however, it should be fairly consistent between observations due to the small range in hardness in Fig. 3.3, which indicates no significant increase in the soft thermal emission. Therefore, the effect of ionisation not due to irradiation should be roughly constant between each observation.

It is, however, significant and likely to be treated in two ways by the reflection model. Either the ionisation parameter or the relativistic effects will be increased to reproduce the additional broadening in the line profile. If the outcome is the latter this should yield inner disc radii values closer to the BH than would be apparent for a self-consistently modelled BHXRB. Therefore, in such a case, I would expect the disc to be more truncated than that estimated in this investigation.

The reflection models used in this Chapter are angle-averaged, thus lacking angle-dependance, which is known to affect the observed spectrum (Magdziarz and Zdziarski, 1995; Matt *et al.*, 1996). Firstly, the observed reflection spectrum will change for different values of disc inclination, since an observer viewing at high inclination (grazing the disc) will effectively observe a larger optical depth. This is because photons emitted at a given depth in the disc atmosphere will see a larger effective depth in order to escape to the observer. Secondly, blurring the reflection spectrum with a relativistic convolution model fails to include the correct relativistic effect on each emitted photon, which have their own angle of emission. Photons emitted from a range of angles will contribute to the spectrum observed at a specific inclination angle. The effect of angle-dependance is reduced at high levels of ξ observed from BHXRBs (García *et al.*, 2014), and since the accretion disc is substantially truncated in these observations, the effect of the relativistic model

should be reduced. Nevertheless, these are two effects not accounted for in this study, and I refer the reader to the work of García *et al.* (2014), who investigate angle-dependance in the latest version of XILLVER.

Although distinct evolution of the inner disc in the hard state of GX 339−4 has been uncovered, this investigation is still limited by the small sampling of other BH sources. Although many sources show similar behaviour (see *e.g.* Dunn *et al.* 2010), some for example do not show full state transitions (*e.g.* Swift J1753.5−0127; Soleri *et al.* 2013) and hence it may be the case that the inner disc evolves differently in the hard state of other BHs.

3.4.1 The effect of the spin parameter

Throughout this analysis I have assumed that the spin of the BH in GX 339−4 is $a = 0.9$. The spin parameter is calculated from the ISCO itself, spanning 6–1.235 $r_{\rm g}$ for the prograde range of spin ($a = 0 - 0.998$). The key assumption is that the disc is at the ISCO and in testing this assumption the inner disc and spin parameters become highly degenerate with each other. Therefore, since the aim of this investigation was to measure the inner disc radius, I fixed the value of the spin to be $a = 0.9$ to keep all the analysis consistent. As alluded to in §3.3.3.1 this is the upper limit found by Kolehmainen and Done (2010) using the continuum method. It is also close to values obtained previously by reflection fitting (Reis *et al.*, 2008; Miller *et al.*, 2008a).

However, defining a spin value has in fact very little effect upon the conclusions presented in this Chapter. For a fixed radius, increased spin will have some effect due to frame dragging, but this is quite minimal, and only observable for the very inner regions of the accretion disc (Dauser *et al.*, 2010). Since the disc is found to be largely truncated, the adopted spin value has little or no effect upon the results of this study.

3.4.2 How well constrained is the inner radius?

Much of the focus in this Chapter is on how the inner radius of the disc is evolving in the hard state. If one just examines absolute values then this would suggest that the disc is always substantially truncated. However, given how degenerate the unknown inclination parameter is with the inner radius, I cannot be sure of this, and instead concentrate more on the trend between observations. At first sight, the magnitude of the confidence limits on the inner radius would suggest that the analysis is uncertain,

perhaps even flawed, but this is simply due to the decreasing relativistic effects at large radii. For example, the fits to the Fe Kα line with RELLINE (Table 3.5) find confidence limits a factor of over 100 larger for Observation 1 than Observation 4. The fit is just as well constrained, and as well as the other parameters, it is just the smaller effect on the spectrum at large radii that drives the increasing limits.

Although the Chapter does not focus upon the absolute values of the inner radius, I am still interested in how well they represent the true value. One test of this is to calculate whether the fitted EW matches that expected for a reflecting slab truncated to the radius inferred before. A disc will subtend a solid angle of $\Omega = 2\pi(\cos\theta_{\rm in} - \cos\theta_{\rm out})$, where the respective angles are to the radii corresponding to the inner and outer radii from the centre of the disc. These are calculated as $\theta = \arctan(R/h)$, where R is the respective disc radius and h is observer's height above the disc. The observer here is the illuminating source, since we are interested in the angle the disc subtends below the source, and I use a height of $20\,r_{\rm g}$. Given that $\mathrm{R_{out}} \gg h$ I can assume $\theta_{\rm out} = 90$. I estimated the expected EW values from García *et al.* (2013) using the values for the ionisation parameter I fitted using XILLVER (Table 3.5). Assuming isotropic emission, the ratio of the EW calculated with RELLINE to the expected value should be equivalent to $\Omega/2\pi$.

I found a reasonable agreement in each case, with the EW ratio factors of 1.17, 0.94, 0.82 and 1.14 larger than the solid angle for Observations 1 to 4 respectively. Each observation is consistent with the EW ratio within the limits on the inner radius parameter. Although this is a good indication that the absolute value of the inner radius is reasonable, some uncertainties still remain. For example, the expected EW is calculated from the whole Fe K region, where Fe Kβ emission could contribute up to $\sim 15\%$ of the EW depending on the ionisation stage. Also flaring of the outer disc is expected (see *e.g.* Corral-Santana *et al.* 2013 and references therein) which could significantly increase the EW observed. The EW is also angle dependent, since at larger inclination emission from a given surface layer has to travel through more of the disc atmosphere to escape (see e.g Matt *et al.* 1996).

3.5 Conclusions

I have systematically analysed how the inner accretion disc evolves in the canonical hard state of GX 339−4 using the Fe line region. These results have shown that the inner accretion disc moves closer to the black hole at higher luminosities, consistent with the broader profile found in the spectra. The poor fit to each spectrum using

a single line model points to a reflection spectrum not dominated by relativistic effects, with significant broadening also arising as a result of ionisation. When this is taken into account I found an improved fit and much larger inner radii, with the two lowest luminosity observations consistent with no relativistic broadening at the 90 % confidence level. However, the absolute values found by modelling reflection features can be affected by degeneracies between parameters, and this is the motivation for a systematic analysis. Therefore, the key result is the strong trend to smaller inner radii at larger luminosities, which should be largely independent of such effects. Extensive analysis of potential parameter and bandpass degeneracies confirm this trend.

The trend uncovered thus fully supports the truncated disc model of the hard state. Furthermore, when extending the analysis to the hard-intermediate state even smaller inner radii are found, such that the disc is consistent with being truncated throughout the entire hard state. It has also been suggested that the break frequency found in the power density spectra of the hard state corresponds to the inner radius of the disc (Gilfanov *et al.*, 1999). Upon comparing this to the results from spectral fitting, a remarkably similar trend is uncovered. Together these two independent conclusions provide very strong evidence in favour of disc truncation in the hard state.

This result implies that the current sample of spin estimates in the hard state are inaccurate. Therefore, any distinct conclusions drawn from these estimates, such as the spin-powering of relativistic jets, may well be biased.

4

Revealing accretion on to black holes: X-ray reflection throughout three outbursts of GX 339−4

In this Chapter I present results from an investigation into how accretion evolves in the outbursts of black hole X-ray binaries. The reflection spectrum describes the reprocessing of coronal photons in the surface layers of the accretion disc, and can hence be used to map the geometry of the disc and corona. I analyse over 500 *Rossi Timing X-ray Explorer* observations covering three full outbursts of the black hole binary GX 339−4, to which I applied a self-consistent treatment of X-ray reflection. Using the coincident evolution of the power-law and reflection components, I show that their non-linear evolution represents changes in the accretion geometry. I reveal that the reflection fraction, the ratio of reflection to power-law flux, is weak but increases as the low/hard state rises. In contrast the reflection dominates the power-law throughout most of the soft state, with increasing supremacy as the source decays. I discuss potential dynamics driving this, favouring inner disc truncation and decreasing coronal height for the hard and soft states respectively. Furthermore, I show that the evolution of the ionisation parameter, power-law slope and high-energy cut-off also agree with this interpretation.

4.1 Introduction

Understanding the dynamics behind black hole state transitions, and the changes they reflect in outbursts has become a long-standing problem. The interplay between the respective soft thermal and hard Comptonised emission ultimately defines the two distinct hard and soft states. However, defining the morphology leading to state transitions, and separating the two states, has proven to be difficult, not least due to an insufficient physical understanding of the corona. Interpreting the role of the jet has also proven to be difficult, even though the X-ray and radio emission correlate well (Corbel *et al.*, 2003; Gallo *et al.*, 2003; Corbel *et al.*, 2013a). Furthermore, the base of the jet has been proposed as a source of hard X-rays (e.g. Beloborodov 1999; Markoff *et al.* 2005), heightening the need to understand the connection between the two. As it is inherently dependent upon the geometry of the corona producing the photons and the disc intercepting them, the reflection spectrum presents the opportunity to infer changes in the two components in comparison to their own specific emission.

GX 339−4 is one of the most active transient systems, exhibiting numerous outbursts since its discovery (Markert *et al.*, 1973), including four complete cycles (with state-changes) in the past twelve years. As a result, GX 339−4 is one of the most studied transient systems, and over the lifetime of *RXTE* (1995–2012) an extensive archive of data has been amassed, allowing an unparalleled timeline to investigate source variability with the same mission. Restricting to periods where both the Proportional Counter Array (PCA; Jahoda *et al.* 2006) and High Energy X-ray Timing Experiment (HEXTE; Rothschild *et al.* 1998) instruments were active this presents three fully sampled outbursts to analyse. In addition, GX 339−4 is the best monitored BHXRB in the radio band, allowing a unique insight into the outburst nature of transient systems. In this Chapter I examine how the X-ray reflection evolves throughout these three outbursts, representing the largest study of its kind to date.

4.2 Observations and Data Reduction

I performed spectral analysis using data from the PCA and the HEXTE onboard *RXTE*. The data were reduced by Dr. Mickaël Coriat using the same procedure described in §2.2.2.2. The data for the variability analysis (i.e. the RMS-Intensity diagrams) were prepared by Dr. Teodoro Munõz-Darias following the method described in §3.2.3.

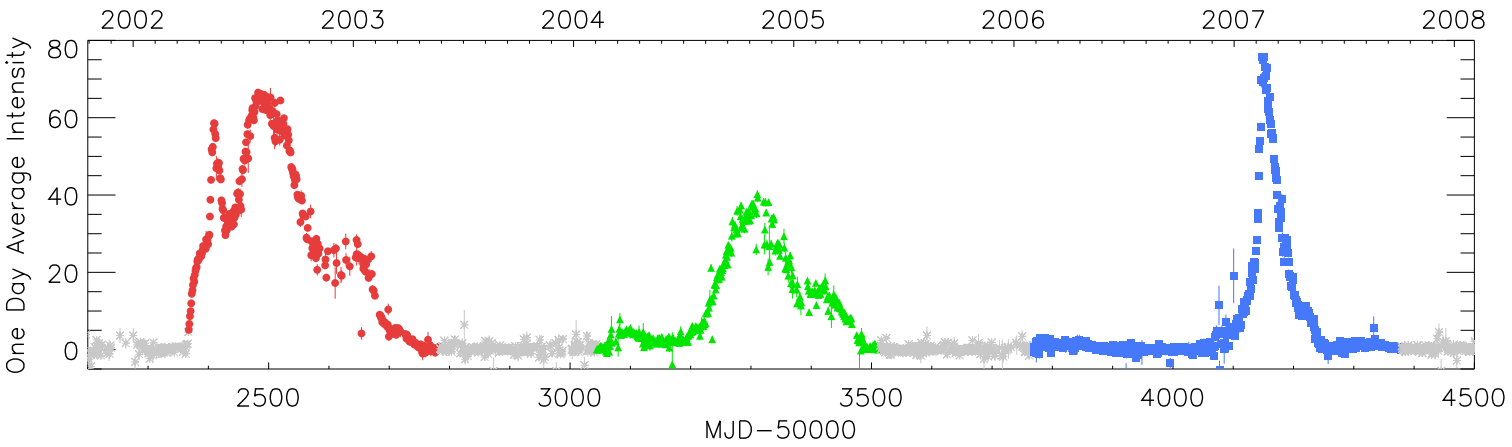

Figure 4.1: The *RXTE* all-sky monitor light-curve of GX 339−4 covering the three outbursts analysed in this Chapter. Red (circles), green (triangles) and blue (squares) correspond to the 2002, 2004 and 2007 outbursts respectively.

Outburst	Start (MJD)	End (MJD)	Total Observations (Exposure)
2002	52367	52784	133 (300 ks)
2004	53044	53514	202 (465 ks)
2007	53769	54379	193 (357 ks)
Total			528 (1122 ks)

Table 4.1: The dates and number of observations used in this study after the selection criteria outlined in §4.3.2 were applied. The threshold for a dataset to be analysed is defined in §4.3.1, such that observations at low flux (*i.e.* the periods of quiescence) and of poor quality were ignored. Also listed is the respective amount of observations and the subsequent total exposure time per outburst.

4.3 Fitting method

There are two significant reasons I used archival *RXTE* observations for this study. Firstly, the PCA (3–50 keV) and HEXTE (25–200 keV) instruments provide an outstanding spectral bandpass. Although the Fe K line is the prominent feature of X-ray reflection, it is ultimately just a fraction of the overall signal. When looking for subtle effects, such as those due to strong gravity, the line profile is a very revealing signature. However, the poor spectral resolution of the PCA (~ 1 keV at 6 keV) renders it insufficient to attempt precise constraints on parameters such as black hole spin. Instead, the large bandpass and effective area allows me to study a much larger fraction of the reflection spectrum, including important signatures such as the Compton hump and Fe edge, which characterise emission over a much larger range. As a result of this, *RXTE* is much more sensitive to how the reflection component is evolving than high-resolution missions such as *XMM-Newton*, which is restricted to the 0.3–10 keV band.

This leads on to the second significant rationale, which is the unprecedented number of observations that *RXTE* offers. In Chapter 3, which was a study of the hard state of GX 339−4 limited to high-resolution *XMM-Newton* and *Suzaku* spectra, I was restricted to just four observations. In this Chapter, however, the sample of the hard state amounts to nearly 350 observations. In total this investigation makes use of more than 500 observations, totalling over 1.1 Ms of PCA exposure time, allowing one of the most detailed investigations to date of how the reflection spectrum is evolving throughout an outburst (Table 4.1 and Figure 4.2). In particular, such high cadence enables a scrupulous analysis of state transitions, which are typically completed within one week.

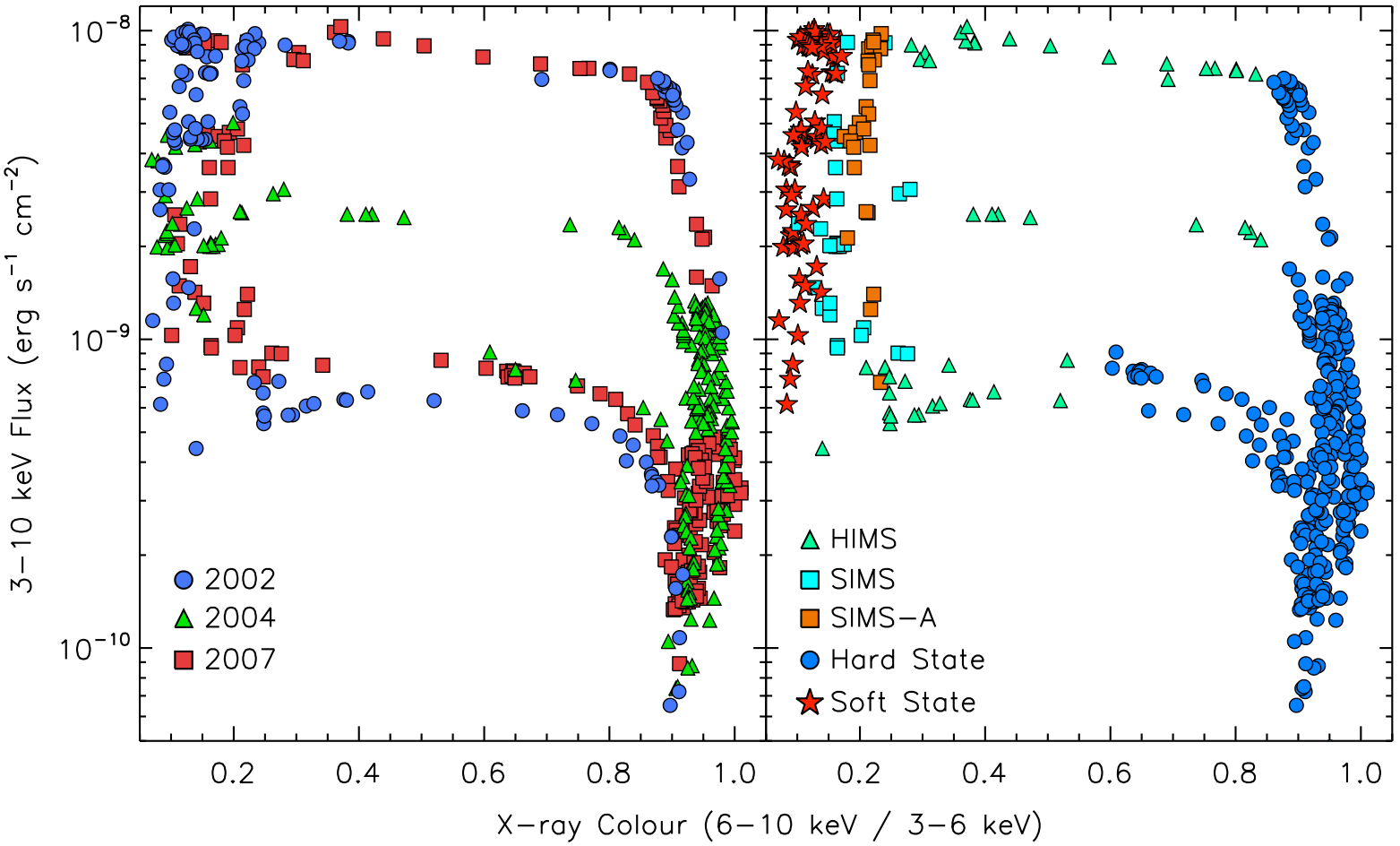

Figure 4.2: Hardness-intensity diagrams of all the observations analysed in this Chapter. Left and right figures correspond to symbols determined by outburst (Table 4.1) or spectral state (§4.3.3).

4.3.1 The adopted model

Many attempts have been made to quantify how X-ray reflection evolves in BHXRBs, but often they have employed phenomenological models focusing upon the Fe K region. Dunn *et al.* (2008) fitted the Fe Kα emission with a single GAUSSIAN line fixed at 6.4 keV, while Rossi *et al.* (2005) applied relativistic broadened emission (LAOR; Laor 1991) with a smeared edge (SMEDGE; Ebisawa *et al.* 1994). Both offer a useful diagnostic of the reflection; however, they only account for a small fraction of the full reflection signal. Furthermore, while the latter may offer a more physical interpretation of the Fe Kα line, the two components are still not physically linked. Ultimately, to fully understand how the reflection component is evolving one must apply a model where all the signatures are physically linked and accounted for. Motivated by this, Reis *et al.* (2013a) recently applied the blurred reflection model KDBLUR∗REFLIONX (Laor, 1991; Ross and Fabian, 2005) to an outburst of XTE J1650−500. Although this presented a significant improvement to previous works, it only focuses upon one outburst of one source. Here I applied an angle-dependent version of the reflection model XILLVER (García and Kallman, 2010; García *et al.*, 2011, 2013) to a much larger sample (Table 4.1). This model offers a significant improvement in the treatment of atomic processes over the more widely used REFLIONX, and in addition includes a larger grid for the photon index and ionisation parameters (see García *et al.* 2013 for a comparison). It should be noted that REFLIONX represents an angle-averaged solution, hence neglecting the important effect of inclination in the observed reflection spectrum (see e.g. Magdziarz and Zdziarski, 1995; Matt *et al.*, 1996; García *et al.*, 2014).

I accounted for interstellar absorption using the model PHABS with the N_H fixed at 0.5×10^{22} cm^{-2}, given that the hydrogen column density towards GX 339−4 is well resolved to be within the range $(0.4–0.6)\times10^{22}$ cm^{-2} (Kong *et al.*, 2000). Since the low-energy cut-off of the PCA is at ~ 3 keV, the ability to constrain the column freely was severely reduced, and I also note that the effect of this moderate column above 3 keV is small.

The remaining continuum was characterised by a combination of a multi-colour blackbody (DISKBB; Mitsuda *et al.* 1984) and Comptonised seed photons (CUTOFFPL). Recently it has been shown by Muñoz-Darias *et al.* (2013) that relativistic effects can strongly affect how the thermal emission is interpreted. However, such impact is fairly weak at the low-moderate inclination GX 339−4 is expected to have (Muñoz-Darias *et al.* 2013 classify GX 339−4 as a 'low inclination' source, meaning $i < 60^{\circ}$), hence DISKBB should describe the thermal accretion disc emission suf-

ficiently well. I modelled the Comptonised emission as a simple power-law with an exponential cut-off. While more physical Comptonisation models exist, they ultimately bring with them further complexity in fitting the data at hand, and is beyond the scope of this study, which is instead focused on reflection.

Another important consideration is the consistency between the fitted continuum and the spectral energy distribution assumed in the reflection model. The illuminating spectrum used in XILLVER assumes a power-law with a high-energy cut-off at 300 keV, making CUTOFFPL the best Comptonisation model to maintain consistency and allowing an accurate determination of relative flux levels. When a smaller cut-off was required I switched to an angular solution of XILLVER including a variable cut-off for the illuminating spectrum, linking the cut-off in the Comptonisation and reflection models. XILLVER also includes a low-energy cut-off at 0.1 keV to prevent the input spectrum being unphysically over-populated with low-energy photons. It should be noted, though, that the reflection spectrum will also be influenced by photons emitted in the disc (Ross and Fabian, 1993, 2007), and this is not currently accounted for by XILLVER, nor is it in any other publicly available reflection model. The disc photons will ionise the lighter elements, which will increase the flux of the reflection spectrum below $\sim$ 10 keV. The spectrum will typically take the form of a larger value of ξ, but see Ross and Fabian (2007) for a detailed analysis of the effect of the accretion disc photons. Finally, I also applied the convolution model RELCONV (Dauser *et al.*, 2010) to account for any relativistic effects. Thus the base model applied to each observation is:

PHABS(DISKBB + CUTOFFPL + RELCONV∗XILLVER)

4.3.2 The fitting procedure

By definition, transient BHXRBs spend the majority of their lifetime in a quiescent state. GX 339−4 is somewhat of an exception to this, being one of the most active of all transient systems, exhibiting four complete outbursts in the past twelve years. Nevertheless, observations during periods of inactivity, or not reaching sufficient statistics through low count rates and short exposures, will require removal. For an observation to be considered I required a PCA pointing with at least 1000 background subtracted counts. I ignore all data below 3 keV (channels ≤ 4) and above 50 keV (channels ≥ 83); however, the regions ≥ 20 keV and ≥ 35 keV must have a minimum of 100 and 50 background subtracted counts respectively to be included. Furthermore, these must amount to at least 10% of the total counts registered in that region.

Model	Parameter	Value	Min	Max
PHABS	N_H (10^{22})	0.5		
DISKBB	T_{in}	0.5	0.1	2
	N_D	1000	0	1e+10
CUTOFFPL	Γ	2	1.2	3.4
	E_c	50	10	300
RELCONV	θ (°)	45		
	r_{in} (r_g)	10	6	1000
	r_{out} (r_g)	1000		
	q	3		
	a	0		
XILLVER	$\log(\xi)$	2.5	1	4.5
	θ (°)	45		

Table 4.2: A list of input parameter values and hard limits for the base model applied to each dataset in this study. Parameters listed without limits indicate that it was fixed at that stated value. The input photon index in the XILLVER model was linked to that of CUTOFFPL. I also assumed solar abundances and a single power-law emissivity index (R^{-q}) for the reflection.

Signatures of the reflection spectrum at hard X-ray energies, such as the Compton hump, offer a large signal in addition to the Fe K line. Additionally, the reflection remains strong at high energies allowing greater constraint. Hence, this underlines why I took such an approach to the upper-energy threshold of the PCA, and similar criteria were therefore applied to the HEXTE to ensure adequate data quality. I required that the combined HEXTE A and B cluster units, if both were available (see §4.2), have a minimum of 1000 background subtracted counts. If this was not the case then the observation was ignored regardless of the merit of the PCA. I fixed the lower energy limit to be 25 keV and allowed the upper bound to be 200 keV; however, this was truncated to 100 keV should there be less than 100 background subtracted counts above this threshold.

In the hard, and some hard-intermediate states, fitting the disc was problematic due to the low-energy cut-off of the PCA. Thermal emission from the disc in the hard state has been uncovered in many sources using instruments extending to softer energies (<1 keV; see e.g. Di Salvo *et al.* 2001; McClintock *et al.* 2001; Kolehmainen *et al.* 2014); however, the signal above 3 keV was not sufficient to constrain the DISKBB parameters. For this reason, if T_{in}<0.1 keV then DISKBB was removed to ensure the analysis is reliable. In such cases the model is likely to be fitting some slight curvature in the Comptonised continuum or having a negligible

effect. I also removed discs with $T_{in}>2$ keV since temperatures are not expected to reach such levels, especially for a low inclination source (see e.g. Dunn *et al.* 2011; Muñoz-Darias *et al.* 2013), and hence suggests an erroneous fit. Additionally, the normalisation value must exceed 50 to flag any severe degeneracy with the disc temperature, and should it be below this value then the disc model was removed. I note that normalisation is of the order 10^3 in the soft state, where the disc is expected to be at the innermost stable circular orbit (ISCO), and should hence represent the lowest values in the outburst. These criteria did not affect the soft and soft-intermediate state observations, all of which retain the disc model within these criteria.

One of the free parameters of the reflection model XILLVER is the photon index of the source illuminating the ionised slab (i.e. the accretion disc), of which the tabulated range is 1.2–3.4. I linked this parameter to the CUTOFFPL photon index to keep the two components self-consistent using the tabulated range as the hard limits. Previous studies of BHXRBs suggest this range should be sufficient; however, it is another motivation for me to use XILLVER instead of REFLIONX, which offers a smaller grid of 1.4–3.3. The high energy cut-off (E_c) was allowed to be free within the range 10 to 300 keV; however, if the parameter reached <15 keV or >250 keV, the cut-off was fixed at 300 keV for the remainder of the analysis. This prevents any erroneous fits and maintains consistency with the assumed illuminating spectrum in the standard version of XILLVER. Only in the bright phase of the hard state was a smaller high energy cut-off required, hence during this period I switched to a larger grid of XILLVER which includes the high energy cut-off of the illuminating spectrum as a fitted parameter. In this case the parameter was linked between the CUTOFFPL and XILLVER models to maintain consistency. I note that the values and evolution of the high energy cut-off are consistent with that found by Motta et al. (2009; see Figure 4.6 and §4.4.1 later in this Chapter).

The other key parameters in XILLVER are the ionisation parameter, ξ (see §1.4.1), the iron abundance (which I assumed to be solar[1]), and the inclination angle of the source. The ionisation parameter was fitted within the range log(1.0–4.5) and a fixed inclination of 45° was applied, which is within the constraints discussed in §1.6. The value of 45° is also consistent with the value resolved using high-resolution data in Chapter 3.

The relativistic effects were modelled using RELCONV, for which the emissivity

[1]I took this approach since studies of chemical abundances in LMXBs have found metallicity values consistent with solar (see e.g. González Hernández *et al.* 2011). In addition, with *RXTE* the Fe abundance will be difficult to constrain, thus fixing it is necessary to ensure it does not create any degeneracy in the fits. I note as well that the Fe abundance should not vary over the timeline of this study, therefore fixing the value ensures consistency in the analysis.

index q, defined as R^{-q} where R is the disc radius, was fixed to be 3. While the spectral resolution of the PCA ($\sim$ 1 keV at 6 keV) allows moderately broad lines to be detected, the more subtle effects of the emissivity profile cannot be resolved, thus the Newtonian value of 3 is a reasonable assumption for this study. I did, however, allow the inner radius to be fitted freely from the ISCO ($6\,r_g$) up to the largest tabulated value of $1000\,r_g$. The outer radius of the disc was fixed to be $1000\,r_g$ and the black hole was assumed to have zero spin. The effect of the latter is rather trivial given the resolution of the PCA and is nevertheless not a significant concern given that the relativistic effects are not the main focus of this Chapter (see instead Chapters 3 and 5). Finally, the inclination was fixed at 45° to be consistent with the reflection model.

Comparing relative flux levels can be hampered by the chosen energy band, hence all fluxes were extrapolated using CFLUX and fitted in the 0.1–1000 keV band unless otherwise stated. As an example, Comptonised photons reprocessed in the cool disc may be down-scattered to energies below the *RXTE* bandpass, hence extrapolating the fit ensures that the truest extent of the spectrum is being measured. The lower limit was chosen to ensure that there is not an unphysical over-population of photons in the cut-off power-law model, which is particularly a problem when the photon index is large ($\Gamma > 2$). The illuminating spectrum in the reflection model also assumes a low-energy cut-off of 0.1 keV to tackle this problem, hence I was therefore keeping the two models consistent by imposing this limit.

To deal with such a vast dataset I fit each observation through an automated routine, therefore Table 4.2 lists the input parameter values applied to the adopted model. The XSPEC version 12.8.0 was used, and all quoted errors are at the 90% confidence level unless otherwise stated. Throughout the study I applied fiducial values of $10\,M_\odot$ and 8 kpc for the black hole mass and distance to GX 339−4 respectively.

4.3.3 Defining spectral states

In order to separate each observation into spectral states I used a combination of timing and spectral characteristics. While the hard and soft states are easily discernible via their spectra in the PCA bandpass, the intermediate periods are qualitatively alike. Muñoz-Darias *et al.* (2011) studied the relation between the RMS amplitude of the variability and flux (Figure 4.3), uncovering marked changes in the transition between states in the three outbursts of GX 339−4 used in this study. The rising hard state follows a distinctive 'hard track' of increasing RMS and flux, with a

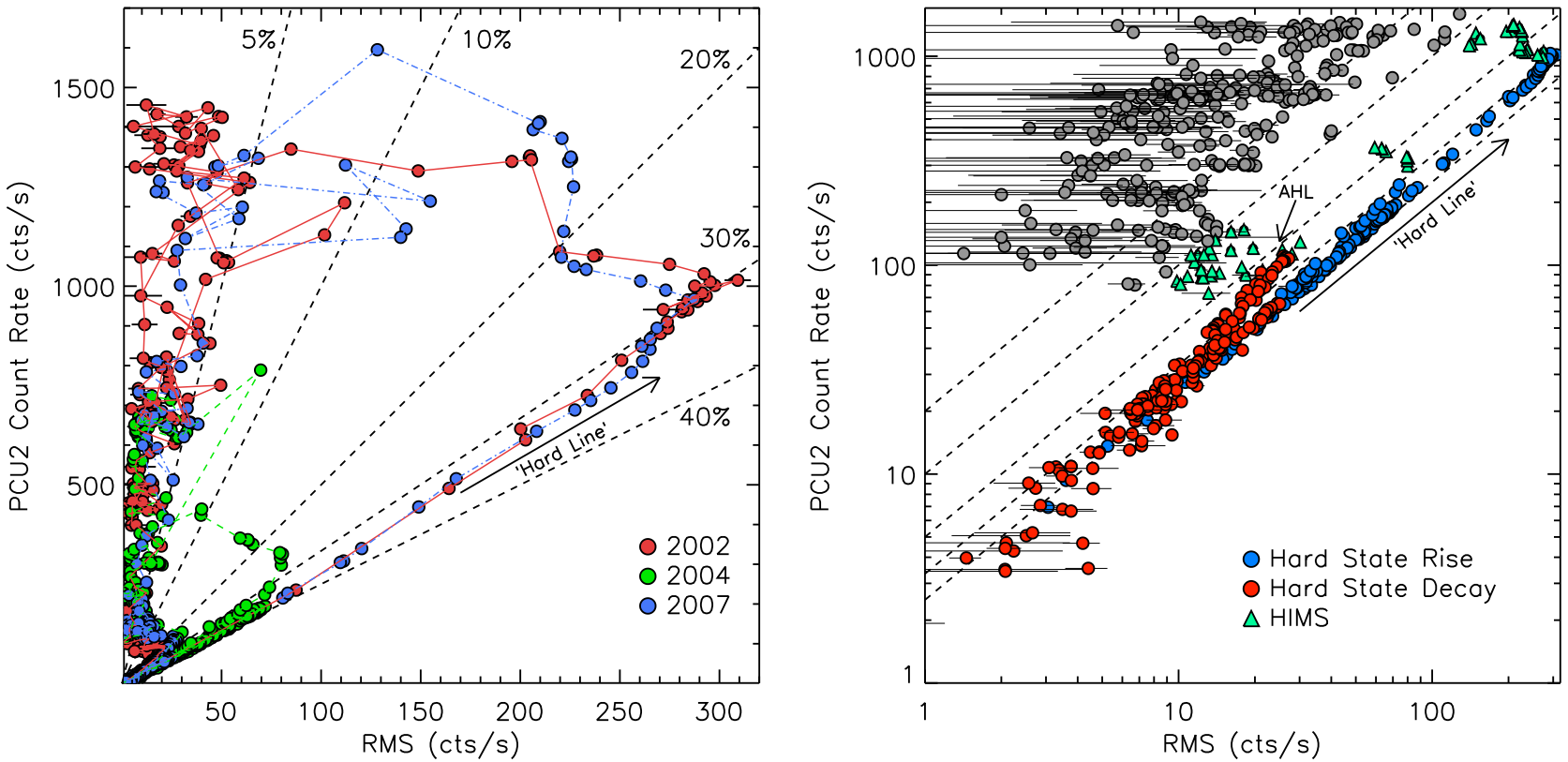

Figure 4.3: RMS-intensity diagrams of the three outbursts of GX 339−4 featured in this study. The dotted lines represent fractional RMS levels. Left: Symbols are colour-coded by outburst and plotted linear-linear to view the entire outburst. Right: The same data with a log-log scale to focus upon the rise (blue) and decay (red) of the hard state. The 'adjacent hard line' (AHL) signifies the return to the hard state, and the SIMS(-A) and soft state observations are plotted as grey points for clarity.

fractional RMS of 30–40 %. Transition into the HIMS occurs as the RMS lessens whilst the flux continues to rise. A further significant decrease in RMS marks the SIMS, which I defined as the region with $<$10 % fractional RMS.

The soft-state is characterised again by a sudden decrease in RMS, and defined here by a fractional RMS of $<$5 %. However, there exists a group of harder observations (X-ray colour $>$0.175; Figure 4.4) at low variability. I note as well that these points lie typically at a slightly higher fractional RMS than the least variable soft-state points. The state classification for these observations is not straightforward since they share properties associated to both SIMS and soft state (see e.g. Belloni *et al.*, 2005, 2011). Nevertheless, I define these points as SIMS-A since many show type-A quasi-periodic oscillations (QPOs), which is in contrast to the normal SIMS ($5 < \mathrm{RMS} < 10$) where type-B oscillations are observed (Motta *et al.*, 2011). Interestingly, the SIMS-A lie off the standard luminosity-temperature relation established by the soft state (§4.4.4). I do note, however, that the 5 % line separating the soft and SIMS should be taken with caution since, for example, fast transitions occurs at this stage of the outburst, leading to hybrid observations (Muñoz-Darias *et al.*, 2011). To this end, some of the SIMS points may be part of the soft state, which seems apparent in Fig. 4.4 (see also §4.5.2), but I continued with the 5% RMS line in order to have a simple and definitive criteria to separate the states. To determine the HIMS to hard state transition I used the 'adjacent hard line' (AHL) described in Muñoz-Darias *et al.* (2011), whereby the decay phase of the hard state displays a clear track in the RMS-intensity diagram. This is indicated by the red circles in the lower plot of Figure 4.3. The transition is not so clear if one attempts to determine it by X-ray colour (Figure 4.2), and thus demonstrates the importance of timing characteristics in determining the state of the system.

4.4 Analysis and results

4.4.1 The Comptonised emission

In Figure 4.5 I display how the photon index Γ evolves with the total unabsorbed luminosity. The shape is remarkably similar to the HID (Figure 4.2), and indicates well how the hardness of the X-ray spectrum is not solely due to the influence of the thermal emission from the accretion disc. The blue points in Figure 4.5a mark the hard state, whereby Γ mainly lies in a narrow range of 1.5–1.7, and appears to remain rather constant despite the hard state spanning over two orders of magnitude in luminosity. However, Figure 4.5b separates the periods of rise (blue) and decay

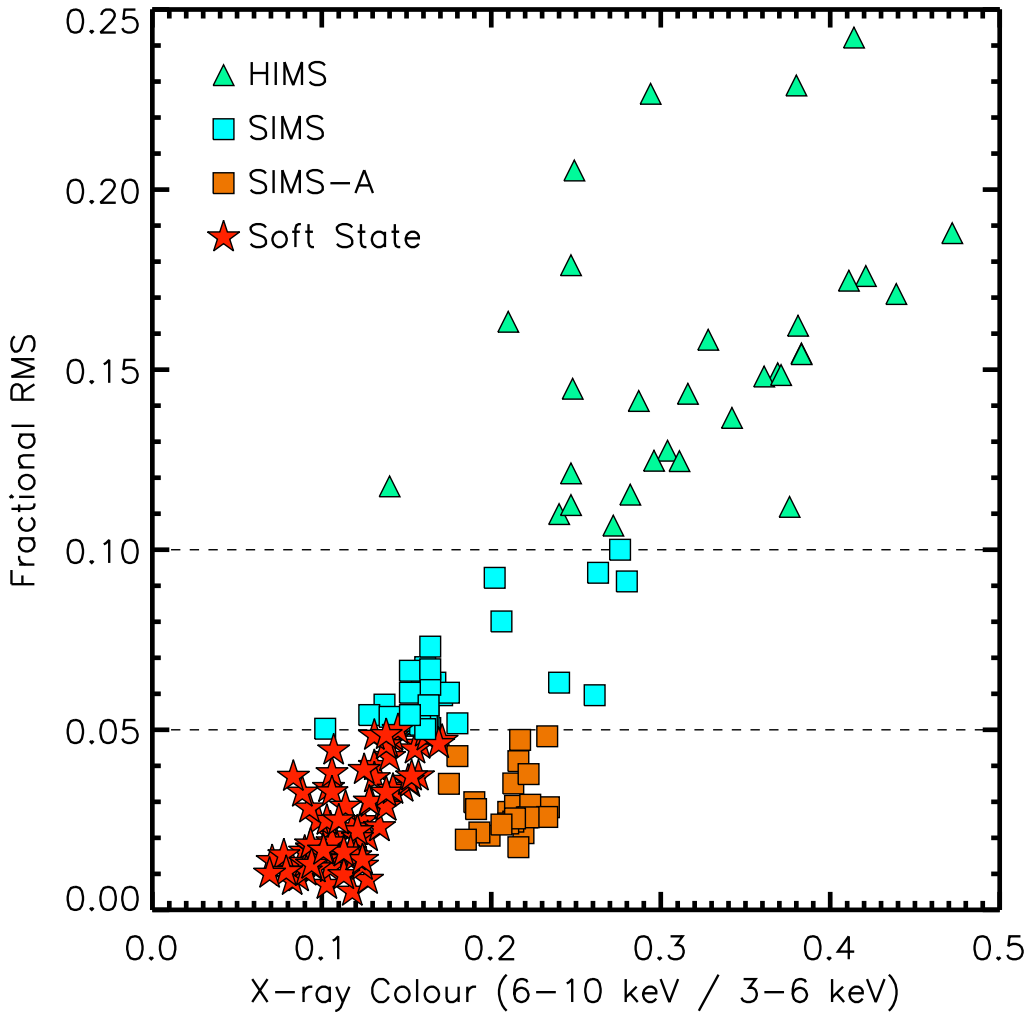

Figure 4.4: Fractional RMS versus spectral hardness displaying how the intermediate and soft spectral states were determined (§4.3.3). The SIMS-A are a cluster of points with low variability (fractional RMS <5 %) and a relatively high spectral hardness (>0.175 %), which I propose as a distinct spectral state (see §4.3.3 and §4.5.2). The hard state was determined by the RMS-intensity relation (Figure 4.3).

(red), and displays quite clearly that above $L_X \sim 10^{37.5}$ Γ tends to become softer as the source rises up the hard track, consistent with an increase in seed photons to cool the corona (see Done *et al.* 2007 and references therein). Furthermore, as the source reaches the hard state in decay the photon index is clearly softer than the rise at that luminosity, appearing to retain a softer slope towards quiescence (although see also Stiele *et al.* 2011). At the lowest luminosities the rise also appears to be softer (see also Sobolewska *et al.* 2011); however, as a result of the data selection criteria, only two points lie at $L_X < 10^{36.5}$ limiting any strong conclusions that can be made.

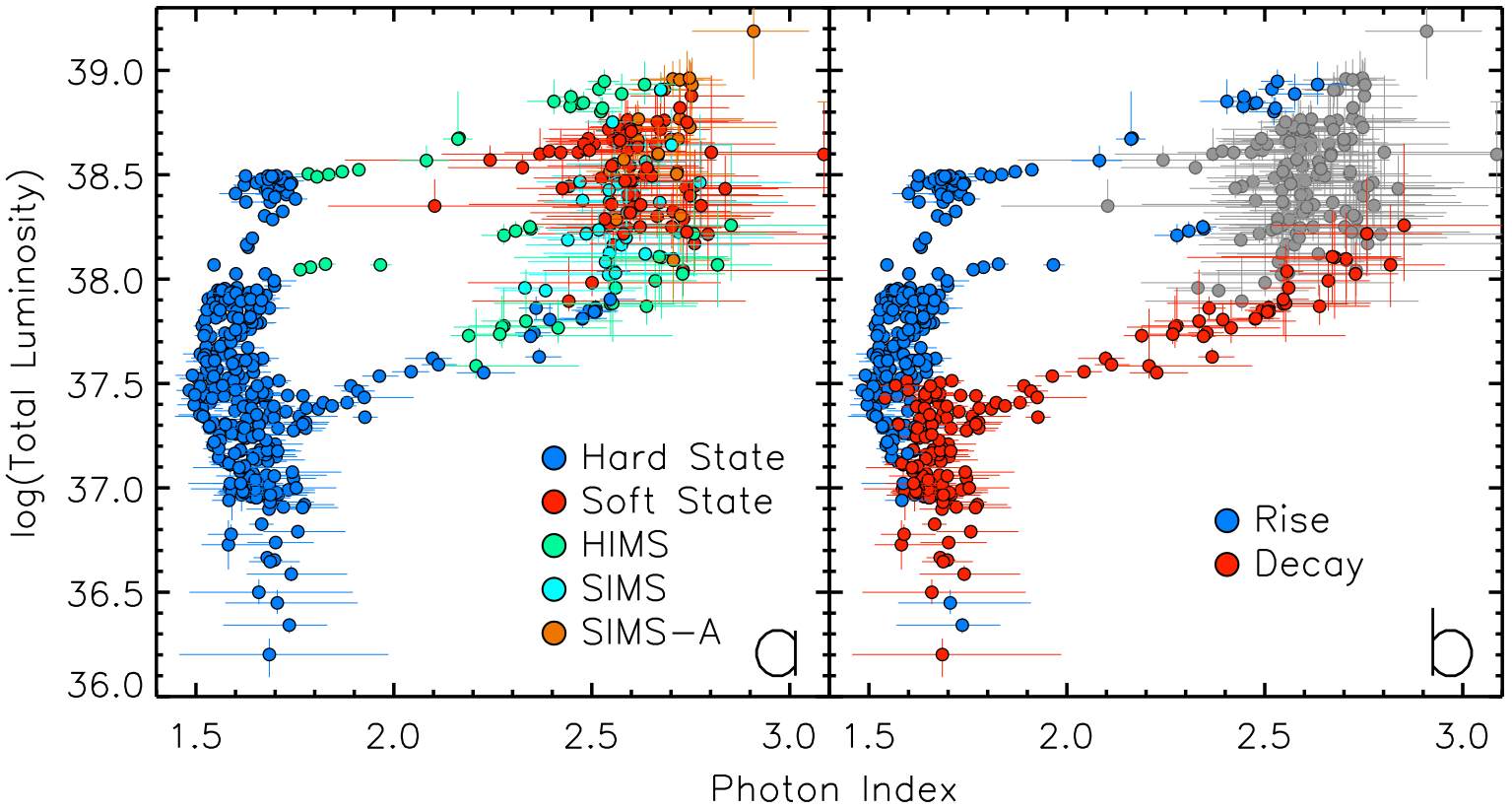

Figure 4.5: The total source luminosity plotted against the power-law photon index Γ. Left: Points coloured by their respective state. Right: The same diagram, however, the soft state, SIMS and SIMS-A observations are now grey, with the HIMS and hard state separated according to the rise or decay phase of the outburst. Observations are plotted randomly to avoid any visual bias. The y-axis is plotted in units of erg s^{-1}.

During the state transition the photon index undergoes very distinct softening, eventually reaching $\Gamma \sim 2.5$. In fact, the bulk of the evolution appears to take place in the HIMS, rather than the SIMS, which itself is consistent with the values recorded in the soft state. The soft state shows some scatter (2.4–2.9), but is ultimately dominated by large confidence intervals due to the diminished signal in the hard band. The SIMS-A are also typically steeper than the SIMS (see also Table 4.4). The decay phase (Figure 4.5b) displays clear hardening as the source makes its way through the soft-hard transition. In Figure 4.5 I plot Γ against the total luminosity calculated between 0.1 and 1000 keV, which accounts for the non-negligible disc flux below 3 keV, therefore displaying the source decay through the transition not so apparent in the 3–10 keV HID (Figure 4.2). This then serves to exhibit clearly how the source hardens monotonically with luminosity towards the hard state.

Throughout this investigation, I model the Comptonised emission with a cut-off power-law fixed at 300 keV, in order to remain consistent with the assumed illuminating spectrum in the reflection model (García *et al.*, 2013). However, as part of my routine, I initially allowed the high energy cut-off to be a free parameter as it has been shown to be significantly lower in the brighter phases of the hard state and subsequent transition (Motta *et al.*, 2009). I allowed the cut-off to be free within the range 10 to 300 keV; however, should it converge on a value lower than 15 keV, or higher than 250 keV, respectively, I deemed the fit to be in error and fix the parameter to be 300 keV. I took this action because below 15 keV the cut-off tended to be fitting the curvature of the disc component, rather than the power-law. Above 250 keV the effect of the cut-off becomes insignificant due to the upper limit on the bandpass of the HEXTE instrument (100 or 200 keV; §4.3.2).

In Figure 4.6 I plot the time-evolution of the high energy cut-off in the 2002 and 2007 outbursts. No cut-off was resolved in any of the 2004 observations; however, the transition luminosity in this outburst was lower than any of the 2002 and 2007 observations which did. Time-zero in Figure 4.6 marks the first observation where the cut-off was determined freely and displays a gradual decrease in energy as the source continues its rise through the hard state. All observations intermediate to the respective first and last resolved observation in Figure 4.6 were able to fit the parameter freely. Furthermore, the final three observations in each outburst took place in the HIMS, confirming this trend continues into the state transition. The high energy cut-off is thought to represent the temperature of the electrons in the corona, hence meaning the power-law emission symbolises thermal Comptonisation. The softening of the photon index and decreasing high energy cut-off are both consistent with increasing amounts of seed photons cooling the corona.

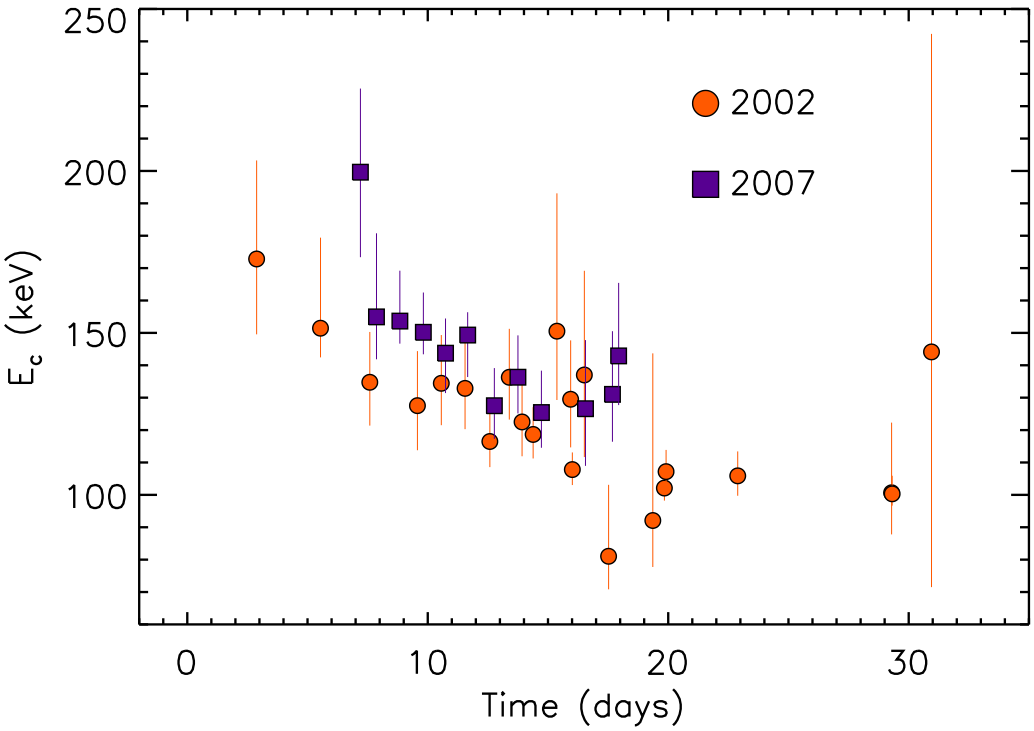

Figure 4.6: Evolution of the high energy cut-off with time. Zero marks the first observation where the cut-off was detected (MJD 52372 and 54122 for the 2002 and 2007 outbursts respectively). No cut-off was resolved in the 2004 outburst observations.

The trend I have found is very consistent with that found by Motta *et al.* (2009) using the same datasets; however, they resolve the cut-off over a longer period than us all the way into the soft state. In this study I am more focused on the reflection, hence to maintain a reasonable timescale for the fitting routine I did not apply such stringent and detailed criteria for detecting the cut-off, hence I refer the interested reader to the work of Motta *et al.* (2009) for a more in depth study of the cut-off.

4.4.2 The reflection fraction (*RF*)

The illumination of the disc by Compton up-scattered photons gives rise to the reflection spectrum, thus one would expect the two components to follow a relatively linear relationship. As an example, increasing the total of Comptonised photons by a factor of two should lead to the same doubling of the power-law flux we observe, and that irradiates the disc, assuming the geometry remains constant. Therefore, in such a case the reflected emission will double as well. Ultimately the situation is not that simple as the surface layers of the disc will also respond to the change, for example by becoming more ionised, which may in turn affect the albedo (but see

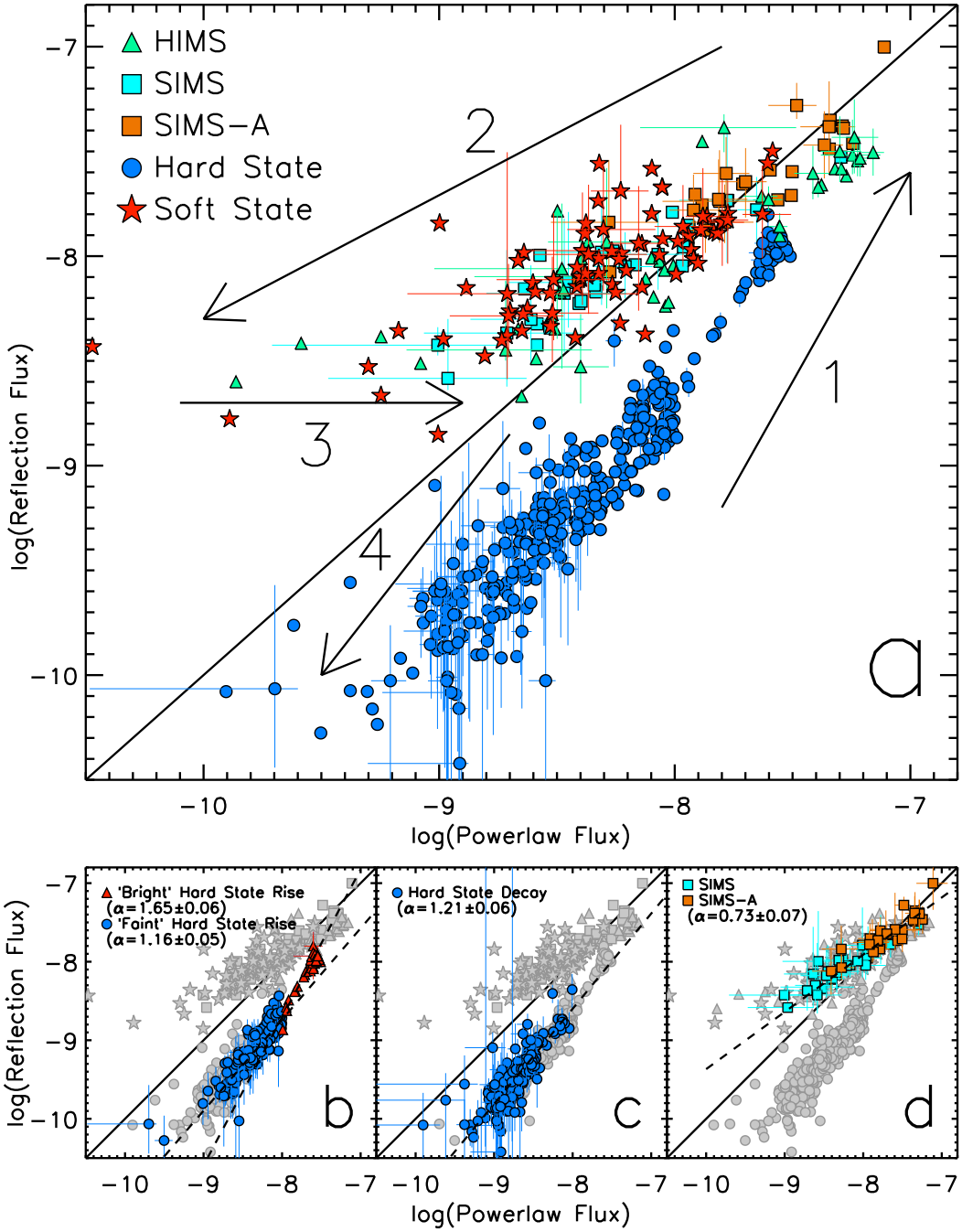

Figure 4.7: This figure displays how the power-law and reflection components evolve in outburst via their respective fluxes. Both scales are identical and the solid line indicates one-to-one quantities. Top: Numbered arrows illustrate how the source progresses throughout the plot in outburst. For clarity I only plot confidence limits for the 2007 outburst in this figure. Bottom: These plots focus on specific states of the outburst with dotted lines representing the best-fit to the highlighted observations, such that $\log_{10} S_{\rm PL} = \alpha \log_{10} S_{\rm Ref} + c$. Left: The rising phase of the hard state, separated into observations with a power-law flux less than (blue circles) or greater than (red triangles) 10^{-8} erg s^{-1}cm^{-2} respectively. Middle: The decaying phase of the outburst (towards quiescence). Right: SIMS and SIMS-A points, fitted together. Errors on the fitted slope are stated at the 1σ confidence level. Each axis is displayed in units of erg s^{-1}cm^{-2}.

§4.4.5). Nevertheless, it serves as a useful example of how the power-law and reflected emission should evolve somewhat identically *if* the accretion geometry does not vary. Alternatively, if the two components do not evolve in a one-to-one manner then there is a considerable chance that the geometry is changing. Thus, observing how these two components evolve together presents a very powerful diagnostic to reveal the underlying accretion dynamics in outburst.

I found that indeed the power-law and reflection are very well correlated, forming strong positive correlations throughout each spectral state (Table 4.3). Here I define the reflection fraction (*RF*) as the ratio of the reflection to the Comptonised flux, such that $RF = 1$ corresponds to an equal quota of both components. Figure 4.7 details the evolution of the two elements throughout the three outbursts studied, with the five principle states colour-coded. The hard state (blue circles) lies exclusively below the solid line indicating $RF = 1$, thus the hard state Comptonised flux always dominates the reflection. The fitted slope to the rising hard track is ~ 1.5; however, it indicates two distinct regions, hence I instead separate the rising hard state into observations above and below a power-law flux of 10^{-8} erg s^{-1}cm^{-2} (Figure 4.7b). At lower luminosities ('faint hard state') the slope is 1.16 ± 0.05, thus signifying a gradually increasing reflection fraction as the total source flux rises. Here the mean reflection fraction is $\sim$0.2. The track of the 'bright hard state' is much steeper (1.65 ± 0.06), marking a clear increase in the rate of increase of the reflection fraction, which itself reaches values up to 0.6. I note that whilst this is coincident with the period where the high energy cut-off was fitted below 300 keV (§4.4.1), this should not be behind this effect as the reflection spectrum includes the same cut-off in the illuminating spectrum it is calculated from. In addition, I fit the decay phase of the hard state as the source returns to quiescence (Figure 4.7c), for which the slope is consistent with the 'faint' regime of the rise (1.16 ± 0.05 vs 1.21 ± 0.06), thus suggesting that the underlying changes responsible for the evolution in the reflection fraction are consistent whether the source is at the onset or end of the outburst. To summarise, I found that there is a substantial increase in the reflection fraction as the overall source flux rises, although it remains less than one throughout the hard state.

The HIMS points (green triangles) are situated almost entirely at larger *RF* than those of the hard state. Furthermore, they are typically close to $RF = 1$. There are, however, two clusters of points from the hard-soft branch due to the lower flux of the transition in the 2004 outburst. The soft-hard branch ($S_{\rm reflection} \sim 10^{-8.5}$ erg s^{-1}cm^{-2}) leads gradually, but directly, on to the hard track, suggesting that

Spearman's Rank Correlations For Various Fitted Parameters

Parameter		Hard State		HIMS		SIMS		SIMS-A		Soft State	
1	2	ρ	p-value	ρ	p-value	ρ	p-value	ρ	p-value	ρ	p-value
$S_{powerlaw}$	$S_{reflection}$	0.938	0	0.871	8.41×10^{-13}	0.916	4.90×10^{-13}	0.900	4.17×10^{-10}	0.735	1.27×10^{-14}
$S_{powerlaw}$	S_{disc}	–	–	0.710^{*}	$3.39\times10^{-8*}$	0.694	1.52×10^{-5}	0.839	8.40×10^{-8}	0.474	1.04×10^{-5}
$S_{reflection}$	S_{disc}	–	–	0.731^{*}	$7.79\times10^{-9*}$	0.601	3.52×10^{-4}	0.653	3.02×10^{-4}	0.438	5.43×10^{-5}
RF	S_{disc}	–	–	-0.528^{*}	$1.64\times10^{-4*}$	-0.701	1.13×10^{-5}	-0.825	2.17×10^{-7}	-0.361	1.07×10^{-3}

Table 4.3: A list of Spearman's rank correlations (ρ) and the the corresponding false correlation probability (p-value) calculated for the flux determined in each model in the five principle spectral states.

the process in decay is progressive rather than sudden. The SIMS(-A) points lie at larger *RF* to the HIMS in the hard-soft transition (those at higher fluxes), continuing the general rise observed so far throughout the states (see also Table 4.4). The soft state itself is almost entirely consistent with a $RF>1$, meaning that the reflection is now dominant over the Comptonised component. There is, however, a lot of scatter, and large confidence limits due to the customary reduced signal in the hard band, thus the slope of the soft state decay can only be fitted when the 2002 outburst is excluded, but nevertheless this confirms that the *RF* increases as the source decays ($\alpha = 0.49 \pm 0.17$). The soft state also tends to show significant variations in variability and spectral hardness throughout its decay (see Figures 4.2 and 4.3), and thus makes several forays into the SIMS and SIMS-A between state transitions. The best-fit to the SIMS and SIMS-A observations yields a slope of 0.73 ± 0.07 (Figure 4.7d), representing a growing domination of the reflection component over the Comptonised emission as the source decays, consistent with the evolution of the reflection and power-law in the soft state. The *RF* is a proxy for the EW of the Fe line, hence this agrees with the soft-state X-ray Baldwin effect[2] previously reported in GX 339−4 (Dunn *et al.*, 2008).

4.4.3 Contrasting emission in spectral states

In Figure 4.8 I display how the X-ray spectrum evolves throughout each spectral state, whilst in Table 4.4 I calculate the mean parameter value accordingly. In the rising hard state a disc model was never required, whilst the Comptonised emission is hard and clearly the dominant source of emission. The Fe line profile is often narrow and the high-energy cutoff is clearly visible in the plotted spectrum. Transition to the HIMS marks increases in the power-law slope, ionisation parameter and reflection fraction. Thermal emission from the disc is now clearly present; however, it remains the weaker of the three spectral components and only dominates below ~ 3 keV.

Into the SIMS there is a distinct softening, in part due to a further increase of Γ. The disc is now much stronger, dominating up to $\sim$6–7 keV, and is the largest source of emission. A broad Fe line is now regularly observed and the ionisation stage is considerably higher than in the hard state. In addition, reflection and Comptonised emission are roughly equal. The SIMS-A is only subtly different from the SIMS,

[2]Baldwin (1977) discovered that the EW of the C-IV line decreased as the ultraviolet luminosity increased in a number of AGN. A similar X-ray Baldwin effect has been found in AGN (Iwasawa and Taniguchi, 1993; Nandra *et al.*, 1997; Bianchi *et al.*, 2007).

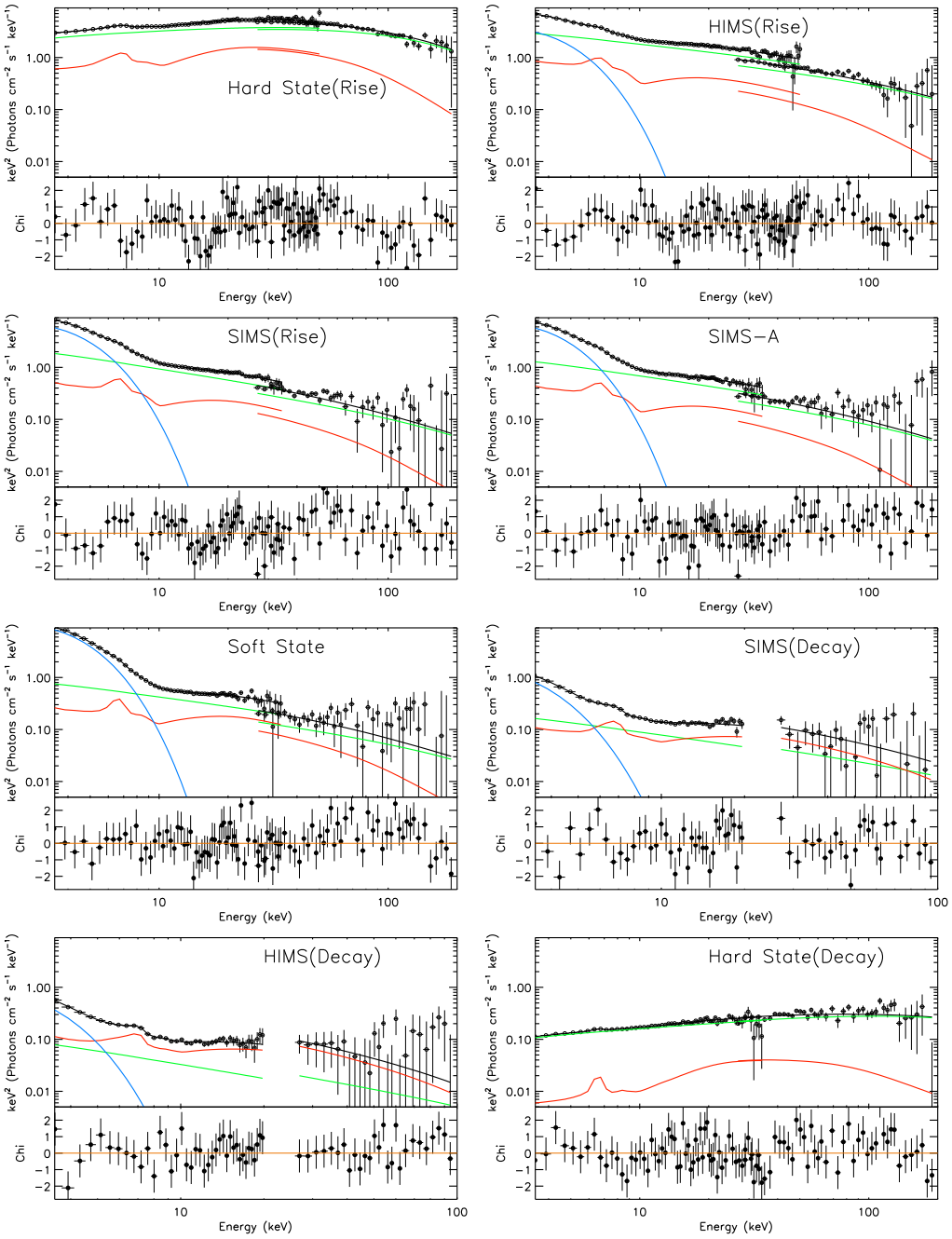

Figure 4.8: Unfolded spectra (top) and data-model residuals (bottom) for the eight states listed in Table 4.4. The disc, cut-off power-law, reflection and total models are displayed by blue, green, red and black lines respectively. The data is also plotted as black open circles. Each vertical scale is equivalent to best display how the spectrum evolves in outburst. Areas where the model overlap and appear to disagree are due to the calibration constant between the PCA and HEXTE instruments. The data-model residuals are plotted in terms of sigma, such that each error bar has a value of one sigma.

the most marked difference being a slightly softer Γ (see also Figure 4.5). Typically the total flux is larger, in fact the SIMS-A represents the peak luminosity for two of the three outbursts in this study. Table 4.4 suggests that this increase is due to greater flux from the power-law and reflection, rather than the disc (see also Figure 4.7d to compare power-law and reflection flux between the SIMS and SIMS-A).

The soft state represents the relative peak of the thermal disc emission, which now dominates the spectrum up to 10 keV. The reflection flux is significantly larger than that of the power-law, which itself decreases substantially as the source decays. Regardless of this, the disc inner radius is often poorly resolved due to the thermal disc emission being highly dominant at 6 keV (see also Kolehmainen *et al.* 2011). As the source decays through the intermediate states the spectral characteristics are similar to the rise, albeit at a lower luminosity. The cooler disc does, however, contribute a much larger portion to the overall flux, and the reflection fraction is typically larger. The ionisation stage remains relatively unchanged, and the inner radius is once again well resolved. Finally, the decay phase of the hard state is much like the rise, described by a hard spectrum and a return to a low reflection fraction and ionisation.

4.4.3.1 The disc inner radius and the ISCO

The disc inner radius is again poorly determined (a larger error) in the hard state, which is likely due to the reduced Fe line signal during low reflection fractions. At this stage of the outburst the line is also expected to be narrow (Kolehmainen *et al.* 2014; Chapter 3; but see also Reis *et al.* 2010), hence making limits on the relativistic broadening difficult with the energy resolution of the PCA ($\sim$ 1 keV at 6 keV). It is interesting to note, however, that there is less scatter in the inner radius fitted during the HIMS and SIMS(-A), both in rise and decay, suggesting that the parameter is being well resolved. Furthermore, the mean value is similar throughout (30–50 $r_{\rm g}$; Table 4.4) which would indicate that there is no significant change in the disc through these states.

The inner radius is known to be very degenerate with the inclination, which is not well known for GX 339−4 (see §1.6), thus I cannot rule out that the inner radius is smaller and represents the ISCO. However, the assumed inclination is very similar to that fitted in Chapter 3 in a study of the hard state of GX 339−4 with *XMM-Newton* and *Suzaku*, allowing a direct comparison. In Figure 4.9 I plot the fitted inner radius against source luminosity using only well constrained values (limits less than the parameter value) and include the values found in Chapter 3. Clearly

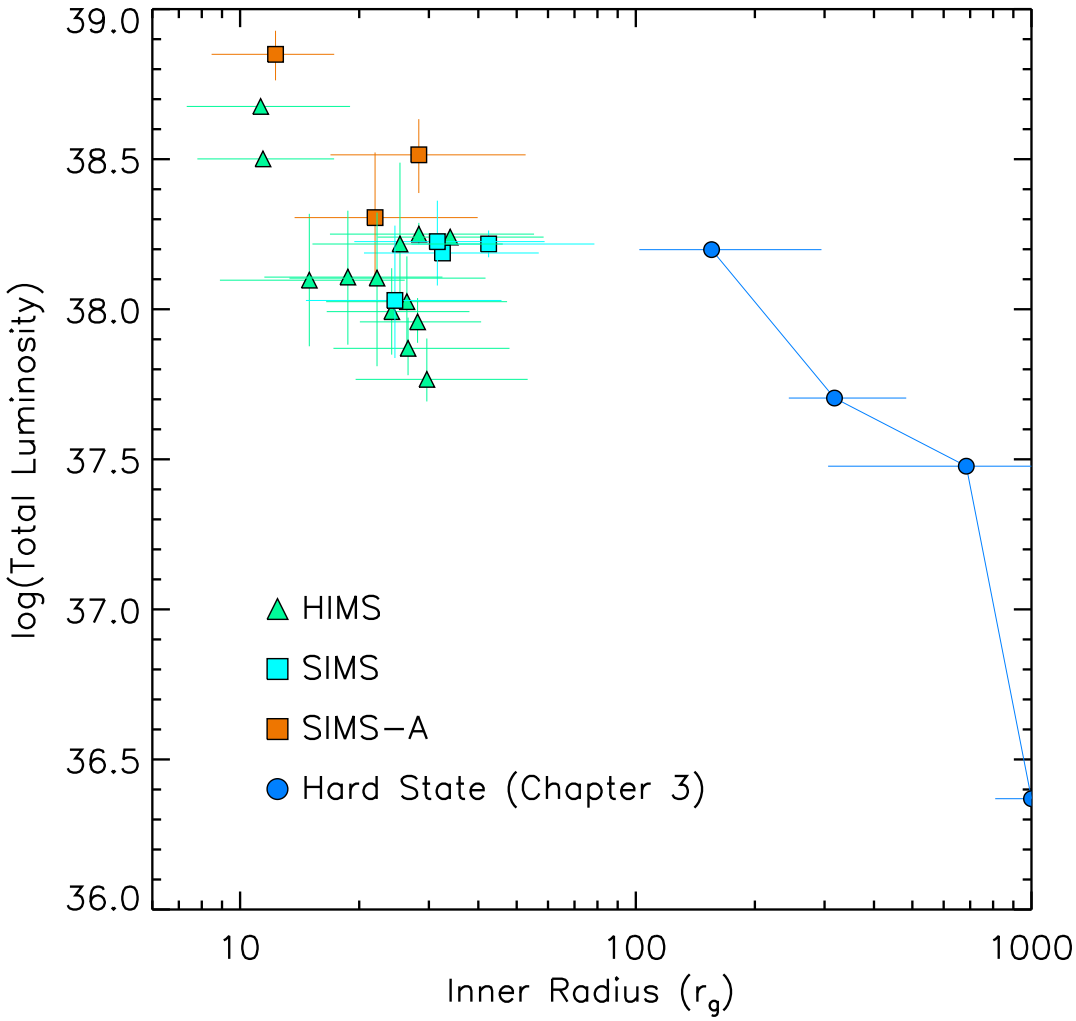

Figure 4.9: The fitted inner radius parameter plotted against the total model luminosity for the intermediate states. I restrict the sample to ensure the parameter was well constrained: both the upper and lower error of the inner radius must be less than the value of the fitted inner radius, which itself must not be at the hard limits of $6\,r_g$ or $1000\,r_g$. For comparison I plot the hard state results from Chapter 3 (Figure 3.10) where I applied the same reflection model and a very similar inclination value (42.1° vs 45°) to higher-resolution data. The HIMS, SIMS and SIMS-A appear to represent a stable inner radius, while in the hard state the disc is truncated.

Mean Parameter Value Per Spectral State								
Parameter	HS(Rise)	HIMS(Rise)	SIMS(Rise)	SIMS-A	HSS	SIMS(Decay)	HIMS(Decay)	HS(Decay)
T_{in}	–	$0.86 \pm 0.09^{*}$	0.76 ± 0.07	0.82 ± 0.08	0.79 ± 0.09	0.67 ± 0.04	$0.65 \pm 0.08^{*}$	–
N_D	–	$958 \pm 474^{*}$	2430 ± 645	1870 ± 219	3249 ± 194	2159 ± 678	$1101 \pm 641^{*}$	–
Γ	1.60 ± 0.06	2.22 ± 0.30	2.57 ± 0.09	2.71 ± 0.12	2.60 ± 0.14	2.55 ± 0.10	2.53 ± 0.22	1.76 ± 0.24
r_{in} (r_g)	255 ± 358	101 ± 259	44 ± 17	47 ± 32	177 ± 298	50 ± 44	28 ± 12	416 ± 449
$\log(\xi)$	2.75 ± 0.52	3.44 ± 0.23	3.40 ± 0.04	3.48 ± 0.25	3.26 ± 0.20	3.42 ± 0.09	3.40 ± 0.20	2.33 ± 0.69
Mean Model Luminosity (10^{37} erg s^{-1})								
Power-law	7.23 ± 6.20	24.4 ± 15.8	8.50 ± 8.39	21.6 ± 14.4	4.98 ± 4.34	2.63 ± 1.99	2.04 ± 1.07	1.79 ± 1.34
Reflection	2.13 ± 2.78	15.6 ± 8.15	9.22 ± 4.58	21.5 ± 14.3	7.93 ± 4.72	4.61 ± 1.81	4.82 ± 2.97	0.39 ± 0.45
Disc	–	$8.84 \pm 4.88^{*}$	13.6 ± 5.73	14.5 ± 5.40	21.4 ± 4.72	7.28 ± 3.64	$2.53 \pm 1.06^{*}$	–
RF	0.23 ± 0.10	0.81 ± 0.56	1.42 ± 0.66	1.16 ± 0.48	2.43 ± 2.22	2.12 ± 0.75	4.00 ± 4.70	0.20 ± 0.13

Table 4.4: The mean value for a number of interesting parameters calculated for each spectral state. The errors represent the standard deviation and are thus only meant as an indication of accuracy.
*Calculated using only observations requiring a disc model.

the HIMS and SIMS(-A) are associated with an inner disc closer to the black hole during the intermediate states, while this figure again indicates the consistent radii recorded throughout this stage. To compare, the inner radius derived from the normalisation of the DISKBB model is $4.19 \pm 0.13\, r_{\rm g}$ in the soft state for the same inclination.

4.4.4 The luminosity-temperature relation

The model I used to fit the thermal component was DISKBB (Mitsuda *et al.*, 1984), which is parameterised by the apparent inner radius of the disc $r_{\rm in}$ and the peak temperature $T_{\rm in}$. As discussed in §1.2, assuming that $f_{\rm col}$ does not vary, the $L_{\rm disc} \propto T_{\rm in}^4$ relation can be used to test whether the inner radius of the accretion disc remains constant.

In Figure 4.10 I plot the observed bolometric disc luminosity versus the inner disc temperature for observations with an X-ray colour (S_{6-10}/S_{3-6}) less than 0.5. Throughout all the states this corresponds to 167 of the 528 observations used in this study. Figure 4.10a plots the soft state and SIMS-A observations (red and orange respectively) with the solid line representing the expected $L_{\rm disc} \propto T_{\rm in}^4$ relation and normalised to coincide with the soft state points, displaying a good match (fitted relation: $L_{\rm disc} \propto T_{\rm in}^{4.13\pm0.04}(1\sigma)$). The SIMS-A observations also appear to follow a similar, albeit marginally steeper, slope (fitted relation: $L_{\rm disc} \propto T_{\rm in}^{4.68\pm0.18}(1\sigma)$); however, they lie on a different plane corresponding to a higher temperature or lower luminosity. The standard SIMS observations fit an even steeper slope of 5.64±0.19

I investigated the observations coeval to the SIMS-A and found that generally a combination of both factors led to the change. Since $L_{\rm disc} = 4\pi r_{\rm in}^2 \sigma T_{\rm in}^4$ this would in either case require a reduction in the inner radius of the disc, a process that is unlikely given that the soft state is expected to represent the innermost stable circular orbit being reached (see the discussion in §1.3.1). Furthermore, Figure 4.10b displays each observation by X-ray colour indicating that there is a trend with spectral hardness which continues even into the hard state. A more likely scenario is an increasing $f_{\rm col}$, hence the dotted lines in Figure 4.10a represent factors 1.1, 1.2 and 1.3 times larger, making the SIMS-A consistent with a moderate modification (see also Dunn *et al.* 2011). Curiously, however, I note that the power-law emission is consistently larger and the reflection fraction generally weaker than the soft state (Figure 4.7), even though the SIMS-A observations are distributed fairly evenly among the range of luminosity the soft state exhibits (Figure 4.2). I examine the SIMS-A further in the discussion (§4.5.2).

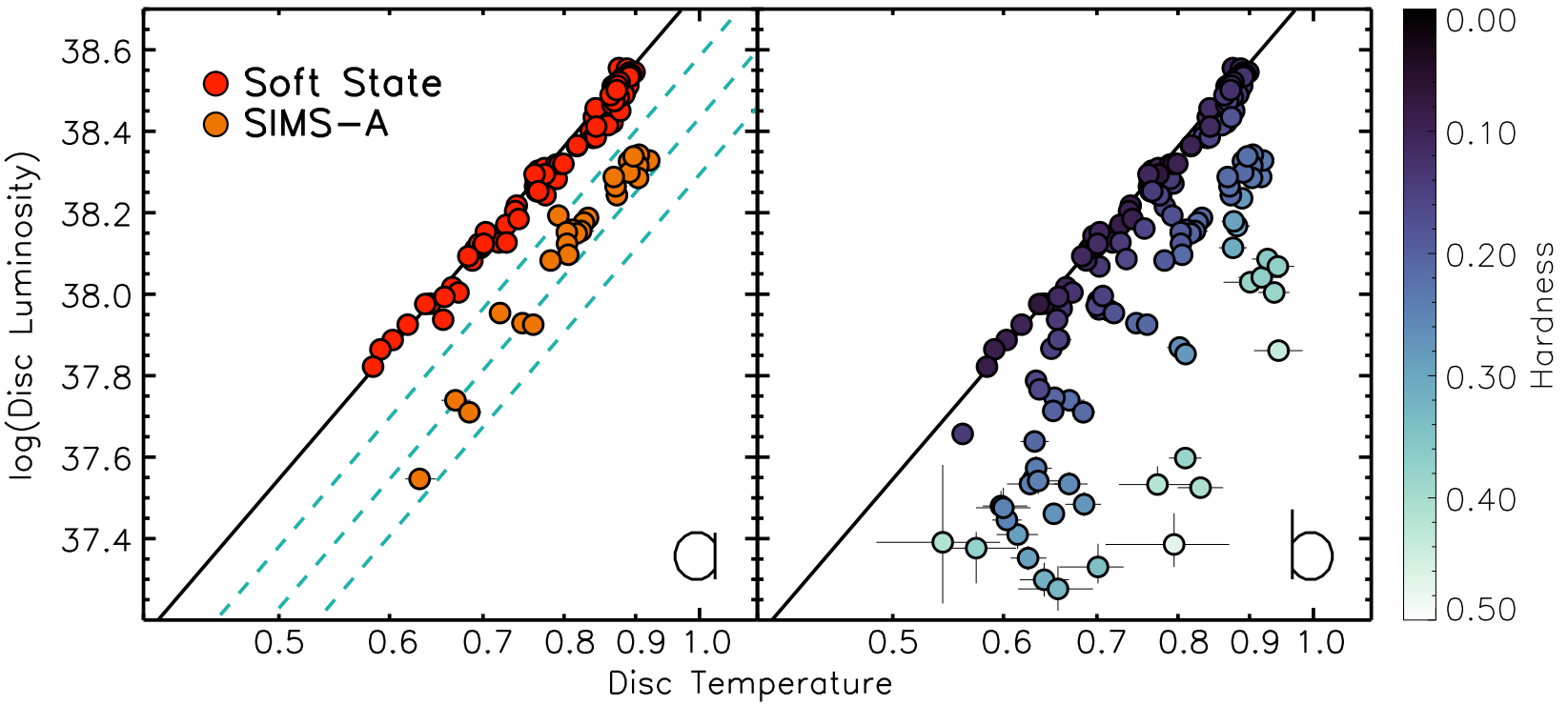

Figure 4.10: The inner disc temperature versus unabsorbed bolometric disc luminosity (0.01–1000 keV). Left: Soft state (red) and SIMS-A (orange) observations. The solid line indicates the $L_{\rm disc} \propto T_{\rm in}^4$ relation which is clearly well fit by the soft state points, while in the SIMS-A the source appears to follow a similar track but at a higher temperature (or lower disc luminosity). The dashed lines indicate increased spectral hardening for factors 1.1, 1.2 and 1.3 larger than the solid line respectively. Right: All disc detections below a hardness of 0.5 are plotted, with the colour scale representing the respective X-ray colour (6–10 keV / 3–6 keV) of the observation. The solid line again indicates the $L_{\rm disc} \propto T_{\rm in}^4$ relation revealing there is a clear drop-off with spectral hardness (see also Dunn et al. 2011). Both figures include errors bars but these are typically smaller than the plotted symbol.

4.4.5 The ionisation parameter

Given the large variation in luminosity as the source progresses through each outburst, it is expected that the ionisation of the disc surface layers should vary too, since by definition the ionisation parameter is a function of the flux illuminating the disc (Eq. 1.8). In Figure 4.11 I plot how the ionisation parameter evolves throughout the outburst using darker colours to represent increased ionisation. There is a large degree of scatter; however, this is not surprising given that this is determined from the soft bandpass and the PCA is limited to > 3 keV and in spectral resolution (but see §4.5.3). Nevertheless, it is easily distinguishable that the soft state generally corresponds to a higher level of ionisation than the hard state.

This is initially quite surprising as the hard state is typically deemed to represent the prime of the Comptonised emission; however, as I have shown in Figure 4.7, the power-law flux remains significant in the soft state. While this can account for the consistently high level of ionisation throughout the outburst, it still fails to account for soft state recording higher values. I discuss two explanations for this in §4.5.4: the effect of thermal emission and inner disc truncation. The high level of ionisation maintained throughout the outburst will mean that the reflection albedo is always high and will not vary much (Ross and Fabian, 1993; Zycki *et al.*, 1994).

I also note that at the onset of the hard state during the soft to hard transition the ionisation parameter appears to be at its weakest. This is, however, the region where the routine can no longer suitably constrain the emission from the accretion disc, and thus removes the DISKBB model. There is, however, a sufficient amount of thermal emission remaining above 3 keV at this stage, hence the reflection model may be accounting for this excess by reducing the ionisation parameter. I therefore disregard any conclusion that can be made from the ionisation parameter during this phase. Once the standard hard track is reached the ionisation returns to a higher level coincident with the rising phase.

4.4.6 Links to compact jets

In the hard state sources always display steady jet emission at GHz frequencies. Furthermore, the X-ray and Radio luminosities appear to be inherently linked, following a non-linear correlation of $L_X \propto L_R^b$, where $0.6 < b < 0.7$ (Corbel *et al.* 2003; Gallo *et al.* 2003; Corbel *et al.* 2013a; but see also Coriat *et al.* 2011; Gallo *et al.* 2012). Recently Corbel *et al.* (2013a) reported a long campaign of quasi-simulatenous X-ray and Radio observations with *RXTE* and the Australia Telescope Compact Ar-

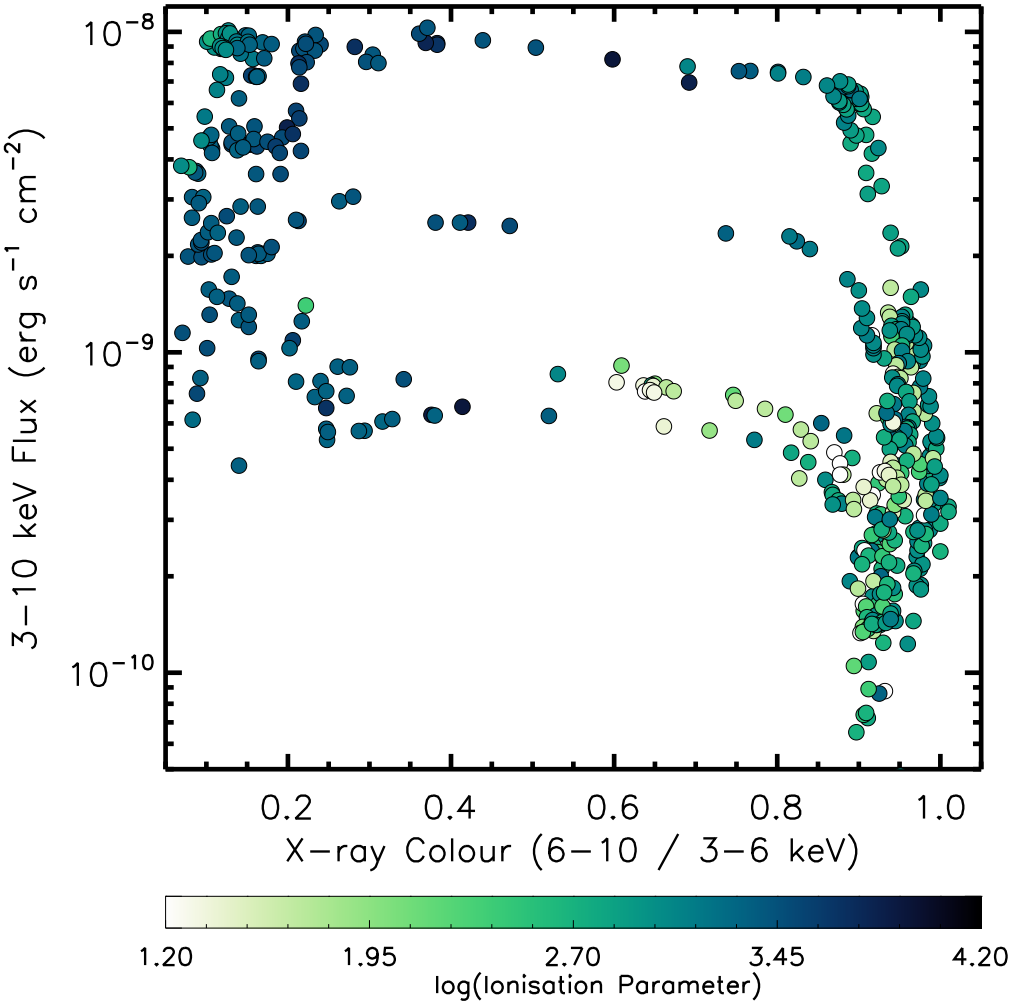

Figure 4.11: Evolution of the ionisation parameter throughout the HID. The colour scale represents increased ionisation with darker colours, hence in the soft state the disc is much more ionised. The units of the ionisation parameters are erg cm s^{-1}.

ray (*ATCA*). This represents the largest sample for a stellar mass black hole, and 32 of these radio observations are coincident (less than 2 days separation) with the data analysed in this Chapter. I therefore investigated how the 8.6 GHz ATCA observations correlate with the results of this investigation.

Both the power-law and reflection are well correlated (positively) with the radio luminosity. The power-law correlation coefficient is 0.771, with a false probability of 2.5×10^{-7} and best fit slope of $b = 0.62 \pm 0.01$, agreeing excellently with Corbel *et al.* (2013a). Since the power-law dominates the total flux in the hard state this agreement is not surprising. The reflection is similarly correlated with a coefficient of 0.664 and a 3.5×10^{-5} chance of a false probability. Reflection also reflects a

Parameter 1	Parameter 2	ρ	p-value
S_{radio}	S_{total}	0.765	3.38×10^{-7}
S_{radio}	$S_{powerlaw}$	0.770	2.54×10^{-7}
S_{radio}	$S_{reflection}$	0.664	3.47×10^{-5}
S_{radio}	Fractional RMS	-0.315	0.0793
S_{radio}	ξ	0.279	0.122
S_{radio}	RF	0.201	0.270
S_{radio}	Γ	-0.013	0.946

Table 4.5: A list of Spearman's rank correlations (ρ), and the corresponding false correlation probability (p-value), calculated for the 8.6 GHz radio flux densities listed in Corbel et al. (2013) against fitted parameters in this study.

similar relation with the radio luminosity, fitting a slope of $b = 0.61 \pm 0.02$. Correlations between the radio luminosity and other interesting parameters are listed in Table 4.5.

4.5 Discussion

In this work I have utilised three outbursts of GX 339−4 to systematically uncover the spectral evolution of black hole binaries. In particular I focus upon the reprocessed reflection spectrum revealing marked changes in the reflection, often not in tandem with the Comptonised emission. As I will discuss now, the most likely explanation for this is distinct evolution of the accretion geometry.

4.5.1 The overall picture

In Figure 4.7 I display how the Comptonised and reflection emission co-evolve as the outburst progresses. In the hard state (1) the power-law is typically responsible for 5 times more flux than the reflection ($RF \sim 0.2$); however, as the source rises the reflection fraction increases, yet always remains below 1. On the other hand, the soft state lies in the main above unity, thus signifying larger levels of reflection than power-law. Furthermore, as the source decays the reflection fraction appears to continue increasing. What makes this interesting is that for a stable geometry the two should vary in tandem as the Comptonised emission feeds the reprocessing observed as the reflection spectrum. Therefore, evolution is a signal of changes in the accretion geometry.

Figure 4.12 illustrates two such transformations that can lead to the observed cy-

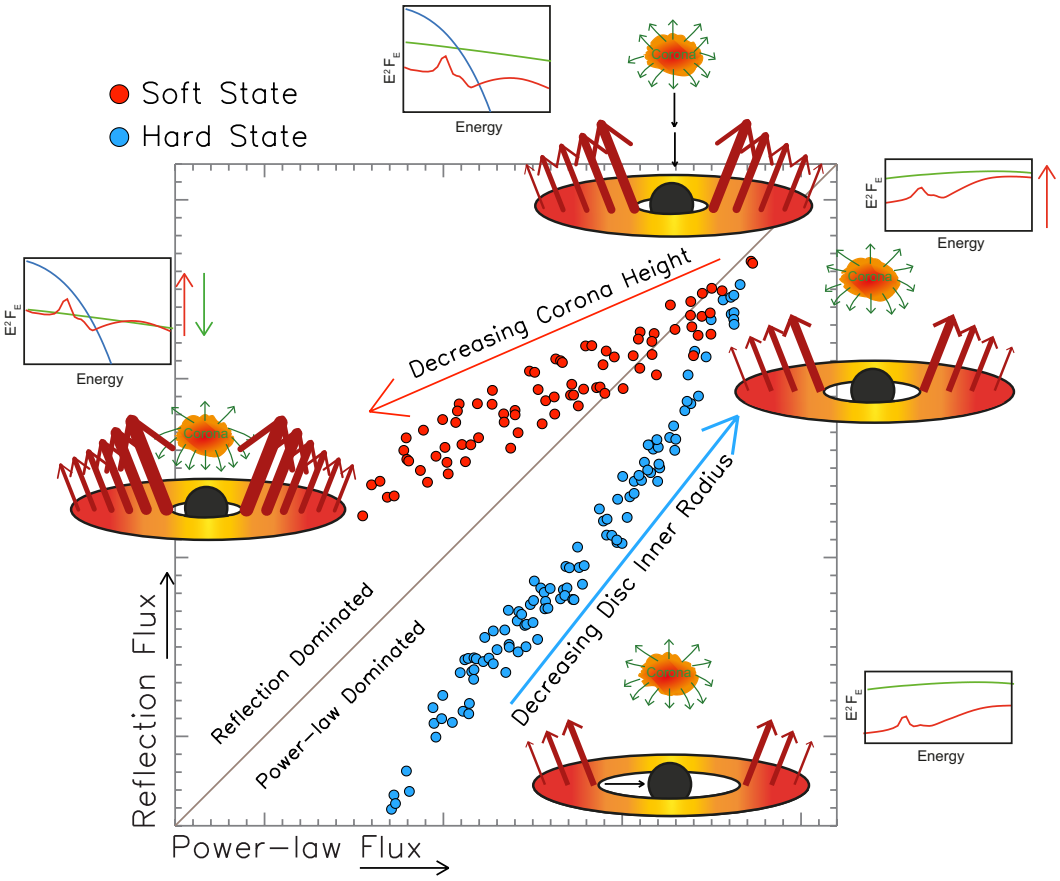

Figure 4.12: An illustration of how geometrical evolution will lead to contrasting changes in the Comptonised and reprocessed emission, and notably an increase in reflection fraction. Hard State (blue): The reflection fraction can be increased by decreasing the inner radius of the accretion disc. For a stable corona this model increases the solid angle subtended by the disc, thus increasing the photons intercepted and reprocessed flux. The Comptonised emission meanwhile remains constant. This interpretation suits the hard state well, where the reflection fraction is low, consistent with the small solid angle of a truncated disc, but gradually increases as the source rises. Soft State: If the scale height of the corona decreases, the portion of Comptonised photons intercepted by the accretion disc will increase, leading to increased reprocessing and thus reflection flux observed at infinity. In addition, the lower height will lead to stronger relativistic effects, ultimately focusing more Comptonised photons on to the disc, and in particular the inner regions. As well as heightened reflection, the Comptonised flux will also decrease as a consequence of the increased anisotropy of the emission. Similar results can be formed with alternative modifications of the corona that ultimately lead to irradiation from a lower mean height. I discuss these models in more details in §4.5.1.

cle portrayed in Figure 4.7. The truncated disc model has become a popular means to describe the observed characteristics of the hard state, such as the hard spectrum and low reflection fraction (see Done *et al.* 2007 for a review and references therein). As the inner radius of the accretion decreases, the solid angle it subtends beneath the illuminating corona increases. More photons are thus intercepted leading to increased reprocessing and reflected flux. In turn, the amount of soft photons entering the corona will increase as the disc moves further towards the black hole, leading to cooling of the hot electrons, which is observed through a softer photon index and high energy cut-off (Figures 4.5 and 4.6).

Beloborodov (1999) proposes an alternative explanation for these trends through a 'dynamic corona', whereby bulk motion of the emitting plasma reduces the irradiation of the disc. Even with a disc at the ISCO this regime can yield the small reflection fractions observed in the hard state, whilst the beaming will also suppress the soft seed photons, hence retaining a hard spectrum ($\Gamma \sim 1.6$). I, however, observe that both *RF* and Γ increase as the source rises through the hard and into the intermediate states (see §4.4.1 and §4.4.2), which would thus require a decreasing bulk motion. This would appear at odds with the favoured internal shocks model outlined in Fender *et al.* (2004), whereby the jet velocity increases with luminosity/state. Given that there is no deviation from the observed trends in *RF* and Γ would suggest that the illuminating medium remains consistent as well. Furthermore, the same process ruling *RF* and Γ is present in the decay of the hard state, whereby they both decrease as the source fades (*RF* fitted slope 1.21 ± 0.06), thus in the dynamic corona regime the jet velocity should systematically increase leading to bright radio flares. The reality is, however, that such flares have only been observed in the rise (Fender *et al.* 2004, see also Corbel *et al.* 2013b), thus I therefore propose the truncated disc model as the favoured interpretation. The high resolution observations analysed in Chapter 3 also confirm that the inner disc radius is truncated and decreases with increasing luminosity in the hard state. The lower values for the ionisation parameter recorded in the hard state also agree with a truncated inner disc (see §4.5.4). The reflection fraction is also almost identical both in magnitude and evolution during the rise and decay (stages 1 and 4) of the hard state (compare Figures 4.7b–c), which argues strongly for an identical dynamic in and out of quiescence.

In contrast, the reflection dominates the Comptonised emission in almost all of the soft state observations ($RF > 1$). Furthermore, as the decay progresses the reflection fraction appears to increase. The scatter in flux due to the reduced hard band signal in the soft state makes fitting the trend difficult; however, if the 2002

outburst is excluded, a slope of $\alpha = 0.49 \pm 0.17$ is resolved (where $\log_{10} S_{\rm PL} = \alpha \log_{10} S_{\rm Ref} + c$). In addition, fitting the SIMS and SIMS-A observations, which track the decay quite well (Figure 4.2), reveals a similar relationship ($\alpha = 0.73 \pm 0.07$). The decay of the disc luminosity fits the expected $L_{\rm disc} \propto T_{\rm in}^4$ relation well, hence the inner disc radius is without any reasonable doubt stable in the soft state (see §4.4.4 and also Gierliński and Done 2004; Steiner *et al.* 2010; Dunn *et al.* 2011), thus the same mechanism as the hard state can be ruled out. Instead, this acts as strong evidence that the underlying changes modifying the reflection fraction are occurring in the corona. I do note, however, that flaring of the accretion disc can increase the amount of reprocessed emission as well (see e.g. Poutanen 2002).

In Figure 4.12 I illustrate the relationship between the coronal height and the amount of reflection and Comptonised flux observed. A reduction in height increases the portion of Comptonised photons intercepted by the accretion disc, leading to increased reprocessing and thus reflection flux observed at infinity. In addition, the lower height will lead to stronger relativistic effects upon each Comptonised photon, ultimately focusing more on to the disc, and in particular the inner regions (Miniutti and Fabian, 2004; Wilkins and Fabian, 2012). This will, firstly, heighten the reflection flux further due to the increased irradiation. Secondly, the Comptonised flux observed will decrease as a result of the increased anisotropy (and focus towards the black hole) of the Comptonised emission with lowering height. It is clear to see then how the coronal height can significantly vary the reflection fraction by coupling enhanced reflection with a diminished power-law, and I therefore favour this solution as the process behind the increasing reflection fraction in the soft state. While I have showcased the corona as a compact 'lamp-post' for illustration purposes, the effect of the coronal height may manifest itself in a different form, such as by varying in extension or collapsing; however, the interpretation is still very much alike: the coronal geometry is expected to be evolving as the source decays in the soft state.

By using the evolving *RF* to constrain the accretion geometry I have assumed that the albedo remains constant. This however may not be true since the surface layers of the disc are subjected to a large range of illumination during the different phases of the outburst. The albedo itself is strongly dependent upon the ionisation of the surface layers, hence it must be considered how this may influence my results. Above 10 keV the scattering cross-section exceeds the absorption cross-section, hence there the albedo of the reflection is close to unity and constant. However, below 10 keV the albedo is strongly influenced by the ionisation stage: as the layers become more ionised the absorptive opacity decreases, leading to more

effective reflection (Ross and Fabian, 1993; Matt *et al.*, 1993; Zycki *et al.*, 1994). Ultimately a fully ionised layer should act like a mirror, corresponding to an albedo of unity.

In the case of BHXRBs the surface layers are expected to be kept highly ionised by the hot thermal emission emerging from the disc itself (Ross and Fabian, 1993), which is evident by the high ionisation parameter values I record throughout this study (see §4.4.5). Furthermore, the ionisation values I record are large enough that the albedo should remain consistently high, and not far from unity (Zycki *et al.*, 1994). I do observe some evolution in the ionisation parameter, which is particularly contrasting between the hard and soft states (Figure 4.11), but this is not enough to change the albedo by more than a factor of 2 (Zycki *et al.*, 1994). As I have described previously, the reflection fraction varies over a much broader range than this in outburst.

4.5.2 On the nature of the SIMS-A observations

When classifying spectral states it became apparent that there are two distinct clusters of points with low variability (RMS$<$5%) isolated by their X-ray colour (6–10/3–6 keV flux; Figure 4.4). I associated the softer points (X-ray colour $<$0.175) with the canonical soft state, whilst the harder points are described by spectra very similar to the SIMS. Additionally, of the 7 observations containing a type-A QPO listed in Motta *et al.* (2011), 6 are in this group. The seventh observation covered what appears to be part of a transition, hence only a portion of the time-series was used by Motta *et al.* (2011), meaning a RMS of $\sim 2\%$ was reported. In this study I utilised the entire observation which raised the RMS to $\sim 6\%$. As a result of this association I labelled these points as SIMS-A. The majority of the SIMS-A observations displaying a type-A QPO are close to the top branch of the HID (Figure 4.2), and given that the feature is weak and broad (Motta *et al.*, 2011), it is likely that many SIMS-A observations where a QPO was not detected simply lack the signal to do so.

As stated before, the SIMS-A has a very similar spectrum to the SIMS (Table 4.4). In the HID (Figure 4.2) the SIMS-A appear to be distributed at a slightly higher luminosity than the SIMS; however, this distinction becomes more clear in Figure 4.7d. The SIMS-A is therefore probably associated with an increase in the Comptonised and reflection components, and is the likely explanation for the hardened X-ray colour. It is also interesting that the SIMS-A remains on the 'soft' slope of $<$1 (Figure 4.7d) describing the general decay of the source, even when there is an

apparent increase in power-law and reflection flux each time the source transitions to it.

The spectrum of the SIMS-A is dominated by the power-law and reflection, whereas the disc flux is relatively weak (Table 4.4). In comparison, the disc generally accounts for the majority of flux in the SIMS, as is of course standard for the soft state as well. In Figure 4.13 I plot the fraction of the total source flux from each component which also emphasises how the disc and Comptonised flux are decreased and increased respectively in the SIMS-A. Interestingly, the SIMS-A tend to roughly follow the L$\propto$T^4 relation (fitted relation: $L_{\rm disc} \propto T_{\rm in}^{4.68\pm0.18}(1\sigma)$) commonly attributed to the soft state, but at a lower luminosity (or higher disc temperature), consistent with a spectral hardening factor 1.1–1.3 times larger (Figure 4.10). An alternative explanation is a reduced disc inner radius; however, this is unlikely given that the soft state is well regarded to harbour a disc extending all the way to the ISCO.

In total there are 13 instances of transitions to the SIMS-A recorded in this study (i.e. excluding observations already in the SIMS-A). Six of these transitioned from the SIMS, of which 5 led to an increase in reflection flux and 4 in power-law flux. In 4 of these the disc flux also decreased. Another six observations transitioned from the soft state, all of which are characterised by increases in power-law and reflection flux in addition to a reduced disc flux. Furthermore, in each case the photon index softened, and all but one of these transitions lead to a net increase in flux. In the remaining observation the source transitioned directly from the HIMS. It is also interesting that the Comptonised and disc fractions plotted in Figure 4.13 isolate the SIMS-A observations quite well, whereas the SIMS appears more to be an extension of the soft state. This is typically true for SIMS observations with RMS in the 5–7 % range, whilst most of the type-B QPOs reported in Motta *et al.* (2011) correspond to observations with a RMS above this level. I note that the choice of the 5 % RMS line separating the SIMS and soft state is rather arbitrary and the true value could be slightly higher. This region is also prone to fast transitions shorter than the typical exposure time of the PCA (Muñoz-Darias *et al.*, 2011).

In relation to the soft state it is quite easy to explain the harder X-ray colour in the SIMS-A, simply since there is a decrease in the soft (disc) contribution whilst the hard (power-law/reflection) increases. However, this fails to explain the consistently low level of variability usually associated with emission from the disc (or lack of Comptonised emission). The SIMS-A do appear to show a similar relationship between the Comptonised fraction and RMS as seen for the SIMS and soft state observations, but offset to a higher fraction. It may be that an additional

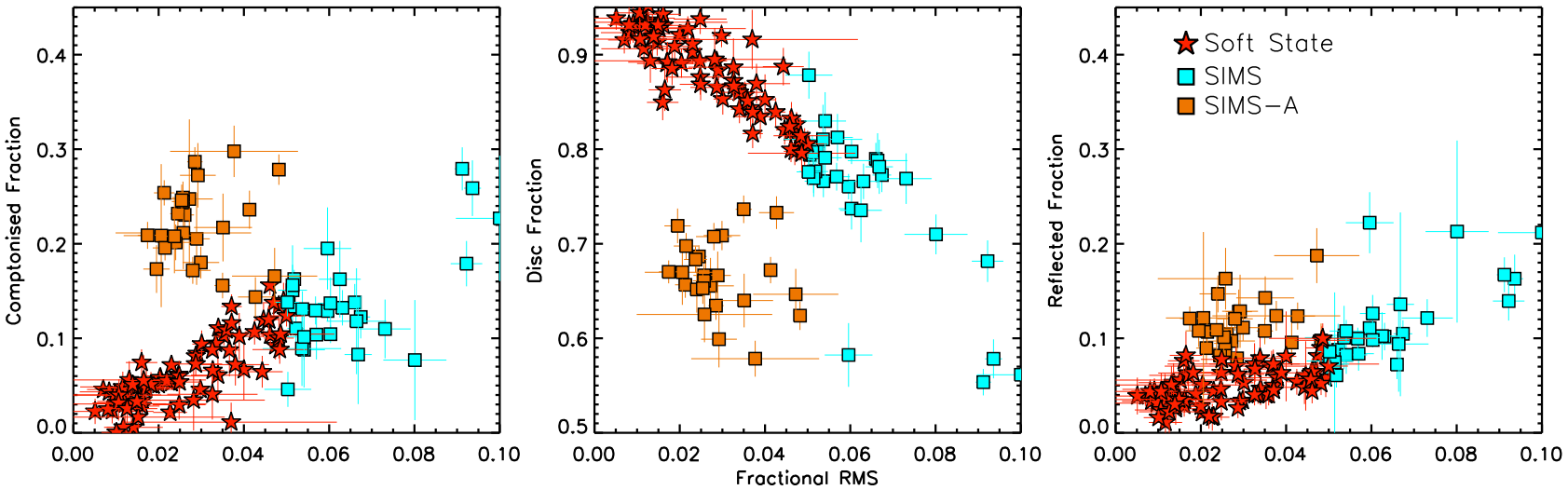

Figure 4.13: The fraction of total source flux that comes from the Comptonised (left figure), disc (middle) and reflection (right) components respectively. I plot the SIMS, SIMS-A and soft state observations to indicate how the source spectrum is different between these three principle states. Whilst the fractional RMS has proven to be a better indicator of state than spectral hardness, clearly the states are not completely distinct, particularly between the SIMS and soft state (see §4.3.3). Note that the plotted reflected fraction is the ratio of the reflection and total source flux, and should not be confused with the *RF*. I calculated each flux in the same band as the RMS (2–15 keV) to make the two axes directly comparable; however, the same trend is seen using 0.1–1000 keV flux as well.

non-variable component is also present but compensated for by the CUTOFFPL model. The same process giving rise to the type-A QPO may be behind the increased hardening of the thermal emission or Comptonised flux as well. I note that the SIMS-A are nevertheless well fitted (Figure 4.14).

4.5.3 The accuracy of this study and comparisons to other works

In using *RXTE* my approach is quantitative more than qualitative, hence it is important to examine the accuracy of the study. To do this I can examine how well investigations with high-resolution missions like *XMM-Newton* and *Suzaku* agree with the results. Such studies of the hard state (Reis *et al.* 2010; Done and Diaz Trigo 2010; Kolehmainen *et al.* 2014; Chapter 3) reveal moderate ionisation ($\log\xi < 3$) and a low reflection fraction akin to the results in this Chapter. Studies of the HIMS are sparse due to the short duration of this state, but observations analysed by Hiemstra *et al.* (2011) and Reis *et al.* (2011, 2012) agree with the evolution outlined in §4.4.3, in particular an increased level of ionisation ($\log\xi > 3$) and reflection fraction (the equivalent width is now 250–450 keV vs. 50–150 keV in the hard state). Kolehmainen *et al.* (2011) investigated the SIMS and soft state of GX 339−4, confirming consistently high ionisation and increased reflection fraction habitual to the soft state in this study. Furthermore, they discuss difficulties in fitting the Fe line profile in the soft state, which is hampered since the disc is providing most of the flux and additional curvature in the continuum at 6 keV. This is the most likely reason for the large scatter in $r_{\rm in}$ during the soft state (Table 4.4).

I can also compare my results to previous work with *RXTE*. Recently Reis *et al.* (2013a) performed a similar analysis with one outburst of the black hole XTE J1650−500 finding similar results. For example, they also plot reflection versus power-law flux displaying similar evolution throughout the states (Figure 4.7). Dunn *et al.* (2008) also studied reflection in GX 339−4, instead fitting the Fe line with a Gaussian. Remarkably, even with this simpler approach, very similar evolution is revealed. In their Figure 8 Dunn *et al.* (2008) plot Fe line flux against 7–20 keV flux (essentially reflection versus power-law flux) finding the same looped evolution and an increased fraction of reflection to power-law in the softer states. Furthermore, the fitted slopes to their 'hard' and 'soft' observations are almost identical to those in this study (Figure 4.7b–d), whilst the evolution of the equivalent width in their Figure 7 is very similar to the trend of its analogous parameter *RF* analysed in this investigation (Figure 4.7).

It is also possible that the three components (disc, power-law and reflection)

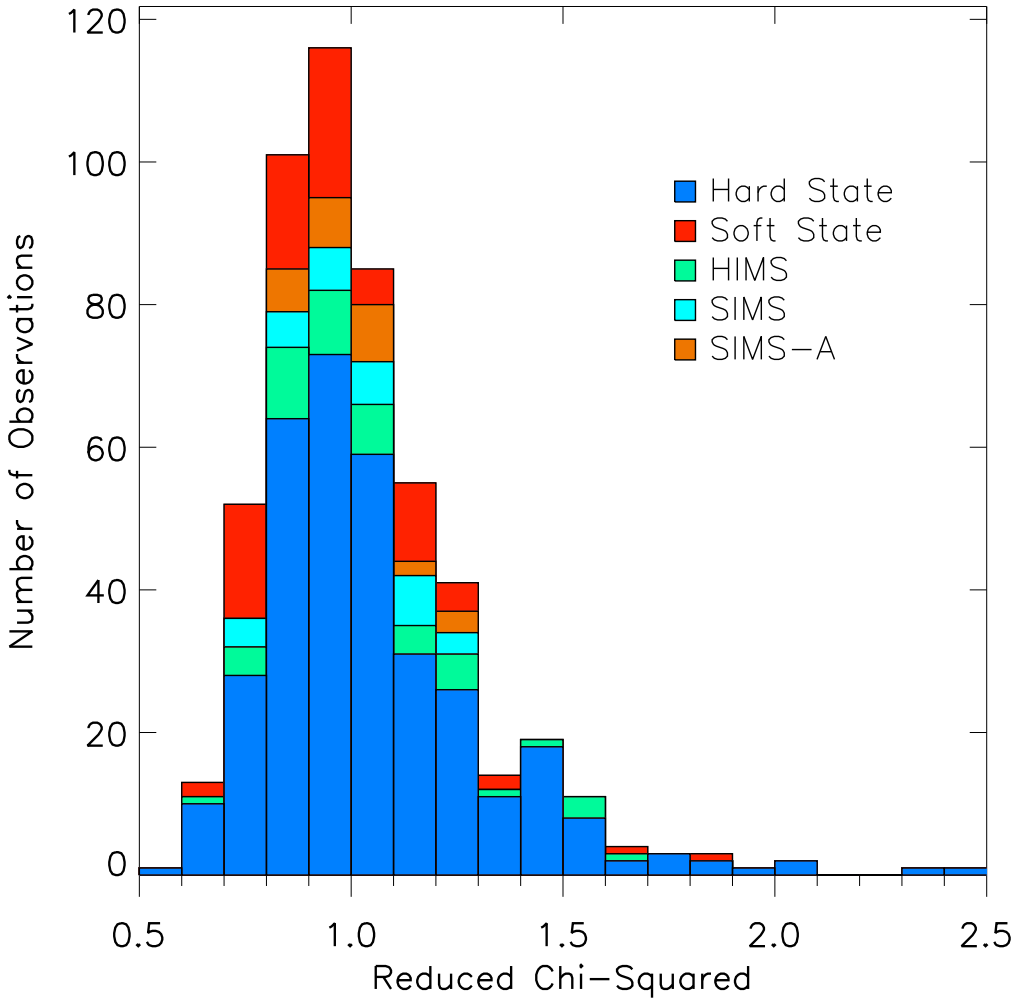

Figure 4.14: The reduced-χ^2 distribution for each best-fit model in the analysis, with 95% of observations reporting ≤ 1.5.

exclusively assumed are not the full description of the X-ray spectra from BHXRBs. For example, in the AGN community much controversy exists due to the potential effect of absorption, and in particular the level, even in some cases presence, of reflection (Miller *et al.*, 2008b). I note, however, that no hallmarks of absorption, such as dips, eclipses or narrow lines, have been observed from this source (Ponti *et al.*, 2012). It should be noted though that the reflection spectrum will also be influenced by photons emitted in the disc (Ross and Fabian, 1993, 2007), and this is not currently accounted for by XILLVER, nor is it in any other publicly available reflection model. This is most likely to have an effect in the soft state where the disc is very strong, and has yet to be investigated in detail. Another caveat is that the reflection spectrum is angle-dependent. This effect is reduced at high levels of ξ observed from BHXRBs (García *et al.*, 2014), so despite the uncertain inclination of

GX 339−4 (see §1.6) this should not significantly affect the results. The reflection should also be dependent upon the geometry of the corona (reflection models use a point source, known as the 'lamppost' model), but this is not as well explored in the literature. In addition, I note that in softer states the statistics in the *HEXTE* data were significantly poorer, thus the reflection is less well constrained, and potentially more suspect to degeneracy. Finally, the chi-squared distribution is excellent, with 95% of observations having a reduced chi-squared of ≤ 1.5 (Figure 4.14).

4.5.4 Why is the reflection spectrum more ionised in the soft state?

In §4.4.5 I analyse the ionisation parameter, defined as the ratio of the illuminating flux and the gas density, where it emerges that the parameter is significant larger in the soft state. This would appear at odds with the state of the illuminating flux, which typically peaks in the brighter stages of the hard state and subsequent transition into the HIMS (Figure 4.7). To explain this one important aspect to consider is the increased disc emission in the soft state, which will undoubtedly have an ionising affect on the surface layers in addition to the illumination from the corona above. To this end Ross and Fabian (2007) investigated the impact of the disc, finding that increased thermal radiation and peak temperature will ultimately result in a more ionised spectrum. In particular, the Fe profile is strongly affected as a result of higher ionisation stages and greater Compton-broadening. My chosen reflection model (XILLVER) does not account for change in the thermal emission throughout the outburst, and thus is likely to react to changes in the disc by varying the ionisation parameter, in particular with an increase in softer states.

Another explanation for the apparent change in illumination could result from varying the area of the disc and thus the solid angle it subtends below the corona. If the inner accretion disc is truncated then the amount of Comptonised photons intercepted by the disc will decrease rapidly. Furthermore, assuming a lamppost geometry, the illumination pattern should roughly go as R^{-3}, thus the reprocessed spectrum will be dominated by emission from the most central region, which in turn likely represents the most ionised zone of the disc because of the peaked illumination there. Even with a small level of truncation the inferred ionisation level will probably diminish significantly, and this contrast may also be heightened if light-bending is at play (see Figure 4.12). This argument works well since, as discussed in §4.5.3, high-resolution spectroscopy resolves the inner disc to be truncated and of a lower ionisation stage in the hard state (Chapter 3).

4.6 Conclusions

In this study I have performed a comprehensive and systematic investigation of X-ray reflection from GX 339−4. In total I analysed 528 observations made by *RXTE*, covering the three full outbursts between 2002 and 2007. This represents the largest study of X-ray reflection applying a self-consistent treatment to date, and in particular such excellent monitoring has allowed a thorough investigation of state transitions, in addition to the canonical hard and soft states (Figure 4.2). Each observation was well described by a combination of thermal disc emission (DISKBB), a cut-off power-law (CUTOFFPL) and relativistically blurred reflection (RELCONV∗XILLVER). All hard state and some HIMS observations did not require a disc due to the 3 keV lower limit to the PCA bandpass, while the bright stages of the hard state display a decreasing high-energy cut-off as the source luminosity rises (Figure 4.6). X-ray reflection is required for the entire duration of the study.

I pay particular detail to how the power-law and reflection co-evolve throughout the outburst which display a very strong positive correlation throughout each state (Table 4.3). Since the reflection arises as a consequence of the power-law irradiating the disc, contrasting evolution acts as a strong indicator of geometrical changes. The hard state is distinctly reflection weak with a typical reflection fraction (the ratio of reflection and power-law flux) of ~ 0.2. The reflection fraction does, however, increase as the source luminosity rises, and is fitted by a slope of ~ 1.2 and ~ 1.7 in the fainter and brighter stages of the hard state rise respectively (Figures 4.7a and 4.7b). The latter indicates a change in the dynamic behind the increasing reflection fraction and occurs during the phase where the high-energy cut-off in the Comptonised emission decreases (Figure 4.6). In stark contrast, the soft state represents a period of strong reflection whereby the reflection fraction exceeds unity for almost the entire state. Furthermore, while there is some scatter, the fitted slope to the 2004 and 2007 outbursts is 0.49 ± 0.17, signifying an increase of the reflection dominance over the power-law emission. As the source decays into the hard state the reflection fraction returns to the same magnitude and slope as in the rise, hence whether the source is heading towards or out of quiescence the accretion geometry is likely to be the same.

I discuss what is driving the contrast between the reflection and power-law in §4.5.1. The favoured interpretation is a truncated inner disc radius and decreasing illuminating source height for the hard and soft states respectively (see Figure 4.12 for an illustration). The hard state inner accretion disc of GX 339−4 was recently found to be truncated, and decreases in radius with increasing luminos-

ity (Chapter 3), which explains qualitatively how the low reflection fraction can be achieved whilst gradually promoting its increase. Softening of the power-law photon index (§4.4.1), a decreasing high-energy cut-off, and a low ionisation parameter (§4.4.5 and §4.5.4) all add strength to the truncated disc interpretation. The decay in disc flux and temperature should directly follow that of a black-body for a constant disc area ($S_{\rm disc} \propto T^4$; Eq 1.6). The soft state tracks a very similar relation of $T^{4.13\pm0.04}$(1σ; Figure 4.10) implying that the inner disc radius is constant and at the ISCO. This immediately explains how the reflection fraction is able to reach unity (essentially a solid angle of 2π) and confines geometrical changes to the corona. I interpret the increase in reflection fraction as the source decays through a decreasing corona height, strengthening the disc illumination and the effects of light-bending.

5

The low/hard state of GX 339−4 with the *XMM-Newton* small window mode: truncation of the disc inner radius?

In this Chapter I analyse three recent observations of GX 339−4 in the hard state, taken during the decay of a bright (peak $\sim 0.05\,L_{Edd}$) failed outburst. Uniquely, these are the first *XMM-Newton* observations of this source using an imaging mode, which significantly enhances the calibration certainty of the data at hand. In particular, thanks to the larger available bandpass, this allows an unprecedented constraint of the thermal accretion disc component and the level of photoelectric absorption. As in Chapter 3, I measure the disc inner radius from the broadened Fe line, but crucially I also measure the inner radius simultaneously from the disc component. I show that the fitted radii agree, which offers compelling evidence that the accretion disc is truncated in the hard state.

5.1 Introduction

The accretion geometry in the hard state is arguably one of the most controversial ambiguities in the BHXRB community today. The truncated disc model is based around the radiatively inefficient flow solutions (e.g. ADAFs; §1.3.1) that can successfully explain accretion at very low $\dot{M}$. In this regime the accretion disc is highly truncated to hundreds or even thousands of gravitational radii (Esin *et al.*, 1997), and so as the accretion rate rises the disc gradually penetrates further into the hot flow (Remillard and McClintock 2006; Done *et al.* 2007; Chapter 1). This is able to explain a number of observables at increasing accretion rates; such as the softening of the power-law component (Chapter 4) and the increase of characteristic frequencies in the power spectra (van der Klis, 2006; Done *et al.*, 2007).

The two leading spectroscopic methods to measure the inner radius come through the thermal accretion disc component and the broadened Fe line from X-ray reflection (see §1.5 for these details of these two techniques). However, as described in Chapter 3, attempts to determine the inner radius of the disc in this manner have led to conflicting results, to the extent that some evidence suggests that the accretion disc may be at the ISCO at as low as $10^{-3}\,L_{Edd}$ (Reis *et al.*, 2010). Furthermore, the spin estimates derived from these two methods do not agree for a number of sources (see e.g. Reis *et al.* 2008 and Shafee *et al.* 2006), despite recent efforts to resolve the disparity. Key to resolving this debate is to simultaneously measure the inner disc radii through both methods. However, a recent study by Kolehmainen *et al.* (2014) using six hard state *XMM-Newton* EPIC-pn timing mode observations of four BHXRBs found the disc and reflection derived inner radii to highly disagree.

In this Chapter I attempt to simultaneously measure the disc and reflection inner radius using three recent observations taken in the small window science mode. These data can potentially achieve a much better constraint on the accretion disc component due to the superior bandpass calibration, and thus offer the most stringent test yet of the two methods and the truncated disc model for the hard state.

5.2 Observations and Data Reduction

GX 339-4 was observed with *XMM-Newton* three times beginning in September 2013 over a period of three days (Table 5.1). These observations took place during the decay of a failed outburst[1] where the source remained in the hard state,

[1] A failed outburst refers to an outburst where the source did not complete a full outburst cycle, and instead remained in the hard state until it again returned to quiescence.

	ObsID	Date	Net Exposure (s)	Count Rate (cts/s)
1	0692341201	2013-09-29 22:49:07	8 540	166 (59)
2	0692341301	2013-09-30 22:29:33	9 426	162 (60)
3	0692341401	2013-10-01 18:25:29	15 036	154 (57)

Table 5.1: An observation log of the *XMM-Newton* datasets taken in September 2013, and used in this study. Net exposures correspond to that remaining after the reduction process and the live time of the science mode (71%) is taken into account. Count rates in brackets refer to the count rate after the data have been corrected for pile-up.

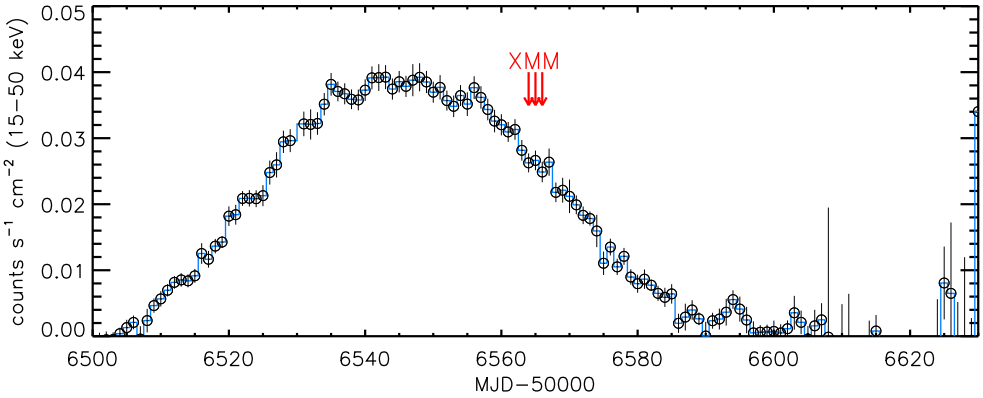

Figure 5.1: A Swift-BAT (15–50 keV) light-curve of the 2013 failed outburst of GX 339−4. The three *XMM-Newton* observations used in this study are indicated, which caught the source after the peak of the outburst. Throughout this period the source remained in the hard state.

reaching a peak X-ray luminosity of $\sim 0.05\,L_{Edd}$ (Fig. 5.1). The EPIC-pn (Strüder *et al.*, 2001) and EPIC-MOS (Turner *et al.*, 2001) cameras were operated in their small window modes, and the 'thin' optical blocking filter was used. In this study I only use the EPIC-pn data since the EPIC-MOS suffers significantly more from the effects of pile-up[2].

Using the *XMM-Newton* Science Analysis System (SAS) version 13.5.0, I reduced the raw observation data files (ODFs) following the procedure outlined in Chapter 2, applying the most recent current calibration files (CCFs). Spectra were extracted through EVSELECT using a circular region with a radius of 900 pixels centred on the source. Background regions were extracted using a circular region of the same size located away from the source, but were only ~ 0.5 % of the source count rate. The nominal calibrated bandpass of the EPIC-pn small window mode is 0.3–10 keV. I found there to be a slight residual in Observation 3 below 0.4 keV when

[2]By a factor of >5: XMM Users Handbook
(http://xmm.esac.esa.int/external/xmm_user_support/documentation/uhb/epicmode.html)

compared to Observations 1 and 2, which was also clear in the pattern distribution produced by EPATPLOT. The pattern distribution of Observations 1 and 2 showed a similar feature, but below 0.3 keV (Fig. 5.2). The origin of this feature is unknown, and since Observation 3 has the best statistics due to the considerably longer exposure (Table 5.1), I used a lower limit of 0.4 keV for all spectra in case the residual was not so obvious in Observations 1 and 2. I also ignored the 1.75–2.35 keV region which contains strong features, which are likely to be of instrumental origin (see also Chapter 3).

I applied the SAS tool EPATPLOT to all of the data sets to check for photon and pattern pile-up, which was found to be high in all three observations (Fig. 5.2). To mitigate the pile-up I investigated a number of annulus extraction regions for the spectra, and found an inner cavity with a radius of 230 pixels to be highly acceptable. This reduced the estimated level of pile-up to be less than 1% for both the single and double events between 0.4–10 keV (Fig. 5.2). The X-ray flux of BHXRBs is very variable, particularly in the hard state, and flares could lead to unique piled-up events. Therefore, for this reason, I ensured the pile-up level was as minimal as possible. All of the analysis in this Chapter was performed using XSPEC v.12.8.0, and all quoted errors are at the 90% confidence level.

5.3 Analysis and Results

I analysed the background-corrected light-curves of each observation, which were producing using the SAS task EPICLCCORR (Fig. 5.3). All three observations show a high level of variability, which is a common feature of the hard state (see e.g. van der Klis 2006; Muñoz-Darias *et al.* 2011). There was, however, little to distinguish between the three observations, and this was confirmed by the time-average spectra (Fig. 5.4), which shows that the three epochs are very similar. In all three spectra there also appears to be a slight excess at 6–7 keV, suggesting that a strong Fe Kα line is present.

To model the spectrum I began by fitting an absorbed power-law, which is often successfully used to describe the hard state (Chapters 3 and 4). To model the X-ray absorption throughout this Chapter I used the package TBNEW_FEO[3], which represents a simplified version of the leading model TBNEW often applied to grating spectra (Wilms *et al.*, 2000). The fit was reasonable ($\chi^2_\nu/\nu = 1.43/5238$; Table 5.2), although not formally acceptable, and both the photon index and column density

[3]In this Chapter I used the 'wilm' abundance and 'vern' cross-sections in XSPEC

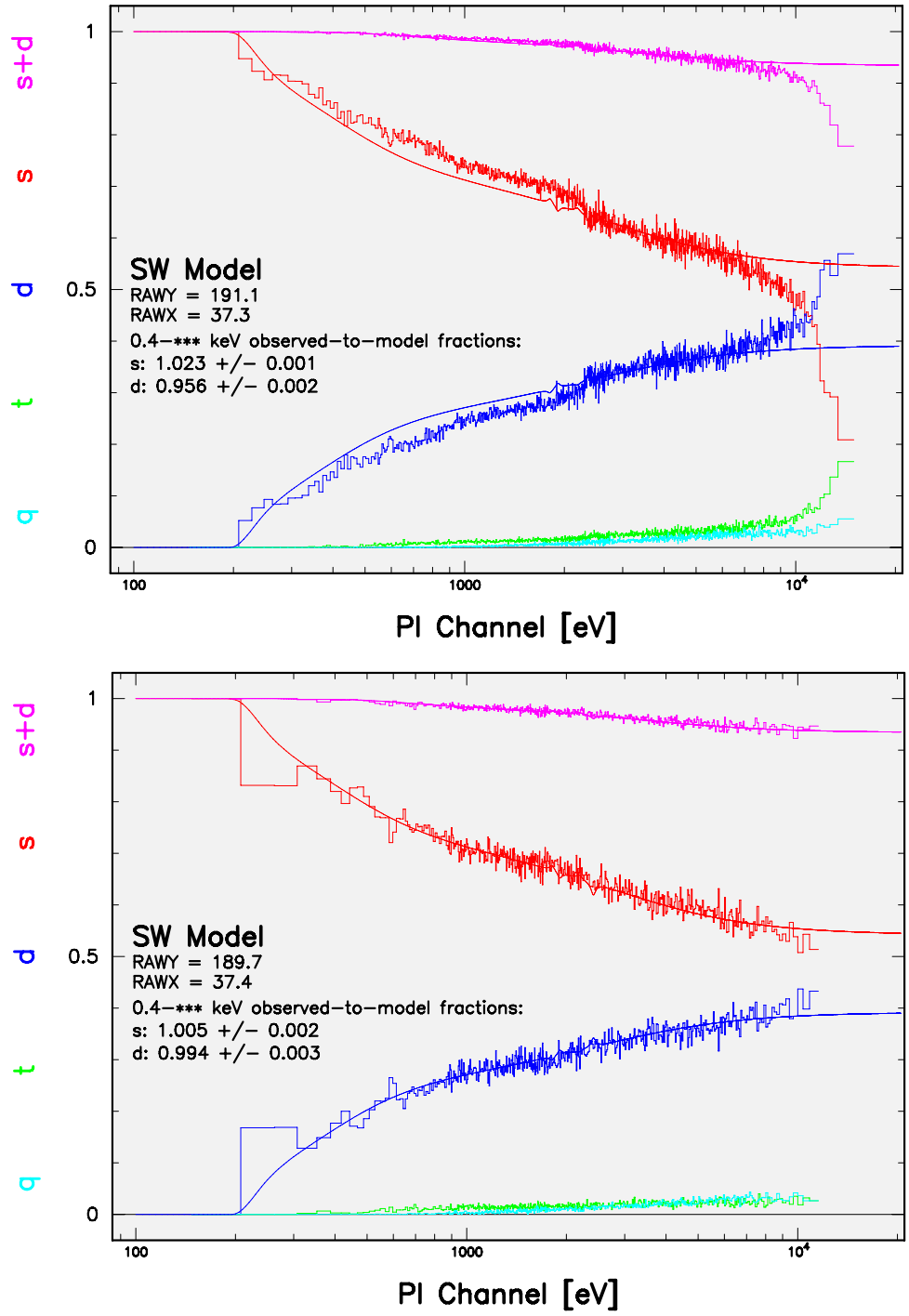

Figure 5.2: Estimates of pile-up in the *XMM-Newton* EPIC-pn observation 1 (Table 5.1) using the SAS task EPATPLOT. Data points represent the fraction of events recorded as singles (s), doubles (d), triples (t) and quadruples (q). The respective solid lines show the expected value if the data were not piled-up. The top figure uses a full extraction region, which shows clear deviations from the expected fractions, and is hence substantially piled-up. The bottom figure uses an annulus of 230 pixels and is in contrast free from pile-up.

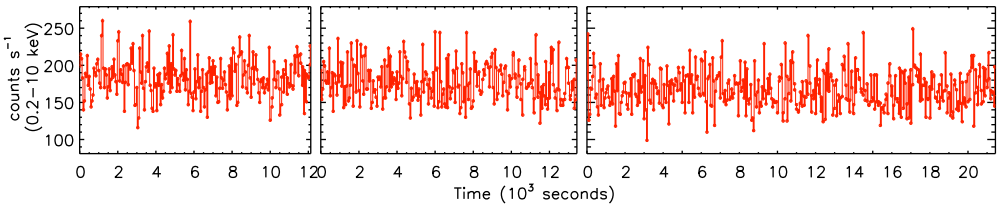

Figure 5.3: The *XMM-Newton* EPIC-pn (0.2–10 keV) light-curve of GX 339−4. There is little variability between the observations suggesting that the time-averaged spectra across all three epochs will be similar. The light-curves also display large intrinsic variability typical of the hard state (van der Klis, 2006).

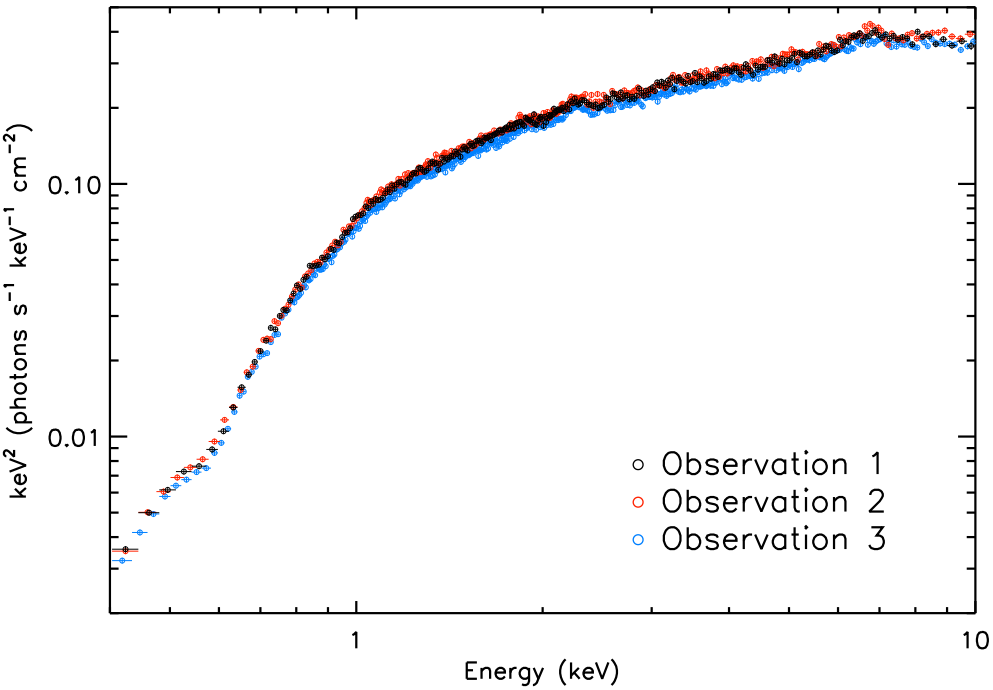

Figure 5.4: The unfolded spectra of the three hard state observations of GX 339−4 used in this study. The spectra are evidently very similar and suggest little spectral evolution between the three observations. There is a slight excess at $\sim 6.4 keV$ indicative of Fe Kα emission.

were typical for GX 339−4 in the hard state (Chapter 3). In particular, a strong excess at ∼7 keV, and drop above 8.5 keV was evident, suggesting a significant amount of X-ray reflection was present. Also, an excess peaking at ∼ 1 keV and a strong edge at 0.6 keV were clear residuals in the spectra.

The excess at ∼ 1 keV is likely to be due to thermal emission from the accretion disc, which is often observed from hard state sources with soft X-ray instruments (Miller *et al.* 2006a; Reis *et al.* 2009; Kolehmainen *et al.* 2014; Chapter 3). I therefore added a multi-colour disk-blackbody model (DISKBB) which considerably improved the fit (χ^2_ν/ν=1.22/5232; Table 5.2); however, strong residuals still remained

below 0.7 keV.

A power-law is of course not a physical model, and can lead to an excess of photons at low energies. Assuming that the hard power-law tail arises through Comptonisation of disc photons, there should be a low-energy cut-off associated with the disc temperature. I therefore replaced the POWERLAW model with NTHCOMP, which describes a thermal Comptonisation spectrum and is commonly accepted to be correct for the hard state[4]. This model includes a high energy cutoff, parameterised by the electron temperature kT_e, which I fixed to be 50 keV. Because of the soft bandpass used in this study this parameter could not be constrained, but the cut-off is not expected to affect the spectrum $<$10 keV. This model also includes a low energy rollover, defined by a seed photon temperature kT_{bb}, which I link to the temperature of the DISKBB component. To this end I also set the seed spectrum to be a disk-blackbody. The other free parameters were the photon index and normalisation, like for the POWERLAW model. Using NTHCOMP the fit was in fact slightly worse (χ^2_ν/ν=1.23/5232; Table 5.2), but not significantly. Nevertheless, I continued with this model since it represents a physical description of the continuum.

A strong edge still remained at $\sim$ 0.6 keV, which is coincident with the O K edge at 0.54 keV (see e.g. Wilms *et al.* 2000). I therefore allowed the O abundance to be a free parameter, which further improved the fit (χ^2_ν/ν=1.17/5229; Table 5.2). All of the observations settled on an O abundance of $\sim$ 1.34, and meant that the soft bandpass was now excellently fit (χ^2_ν=1.04 below 5 keV).

Figure 5.5 shows the model residuals to the best-fit continuum model (Model–4 in Table 5.2), which displays a strong Fe Kα emission line and corresponding edge. To model this I use the X-ray reflection model RELXILL which combines the relativistic RELCONV code of Dauser *et al.* (2010) and the angle-resolved X-ray reflection table XILLVER of García *et al.* (2014). This represents the first code to prescribe the correct reflection spectrum for each relativistically calculated emission angle, as apposed to the usual relativistic convolution treatment to the spectrum (e.g. RELCONV$*$XILLVER).

Following Chapter 3 I assumed an emissivity profile of R^{-3} and a spin of 0.9. I also linked the photon index in NTHCOMP to the illuminating index in RELXILL. The ionisation parameter ξ (Eq. 1.8), the disc inner radius r_{in}, and the model normalisation were all fitted freely. Finally, the inclination was fitted jointly by the three spectra. For all three observations the inner radius was found to be mod-

[4]For example, Chapter 4 displays evidence of the high-energy cut-off, which is thought to represent the electron temperature of the corona and acts as evidence for thermal Comptonisation. See also the review by Done *et al.* 2007.

Parameter	Model–1	Model–2	Model–3	Model–3b
		Observation 1		
N_H (10^{22} cm^{-2})	0.52 ± 0.01	0.64 ± 0.02	0.64 ± 0.02	0.64 ± 0.02
A_O				1.34 ± 0.06
T_{in}		0.21 ± 0.01	0.20 ± 0.01	0.19 ± 0.01
N_{BB} (10^3)		$7.89^{+3.75}_{-2.67}$	$10.76^{+4.86}_{-3.53}$	$24.83^{+9.40}_{-7.21}$
Γ	1.61 ± 0.01	1.59 ± 0.01	1.62 ± 0.01	1.63 ± 0.01
N_{Comp}	0.17 ± 0.01	0.16 ± 0.01	0.16 ± 0.01	0.17 ± 0.01
χ^2/ν	2290/1705	2011/1703	2026/1703	1943/1702
		Observation 2		
N_H (10^{22} cm^{-2})	0.51 ± 0.01	0.61 ± 0.02	0.61 ± 0.02	$0.61^{+0.02}_{-0.01}$
A_O				1.30±0.06
T_{in}		0.23 ± 0.01	0.22 ± 0.02	0.20 ± 0.01
N_{BB} (10^3)		$4.29^{+2.02}_{-1.43}$	$5.77^{+2.67}_{-1.92}$	$13.32^{+5.37}_{-4.02}$
Γ	1.60 ± 0.01	1.57 ± 0.01	1.60 ± 0.01	1.61 ± 0.01
N_{Comp}	0.17±0.01	0.16±0.01	0.16±0.01	0.16±0.01
χ^2/ν	2453/1743	2158/1741	2173/1741	2106/1740
		Observation 3		
N_H (10^{22} cm^{-2})	0.51±0.01	0.62±0.01	0.61±0.02	0.61±0.02
A_O				1.34±0.05
T_{in}		0.23±0.01	0.22±0.01	0.20±0.01
N_{BB} (10^3)		$4.09^{+1.45}_{-1.10}$	$5.56^{+1.91}_{-1.48}$	$13.05^{+3.14}_{-3.97}$
Γ	1.60±0.01	1.55±0.01	1.59±0.01	1.60±0.01
N_{Comp}	0.16±0.01	0.15±0.01	0.15±0.01	0.15±0.01
χ^2/ν	2735/1790	2195/1788	2220/1788	2092/1787

Table 5.2: Results from various continuum model fits.
Model–1: TBNEW-FEO∗(POWERLAW)
Model–2: TBNEW-FEO∗(DISKBB+POWERLAW)
Model–3: TBNEW-FEO∗(DISKBB+NTHCOMP)
Model–3b: The same as Model–3, but the O abundance in TBNEW-FEO (A_O) is now a free parameter.

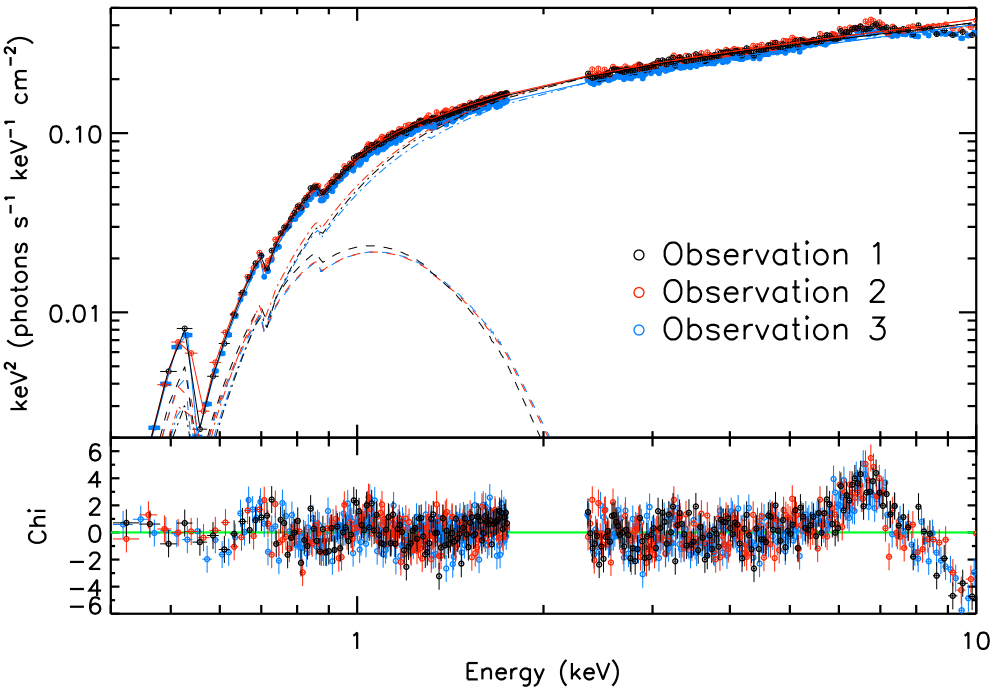

Figure 5.5: Unfolded spectra and model residuals to the best-fit continuum model (Model–4; Table 5.2). There is a clear excess and edge around 7 keV, which strongly suggests an Fe emission line and corresponding edge are present in the spectra.

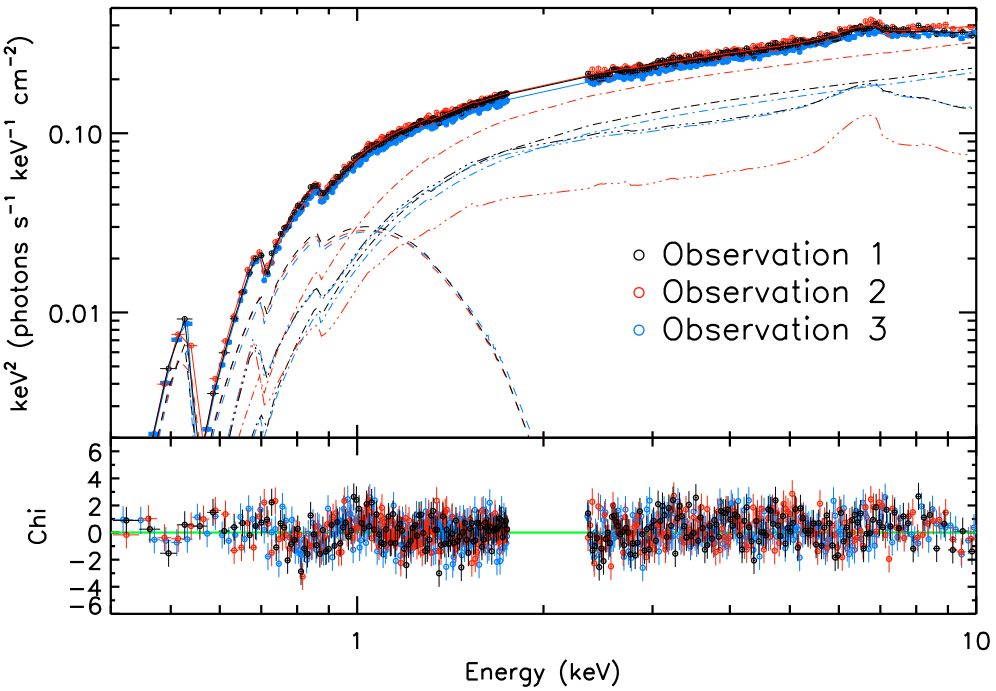

Figure 5.6: Unfolded spectra and model residuals to the best-fit continuum+reflection model (Table 5.3), which represents an excellent fit over the entire bandpass.

Parameter	Observation 1	Observation 2	Observation 3
N_H (10^{22} cm^{-2})	$0.76^{+0.01}_{-0.02}$	0.74±0.01	$0.74^{+0.03}_{-0.02}$
A_O	$1.52^{+0.03}_{-0.06}$	$1.50^{+0.05}_{-0.04}$	$1.55^{+0.04}_{-0.02}$
T_{in}	0.16±0.01	0.16±0.01	0.17±0.01
N_{BB} (10^5)	$1.34^{+0.28}_{-0.18}$	$1.09^{+22.1}_{-0.19}$	$0.89^{+0.43}_{-0.20}$
$r_{in(BB)}$	25^{+3}_{-2}	29±3	26^{+3}_{-6}
Γ	1.62±0.02	1.65±0.01	$1.59^{+0.02}_{-0.03}$
N_{Comp}	0.092±0.01	0.14±0.01	0.08±0.01
$r_{in(Ref)}$	21^{+17}_{-9}	27^{+6}_{-6}	16^{+7}_{-4}
$i(^\circ)$		30^{+5}_{-4}	
$\log\xi$	3.17±0.06	$3.03^{+0.05}_{-0.03}$	$3.17^{+0.06}_{-0.05}$
N_{Ref} (10^{-6})	0.34±0.03	$0.26^{+0.03}_{-0.04}$	$0.32^{+0.03}_{-0.02}$
χ^2/ν		5322/5219	

Table 5.3: The best-fit model and MCMC derived 90% confidence limits for fits to the three GX 339−4 observations. The emissivity profile and black hole spin in RELXILL are fixed to be R^{-3} and 0.9 respectively. The inclination parameter is fitted jointly between the three spectra.

erately truncated at $\sim 20\,r_g$, and the fit was excellent over the whole bandpass (χ^2_ν/ν=5322/5219; Fig. 5.6). Given the excellent constraint on the disc emission allowed by the calibrated bandpass down to 0.4 keV, I also investigated how the inner radius derived from the disc compared to that from the reflection. The normalisation of DISKBB is defined as

$$N_{BB} = 1.19 \left(\frac{R_{in}}{D_{10\,kpc}} \right)^2 \cos i \tag{5.1}$$

where D is the distance to the source in units of 10 kpc, R_{in} is the disc inner radius in km, and i is the inclination of the disc, which I assume to be the same as fitted by the reflection component (Table 5.3). The 1.19 factor accounts for the spectral hardening factor f_{col} and that T_{in} occurs at a radius somewhat larger than r_{in} (Kubota *et al.*, 1998). I do note, however, that f_{col} may be larger in the hard state (see Chapter 4). After converting to gravitational radii[5] I found that the inner radii derived from the disc and reflection are very consistent (Table 5.3; Figure 5.7). To

[5] $1\ R_g = 14.78(M_{BH}/10M_\odot)$ km

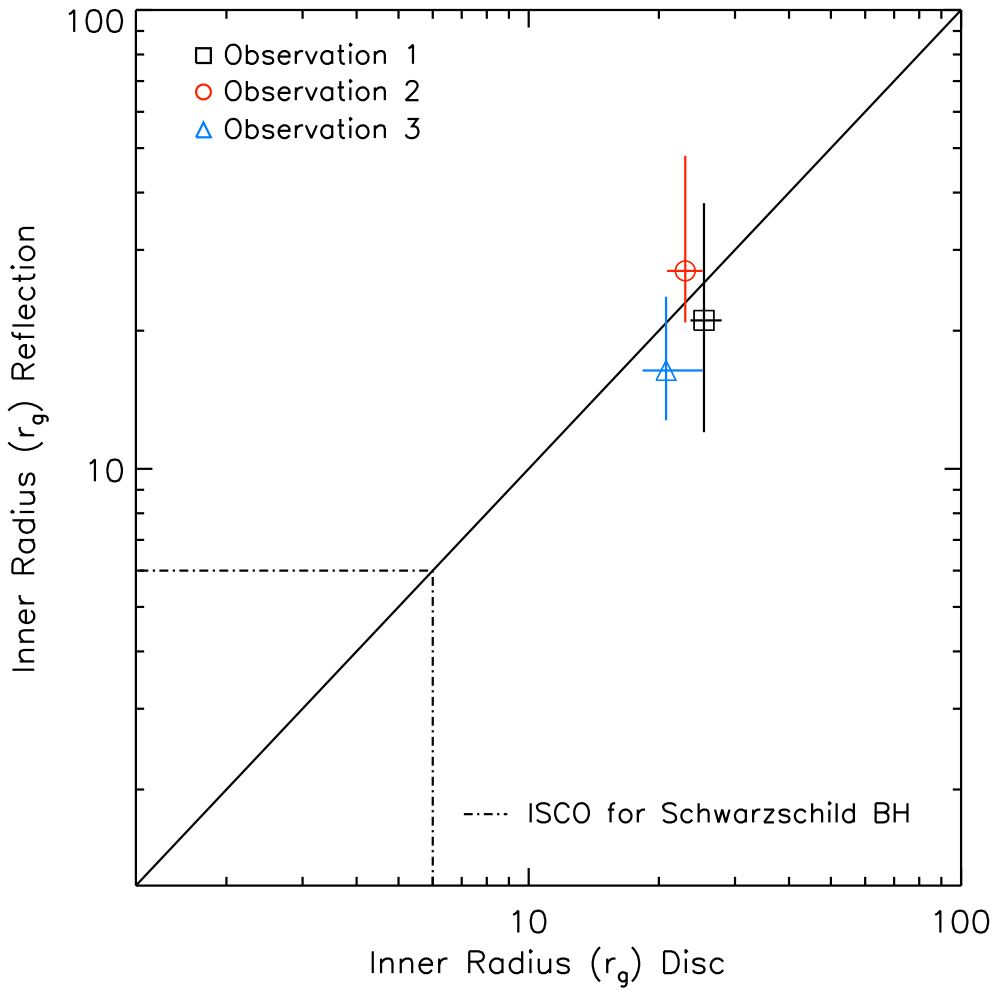

Figure 5.7: The inner radius of the accretion disc, fitted by the disc (x-axis) and reflection (y-axis) components. The methods agree quite well, and in particular the inner radius from the disc is very well constrained. The dot-dash line indicates the innermost stable circular orbit for a zero spin black hole, showing that both methods, from all three observations, are consistent with a truncated accretion disc.

probe this connection further I performed a MCMC analysis on the best-fit parameters. Following the procedure utilised in Chapters 2 and 3, I produced six 55,000 element chains, of which the first 5000 elements were discarded ('burnt'). Each chain was run from a random perturbation away from the best fit, and the chain proposal was taken from the diagonal of the subsequent covariance matrix. The probability distributions were assumed to be gaussian, and a rescaling factor of 5×10^{-4} was applied to ensure the rule-of-thumb 0.75 fraction of repeated values was obtained. The confidence limits derived from the resultant 300,000 element chain are presented in Table 5.3.

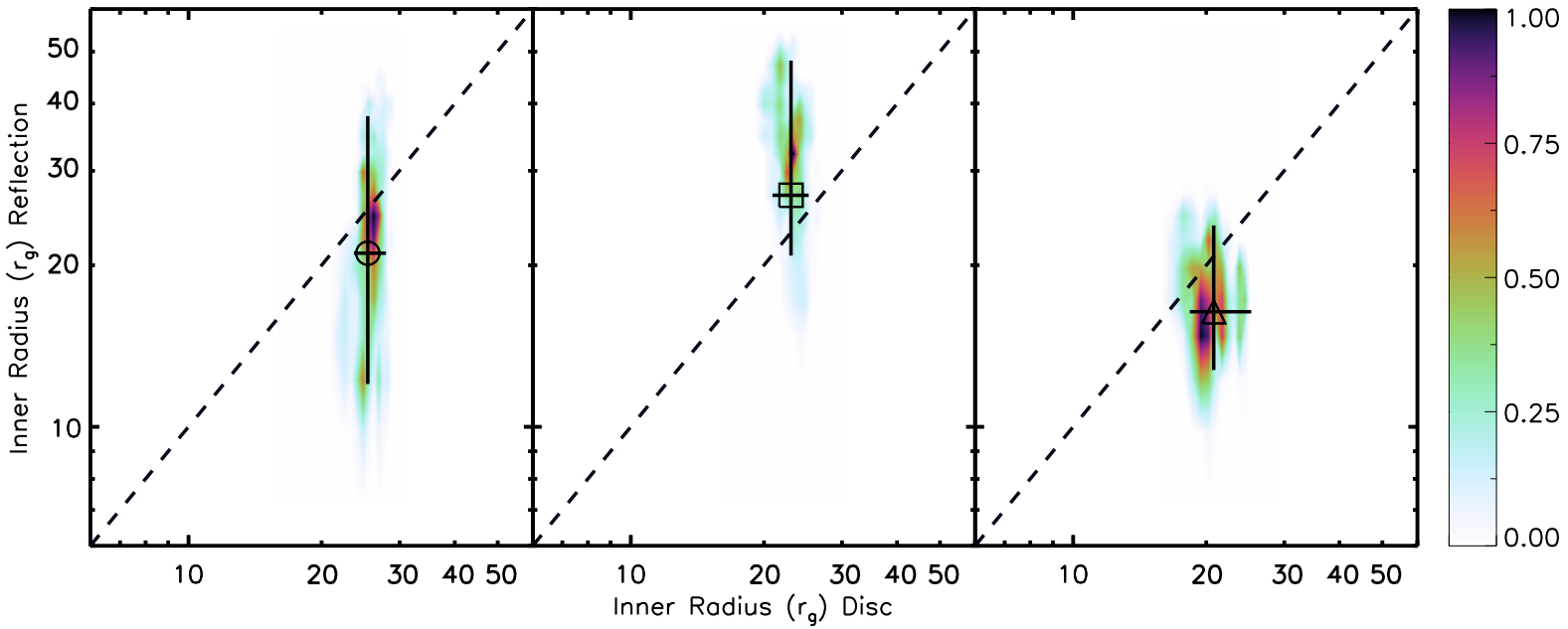

Figure 5.8: MCMC derived confidence intervals for the inner radius of the accretion disc from the disc (x-axis) and reflection (y-axis) components. The confidence density is scaled such that the maximum density value is 1, and thus displays good consistency with the over-plotted values from Table 5.3. The left, middle and right panels refer to Observations 1, 2 and 3.

Parameter	Observation 1	Observation 2	Observation 3
$r_{in(BB)}$	29^{+5}_{-4}	32^{+5}_{-4}	30 ± 4
$r_{in(Ref)}$	74^{+160}_{-31}	80^{+59}_{-27}	38^{+20}_{-12}
$i(^\circ)$		45	
χ^2/ν		5343/5220	

Table 5.4: The best-fit inner radii from the disc and reflection components when using $i = 45^\circ$. All of the other fit parameters were consistent at the 90% confidence level with those listed in Table 5.3.

The agreement between the inner radii calculated from the reflection and disc components is good, despite the relatively short exposure of the data. Figures 5.7 and 5.8 compares the respective radii and presents compelling evidence that the inner disc is truncated at 20–30 r_g. Furthermore, the disc component radii are extremely consistent between the three observations, despite the weakness of the component in the hard state. The confidence limits of the reflection radii are larger, but considering the short exposures and low flux this is to be expected, and the three observations are still consistent within the error bars.

5.4 Discussion and Conclusions

In this Chapter I have presented an analysis of three recent observations of GX 339−4 in the hard state, during the decay phase of a failed outburst. These observations utilised the small window science mode, and represents one of the first hard state observations of a black hole using an *XMM-Newton* EPIC-pn imaging mode. The importance of this is that it allows a well calibrated bandpass down to 0.3 keV, whereas the fast modes that are usually employed are restricted to above 0.7 keV. This also removes further calibration issues associated with the fast modes, such as how pile-up affects the spectrum (see Miller *et al.* 2010), the lack of source-free background regions (Ng *et al.*, 2010), and how to correct charge-transfer inefficiency at high count rates (see Walton *et al.* 2012).

In addition, the bandpass down to 0.4 keV allows an unprecedented constraint of the level of photoelectric absorption and the thermal quasi-blackbody component associated with the accretion disc. This allowed me to achieve an excellent constraint on the disc inner radius from both the disc and reflection components, which both agree on a moderately truncated inner disc.

The jointly fit inclination is smaller than expected, given the constraints dis-

cussed in §1.6. I re-analysed the observations fixing the inclination to $i = 45°$, which is a more reasonable value. The fitted radii increase, and the change was considerably larger for the reflection parameters (Table 5.4). As I show in Chapter 3, a higher inclination would act to increase the reflection inner radius, and from Eq. 5.1 would have the same effect on the inner radius from the disc component, so this change is expected. The larger confidence limits on the reflection parameters arise since at larger radii the effect on the profile is smaller. I note, though, that the fit is considerably worse when $i = 45°$ ($\Delta\chi^2 = +21$ for one less degree of freedom). As for the results in Chapter 3, the assumption of a spin of 0.9, and an emissivity profile of R^{-3} should have little effect on the results presented here. The disc is still truncated enough that the adopted value of spin will only have a very small effect on the line profile (Dauser *et al.*, 2010), and the emissivity profile will be roughly R^{-3} for a reasonable coronal height (e.g. $10\,r_{\rm g}$; Dauser *et al.* 2013). In comparison to the results in Chapter 3, this observation slots in between Observations 2 and 3. The fitted radii are significantly less; however, this may be, at least in part, due to the smaller fitted inclination which is known to have this effect (see Fig. 3.12). Also, following the analysis in Chapter 4, from Fig. 5.5 it would seem that the reflection is rather high in comparison to the Comptonised spectrum in Observations 1 and 3. Still, given the small variation in $r_{\rm in}$ from both methods over the three observations this would suggest that the result is not significantly affected. New observations with a longer exposure will allow the constraint on the reflection to be improved.

In all, this is the first time that the disc and reflection methods have been applied simultaneously to confirm the presence of a truncated accretion disc in the hard state, and adds to a growing body of direct evidence for the truncated disc model.

6

Conclusions & Future Work

The projects that collectively make up this thesis have aimed to resolve the controversy surrounding black hole spin estimates, and the state of the accretion disc in the hard state. In this Chapter, I summarise these works and discuss how they may impact future studies of BHXRBs.

Motivated by the lack of evidence for the spin powering of jets, and the discrepancy between many spin estimates via the reflection and continuum methods, Chapter 2 investigates the systematic uncertainties associated with the reflection technique. I discovered that for the best available data, and most current codes, model degeneracies can severely affect the determined value of spin. I showed that relativistic line models are particularly susceptible to this, and are ultimately unusable for measuring black hole spin. Self-consistent reflection models are less at risk, in part because the emission stage is hard-wired into the model, but nevertheless, they can be significantly affected as well. I isolated the inclination parameter to be particularly degenerate, and emphasised the need for additional constraints on the disc inclination, through the binary system or jet inclination. I also found that two of the published spin estimates are likely to be incorrect.

Uncovering these uncertainties motivated the approach of Chapter 3. A number of spin estimates through the reflection method have taken place during the hard state, where a range of evidence points towards the disc being truncated from the

ISCO. The reflection method is often applied to single high-resolution observations (e.g. with *XMM-Newton*), and is thus highly susceptible to the degeneracies uncovered in Chapter 2. I instead simultaneously analysed four observations of GX 339−4 in the hard state, covering over two magnitudes in luminosity. This allowed me to jointly fit degenerate parameters like the unknown disc inclination, which should remain constant. I then revealed that in fact the disc is substantially truncated from the ISCO, which therefore renders spin estimates impossible in the hard state. This analysis included the dataset that had previously been used to measure the spin of GX 339−4. Furthermore, I showed that as the source luminosity increases the disc inner radius moves closer to the black hole, which is a key component of the truncated disc model. I also rigorously tested this result through MCMC analysis, different bandpass lengths, alternative emissivity scenarios, a full range of inclination values, and found it to be very secure.

The number of high-resolution observations is greatly limited; however, whilst *RXTE* has much poorer spectral resolution, it offers an outstanding number of observations. In Chapter 4 I therefore analysed over 500 observations of GX 339−4 with *RXTE*, covering three full outbursts, to investigate how the power-law and reflection components co-evolve. In a quantitative manner this is highly revealing since reflection arises from the power-law irradiating the disc, so for a stable accretion geometry the two should evolve linearly. If they do not, this signals changes in the accretion geometry. I showed that in the hard state the reflection/power-law ratio increases as the source luminosity rises, consistent, as found in Chapter 3, with the inner disc moving inwards allowing more photons to be reflected. This ratio approaches one during the state transition, suggesting the disc is then close to the ISCO, and after continues to increase as the source decays through the soft state. Since the inner disc is consistent with being at the ISCO in the soft state (via the L–T^4 relation), this reveals that the increasing ratio *must* be promoted by the corona, which is consistent with it undergoing a gradual collapse.

One can measure the inner radius of the accretion disc via the disc or reflection component. The former is suited to the soft state, where the disc accounts for $> 80\,\%$ of the X-ray flux; however, the disc flux swamps the Fe line used to measure the spin via reflection, and also presents a highly curved continuum upon which the Fe line is superimposed, which makes determining the relativistic broadening of the Fe line difficult. Ideal for the reflection method is a simple power-law continuum, such as in the hard state; however, then the disc flux and peak temperature are significantly reduced, making it extremely difficult to constrain. To this end, a recent attempt by Kolehmainen *et al.* (2014) with *XMM-Newton* timing mode data found

the two methods to highly disagree in the hard state. The small window science mode of the *XMM-Newton* EPIC-pn camera can limit the extent of pile-up from a BHXRB and also offer an unprecedented bandpass calibration down to 0.3 keV. This allows the disc and photoelectric absorption to be well determined, and thus enables the inner disc radius to be accurately measured via both the disc and reflection simultaneously. In Chapter 5 I analyse three new hard state observations of GX 339−4 taken with the small window science mode, which had previously only been observed in the less well calibrated fast modes. As in Chapter 3, I jointly fit the degenerate inclination parameter, and then compare the simultaneously resolved disc and reflection components. I find that they both agree on a truncated inner accretion disc, and offer further compelling evidence for the truncated disc model in the hard state.

There are a number of general conclusions that can be drawn from these studies.

- Firstly, the measurement of black hole spin, at least through the reflection method, is much more uncertain than previously realised. This may be the reason for the lack of evidence for the spin powering of jets from BHXRBs, and the discrepancy between continuum and reflection spin estimates for some BHXRBs.

- Secondly, the detection of broad iron lines in the hard state as evidence for an accretion disc at the ISCO appears to be in jeopardy. Instead, X-ray reflection in the hard state shows that not only is the disc inner radius truncated, but it is also consistent with a gradual move inwards as the source luminosity rises.

- Thirdly, X-ray reflection can also be used to probe the form of the corona, and has revealed it must gradually collapse as the soft state progresses, which may be linked to the eventual state transition back to the hard state.

- Finally, applied correctly, and through systematic analysis, X-ray reflection is a robust and powerful technique to probe the regions close to a black hole.

6.1 Future Work

The work presented in this thesis has established new insights into the geometry of accretion on to black holes. However, it is heavily dependent upon one source, GX 339−4. This source was employed because it frequently undergoes outburst, which has led to it assuming an extensive archive of X-ray observations for a transient

source, particularly in the hard state. To this end, GX 339−4 has come to define a significant amount of what we understand about transient BHXRBs. However, this of course presents the danger that GX 339−4 is not a 'typical' source, if such a thing exists, and this was highlighted in recent years by the revelation that a number of sources are 'radio-quiet', in that they do not follow the empirical non-linear X-ray–radio correlation originally established by GX 339−4 (Corbel *et al.*, 2003; Gallo *et al.*, 2003; Coriat *et al.*, 2011; Gallo *et al.*, 2012; Corbel *et al.*, 2013a).

It is therefore crucial that we extend these studies towards a number of other transient sources. As highlighted before, GX 339−4 was used in Chapter 3 because it offers the best coverage of the hard state with high-resolution instruments; however, this still only amounted to four observations. Applying the same systematic method to another transient source is not currently possible due to a lack of observations, and will instead form the focus of forthcoming *XMM-Newton* proposals in order to increase the demography of accretion in the hard state. Furthermore, in light of Chapter 5, which utilised relatively short exposures, the case to increase the number of BHXRB observations with high-resolution instruments has certainly been strengthened.

With *RXTE* a number of sources have been observed over the full outburst cycle, thus the natural progression is to extend Chapter 4 into a global study of accretion in BHXRBs. This is an immediate aim of mine, and would provide a valuable test of whether the accretion evolution revealed in GX 339−4 holds for all BHXRBs. It seems from the literature that a number of 'radio-quiet' sources have weaker (smaller EW) Fe lines, which would be robustly tested by this study. Furthermore, it has been suggested that the X-ray corona is in fact the launching point of the jet (Beloborodov, 1999; Markoff *et al.*, 2005), and may be behind the weaker reflection. Ultimately as well, this study has the potential to constrain the geometry of the corona, since it will sample sources over a range of inclination.

Looking further forwards, the recent arrival of *NuSTAR*, which will be followed next year by *Astro-H*, will offer new and improved insights into accretion in BHXRBs. In particular, they present a significant advance in monitoring above 10 keV, and thus combine the benefits of a broad bandpass (Chapter 4) with detail allowed by high-resolution spectroscopy (Chapters 3 and 5). These observatories, in addition to further observations with the current instruments, will be key to establishing how the accretion geometry evolves in outburst.

BIBLIOGRAPHY

Abramowicz M. A., Czerny B., Lasota J. P., Szuszkiewicz E., 1988, Astrophys. J., 332, 646

Anders E., Grevesse N., 1989, Geochimica et Cosmochimica Acta, 53, 197

Baldwin J. A., 1977, Astrophys. J., 214, 679

Ballantyne D. R., Ross R. R., Fabian A. C., 2001, Mon. Not. R. Astron. Soc., 327, 10

Balucinska-Church M., McCammon D., 1992, Astrophys. J., 400, 699

Bardeen J. M., Press W. H., Teukolsky S. A., 1972, Astrophys. J., 178, 347

Beckwith K., Done C., 2004, Mon. Not. R. Astron. Soc., 352, 353

Belloni T., Homan J., Casella P., van der Klis M., Nespoli E., Lewin W. H. G., Miller J. M., Méndez M., 2005, Astron. Astrophys., 440, 207

Belloni T., Parolin I., Del Santo M., Homan J., Casella P., Fender R. P., Lewin W. H. G., Méndez M., Miller J. M., van der Klis M., 2006, Mon. Not. R. Astron. Soc., 367, 1113

Belloni T., Psaltis D., van der Klis M., 2002, Astrophys. J., 572, 392

Belloni T. M., Motta S. E., Muñoz-Darias T., 2011, Bulletin of the Astronomical Society of India, 39, 409

Beloborodov A. M., 1999, Astrophys. J. Lett., 510, L123

Bianchi S., Guainazzi M., Matt G., Fonseca Bonilla N., 2007, Astron. Astrophys., 467, L19

Blandford R. D., Znajek R. L., 1977, Mon. Not. R. Astron. Soc., 179, 433

Brenneman L. W., Reynolds C. S., 2006, Astrophys. J., 652, 1028

Cabanac C., Fender R. P., Dunn R. J. H., Körding E. G., 2009, Mon. Not. R. Astron. Soc., 396, 1415

Cackett E. M., Miller J. M., Bhattacharyya S., Grindlay J. E., Homan J., van der Klis M., Miller M. C., Strohmayer T. E., Wijnands R., 2008, Astrophys. J., 674, 415

Casares J., Jonker P. G., 2013, Space Sci. Rev

Casella P., Belloni T., Stella L., 2005, Astrophys. J., 629, 403

Cassatella P., Uttley P., Wilms J., Poutanen J., 2012, Mon. Not. R. Astron. Soc., 422, 2407

Chiang C.-Y., Reis R. C., Walton D. J., Fabian A. C., 2012, Mon. Not. R. Astron. Soc., 425, 2436

Churazov E., Gilfanov M., Revnivtsev M., 2001, Mon. Not. R. Astron. Soc., 321, 759

Corbel S., Aussel H., Broderick J. W., Chanial P., Coriat M., Maury A. J., Buxton M. M., Tomsick J. A., Tzioumis A. K., Markoff S., Rodriguez J., Bailyn C. D., Brocksopp C., Fender R. P., Petrucci P. O., Cadolle-Bel M., Calvelo D., Harvey-Smith L., 2013a, Mon. Not. R. Astron. Soc., 431, L107

Corbel S., Aussel H., Broderick J. W., Chanial P., Coriat M., Maury A. J., Buxton M. M., Tomsick J. A., Tzioumis A. K., Markoff S., Rodriguez J., Bailyn C. D., Brocksopp C., Fender R. P., Petrucci P. O., Cadolle-Bel M., Calvelo D., Harvey-Smith L., 2013b, Mon. Not. R. Astron. Soc., 431, L107

Corbel S., Nowak M. A., Fender R. P., Tzioumis A. K., Markoff S., 2003, Astron. Astrophys., 400, 1007

Coriat M., Corbel S., Prat L., Miller-Jones J. C. A., Cseh D., Tzioumis A. K., Brocksopp C., Rodriguez J., Fender R. P., Sivakoff G. R., 2011, Mon. Not. R. Astron. Soc., 414, 677

Coriat M., Fender R. P., Dubus G., 2012, Mon. Not. R. Astron. Soc., 424, 1991

Corral-Santana J. M., Casares J., Muñoz-Darias T., Rodríguez-Gil P., Shahbaz T., Torres M. A. P., Zurita C., Tyndall A. A., 2013, Science, 339, 1048

Curran P. A., Maccarone T. J., Casella P., Evans P. A., Landsman W., Krimm H. A., Brocksopp C., Still M., 2011, Mon. Not. R. Astron. Soc., 410, 541

Dauser T., Garcia J., Wilms J., Böck M., Brenneman L. W., Falanga M., Fukumura K., Reynolds C. S., 2013, Mon. Not. R. Astron. Soc., 430, 1694

Dauser T., Wilms J., Reynolds C. S., Brenneman L. W., 2010, Mon. Not. R. Astron. Soc., 409, 1534

Davis S. W., Blaes O. M., Hubeny I., Turner N. J., 2005, Astrophys. J., 621, 372

de La Calle Pérez I., Longinotti A. L., Guainazzi M., Bianchi S., Dovčiak M., Cappi M., Matt G., Miniutti G., Petrucci P. O., Piconcelli E., Ponti G., Porquet D., Santos-Lleó M., 2010, Astron. Astrophys., 524, A50

Di Salvo T., Done C., Życki P. T., Burderi L., Robba N. R., 2001, Astrophys. J., 547, 1024

Done C., Diaz Trigo M., 2010, Mon. Not. R. Astron. Soc., 407, 2287

Done C., Gierliński M., 2006, Mon. Not. R. Astron. Soc., 367, 659

Done C., Gierliński M., Kubota A., 2007, Astron. Astrophys. Rev, 15, 1

Done C., Jin C., Middleton M., Ward M., 2013, Mon. Not. R. Astron. Soc., 434, 1955

Done C., Kubota A., 2006, Mon. Not. R. Astron. Soc., 371, 1216

Dovčiak M., Karas V., Yaqoob T., 2004, Astrophys. J. Suppl. Ser., 153, 205

Dunn R. J. H., Fender R. P., Körding E. G., Belloni T., Cabanac C., 2010, Mon. Not. R. Astron. Soc., 403, 61

Dunn R. J. H., Fender R. P., Körding E. G., Belloni T., Merloni A., 2011, Mon. Not. R. Astron. Soc., 411, 337

Dunn R. J. H., Fender R. P., Körding E. G., Cabanac C., Belloni T., 2008, Mon. Not. R. Astron. Soc., 387, 545

Ebisawa K., Ogawa M., Aoki T., Dotani T., Takizawa M., Tanaka Y., Yoshida K., Miyamoto S., Iga S., Hayashida K., Kitamoto S., Terada K., 1994, Publ. Astron. Soc. Jpn., 46, 375

Esin A. A., McClintock J. E., Drake J. J., Garcia M. R., Haswell C. A., Hynes R. I., Muno M. P., 2001, Astrophys. J., 555, 483

Esin A. A., McClintock J. E., Narayan R., 1997, Astrophys. J., 489, 865

Fabian A. C., Iwasawa K., Reynolds C. S., Young A. J., 2000, Publ. Astron. Soc. Pac., 112, 1145

Fabian A. C., Parker M. L., Wilkins D. R., Miller J. M., Kara E., Reynolds C. S., Dauser T., 2014, ArXiv e-prints

Fabian A. C., Pringle J. E., Rees M. J., 1975, Mon. Not. R. Astron. Soc., 172, 15P

Fabian A. C., Rees M. J., Stella L., White N. E., 1989, Mon. Not. R. Astron. Soc., 238, 729

Fabian A. C., Ross R. R., 2010, Space Sci. Rev, 157, 167

Fabian A. C., Vaughan S., Nandra K., Iwasawa K., Ballantyne D. R., Lee J. C., De Rosa A., Turner A., Young A. J., 2002, Mon. Not. R. Astron. Soc., 335, L1

Fabian A. C., Wilkins D. R., Miller J. M., Reis R. C., Reynolds C. S., Cackett E. M., Nowak M. A., Pooley G. G., Pottschmidt K., Sanders J. S., Ross R. R., Wilms J., 2012, Mon. Not. R. Astron. Soc., p. 3135

Fender R., Belloni T., 2012, Science, 337, 540

Fender R. P., Belloni T. M., Gallo E., 2004, Mon. Not. R. Astron. Soc., 355, 1105

Fender R. P., Gallo E., Jonker P. G., 2003, Mon. Not. R. Astron. Soc., 343, L99

Fender R. P., Gallo E., Russell D., 2010, Mon. Not. R. Astron. Soc., 406, 1425

Frank J., King A., Raine D. J., 2002, *Accretion Power in Astrophysics: Third Edition*

Gallo E., Fender R. P., Pooley G. G., 2003, Mon. Not. R. Astron. Soc., 344, 60

Gallo E., Miller B. P., Fender R., 2012, Mon. Not. R. Astron. Soc., 423, 590

García J., Dauser T., Lohfink A., Kallman T. R., Steiner J. F., McClintock J. E., Brenneman L., Wilms J., Eikmann W., Reynolds C. S., Tombesi F., 2014, Astrophys. J., 782, 76

García J., Dauser T., Reynolds C. S., Kallman T. R., McClintock J. E., Wilms J., Eikmann W., 2013, Astrophys. J., 768, 146

García J., Kallman T., 2009, in Hubeny I., Stone J. M., MacGregor K., Werner K. (eds.), *American Institute of Physics Conference Series*, vol. 1171 of *American*

Institute of Physics Conference Series, pp. 363–364
García J., Kallman T. R., 2010, Astrophys. J., 718, 695
García J., Kallman T. R., Mushotzky R. F., 2011, Astrophys. J., 731, 131
George I. M., Fabian A. C., 1991, Mon. Not. R. Astron. Soc., 249, 352
Gierliński M., Done C., 2004, Mon. Not. R. Astron. Soc., 347, 885
Gierliński M., Done C., Page K., 2008, Mon. Not. R. Astron. Soc., 388, 753
Gierliński M., Zdziarski A. A., Poutanen J., Coppi P. S., Ebisawa K., Johnson W. N., 1999, Mon. Not. R. Astron. Soc., 309, 496
Gilfanov M., Churazov E., Revnivtsev M., 1999, Astron. Astrophys., 352, 182
González Hernández J. I., Casares J., Rebolo R., Israelian G., Filippenko A. V., Chornock R., 2011, Astrophys. J., 738, 95
Gou L., McClintock J. E., Steiner J. F., Narayan R., Cantrell A. G., Bailyn C. D., Orosz J. A., 2010, Astrophys. J. Lett., 718, L122
Han P., Qu J., Zhang S., Wang J., Song L., Ding G., Yan S., Lu Y., 2011, Mon. Not. R. Astron. Soc., 413, 1072
Hiemstra B., Méndez M., Done C., Díaz Trigo M., Altamirano D., Casella P., 2011, Mon. Not. R. Astron. Soc., 411, 137
Homan J., Wijnands R., van der Klis M., Belloni T., van Paradijs J., Klein-Wolt M., Fender R., Méndez M., 2001, Astrophys. J. Suppl. Ser., 132, 377
Hynes R. I., Steeghs D., Casares J., Charles P. A., O'Brien K., 2003, Astrophys. J. Lett., 583, L95
Iwasawa K., Taniguchi Y., 1993, Astrophys. J. Lett., 413, L15
Jahoda K., Markwardt C. B., Radeva Y., Rots A. H., Stark M. J., Swank J. H., Strohmayer T. E., Zhang W., 2006, Astrophys. J. Suppl. Ser., 163, 401
King A. R., Kolb U., 1999, Mon. Not. R. Astron. Soc., 305, 654
Kirsch M. G. F., Schönherr G., Kendziorra E., Freyberg M. J., Martin M., Wilms J., Mukerjee K., Breitfellner M. G., Smith M. J. S., Staubert R., 2006, Astron. Astrophys., 453, 173
Kokubun M., Makishima K., Takahashi T., Murakami T., Tashiro M., Fukazawa Y., Kamae T., Madejski G. M., Nakazawa K., Yamaoka K., Terada Y., Yonetoku D., Watanabe S., Tamagawa T., Mizuno T., Kubota A., Isobe N., Takahashi I., Sato G., Takahashi H., Hong S., Kawaharada M., Kawano N., Mitani T., Murashima M., Suzuki M., Abe K., Miyawaki R., Ohno M., Tanaka T., Yanagida T., Itoh T., Ohnuki K., Tamura K.-I., Endo Y., Hirakuri S., Hiruta T., Kitaguchi T., Kishishita T., Sugita S., Takahashi T., Takeda S., Enoto T., Hirasawa A., Katsuta J., Matsumura S., Onda K., Sato M., Ushio M., Ishikawa S.-N., Murase K., Odaka H., Suzuki M., Yaji Y., Yamada S., Yamasaki T., Yuasa T., Hxd Team, 2007, Publ.

Astron. Soc. Jpn., 59, 53
Kolehmainen M., Done C., 2010, Mon. Not. R. Astron. Soc., 406, 2206
Kolehmainen M., Done C., Díaz Trigo M., 2011, Mon. Not. R. Astron. Soc., 416, 311
Kolehmainen M., Done C., Díaz Trigo M., 2014, Mon. Not. R. Astron. Soc., 437, 316
Kong A. K. H., Kuulkers E., Charles P. A., Homer L., 2000, Mon. Not. R. Astron. Soc., 312, L49
Körding E. G., Migliari S., Fender R., Belloni T., Knigge C., McHardy I., 2007, Mon. Not. R. Astron. Soc., 380, 301
Koyama K., Tsunemi H., Dotani T., Bautz M. W., Hayashida K., Tsuru T. G., Matsumoto H., Ogawara Y., Ricker G. R., Doty J., Kissel S. E., Foster R., Nakajima H., Yamaguchi H., Mori H., Sakano M., Hamaguchi K., Nishiuchi M., Miyata E., Torii K., Namiki M., Katsuda S., Matsuura D., Miyauchi T., Anabuki N., Tawa N., Ozaki M., Murakami H., Maeda Y., Ichikawa Y., Prigozhin G. Y., Boughan E. A., Lamarr B., Miller E. D., Burke B. E., Gregory J. A., Pillsbury A., Bamba A., Hiraga J. S., Senda A., Katayama H., Kitamoto S., Tsujimoto M., Kohmura T., Tsuboi Y., Awaki H., 2007, Publ. Astron. Soc. Jpn., 59, 23
Kubota A., Done C., 2004, Mon. Not. R. Astron. Soc., 353, 980
Kubota A., Tanaka Y., Makishima K., Ueda Y., Dotani T., Inoue H., Yamaoka K., 1998, Publ. Astron. Soc. Jpn., 50, 667
Laor A., 1991, Astrophys. J., 376, 90
Leahy D. A., Darbro W., Elsner R. F., Weisskopf M. C., Kahn S., Sutherland P. G., Grindlay J. E., 1983, Astrophys. J., 266, 160
Li L.-X., Zimmerman E. R., Narayan R., McClintock J. E., 2005, Astrophys. J. Suppl. Ser., 157, 335
Lightman A. P., White T. R., 1988, Astrophys. J., 335, 57
Maccarone T. J., 2002, Mon. Not. R. Astron. Soc., 336, 1371
Maccarone T. J., 2003, Astron. Astrophys., 409, 697
Magdziarz P., Zdziarski A. A., 1995, Mon. Not. R. Astron. Soc., 273, 837
Markert T. H., Canizares C. R., Clark G. W., Lewin W. H. G., Schnopper H. W., Sprott G. F., 1973, Astrophys. J. Lett., 184, L67
Markoff S., Nowak M. A., Wilms J., 2005, Astrophys. J., 635, 1203
Markwardt C. B., Beardmore A. P., Miller J., Swank J. H., 2009a, The Astronomer's Telegram, 2120, 1
Markwardt C. B., Swank J. H., 2009, The Astronomer's Telegram, 2108, 1
Markwardt C. B., Swank J. H., Barthelmy S. D., Baumgartner W. H., Burrows

D. N., Evans P. A., Holland S. T., Hoversten E. A., Page K. L., 2009b, The Astronomer's Telegram, 2258, 1

Markwardt C. B., Swank J. H., Krimm H. A., Pereira D., Strohmayer T. E., 2009c, The Astronomer's Telegram, 2107, 1

Matt G., Fabian A. C., Ross R. R., 1993, Mon. Not. R. Astron. Soc., 262, 179

Matt G., Fabian A. C., Ross R. R., 1996, Mon. Not. R. Astron. Soc., 278, 1111

Matt G., Perola G. C., Piro L., 1991, Astron. Astrophys., 247, 25

McClintock J. E., Haswell C. A., Garcia M. R., Drake J. J., Hynes R. I., Marshall H. L., Muno M. P., Chaty S., Garnavich P. M., Groot P. J., Lewin W. H. G., Mauche C. W., Miller J. M., Pooley G. G., Shrader C. R., Vrtilek S. D., 2001, Astrophys. J., 555, 477

McClintock J. E., Horne K., Remillard R. A., 1995, Astrophys. J., 442, 358

McClintock J. E., Narayan R., Davis S. W., Gou L., Kulkarni A., Orosz J. A., Penna R. F., Remillard R. A., Steiner J. F., 2011, Classical and Quantum Gravity, 28 (11), 114009

McClintock J. E., Narayan R., Garcia M. R., Orosz J. A., Remillard R. A., Murray S. S., 2003, Astrophys. J., 593, 435

McClintock J. E., Narayan R., Steiner J. F., 2013, Space Sci. Rev

McClintock J. E., Shafee R., Narayan R., Remillard R. A., Davis S. W., Li L.-X., 2006, Astrophys. J., 652, 518

McHardy I. M., Koerding E., Knigge C., Uttley P., Fender R. P., 2006, Nature, 444, 730

McKinney J. C., 2005, Astrophys. J. Lett., 630, L5

Merloni A., Fabian A. C., Ross R. R., 2000, Mon. Not. R. Astron. Soc., 313, 193

Meyer F., Meyer-Hofmeister E., 1981, Astron. Astrophys., 104, L10

Middleton M. J., Miller-Jones J. C. A., Fender R. P., 2014, Mon. Not. R. Astron. Soc., 439, 1740

Migliari S., Fender R. P., van der Klis M., 2005, Mon. Not. R. Astron. Soc., 363, 112

Miller J. M., 2007, Ann. Rev. Astron. Astrophys., 45, 441

Miller J. M., Cackett E. M., Reis R. C., 2009, Astrophys. J. Lett., 707, L77

Miller J. M., D'Aì A., Bautz M. W., Bhattacharyya S., Burrows D. N., Cackett E. M., Fabian A. C., Freyberg M. J., Haberl F., Kennea J., Nowak M. A., Reis R. C., Strohmayer T. E., Tsujimoto M., 2010, Astrophys. J., 724, 1441

Miller J. M., Fabian A. C., Wijnands R., Reynolds C. S., Ehle M., Freyberg M. J., van der Klis M., Lewin W. H. G., Sanchez-Fernandez C., Castro-Tirado A. J., 2002, Astrophys. J. Lett., 570, L69

Miller J. M., Homan J., Miniutti G., 2006a, Astrophys. J. Lett., 652, L113

Miller J. M., Homan J., Steeghs D., Rupen M., Hunstead R. W., Wijnands R., Charles P. A., Fabian A. C., 2006b, Astrophys. J., 653, 525

Miller J. M., Reynolds C. S., Fabian A. C., Cackett E. M., Miniutti G., Raymond J., Steeghs D., Reis R., Homan J., 2008a, Astrophys. J. Lett., 679, L113

Miller L., Turner T. J., Reeves J. N., 2008b, Astron. Astrophys., 483, 437

Miller-Jones J. C. A., Jonker P. G., Ratti E. M., Torres M. A. P., Brocksopp C., Yang J., Morrell N. I., 2011, Mon. Not. R. Astron. Soc., 415, 306

Miniutti G., Fabian A. C., 2004, Mon. Not. R. Astron. Soc., 349, 1435

Miniutti G., Fabian A. C., Miller J. M., 2004, Mon. Not. R. Astron. Soc., 351, 466

Mitsuda K., Inoue H., Koyama K., Makishima K., Matsuoka M., Ogawara Y., Suzuki K., Tanaka Y., Shibazaki N., Hirano T., 1984, Publ. Astron. Soc. Jpn., 36, 741

Morningstar W. R., Miller J. M., Reis R. C., Ebisawa K., 2014, Astrophys. J. Lett., 784, L18

Motta S., Belloni T., Homan J., 2009, Mon. Not. R. Astron. Soc., 400, 1603

Motta S., Muñoz-Darias T., Casella P., Belloni T., Homan J., 2011, Mon. Not. R. Astron. Soc., 418, 2292

Motta S. E., Casella P., Muñoz-Darias T., Henze M., Sanna A., Fender R., Belloni T., 2014, Mon. Not. R. Astron. Soc., submitted

Muñoz-Darias T., Casares J., Martínez-Pais I. G., 2008, Mon. Not. R. Astron. Soc., 385, 2205

Muñoz-Darias T., Coriat M., Plant D. S., Ponti G., Fender R. P., Dunn R. J. H., 2013, Mon. Not. R. Astron. Soc., 432, 1330

Muñoz-Darias T., Motta S., Belloni T. M., 2011, Mon. Not. R. Astron. Soc., 410, 679

Muñoz-Darias T., Motta S., Pawar D., Belloni T. M., Campana S., Bhattacharya D., 2010, Mon. Not. R. Astron. Soc., 404, L94

Nandra K., George I. M., Mushotzky R. F., Turner T. J., Yaqoob T., 1997, Astrophys. J. Lett., 488, L91

Nandra K., O'Neill P. M., George I. M., Reeves J. N., 2007, Mon. Not. R. Astron. Soc., 382, 194

Narayan R., McClintock J. E., 2012, Mon. Not. R. Astron. Soc., 419, L69

Narayan R., McClintock J. E., Yi I., 1996, Astrophys. J., 457, 821

Narayan R., Yi I., 1995, Astrophys. J., 452, 710

Nayakshin S., Kallman T. R., 2001, Astrophys. J., 546, 406

Nayakshin S., Kazanas D., Kallman T. R., 2000, Astrophys. J., 537, 833

Ng C., Díaz Trigo M., Cadolle Bel M., Migliari S., 2010, Astron. Astrophys., 522, A96

Novikov I. D., Thorne K. S., 1973, in Dewitt C., Dewitt B. S. (eds.), *Black Holes (Les Astres Occlus)*, pp. 343–450

Orosz J. A., McClintock J. E., Aufdenberg J. P., Remillard R. A., Reid M. J., Narayan R., Gou L., 2011, Astrophys. J., 742, 84

Orosz J. A., McClintock J. E., Remillard R. A., Corbel S., 2004, Astrophys. J., 616, 376

Özel F., Psaltis D., Narayan R., McClintock J. E., 2010, Astrophys. J., 725, 1918

Penrose R., 1969, Nuovo Cimento Rivista Serie, 1, 252

Petrucci P.-O., Cabanac C., Corbel S., Koerding E., Fender R., 2014, Astron. Astrophys., 564, A37

Ponti G., Cappi M., Vignali C., Miniutti G., Tombesi F., Dadina M., Fabian A. C., Grandi P., Kaastra J., Petrucci P. O., Bianchi S., Matt G., Maraschi L., Malaguti G., 2009, Mon. Not. R. Astron. Soc., 394, 1487

Ponti G., Fender R. P., Begelman M. C., Dunn R. J. H., Neilsen J., Coriat M., 2012, Mon. Not. R. Astron. Soc., 422, L11

Poutanen J., 2002, Mon. Not. R. Astron. Soc., 332, 257

Reis R. C., Fabian A. C., Miller J. M., 2010, Mon. Not. R. Astron. Soc., 402, 836

Reis R. C., Fabian A. C., Ross R. R., Miller J. M., 2009, Mon. Not. R. Astron. Soc., 395, 1257

Reis R. C., Fabian A. C., Ross R. R., Miniutti G., Miller J. M., Reynolds C., 2008, Mon. Not. R. Astron. Soc., 387, 1489

Reis R. C., Miller J. M., Fabian A. C., Cackett E. M., Maitra D., Reynolds C. S., Rupen M., Steeghs D. T. H., Wijnands R., 2011, Mon. Not. R. Astron. Soc., 410, 2497

Reis R. C., Miller J. M., Reynolds M. T., Fabian A. C., Walton D. J., 2012, Astrophys. J., 751, 34

Reis R. C., Miller J. M., Reynolds M. T., Fabian A. C., Walton D. J., Cackett E., Steiner J. F., 2013a, Astrophys. J., 763, 48

Reis R. C., Reynolds M. T., Miller J. M., Walton D. J., Maitra D., King A., Degenaar N., 2013b, Astrophys. J., 778, 155

Remillard R. A., McClintock J. E., 2006, Ann. Rev. Astron. Astrophys., 44, 49

Reynolds C. S., 2013, Space Sci. Rev

Reynolds C. S., Brenneman L. W., Lohfink A. M., Trippe M. L., Miller J. M., Fabian A. C., Nowak M. A., 2012, Astrophys. J., 755, 88

Reynolds C. S., Fabian A. C., Makishima K., Fukazawa Y., Tamura T., 1994, Mon.

Not. R. Astron. Soc., 268, L55
Reynolds C. S., Nowak M. A., 2003, Phys. Rep., 377, 389
Roberts T. P., 2007, ApSS, 311, 203
Ross R. R., Fabian A. C., 1993, Mon. Not. R. Astron. Soc., 261, 74
Ross R. R., Fabian A. C., 2005, Mon. Not. R. Astron. Soc., 358, 211
Ross R. R., Fabian A. C., 2007, Mon. Not. R. Astron. Soc., 381, 1697
Ross R. R., Fabian A. C., Young A. J., 1999, Mon. Not. R. Astron. Soc., 306, 461
Rossi S., Homan J., Miller J. M., Belloni T., 2005, Mon. Not. R. Astron. Soc., 360, 763
Rothschild R. E., Blanco P. R., Gruber D. E., Heindl W. A., MacDonald D. R., Marsden D. C., Pelling M. R., Wayne L. R., Hink P. L., 1998, Astrophys. J., 496, 538
Russell D. M., Gallo E., Fender R. P., 2013, Mon. Not. R. Astron. Soc., 431, 405
Russell D. M., Miller-Jones J. C. A., Maccarone T. J., Yang Y. J., Fender R. P., Lewis F., 2011, Astrophys. J. Lett., 739, L19
Rykoff E. S., Miller J. M., Steeghs D., Torres M. A. P., 2007, Astrophys. J., 666, 1129
Sana H., de Mink S. E., de Koter A., Langer N., Evans C. J., Gieles M., Gosset E., Izzard R. G., Le Bouquin J.-B., Schneider F. R. N., 2012, Science, 337, 444
Shafee R., McClintock J. E., Narayan R., Davis S. W., Li L.-X., Remillard R. A., 2006, Astrophys. J. Lett., 636, L113
Shahbaz T., Fender R., Charles P. A., 2001, Astron. Astrophys., 376, L17
Shakura N. I., Sunyaev R. A., 1973, Astron. Astrophys., 24, 337
Shapiro S. L., Lightman A. P., 1976, Astrophys. J., 204, 555
Shaposhnikov N., Markwardt C., Swank J., Krimm H., 2010, Astrophys. J., 723, 1817
Shaposhnikov N., Markwardt C. B., Swank J. H., 2009, The Astronomer's Telegram, 2269, 1
Shidatsu M., Ueda Y., Tazaki F., Yoshikawa T., Nagayama T., Nagata T., Oi N., Yamaoka K., Takahashi H., Kubota A., Cottam J., Remillard R., Negoro H., 2011, Publ. Astron. Soc. Jpn., 63, 785
Shimura T., Takahara F., 1995, Astrophys. J., 445, 780
Sobolewska M. A., Papadakis I. E., Done C., Malzac J., 2011, Mon. Not. R. Astron. Soc., 417, 280
Soleri P., Muñoz-Darias T., Motta S., Belloni T., Casella P., Méndez M., Altamirano D., Linares M., Wijnands R., Fender R., van der Klis M., 2013, Mon. Not. R. Astron. Soc., 429, 1244

Steiner J. F., McClintock J. E., Narayan R., 2013, Astrophys. J., 762, 104

Steiner J. F., McClintock J. E., Remillard R. A., Gou L., Yamada S., Narayan R., 2010, Astrophys. J. Lett., 718, L117

Stiele H., Motta S., Muñoz-Darias T., Belloni T. M., 2011, Mon. Not. R. Astron. Soc., 418, 1746

Strüder L., Briel U., Dennerl K., Hartmann R., Kendziorra E., Meidinger N., Pfeffermann E., Reppin C., Aschenbach B., Bornemann W., Bräuninger H., Burkert W., Elender M., Freyberg M., Haberl F., Hartner G., Heuschmann F., Hippmann H., Kastelic E., Kemmer S., Kettenring G., Kink W., Krause N., Müller S., Oppitz A., Pietsch W., Popp M., Predehl P., Read A., Stephan K. H., Stötter D., Trümper J., Holl P., Kemmer J., Soltau H., Stötter R., Weber U., Weichert U., von Zanthier C., Carathanassis D., Lutz G., Richter R. H., Solc P., Böttcher H., Kuster M., Staubert R., Abbey A., Holland A., Turner M., Balasini M., Bignami G. F., La Palombara N., Villa G., Buttler W., Gianini F., Lainé R., Lumb D., Dhez P., 2001, Astron. Astrophys., 365, L18

Svoboda J., Dovčiak M., Goosmann R., Karas V., 2009, Astron. Astrophys., 507, 1

Takahashi T., Abe K., Endo M., Endo Y., Ezoe Y., Fukazawa Y., Hamaya M., Hirakuri S., Hong S., Horii M., Inoue H., Isobe N., Itoh T., Iyomoto N., Kamae T., Kasama D., Kataoka J., Kato H., Kawaharada M., Kawano N., Kawashima K., Kawasoe S., Kishishita T., Kitaguchi T., Kobayashi Y., Kokubun M., Kotoku J., Kouda M., Kubota A., Kuroda Y., Madejski G., Makishima K., Masukawa K., Matsumoto Y., Mitani T., Miyawaki R., Mizuno T., Mori K., Mori M., Murashima M., Murakami T., Nakazawa K., Niko H., Nomachi M., Okada Y., Ohno M., Oonuki K., Ota N., Ozawa H., Sato G., Shinoda S., Sugiho M., Suzuki M., Taguchi K., Takahashi H., Takahashi I., Takeda S., Tamura K.-I., Tamura T., Tanaka T., Tanihata C., Tashiro M., Terada Y., Tominaga S., Uchiyama Y., Watanabe S., Yamaoka K., Yanagida T., Yonetoku D., 2007, Publ. Astron. Soc. Jpn., 59, 35

Tamura M., Kubota A., Yamada S., Done C., Kolehmainen M., Ueda Y., Torii S., 2012, ArXiv e-prints

Tanaka Y., Nandra K., Fabian A. C., Inoue H., Otani C., Dotani T., Hayashida K., Iwasawa K., Kii T., Kunieda H., Makino F., Matsuoka M., 1995, Nature, 375, 659

Tarter C. B., Tucker W. H., Salpeter E. E., 1969, Astrophys. J., 156, 943

Tauris T. M., van den Heuvel E. P. J., 2006, *Formation and evolution of compact stellar X-ray sources*, pp. 623–665

Tchekhovskoy A., Narayan R., McKinney J. C., 2011, Mon. Not. R. Astron. Soc.,

418, L79

Thorne K. S., 1974, Astrophys. J., 191, 507

Tomsick J. A., Kalemci E., Kaaret P., Markoff S., Corbel S., Migliari S., Fender R., Bailyn C. D., Buxton M. M., 2008, Astrophys. J., 680, 593

Tomsick J. A., Yamaoka K., Corbel S., Kaaret P., Kalemci E., Migliari S., 2009, Astrophys. J. Lett., 707, L87

Turner M. J. L., Abbey A., Arnaud M., Balasini M., Barbera M., Belsole E., Bennie P. J., Bernard J. P., Bignami G. F., Boer M., Briel U., Butler I., Cara C., Chabaud C., Cole R., Collura A., Conte M., Cros A., Denby M., Dhez P., Di Coco G., Dowson J., Ferrando P., Ghizzardi S., Gianotti F., Goodall C. V., Gretton L., Griffiths R. G., Hainaut O., Hochedez J. F., Holland A. D., Jourdain E., Kendziorra E., Lagostina A., Laine R., La Palombara N., Lortholary M., Lumb D., Marty P., Molendi S., Pigot C., Poindron E., Pounds K. A., Reeves J. N., Reppin C., Rothenflug R., Salvetat P., Sauvageot J. L., Schmitt D., Sembay S., Short A. D. T., Spragg J., Stephen J., Strüder L., Tiengo A., Trifoglio M., Trümper J., Vercellone S., Vigroux L., Villa G., Ward M. J., Whitehead S., Zonca E., 2001, Astron. Astrophys., 365, L27

van den Heuvel E. P. J., 1992, "Endpoints of stellar evolution: The incidence of stellar mass black holes in the galaxy", Tech. rep.

van der Klis M., 1995, X-ray Binaries, pp. 252–307

van der Klis M., 2006, *Rapid X-ray Variability*, pp. 39–112, Cambridge Univ. Press, Cambridge

Walton D. J., Reis R. C., Cackett E. M., Fabian A. C., Miller J. M., 2012, Mon. Not. R. Astron. Soc., 422, 2510

Wilkins D. R., Fabian A. C., 2012, Mon. Not. R. Astron. Soc., 424, 1284

Wilms J., Allen A., McCray R., 2000, Astrophys. J., 542, 914

Yamada S., Makishima K., Uehara Y., Nakazawa K., Takahashi H., Dotani T., Ueda Y., Ebisawa K., Kubota A., Gandhi P., 2009, Astrophys. J. Lett., 707, L109

Zdziarski A. A., Poutanen J., Paciesas W. S., Wen L., 2002, Astrophys. J., 578, 357

Zhang S. N., Cui W., Chen W., 1997, Astrophys. J. Lett., 482, L155

Zycki P. T., Krolik J. H., Zdziarski A. A., Kallman T. R., 1994, Astrophys. J., 437, 597